JUNO Conceptual Design Report

August 27, 2015

Abstract

The Jiangmen Underground Neutrino Observatory (JUNO) is proposed to determine the neutrino mass hierarchy using an underground liquid scintillator detector. It is located 53 km away from both Yangjiang and Taishan Nuclear Power Plants in Guangdong, China. The experimental hall, spanning more than 50 meters, is under a granite mountain of over 700 m overburden. Within six years of running, the detection of reactor antineutrinos from Yangjiang and Taishan Nuclear Power Plants can resolve the neutrino mass hierarchy at a confidence level of 3-4σ. Meanwhile, the excellent energy resolution and large fiducial volume will lead to precise determination of the neutrino oscillation parameters $\sin^2\theta_{12}$, Δm^2_{21}, and $|\Delta m^2_{ee}|$ to an accuracy of better than 1%. As a multipurpose underground neutrino observatory, the JUNO detector can also observe neutrinos/antineutrinos from terrestrial and extra-terrestrial sources, including the supernova burst neutrinos, diffused supernova neutrinos, geoneutrinos, atmospheric neutrinos and solar neutrinos, which provide exciting opportunities to address important topics in neutrino and astro-particle physics. JUNO is also sensitive to new physics beyond the Standard Model, including sterile neutrinos, neutrinos from dark-matter annihilation, proton decays, as well as scenarios of nonstandard neutrino interactions and Lorentz/CPT invariance violations.

The central detector (CD), which contains 20,000 tons liquid scintillator and ∼17,000 PMTs, is designed to have a very good energy resolution of 3% and a long lifetime of over 20 years. The baseline option of the central detector is an acrylic sphere of 35 m in diameter supported by a stainless-steel structure. The acrylic sphere will be built from hundreds of acrylic sheets with a thickness of 12 cm by the bulk-polymerization technology. The backup option of the central detector is a balloon supported by acrylic panels in a steel tank. The PMT assembly design including water sealing, implosion protection and installation on the detector is in progress, and a prototype to study the performance of PMTs is under preparation.

The CD is filled with liquid scintillator (LS) which serves as the target for the detection of neutrinos and antineutrinos. The current choice of the LS is: linear alkyl benzene (LAB) as the solvent, plus PPO as the scintillation fluor and a wavelength-shifter (Bis-MSB). The energy resolution of JUNO is required to be 3% at 1MeV, corresponding to at least 1,100 photoelectrons (pe) per MeV of deposited energy. Low-background environment is crucial since only a few tens of neutrino events will be detected per day. As a consequence, light yield, fluorescence time profile, transparency and radio-purity are the key features of the LS. A scheme for mass production of LS will be set up to comprise all steps from the raw material production, transportation, local facilities for liquid-handling and purification, instrumentation for quality control as well as safety and cleaning methods.

The veto system is used for muon detection, muon induced background study and reduction. It consists of a Water Cherenkov detector and a Top Tracker system. The Water Cherenkov detector is a pool filled with purified water and instrumented with PMTs surrounding the CD. The PMT arrangement is optimized for high muon detection efficiency and good track resolution. The surface of this detector is covered by Tyvek as reflecting and diffusing sheets to increase the light detection. High quality

ultrapure water is required to achieve the designed performance. A water circulation and purification system with a capacity of 20,000 - 30,000 tons will be built. The OPERA Target Tracker made of scintillating strips and readout by multi-anode PMTs will be re-used as the Top Tracker to reconstruct the cosmic muons' direction, covering ∼1/3 of the top area. This independent muon information will help muon tagging, track reconstruction and efficency study to understand and reduce cosmogenic backgrounds.

The photon detectors, PMTs, are mounted on a spherical surface of ∼38 m in diameter as tightly as possible, covering ∼75% of the surface area of the sphere. The total number of inward facing PMTs to detect scintillating photons generated in the CD is ∼17,000 if 508 mm (20") diameter PMTs are used. Additional ∼1,600 outward facing PMTs will be used to detect Cherenkov photons in the buffer water surrounding the vessel of liquid scintillator. The possibility of using small 3" diameter PMTs to fill the gaps among the large 20" PMTs to improve the energy and vertex resolution is being considered. Main requirements for JUNO PMTs are high and uniform quantum efficiency (QE), good single photoelectron detector capability, large dynamic range, low noise rate, low late and after-pulse rate, low transit time spread, high reliability, long lifetime and low system cost. PMT samples or prototypes from three manufacturers are being evaluated and the choice will be made in near future. The earth's magnetic field will affect the performance of the PMTs. A compensation coil system will be utilized as shielding to reduce this effect. The coil will be installed around the CD and inside the water pool.

For neutrino mass hierarchy determination, the JUNO detector needs to be thoroughly calibrated to achieve an overall energy resolution of 3% at 1 MeV, and energy nonlinearity better than 1%. The calibration system should be capable of deploying multiple sources (light, γ, e^+, e^-, neutron and α), covering the entire energy range of inverse-β decay, and achieve a full-volume position coverage inside the detector. The source geometry also needs to be specially designed to minimize the shadowing effects and the energy loss effects. An ultrasonic positioning system is envisioned to achieve a source positioning accuracy of better than 3 cm, serving as a benchmark system for the reconstruction as well as the detector response correction. Several complementary calibration subsystems with different position coverage and usage frequencies are selected for further investigations.

The JUNO electronics consists of two readout systems for the central detector and veto detector. Its main task is to read out signals from the PMTs of the two subdetectors, to process the data and then to transfer the data to the DAQ system. The readout electronics consists of amplification, analog to digital conversion, data processing, collection and transmission, triggering, high voltage control, etc. All channels in the system will be recorded by high-speed sampling, and then the data containing possible physics events will be selected by the trigger. Since the whole detector will be in water, to avoid signal loss due to long distance transmission, most parts of electronics system will also be put in the water, close to the detector body. So the electronics system needs to be a reliable underwater high-speed sampling system.

The data acquisition (DAQ) system will record all the events passing trigger criteria including signal and background events. The DAQ must record data from the electronics systems of central detector and veto detector with precise timing and charge information. The DAQ builds a full event with data fragments from different subdetectors, analyzes and processes the data, and saves all the relevant data to disk. The

design baseline requires reading out event data at the rate of 2GB/s, which will be increased to 10GB/s when a 10 kpc distance supernova explosion happens. A distributed architecture is needed to fulfill these requirements and a modular and extendible data flow schema is also required.

The detector control system (DCS) aims at establishing long-term monitoring of the parameters that might affect the performance of the experiment equipment. The parameters include temperature, humidity, liquid level of the LS, gas pressure and the pressure in the experimental hall etc. Some subsystems need to provide device control such as calibration system, gas system, water cycle system and power system. The real time operation states of the devices will be monitored and recorded into the database.

The experimental data collected by the JUNO detector are transferred to the data center through a dedicated network for further data processing and analysis. A rough estimation suggests a level of 10,000 CPU cores and 10 PB disk storage connected by a 40 Gbps backbone high-speed network. For possible peak demands, the platform is required to be able to integrate the computing resources from all JUNO members via a distributed computing environment. The offline system will calibrate raw data from the detector, produce reconstructed data, generate Monte Carlo data, and provide software tools for physics analysis. The offline software includes framework and experiment related software. The framework is the underlying software supporting the whole system. Based on the framework, the experiment related software will be developed, such as software for event data model, data I/O, event generation, detector simulation, event reconstruction, physics analysis, geometry service, event display, and database service, etc.

After the completion of civil construction, all subsystems will be installed to form the complete JUNO detector. The guidelines for integration, assembly, installation and commissioning need to be established and proper regulations will be introduced to control the onsite progress. The standardized review process will be implemented to ensure the experimental equipment meets the requirements for both performance and safety.

JUNO Collaboration

Zelimir Djurcic[1], Vic Guarino[1], Anatael Cabrera[2], Hervé De Kerret[2], Cristina Volpe[2], Xinheng Guo[3], Jing Xu[3], Shouyang Hu[4], Hanxiong Huang[4], Siyu Jian[4], Xiaomei Li[4], Xinglong Li[4], Hao Liang[4], Jie Ren[4], Xichao Ruan[4], Minshan Zheng[4], Jing Zhou[4], Jose Busto[5], Damien Dornic[5], Jiaxing Li[6], Dongmei Xia[6], Wenxiong Zhou[6], Rupert Leitner[7], Viktor Pec[7], Bedrich Roskovec[7], Vit Vorobel[7], Pingping Chen[8], Li Kang[8], Ruiting Lei[8], Shanfeng Li[8], Yi Li[8], Shengxin Lin[8], Bin Ren[8], Caishen Wang[8], Yadong Wei[8], Lei Yang[8], Chiye Yu[8], Zhijian Zhang[8], Hua Zheng[8], Fengpeng An[9], Tobias Lachenmaier[10], Alexander Tietzsch[10], Christian Grewing[11], Michael Karagounis[11], Andre Kruth[11], Pavithra Muralidharan[11], Nina Parkalian[11], Markus Robens[11], Stefan Van Waasen[11], Yu Yao[11], Ugur Yegin[11], Can Fang[12], Daojin Hong[12], Jingjing Liang[12], Hongbang Liu[12], Xiangdong Ruan[12], Lei Huo[13], Jianli Liu[13], Guoli Wang[13], Jingbo Zhang[13], Daniel Bick[14], Caren Hagner[14], Markus Kaiser[14], Sebastian Lorenz[14], Björn Wonsak[14], Haonan Gan[15], Chuan Lu[15], Yufei Xi[15], Guangpeng An[16], Xiao Cai[16], Guofu Cao[16], Jun Cao[16], Jinfan Chang[16], Mingming Chen[16], Xuan Chen[16], Yaping Cheng[16], Ziyan Deng[16], Yayun Ding[16], Jian Fang[16], Marco Grassi[16], Minghao Gu[16], Mengyun Guan[16], Wanlei Guo[16], Ziguo Han[16], Jiajun Hao[16], Miao He[16], Yuekun Heng[16], Shaojing Hou[16], Jun Hu[16], Tao Hu[16], Wei Hu[16], Soeren Jetter[16], Xiaolu Ji[16], Xiaoshan Jiang[16], Bowen Kan[16], Xiangcui Lei[16], Fei Li[16], Nan Li[16], Weidong Li[16], Weiguo Li[16], Xiaonan Li[16], Yufeng Li[16], Tao Lin[16], Gang Liu[16], Jinchang Liu[16], Shulin Liu[16], Haoqi Lu[16], Jiashu Lu[16], Junguang Lu[16], Fengjiao Luo[16], Qiumei Ma[16], Si Ma[16], Xiaoyan Ma[16], Jian Min[16], Zhe Ning[16], Fazhi Qi[16], Sen Qian[16], Xiaohui Qian[16], Zhonghua Qin[16], Jingyan Shi[16], Gongxing Sun[16], Xilei Sun[16], Yongzhao Sun[16], Ruiguang Wang[16], Yifang Wang[16], Zheng Wang[16], Zhigang Wang[16], Zhimin Wang[16], Wei Wei[16], Liangjian Wen[16], Yijie Wen[16], Zhi Wu[16], Jingkai Xia[16], Yuguang Xie[16], Jilei Xu[16], Lingyu Xu[16], Baojun Yan[16], Xiongbo Yan[16], Changgen Yang[16], Mei Ye[16], Boxiang Yu[16], Zeyuan Yu[16], Shan Zeng[16], Tingxuan Zeng[16], Liang Zhan[16], Chengcai Zhang[16], Guoqing Zhang[16], Jiawen Zhang[16], Jie Zhang[16], Kun Zhang[16], Peng Zhang[16], Xiaomei Zhang[16], Xuan Zhang[16], Yinhong Zhang[16], Yongjie Zhang[16], Yongpeng Zhang[16], Jie Zhao[16], Mei Zhao[16], Tianchi Zhao[16], Yubin Zhao[16], Weili Zhong[16], Li Zhou[16], Shun Zhou[16], Kejun Zhu[16], Honglin Zhuang[16], Jiaheng Zou[16], Marica Baldoncini[17], Giovanni Fiorentini[17], Fabio Mantovani[17], Michele Montuschi[17], Barbara Ricci[17], Virginia Strati[17], Alessandro Paoloni[18], Lucia Votano[18], Vito Antonelli[19], Augusto Brigatti[19], Davide D'angelo[19], Richard Ford[19], Marco Giammarchi[19], Paolo Lombardi[19], Livia Ludhova[19], Emanuela Meroni[19], Lino Miramonti[19], Sergio Parmeggiano[19], Gioacchino Ranucci[19], Alessandra Re[19], Paolo Saggese[19], Marco Bellato[20], Stefano Dusini[20], Ivano Lippi[20], Guang Meng[20], Mauro Mezzetto[20], Luca Stanco[20], Fausto Ortica[21], Nicomede Pelliccia[21], Aldo Romani[21], Stefano Mari[22], Giuseppe Salamanna[22], Leonid Bezrukov[23], Evgeny Doroshkevich[23], Svetlana Krokhaleva[23], Bayarto Lubsandorzhiev[23], Sultim Lubsandorzhiev[23], Vladimir Lyashuk[23], Valery Sinev[23], Igor Tkachev[23], Evgeny Yanovich[23], Thomas Adam[24], Eric Baussan[24], Timothée Brugière[24], Marcos Dracos[24], Gérard Gaudiot[24], Cécile Jollet[24], Anselmo Meregaglia[24], Pascal Poussot[24], Jacky Schuler[24], Jacques Wurtz[24], Paul Hackspacher[25], Michael Wurm[25], Alexander Olshevskiy[26], Nikolay Anfimov[26], Artem Chukanov[26], Sergey Dmitrievsky[26], Maria Dolgareva[26], Dmitry Fedoseev[26], Andrey Formozov[26], Maxim Gonchar[26], Yuri Gornushkin[26], Vasily Gromov[26], Denis Korablev[26], Alexey Krasnoperov[26], Zinovy Krumshteyn[26], Nikolay Morozov[26], Dmitry Naumov[26], Elena Naumova[26], Igor Nemchenok[26], Taras Rezinko[26], Arseniy Rybnikov[26], Andrey Sadovsky[26], Alexandr Selyunin[26], Oleg Smirnov[26], Dmitriy Taichenachev[26], Jingbin Lu[27], Margherita Buizza Avanzini[28], Olivier Drapier[28], Michel Gonin[28], Matthieu Licciardi[28], Thomas Mueller[28], Yixue Chen[29], Ran Han[29], Fan Lu[29], Xubo Ma[29], Kuo-Lun Jen[30], Guey-Lin Lin[30], Yen-Hsun Lin[30], Chia-Hao Wu[30], Dewen Cao[31], Shenjian Chen[31], Xiaozhong Huang[31], Ming Qi[31], Hongxin Wang[31], Wenwen Wang[31], Haibo Yang[31], Yuzhen Yang[31], Guangyou Yu[31], Simon Blyth[32], Yee Hsiung[32], Bei-Zhen Hu[32], Hsiao-Ru Pan[32], Yu-Chen Tung[32], Yun Chang[33], Chung-Hsiang Wang[33], Xinying Li[34], Jinyan Liu[34], Yuanyuan Liu[34], Cui Wang[34], Yin Xu[34], Yujiao Yang[34], Chunxu Yu[34], Xiangyu Zheng[34], Yajun Mao[35], Hao Qiao[35], Siguang Wang[35], Ying Yuan[35], Marco Díaz[36], Yury Malyshkin[36], Juan Ochoa-ricoux[36], Christoph Genster[36], Florian Lenz[36], Michael Soiron[36], Achim Stahl[36], Jochen Steinmann[36], Marcel Weifels[36], Christopher Wiebusch[36], Quanyou Chen[37], Xingtao Huang[37], Chao Li[37], Teng Li[37], Meng Wang[37], Qun Wu[37], Mengting Yang[37], Guodong Guo[38], Jianglai Liu[38], Feiyang Zhang[38], Tao Zhang[38], Yuanyuan Zhang[38], Frédéric

Yermia[39], Zhibing Li[40], Hu Liu[40], Jian Tang[40], Wei Wang[40], Steven Chan-fai Wong[40], Zhengyun You[40], Honghao Zhang[40], Yumei Zhang[40], Xiao Fang[41], Chaowen Yang[41], Rong Zhou[41], Marianne Göger-neff[42], Dominikus Hellgartner[42], Lothar Oberauer[42], Sabrina Prummer[42], Julia Sawatzki[42], Shaomin Chen[43], Zhi Deng[43], Guanghua Gong[43], Hui Gong[43], Liping Lei[43], Fule Li[43], Gang Shi[43], Yongjiu Shi[43], Yi Wang[43], Yuanqing Wang[43], Zhe Wang[43], Zongyi Wang[43], Zhenxiong Yuan[43], Pan Zeng[43], Yan Zhou[43], Liang Zong[43], Shi Chen[44], Qian Liu[44], Yuning Zhang[44], Yangheng Zheng[44], Barbara Clerbaux[45], Laurent Favart[45], Yifan Yang[45], William Mcdonough[46], Scott Wipperfurth[46], Xiangdong Ji[47], Mengjiao Xiao[47], Riccardo Brugnera[48], Alberto Garfagnini[48], Chiara Sirignano[48], Timo Enqvist[49], Pasi Kuusiniemi[49], Qi An[50], Wenju Huo[50], Di Jiang[50], Hao Liang[50], Qin Liu[50], Shubin Liu[50], Haiping Peng[50], Yongjie Sun[50], Nan Zhou[50], Hao Cai[51], Xuefeng Ding[51], Xingchen Ye[51], Zhenyu Zhang[51], Xiang Zhou[51], Haiwen Zhu[51], Donghua Fan[52], Yongbing Long[52], Yi Wang[52], Guorong Zhou[52], Yuhang Guo[53], Zhipeng Lv[53], Qingmin Zhang[53], Shu Luo[54], Ara Ioannisian[55], Daniel Ioannisyan[55], Narine Kazarian[55], Davit Mayilyan[55]

[1] *Argonne National Laboratory, Argonne, IL, USA*
[2] *Astro-Particle Physics Laboratory (CNRS/CEA/Paris7/Observatoire de Paris), Paris, France*
[3] *Beijing Normal University, Beijing, China*
[4] *China Institute of Atomic Energy, Beijing, China*
[5] *Centre de Physique des Particules de Marseille, Marseille, France*
[6] *Chongqing University, Chongqing, China*
[7] *Charles University, Faculty of Mathematics and Physics, Prague, Czech Republic*
[8] *Dongguan University of Technology, Dongguan, China*
[9] *East China University of Science and Technology, Shanghai, China*
[10] *Eberhard Karls Universität Tübingen, Physikalisches Institut, Tübingen, Germany*
[11] *Forschungszentrum Jülich GmbH, Central Institute of Engineering, Electronics and Analytics - Electronic Systems(ZEA-2), Jülich, Germany*
[12] *Guangxi University, Nanning, China*
[13] *Harbin Institute of Technology, Harbin, China*
[14] *Institute of Experimental Physics, University of Hamburg, Hamburg, Germany*
[15] *Institute of Hydrogeology and Environmental Geology, Chinese Academy of Geological Sciences, Shijiazhuang, China*
[16] *Institute of High Energy Physics, Beijing, China*
[17] *Department of Physics and Earth Science, University of Ferrara and INFN Sezione di Ferrara, Ferrara, Italy*
[18] *Laboratori Nazionali di Frascati dell'INFN, Roma, Italy*
[19] *INFN Sezione di Milano and Dipartimento di Fisica dell Università di Milano, Milano, Italy*
[20] *INFN Sezione di Padova, Padova, Italy*
[21] *INFN and University of Perugia - Department of Chemistry, Biology and Biotechnology, Perugia, Italy*
[22] *University of Roma Tre and INFN Sezione Roma Tre, Roma, Italy*
[23] *Institute for Nuclear Research of the Russian Academy of Sciences, Moscow, Russia*
[24] *Institut Pluridisciplinaire Hubert Curien, Université de Strasbourg, CNRS/IN2P3, Strasbourg, France*
[25] *Institute of Physics and EC PRISMA, Johannes-Gutenberg University Mainz, Mainz, Germany*
[26] *Joint Institute for Nuclear Research, Dubna, Russia*
[27] *Jilin University, Changchun, China*
[28] *Leprince-Ringuet Laboratory Ecole Polytechnique, Palaiseau Cedex, France*
[29] *North China Electric Power University, Beijing, China*
[30] *Institute of Physics National Chiao-Tung University, Hsinchu, Taiwan, China*
[31] *Nanjing University, Nanjing, China*
[32] *Department of Physics, National Taiwan University, Taipei, Taiwan, China*
[33] *National United University, Miao-Li, Taiwan, China*
[34] *Nankai University, Tianjin, China*
[35] *School of Physics, Peking University, Beijing, China*
[36] *III. Physikalisches Institut B, RWTH Aachen University, Aachen, Germany*
[37] *Shandong University, Jinan, China*
[38] *Shanghai Jiao Tong University, Shanghai, China*

[39] *SUBATECH, CNRS/IN2P3, Université de Nantes, Ecole des Mines de Nantes, Nantes, France*
[40] *Sun Yat-Sen University, Guangzhou, China*
[41] *Sichuan University, Chengdu, China*
[42] *Technical University of Munich, Garching, Germany*
[43] *Tsinghua University, Beijing, China*
[44] *University of Chinese Academy of Sciences, Beijing, China*
[45] *Université Libre de Bruxelles, Brussels, Belgium*
[46] *Department of Geology, University of Maryland, College Park, MD 20742, USA*
[47] *Department of Physics, University of Maryland, College Park, MD, USA*
[48] *Dipartimento di Fisica e Astronomia dell'Università di Padova and INFN Sezione di Padova, Padova, Italy*
[49] *Oulu Southern Institute, University of Oulu, Pyhasalmi, Finland*
[50] *University of Science and Technology of China, Hefei, China*
[51] *Wuhan University, Wuhan, China*
[52] *Wuyi University, Jiangmen, China*
[53] *Xi'an Jiaotong University, Xi'an, China*
[54] *Xiamen University, Xiamen, China*
[55] *Yerevan Physics Institute, Yerevan, Armenia*

Contents

List of Figures ix

List of Tables xvii

1 Introduction 1
1.1 Neutrino Physics: Status and Prospect . . . 1
1.1.1 Fundamentals of Massive Neutrinos . . . 1
1.1.2 Open Issues of Massive Neutrinos . . . 2
1.2 JUNO Experiment . . . 3
1.3 Physics Potentials . . . 5
1.3.1 Mass Hierarchy . . . 5
1.3.2 Precision Measurement of Mixing Parameters . . . 7
1.3.3 Supernova Neutrinos . . . 9
1.3.4 Diffuse Supernova Neutrino Background . . . 12
1.3.5 Solar Neutrinos . . . 14
1.3.6 Atmospheric Neutrinos . . . 17
1.3.7 Geo-Neutrinos . . . 17
1.3.8 Nucleon Decay . . . 19
1.3.9 Light Sterile Neutrinos . . . 20
1.3.10 Indirect Dark Matter Search . . . 21
1.3.11 Other Exotic Searches . . . 22

2 Central Detector 27
2.1 Introduction and requirement of the central detector . . . 27
2.2 Baseline option: Acrylic Sphere with Stainless-Steel Support . . . 29
2.2.1 Introduction and the design requirements . . . 29
2.2.2 Stainless-steel Supporting Structure . . . 30
2.2.2.1 Double Layer Stainless-Steel Truss . . . 30
2.2.2.2 Single Layer Stainless-Steel Truss . . . 31
2.2.2.3 Equator Supporting Method . . . 32
2.2.3 The Acrylic Sphere . . . 33
2.2.4 Joint of the Acrylic and Truss . . . 34
2.2.5 Finite Element Analysis and Testing . . . 35
2.2.5.1 Global FEA . . . 35
2.2.5.2 Local FEA of the Supporting Point of the Acrylic Sphere 41
2.2.5.3 Prototype and Testing of the Supporting Structure of the Acrylic Sphere . . . 42
2.2.5.4 Optimization of the Detector Structure . . . 46

2.2.6 Study of the Acrylic Properties . . . 48
2.3 Backup option: Balloon in a steel tank . . . 52
2.3.1 Introduction . . . 52
2.3.2 Balloon . . . 53
2.3.3 Acrylic Structure for the Balloon Support . . . 53
2.3.4 Stainless-steel Spherical Tank . . . 54
2.3.5 Installation Issues . . . 56
2.3.6 Conclusions . . . 57
2.4 PMT assembly . . . 57
2.4.1 PMT testing and validation . . . 57
2.4.2 High Voltage System of PMTs . . . 57
2.4.3 PMT related Structure Design . . . 59
2.5 Prototype . . . 63
2.5.1 Motivations of the Prototype Detector . . . 63
2.5.2 Prototype Design . . . 63
2.5.3 Expected Performance . . . 65
2.6 Construction of the central detector . . . 66
2.6.1 Assembly of the Stainless-steel Truss . . . 66
2.6.2 Construction of the Acrylic Sphere . . . 67
2.6.3 PMT Installation . . . 67
2.6.4 Filling system for the Liquid Scintillator . . . 68
2.7 Reliability and Risk analysis . . . 70
2.8 Schedule . . . 71

3 Liquid Scintillator 75
3.1 Introduction . . . 75
3.2 Specifications . . . 76
3.3 Study of Optical Properties . . . 77
3.3.1 Light Yield . . . 77
3.3.1.1 Effect of Fluor Concentrations . . . 77
3.3.1.2 Temperature Dependence . . . 78
3.3.1.3 Energy Non-linearity of Electron Signals . . . 78
3.3.2 Optical Transparency . . . 80
3.3.2.1 Characterization of Attenuation Spectrum . . . 81
3.3.2.2 Long-range Measurement of Attenuation Length . . . 82
3.3.2.3 Determination of Scattering Lengths . . . 82
3.3.2.4 Organic Impurities from GC-MS Measurements . . . 85
3.3.3 Long-term Stability . . . 86
3.3.4 Selection of Raw Materials . . . 86
3.3.4.1 Solvent . . . 86
3.3.4.2 Fluor (PPO) and Wavelength Shifter (bis-MSB) . . . 87
3.3.5 Purification Techniques . . . 88
3.3.5.1 Fractional Distillation of LAB . . . 89
3.3.5.2 Purification of LAB by Aluminum Columns . . . 90
3.3.5.3 Further Purification Techniques Applied to LS . . . 91
3.3.5.4 Purification of Fluors . . . 91
3.4 Radiopurity Studies . . . 92

3.4.1 Experimental Setups . . . 94
3.4.1.1 Low-background Gamma Spectrometer . . . 94
3.4.1.2 Assays with Loaded Scintillator Samples . . . 94
3.4.1.3 Purification Test with a Daya Bay AD . . . 96
3.4.2 Purification Methods . . . 97
3.4.2.1 Aluminum Columns . . . 97
3.4.2.2 Distillation of LAB . . . 98
3.4.2.3 Water Extraction . . . 99
3.4.2.4 Nitrogen Stripping . . . 99
3.5 Mass Production of 20 kton LS . . . 100
3.6 Risk Assessment . . . 102
3.7 Schedule . . . 103

4 Veto Detector 107
4.1 Experiment Requirements . . . 107
4.2 Detector Design . . . 109
4.2.1 The Central Detector as a Muon Tracker . . . 110
4.2.2 Water Cherenkov Detector . . . 110
4.2.2.1 Tyvek Reflector Film . . . 114
4.2.2.2 Calibration system . . . 115
4.2.3 Top Tracker . . . 115
4.2.3.1 OPERA Target Tracker . . . 116
4.3 Water System . . . 124
4.3.1 Water Production on Surface . . . 126
4.3.2 Water Production Underground . . . 126
4.3.3 Water Circulation/Purification Underground . . . 127
4.4 Geomagnetic Field Shielding System . . . 127
4.5 Mechanical Structures and Installation . . . 130
4.5.1 Support Structure over the Pool . . . 130
4.5.2 Support Structure for PMTs . . . 131
4.5.3 Sealing of the Pool . . . 131
4.5.4 Lining and Thermal Insulation Layer of the Pool . . . 132
4.5.5 Installation . . . 133
4.6 Prototype . . . 133
4.6.1 Geomagnetic Shielding Prototype . . . 133
4.7 Detector Construction and Transportation . . . 133
4.8 Risk and Safety Issues . . . 133
4.9 Schedule . . . 133

5 PMT 137
5.1 Design Goals and Specifications . . . 137
5.1.1 Introduction . . . 137
5.1.2 PMT Spectications . . . 137
5.2 MCP-PMT R&D . . . 140
5.2.1 MCP-PMT R&D at IHEP . . . 140
5.2.2 Large Area High Efficiency MCP-PMT Project . . . 142
5.2.2.1 Basic Concept of Large Area MCP-PMT . . . 143

5.2.2.2 MCP and MCP Assembly . . . 143
5.2.2.3 Glass Tube and Raw Materials . . . 144
5.2.2.4 Photocathode . . . 146
5.3 Organization of the MCP-PMT R&D Project . . . 147
5.3.1 Introduction . . . 147
5.3.2 Capability of the Collaboration . . . 148
5.3.2.1 IHEP (Beijing) . . . 148
5.3.2.2 XIOPM . . . 150
5.3.2.3 NORINCO Group . . . 151
5.4 R&D Results and Plan . . . 153
5.4.1 Status of MCP-PMT R&D . . . 153
5.4.1.1 8 inch MCP-PMT Prototype R&D . . . 153
5.4.1.2 20 inch Glass Bulb and Transition Section . . . 154
5.4.1.3 Improving the Testing System . . . 154
5.4.2 Status of Commercial PMTs . . . 155
5.4.2.1 Hamamatsu . . . 155
5.4.2.2 HZC Photonics . . . 156
5.5 Risk Analysis . . . 156
5.5.1 Risk due to Low Photon Detection Efficiency . . . 156
5.5.2 Risk Related to MCP Aging . . . 157
5.5.3 Risk due to PMT Radiation Background . . . 159
5.5.3.1 Radiation Background Requirements . . . 159
5.5.4 Risk due to Nonuniformity of MCP PCE . . . 160
5.6 Schedule . . . 161

6 The Central Detector Calibration System 163
6.1 Requirements on the Calibration System . . . 163
6.2 Conceptual Designs . . . 166
6.2.1 Housing and Interfaces . . . 166
6.2.2 Sources . . . 167
6.2.2.1 Routine Sources . . . 167
6.2.2.2 Mini-balloon . . . 168
6.2.2.3 Pulsed Light Source . . . 169
6.2.3 Source Deployment Systems for the Detector Interior . . . 170
6.2.3.1 Source Locating Systems . . . 170
6.2.3.2 ACU . . . 170
6.2.3.3 Rope Loop System . . . 171
6.2.3.4 Remotely Operated Under-liquid-scintillator Vehicles . 175
6.2.4 Conceptual Design of the Guide Tube System . . . 176
6.2.5 A Pelletron-based Beam Calibration System . . . 178
6.2.6 Diffused Short-lived Isotope Calibration . . . 187
6.3 R&D Status and Plans . . . 187
6.3.1 Sources . . . 187
6.3.2 Rope Loop System . . . 187
6.3.3 ROV . . . 187
6.3.4 Source Positioning System . . . 188
6.3.5 Pre-installed Guide Tubes . . . 188

6.3.6 Pelletron System . . . 188
6.3.7 Diffused Short-lived Isotope Calibration . . . 188
6.4 System Reliability and Safety Concerns . . . 189
6.5 Schedule . . . 189

7 Readout electronics and trigger 193
7.1 Design considerations and specifications . . . 193
7.1.1 Energy reconstruction . . . 194
7.1.1.1 Photoelectron counting . . . 194
7.1.1.2 Dynamic range . . . 196
7.1.2 Photon timing . . . 196
7.1.2.1 Reconstruction of point-like events . . . 196
7.1.2.2 Reconstruction of cosmic muons . . . 197
7.1.2.3 Limitations in timing . . . 198
7.1.3 Triggering schemes . . . 198
7.1.4 List of specifications . . . 200
7.2 External readout scheme . . . 200
7.2.1 System layout . . . 201
7.2.2 Signal amplification and digitization . . . 202
7.2.3 Data processing and transmission . . . 202
7.2.4 Trigger system . . . 203
7.2.4.1 Trigger rates and threshold . . . 203
7.2.4.2 Trigger setup . . . 204
7.2.5 Clock system . . . 204
7.2.6 Power supply and electronics crates . . . 206
7.3 Intermediate readout scheme . . . 206
7.3.1 Signal processing . . . 207
7.3.2 Trigger and clock systems . . . 207
7.3.3 Submerged processing units . . . 208
7.4 Underwater readout scheme . . . 210
7.4.1 Overview . . . 210
7.4.1.1 The ‘intelligent’ PMT . . . 211
7.4.1.2 Central Underwater Units . . . 212
7.4.1.3 The Online Computer-Farm . . . 213
7.4.1.4 Expected data rates and buffer sizes . . . 213
7.4.2 The ‘intelligent’ PMT . . . 214
7.4.2.1 High Voltage . . . 214
7.4.2.2 Clock System . . . 214
7.4.2.3 Baseline Adjustment . . . 216
7.4.2.4 Internal Trigger . . . 218
7.4.2.5 Flash-ADC . . . 218
7.4.2.6 Time Measurements . . . 218
7.4.2.7 Self-Calibration . . . 219
7.4.2.8 Internal test devices . . . 219
7.4.2.9 Mechanics . . . 220
7.4.2.10 Power . . . 220
7.5 Development plan . . . 221

7.5.1 Characterization of PMT response . . . 221
7.5.2 Signal amplification . . . 222
7.5.3 Cables and connectors . . . 223
7.5.3.1 External readout scheme . . . 223
7.5.3.2 Intermediate readout scheme . . . 223
7.5.4 ADC selection and circuit design . . . 224
7.5.5 Design of waveform digitization ASIC . . . 225
7.5.5.1 Design of an ASIC for high-speed waveform sampling . 225
7.5.5.2 Design of a high-speed FADC . . . 226
7.5.6 Data processing and transmission . . . 227
7.5.6.1 External readout scheme: ATCA modules . . . 227
7.5.6.2 Intermediate readout scheme . . . 228
7.5.7 Design of trigger and clock . . . 228
7.5.8 Design for system reliability . . . 229
7.5.8.1 Specifications for reliability . . . 229
7.5.8.2 Reliability engineering . . . 229
7.6 Manufacture and assembly . . . 230
7.6.1 Production . . . 230
7.6.2 Aging and long-term tests . . . 230
7.6.3 Installation . . . 231
7.6.4 Reliability . . . 231
7.7 Risk analysis . . . 231
7.7.1 Three read-out schemes . . . 231
7.7.2 Design risks . . . 232
7.7.3 Production risks . . . 232
7.7.4 Installation risks . . . 232
7.8 Schedule . . . 232

8 DAQ and DCS 235
8.1 Data Acquisition System . . . 235
8.1.1 System Requirements . . . 235
8.1.1.1 Event Rate . . . 235
8.1.1.2 Readout Data Rate Estimation . . . 236
8.1.1.3 Data Process Requirements . . . 236
8.1.1.4 Other Functional Requirements . . . 236
8.1.2 Conceptual Design Schema . . . 237
8.1.3 R&D Plan . . . 238
8.1.4 Manufacture, Developing and Installation . . . 239
8.1.5 Risk Analysis and Safety Evaluation . . . 239
8.1.6 Schedule . . . 240
8.2 Detector Control System . . . 240
8.2.1 Requirements . . . 240
8.2.1.1 System Requirement . . . 240
8.2.1.2 Function Requirement . . . 241
8.2.1.3 System Schema Design . . . 241

9 Offline Software And Computing 245

9.1 Design Goals and Requirements . . . 245
9.1.1 Requirement Analysis . . . 245
9.1.2 Introduction . . . 247
9.2 Offline Software Design . . . 247
9.2.1 Software Platform . . . 247
9.2.2 Event Model . . . 249
9.2.3 Geometry . . . 250
9.2.4 Generator . . . 251
9.2.5 Detector Simulation . . . 252
9.2.5.1 Description of detector geometry . . . 252
9.2.5.2 Physics processes . . . 252
9.2.5.3 Hit recording . . . 253
9.2.5.4 User interface . . . 253
9.2.6 Digitizer Simulation . . . 253
9.2.7 Background mixing . . . 254
9.2.8 Event Reconstruction . . . 254
9.2.8.1 PMT waveform reconstruction . . . 254
9.2.8.2 Vertex reconstruction in the Central Detector . . . 254
9.2.8.3 Visible energy reconstruction . . . 255
9.2.8.4 Muon tracking . . . 255
9.2.9 Event Display . . . 255
9.2.9.1 Detector description and display . . . 256
9.2.9.2 Event data and display . . . 256
9.2.9.3 Graphical User Interface . . . 257
9.2.9.4 Graphic-based analysis and tuning . . . 257
9.2.10 Database Service . . . 257
9.3 Computing System Design . . . 258
9.3.1 Computing Network and Public Network Environment . . . 258
9.3.1.1 Network Information System Security . . . 258
9.3.2 Data transfer and sharing . . . 259
9.3.3 Computation and Storage . . . 260
9.3.3.1 Local Cluster . . . 260
9.3.3.2 Computing Virtualization . . . 260
9.3.3.3 Distributed Storage Management and Data Sharing . . . 261
9.3.3.4 Distributed computation . . . 262
9.3.4 Maintenance and service support . . . 262
9.3.4.1 Network support platform . . . 262
9.3.4.2 Fine-grained monitoring and maintenance . . . 262
9.3.4.3 Information Service Platform . . . 262
9.4 Software Development and Quality Control . . . 263

10 Civil Design and Facility 267
10.1 Experimental Site Location and Layout . . . 267
10.1.1 Experiment Site Location . . . 267
10.1.2 Experiment Hall Layout . . . 268
10.1.2.1 Underground Cavities . . . 269
10.1.2.2 Layout of Surface Constructions . . . 270

10.2 Geological Survey 275
10.2.1 Geographical Conditions of the Region 275
10.2.2 Geological Survey 276
10.2.2.1 Engineering Geological Conditions of the Inclined Shaft 276
10.2.2.2 Engineering Geological Conditions of the Vertical Shaft 279
10.2.2.3 Engineering Geological Conditions of the Experimental Hall 280
10.2.2.4 Stability Assessment of the Enclosing Rock 282
10.3 Utility Systems 287
10.3.1 **Power distribution and grounding system** 287
10.3.2 **Ventilation and air-conditioning system** 287
10.3.3 **Water supply and drainage system** 288
10.3.4 **Fire control system** 288
10.3.5 **Communication system** 289
10.4 Risk Analysis and Measures 289
10.5 Schedule 290

11 Assembly, Installation and Engineering Issues 291
11.1 Introduction 291
11.1.1 Main Tasks 291
11.1.2 Contents 291
11.2 Design Standards, Guidelines and Reviews 292
11.2.1 Introduction 292
11.2.2 Institutional Standards 292
11.2.3 Design Loads 292
11.2.4 Materials Data 293
11.2.5 Analysis Methods 293
11.2.6 Failure Criteria 294
11.2.7 Factor of Safety 294
11.2.8 Specific Safety Guidelines for JUNO 295
11.2.9 Documentation 295
11.2.10 Design Reviews 296
11.3 On-site management 298
11.4 Equipment and Tools Preparation on Sit 298
11.5 Main Process of Installation 299

List of Figures

1.1 Location of the JUNO site. The distances to the nearby Yangjiang NPP and Taishan NPP are both 53 km. Daya Bay NPP is 215 km away. Huizhou and Lufeng NPPs have not been approved yet. Three metropolises, Hong Kong, Shenzhen, and Guangzhou, are also shown. . 4

1.2 A schematic view of the JUNO detector. 4

1.3 Neutrino energy spectra (upper panel) and their ratio (lower panel) with the true (NH) and fit (IH) MHs. 6

1.4 The MH discrimination ability as the function of the baseline (left panel) and as the function of the baseline difference of two reactors (right panel). 6

1.5 The comparison of the MH sensitivity for the ideal and actual distributions of the reactor cores and baselines. The real distribution gives a degradation of $\Delta\chi^2_{\rm MH} \simeq 5$. 7

1.6 the reactor-only (dashed) and combined (solid) distributions of the $\Delta\chi^2$ function, where a 1% relative error of $\Delta m^2_{\mu\mu}$ is assumed and the CP-violating phase (δ) is assigned to be $90^\circ/270^\circ$ ($\cos\delta = 0$) for illustration. The black and red lines are for the true (normal) and false (inverted) neutrino MH, respectively. 8

1.7 Three phases of neutrino emission from a core-collapse SN, from left to right: (1) Infall, bounce and initial shock-wave propagation, including prompt ν_e burst. (2) Accretion phase with significant flavor differences of fluxes and spectra and time variations of the signal. (3) Cooling of the newly formed neutron star, only small flavor differences between fluxes and spectra. 10

1.8 The neutrino event spectra with respect to the visible energy $E_{\rm d}$ in the JUNO detector for a SN at 10 kpc, where no neutrino flavor conversions are assumed for illustration and the average neutrino energies are $\langle E_{\nu_e}\rangle = 12$ MeV, $\langle E_{\overline{\nu}_e}\rangle = 14$ MeV and $\langle E_{\nu_x}\rangle = 16$ MeV. (See the text for details) 12

1.9 Exclusion contour at 90% C.L. as a function of the mean energy of the SN spectrum $\langle E_{\overline{\nu}_e}\rangle$ and the flux amplitude (SN rate times total emitted energy per SN). We assume 5% background uncertainty and no DSNB signal detection ($N_{\rm det} = \langle N_{\rm bg}\rangle$) after 10 yrs. 13

1.10 (a)On the top, the expected singles spectra at JUNO with the radio purity assumption 10^{-16}g/g for ^{238}U and ^{232}Th, 10^{-17}g/g for ^{40}K and ^{14}C. (b) On the bottom, assuming a background level one order of magnitude better for ^{238}U, ^{232}Th and for ^{40}K, ^{14}C. 15

1.11 The MH sensitivities of atmospheric neutrinos as a function of livetime for the true NH (upper panel) and IH (lower panel) cases. 16

1.12 The simulated hit time distribution of photoelectrons (PEs) from a $K^+ \to \mu^+\nu_\mu$ event at JUNO. 20
1.13 The 90% C.L. sensitivity to the proton lifetime in the decay mode $p \to K^+ + \overline{\nu}$ at JUNO as a function of time. In comparison, Super-Kamiokande's sensitivity is also projected [29]. 21
1.14 22

2.1 Logo in CentralDetector 28
2.2 Logo in CentralDetector 29
2.3 Logo in CentralDetector 31
2.4 Single layer steel truss 32
2.5 Acrylic sphere supported at equator 33
2.6 Detailed view of the support at equator by separated points 33
2.7 Schematic view of the acrylic sphere 34
2.8 Logo in CentralDetector 35
2.9 Logo in CentralDetector 35
2.10 Stress distribution on the acrylic sphere 37
2.11 Stress distribution of the steel truss 38
2.12 Deflection of the central detector 39
2.13 Stress on the acrylic sphere and steel truss under seismic condition . . . 39
2.14 Stability analysis of the central detector 40
2.15 Failure analysis of the central detector for (a) condition 1, (b)condition 2, (c)condition 3 and (d)condition 4. 41
2.16 the structure of the connecting joint 42
2.17 Analysis results for fixed constraint 43
2.18 Analysis results for simple constraint 44
2.19 the prototype and test 45
2.20 layout of the measuring points 45
2.21 load-strain curve of the measurement points 45
2.22 Comparison of stress between measurement and FEA 46
2.23 Third prototype test 47
2.24 Inner layer truss after sparsifying the truss members 47
2.25 Performance of the acrylic after aging 49
2.26 cross section of the broken acrylic 50
2.27 Creep curve of the acrylic under different stress 52
2.28 Schematic view of stainless-steel tank and the balloon 52
2.29 The acrylic supporting structure for the balloon 54
2.30 the stress and deformation of the acrylic support 55
2.31 A preliminary structure of the stainless-steel tank 55
2.32 conceptual view of PMT potting structure 59
2.33 Simulation of PMT implosion 60
2.34 Peak pressure of the shock wave 61
2.35 strength of the shock wave as a function of distance 61
2.36 strength of the shock wave as a function of PMT volume 61
2.37 strength of the shock wave as a function of pressure 61
2.38 the setup for implosion test 62
2.39 Simulation of the PMT implosion 62

2.40 the prototype design 64
2.41 The side view of the prototype detector 64
2.42 the shielding system 65
2.43 Geant4 simulation geometry 66
2.44 PMT module with the stainless-steel backplate 68
2.45 Installation of the PMT module 68
2.46 Using profile steel for PMT installation 69
2.47 Sketch of the LS filling system 70

3.1 Schematic of the setup for light-out measurements 78
3.2 Foto of the setup for LY measurements 78
3.3 Setup for measuring temperature-dependence of LY 79
3.4 Conceptual drawing of the electron non-linearity setup 79
3.5 Photograph of the electron non-linearity setup 80
3.6 UV-Vis attenuation spectra of LAB samples 81
3.7 UV-Vis attenuation spectrum: Impact of fluors 82
3.8 Setup for attenuation length measurement 83
3.9 Schematic setup for scattering length measurements 84
3.10 GC-MS Chromatogram of LAB 85
3.11 Setup for LS aging tests 86
3.12 UV-Vis attenuation spectra of LAB from different providers 87
3.13 UV-vis attenuation spectra of LAB doped with PPO 88
3.14 UV-vis attenuation spectra with PPO from selected providers 89
3.15 UV-vis attenuation spectra of LAB with Bis-MSB 90
3.16 UV-vis attenuation spectra before and after purification 91
3.17 UV-Vis spectra of LAB before and after distillation 92
3.18 UV-Vis spectra of LAB before and after column purification 92
3.19 Laboratory setup for radon-loading of LS samples 94
3.20 Natural thorium decay chain 95
3.21 Setup for measuring radio-purification efficiency 96
3.22 Sample pulse of a fast ^{212}Bi-^{212}Po coincidence 96
3.23 Bi/Po event spectra before and after column purification 98
3.24 Setup for distillation tests 99
3.25 Schematic drawing of ultrapure N2 production unit 100
3.26 Schematic drawing of LS purification plants 101

4.1 Thickness of water vs gamma and neutron attenuation 108
4.2 Veto systems of JUNO 109
4.3 Muon efficiency vs time 111
4.4 Muon detection efficiency vs Number of PMT threshold 111
4.5 Simple water Cherenkov detector option. Uniformed distribution of PMTs. PMTs at the top of water pool are facing outward. PMTs at the bottom and on the barrel are facing inward. 113
4.6 Various muon tracks with reconstructed points at pool surface or central detector. 113
4.7 Resolution of the reconstructed points on the central detector 113
4.8 Production of the Tyvek reflector 115
4.9 Reflectivity of different types of Tyvek 115

4.10 LED 116
4.11 Schematic view of a plastic scintillator strip wall. 116
4.12 Target Tracker walls hanging in between two brick walls inside the OPERA detector. 116
4.13 Particle detection principle in a scintillating strip. 117
4.14 Schematic view of an end–cap of a scintillator strip module. 117
4.15 TT electronics including DAQ card. All elements in red will be replaced. 118
4.16 Architecture of a single channel of the OPERA–ROC chip. 118
4.17 Configurations considered for the induced noise. 119
4.18 Configurations considered for the Top Tracker coverage. 120
4.19 Architecture of the MAROC3 chip. 124
4.20 Flow rate vs one cycle time 125
4.21 General view of water production system on ground 126
4.22 General view of water production system underground 126
4.23 General view of water circulation/purification system on ground 127
4.24 Earth magnetic in Jiangmen 128
4.25 PMT collection efficiency vs the external magnetic field 128
4.26 One group earth magnetic shield system 129
4.27 Magnetic field distribution with one group system 129
4.28 The top support structure 130
4.29 PMT support structure of DayaBay 130
4.30 The cover design of Daya Bay 131
4.31 The wire design option for cover installation of Daya Bay experiment . 131
4.32 Lead rail for rubberized fabric cover option installation 132

5.1 Specifications of PMTs for JUNO 139
5.2 The photocathode sensitivity and quantum efficiencies of various photocathodes 141
5.3 The conceptual drawing of the high efficiency spherical PMT with two sets of MCP electron multipliers 142
5.4 MCP-PMT electro-optic simulation with Earth magnetic field 144
5.5 Simulation for MCP functionality 145
5.6 Vacuum sealed 20inch glass bulb on a CMM for mechanical accuracy measurements 146
5.7 QE 147
5.8 Flow chart of the large area MCP-PMT R&D process 148
5.9 Organization of the existing PMT test lab at IHEP 149
5.10 PMT measurement results at IHEP 150
5.11 MCP-PMT fabrication process at XIOPM 151
5.12 Equipment for fabricating 20 inch MCP-PMTs developed by NORINCO using photocathode transfer technology 152
5.13 QE values and SPE spectra of the 8 inch MCP-PMT 153
5.14 20 inch glass bulb, its defect inspection and transition sections 154
5.15 20 inch MCP-PMT Prototype 155
5.16 PMT test system at IHEP 155
5.17 Spectral response of common bialkali photocathode and the emission spectrum of liquid scintillator (red curve) 157

5.18 QEs vs. wavelengths for conventional bialkali, SBA and UBA photocathodes . . . 158
5.19 The MCP coating scheme . . . 160

6.1 Illustration of a seal calibration house on top of the detector. . . . 166
6.2 Concept of a calibration house. . . . 167
6.3 Illustration of a typical source/weight assembly used in Daya Bay, envisioned for JUNO as well. . . . 168
6.4 an example JUNO Monte Carlo spectrum in photoelectrons for the ^{60}Co source with source geometry. . . . 168
6.5 The mini-balloon source concept. . . . 169
6.6 Comparison of ^{40}K spectra with a 10 μm balloon and without. . . . 169
6.7 A typical placement of the ultrasonic receivers. . . . 171
6.8 A sketch of the ACU system. . . . 171
6.9 Rope loop solution and its 2-dimensional coverage . . . 172
6.10 3-point hang design and volume coverage . . . 172
6.11 An overview sketch of the rope loop system. . . . 173
6.12 Illustration of a 4-rope design. . . . 173
6.13 An illustration of a spool drive. . . . 174
6.14 One of the quick connection option. . . . 174
6.15 An alternative quick connection option. . . . 175
6.16 The source storage ring. . . . 176
6.17 ROV, its umbilical cable and the loaded radioactive source . . . 177
6.18 The guide tube system. . . . 177
6.19 The conceptual design of the source capsule inside the guide tube. . . . 178
6.20 Diagram illustrating the principle of a pelletron. As the drive pulley and the terminal pulley rotate clockwise, the chain transports the positive charge to the terminal shell and builds up a high voltage that could be higher than 25 MV. By reversing the polarities of the charging voltages, the pelletron can easily switch to accelerate electrons and negative ions. 179
6.21 The conceptual design of the pelletron system . . . 179
6.22 A conceptual design of the beam pipe endcap inside the LS detector. The transparent acrylic pipe and the Mylar window make sure the scintillation light can largely pass through. Two beam monitors near the top and bottom of the beam will allow diagnostics of beam position and area when the beam first enters the detector vertically downward and near the exit point of the beam out of the beam. . . . 180
6.23 (Left panel) Calculated required wall thickness of the stainless steel calibration tube is plotted as a function of the radius of the calibration tube to balance the buoyancy force. (Right panel) The corresponding weight of the 20 m long calibration tube is plotted. . . . 184
6.24 (Left) Illustration of calibration tube of Pelletron inside the JUNO central detector. (Middle) Curved Mylar window for the calibration tube. (Right) Endcap of the calibration tube with the curved Mylar window. 184
6.25 Energy loss of the electrons and positrons inside the curved Mylar window. For electron, the prompt energy was shifted to match that of positron. The traipzoid represents 0.1% band of the energy scale. . . . 185

6.26 (Left) The energy response of positron injecting through the calibration tube (red) is compared to that of the positron in the detector without the calibration tube(black). (Right) The difference in energy is shown with respect of the true positron prompt energy. The increase of difference reflects the shadowing effect of the calibration tube 185
6.27 (Top) The bias of energy response (1-2%) due to the shadowing effect of the calibration tube is shown with respect of the true prompt energy. (Bottom) The residual bias of energy response ($< 0.1\%$) after the correction of energy loss and the shadowing effect is shown with respect of the true prompt energy. 186

7.1 Pulse shape discrimination in JUNO LS 197
7.2 Scheme for external readout electronics 201
7.3 Scheme for signal amplification and digitization 202
7.4 Data processing and transmission in the external scheme 203
7.5 Event spectrum for coinciding PMT hits 205
7.6 ATCA crate 206
7.7 Intermediate scheme for readout electronics 207
7.8 Readout Electronics 208
7.9 Representation of the intermediate scheme 208
7.10 Readout Electronics 209
7.11 Side panels of submerged processing units 209
7.12 Readout Electronics 210
7.13 Readout Electronics 212
7.14 Voltage divider for the MCP-PMT base 215
7.15 Cockroft-Walton multiplier 215
7.16 Prototype for HV module 216
7.17 Circuit for baseline adjustment 217
7.18 Self-calibration scheme 219
7.19 Mechanical realization of the intelligent PMT 220
7.20 Readout Electronics 222
7.21 Compatibility tests of cables and LS 224
7.22 Underwater connectors 225
7.23 Readout Electronics 226
7.24 FEE block diagram for ATCA modules 227
7.25 Block diagram of processing unit 228
7.26 White Rabbit system 229

8.1 DAQ Conceptual Architecture Design Diagram 238
8.2 DAQ Event Building Collaboration Diagram 239
8.3 DAQ Event Filter Collaboration Diagram 240
8.4 Framework Design of Detector Control System 241

9.1 Offline Software Platform 248
9.2 Event Model 250

9.3 An illustration of the muon tracking. The red line is the muon track to be fitted, R_c is the light source which provides the first hit to the PMT at R_i, determined by the intersection angle θ. If R_c is calculated to be outside the detector, it will be set as the injection point R_0. 256
9.4 WAN topology 258
9.5 Storage architecture 261
9.6 Monitoring tool architecture 263

10.1 Physics required site region, shadow is granite area 271
10.2 Experimental Hall Location (position 4) in the granite area with dash line 272
10.3 Layout of the Site 272
10.4 Layout of the Underground Facility 273
10.5 Sideview of the Experimental Hall 274
10.6 Map of the Project Region 275
10.7 Engineering Geological survey in the Experiment Region 277
10.8 Topography near the Access Entry of Inclined Shaft. The underground facility is at left. The entry of inclined shaft is at right. 278
10.9 Geophysical Investigation of Inclined Shaft 279
10.10 Topography at the Entry of the Vertical Shaft 283
10.11 Some Cores Samples from the exploring drill well in the Vertical Shaft 284
10.12 Geologic Diagram Obtained with the High-Frequency Magnetotelluric Method near the Explerimental Hall 285
10.13 Measured Underground Temperature 286

List of Tables

1.1 The best-fit values, together with the 1σ and 3σ intervals, for the six three-flavor neutrino oscillation parameters from a global analysis of current experimental data [5]. 3
1.2 Summary of the thermal power and baseline to the JUNO detector for the Yangjiang (YJ) and Taishan (TS) reactor cores, as well as the remote reactors of Daya Bay (DYB) and Huizhou (HZ). 3
1.3 Current precision for the five known oscillation parameters. The dominant experiments and their corresponding 1σ accuracy and global precision from global fitting groups [5] are shown in the first, second and third row, respectively. 8
1.4 Precision of $\sin^2\theta_{12}$, Δm^2_{21} and $|\Delta m^2_{ee}|$ from the nominal setup to those with more systematic uncertainties. The systematics are added one by one from the left cell to right cell. 8
1.5 Numbers of neutrino events in JUNO for a SN at a galactic distance of 10 kpc. 10
1.6 The expected detection significance after 10 years of data taking for different DSNB models with $\langle E_{\bar{\nu}_e}\rangle$ ranging from 12 MeV to 21 MeV ($\Phi = \Phi_0$). Results are given based on either a rate-only or spectral fit analysis and assuming 5% or 20% for background uncertainty. 14
1.7 Signal and backgrounds considered in the geoneutrino sensitivity study: the number of expected events for all components contributing to the IBD spectrum in the 0.7 - 12 MeV energy region of the prompt signal. We have assumed 80% antineutrino detection efficiency and 17.2 m radial cut (18.35 kton of liquid scintillator). 18
1.8 Precision of the reconstruction of geoneutrino signal. See the text for details. 19

2.1 Maximum stress and deformation for each loading condition 36
2.2 Impact analysis of liquid level 37
2.3 Temperature impact on stress 40
2.4 Comparison of FEA and measurement for the third prototype 46
2.5 Results from FEA after optimization 48
2.6 Strength of the acrylic after outdoor exposure 50
2.7 Comparison of the different bonding techniques 50
2.8 USB bus adapter 58
2.9 20” PMT HV module 58
2.10 HV value of PMT dynode 59

3.1 Requirements for LS radiopurity 93

3.2 Comparison of Al_2O_3 radioactivity levels 97
3.3 Table of material properties 103

4.1 Resolution of reconstructed points on the muon tracks. 112
4.2 Noise rate for several TT conditions. (a) is under 1 p.e. threshold and (b) is under 2 p.e. threshold. (1)no concrete; (2)10 cm concrete. 121
4.3 Rate of "fake" tracks for several TT conditions.(a) is under 1 p.e. threshold and (b) is under 2 p.e. threshold. (1)no concrete; (2)10 cm concrete. 121
4.4 Noise rate induced by ^{9}Li and ^{8}He for case (a) of Fig. 4.17. 122
4.5 Noise rate induced by ^{9}Li and ^{8}He for case (b) of Fig. 4.17. 123
4.6 Expected noise rate from fast neutrons for case (c) of Fig. 4.17 and for the configuration of TT (4XY, Rtg) of Fig. 4.18. 123

5.1 PMTs required by JUNO 137
5.2 Achievements and status 153
5.3 Chemical composition of the GG-17 glass and raw materials 159
5.4 the schedule of the mass production 161

6.1 Summary of the different types of calibration goals, methods and requirements 165
6.2 Radioactive sources under consideration in JUNO. 167
6.3 Yearly targets 189

7.1 Input for trigger rate MC 204
7.2 Data volume needed per single photoelectron. 213
7.3 Survey and attenuation results for three samples of 100 m long coaxial cables from Tianjin 609 Cable co. 223
7.4 Overview of FADC chips 225

8.1 JUNO DAQ Data Rate Estimation 237

10.1 Result of Rock radioactivity Test in Borehole ZK1 284

Chapter 1

Introduction

1.1 Neutrino Physics: Status and Prospect

1.1.1 Fundamentals of Massive Neutrinos

In the Standard Model [1] of particle physics, the weak charged-current interactions of leptons and quarks can be written as

$$\begin{aligned}\mathcal{L}_{\rm cc} = & - \frac{g}{\sqrt{2}} \left[\overline{(e \quad \mu \quad \tau)_{\rm L}} \, \gamma^\mu \, U \begin{pmatrix} \nu_1 \\ \nu_2 \\ \nu_3 \end{pmatrix}_{\rm L} W^-_\mu \right. \\ & \left. + \overline{(u \quad c \quad t)_{\rm L}} \, \gamma^\mu \, V \begin{pmatrix} d \\ s \\ b \end{pmatrix}_{\rm L} W^+_\mu \right] + \text{h.c.} \, , \end{aligned} \tag{1.1}$$

where all the fermion fields are the mass eigenstates, U is the 3×3 Maki-Nakagawa-Sakata-Pontecorvo (MNSP) matrix [2], and V denotes the 3×3 Cabibbo-Kobayashi-Maskawa (CKM) matrix [3].

Given the basis in which the flavor eigenstates of the three charged leptons are identified with their mass eigenstates, the flavor eigenstates of the three active neutrinos and n sterile neutrinos read as

$$\begin{pmatrix} \nu_e \\ \nu_\mu \\ \nu_\tau \\ \vdots \end{pmatrix} = \begin{pmatrix} U_{e1} & U_{e2} & U_{e3} & \cdots \\ U_{\mu 1} & U_{\mu 2} & U_{\mu 3} & \cdots \\ U_{\tau 1} & U_{\tau 2} & U_{\tau 3} & \cdots \\ \vdots & \vdots & \vdots & \ddots \end{pmatrix} \begin{pmatrix} \nu_1 \\ \nu_2 \\ \nu_3 \\ \vdots \end{pmatrix} \, . \tag{1.2}$$

where ν_i is a neutrino mass eigenstate with the physical mass m_i (for $i = 1, 2, \cdots, 3+n$). Equation (1.1) tells us that a ν_α neutrino can be produced from the $W^+ + \ell^-_\alpha \to \nu_\alpha$ interaction, and a ν_β neutrino can be detected through the $\nu_\beta \to W^+ + \ell^-_\beta$ interaction (for $\alpha, \beta = e, \mu, \tau$). So oscillation may happen if the ν_i beam with energy $E \gg m_i$ travels a proper distance L. In vacuum, the oscillation probability of the $\bar{\nu}_e \to \bar{\nu}_e$ transition turns out to be

$$P(\overline{\nu}_e \to \overline{\nu}_e) = 1 - \frac{4}{\left(\sum_i |U_{ei}|^2 \right)^2} \sum_{i<j} \left(|U_{ei}|^2 |U_{ej}|^2 \sin^2 \frac{\Delta m^2_{ij} L}{4E} \right) \, , \tag{1.3}$$

with $\Delta m^2_{ij} \equiv m^2_i - m^2_j$ being the mass-squared difference. Note that the denominator on the right-hand side of Eq. (1.5) is not equal to one if there are heavy sterile antineutrinos which mix with the active antineutrinos but do not take part in the flavor oscillations. Note also that the terrestrial matter effects on $P(\overline{\nu}_e \to \overline{\nu}_e)$ are negligibly small, because the typical value of E is only a few MeV and that of L is usually less than several hundred km for a realistic reactor-based $\overline{\nu}_e \to \overline{\nu}_e$ oscillation experiment.

If the 3×3 MNSP matrix U is exactly unitary, it can be parametrized in terms of three flavor mixing angles and three CP-violating phases in the following standard way [4]:

$$\begin{aligned} U &= \begin{pmatrix} 1 & 0 & 0 \\ 0 & c_{23} & s_{23} \\ 0 & -s_{23} & c_{23} \end{pmatrix} \begin{pmatrix} c_{13} & 0 & s_{13}e^{-\mathrm{i}\delta} \\ 0 & 1 & 0 \\ -s_{13}e^{\mathrm{i}\delta} & 0 & c_{13} \end{pmatrix} \begin{pmatrix} c_{12} & s_{12} & 0 \\ -s_{12} & c_{12} & 0 \\ 0 & 0 & 1 \end{pmatrix} P_\nu \\ &= \begin{pmatrix} c_{12}c_{13} & s_{12}c_{13} & s_{13}e^{-\mathrm{i}\delta} \\ -s_{12}c_{23} - c_{12}s_{13}s_{23}e^{\mathrm{i}\delta} & c_{12}c_{23} - s_{12}s_{13}s_{23}e^{\mathrm{i}\delta} & c_{13}s_{23} \\ s_{12}s_{23} - c_{12}s_{13}c_{23}e^{\mathrm{i}\delta} & -c_{12}s_{23} - s_{12}s_{13}c_{23}e^{\mathrm{i}\delta} & c_{13}c_{23} \end{pmatrix} P_\nu \,, \end{aligned} \tag{1.4}$$

where $c_{ij} \equiv \cos\theta_{ij}$ and $s_{ij} \equiv \sin\theta_{ij}$ (for $ij = 12, 13, 23$) are defined, and $P_\nu = \mathrm{Diag}\{e^{\mathrm{i}\rho}, e^{\mathrm{i}\sigma}, 1\}$ denotes the diagonal Majorana phase matrix which has nothing to do with neutrino oscillations. In this case,

$$\begin{aligned} P(\overline{\nu}_e \to \overline{\nu}_e) &= 1 - \sin^2 2\theta_{12} c^4_{13} \sin^2 \frac{\Delta m^2_{21} L}{4E} \\ &- \sin^2 2\theta_{13} \left[c^2_{12} \sin^2 \frac{\Delta m^2_{31} L}{4E} + s^2_{12} \sin^2 \frac{\Delta m^2_{32} L}{4E} \right] \,, \end{aligned} \tag{1.5}$$

in which $\Delta m^2_{32} = \Delta m^2_{31} - \Delta m^2_{21}$. The oscillation terms driven by Δm^2_{21} and $\Delta m^2_{31} \simeq \Delta m^2_{32}$ can therefore be used to determine θ_{12} and θ_{13}, respectively.

1.1.2 Open Issues of Massive Neutrinos

Although we have known quite a lot about massive neutrinos, where the current status of neutrino oscillation measurements can be summarized in Table 2.1, we have many open questions about their fundamental properties and their unique roles in the Universe [6]. In the following we concentrate on some intrinsic flavor issues of massive neutrinos which may related to future neutrino experiments:

(a) The nature of neutrinos and their mass spectrum;
Question (1): Dirac or Majorana nature?
Question (2): Normal or inverted mass hierarchy?
Question (3): The absolute mass scale?
(b) Lepton flavor mixing pattern and CP violation;
Question (4): The octant of θ_{23}?
Question (5): The Dirac CP-violating phase δ?
Question (6): The Majorana CP-violating phases ρ and σ?
(c) Extra neutrino species and unitarity tests;
Question (7): Extra light or heavy sterile neutrinos?
Question (8): Direct and indirect non-unitary effects?

Table 1.1: The best-fit values, together with the 1σ and 3σ intervals, for the six three-flavor neutrino oscillation parameters from a global analysis of current experimental data [5].

Parameter	Best fit	1σ range	3σ range
Normal neutrino mass hierarchy ($m_1 < m_2 < m_3$)			
$\Delta m^2_{21}/10^{-5}$ eV^2	7.54	7.32 — 7.80	6.99 — 8.18
$\Delta m^2_{31}/10^{-3}$ eV^2	2.47	2.41 — 2.53	2.27 — 2.65
$\sin^2\theta_{12}/10^{-1}$	3.08	2.91 — 3.25	2.59 — 3.59
$\sin^2\theta_{13}/10^{-2}$	2.34	2.15 — 2.54	1.76 — 2.95
$\sin^2\theta_{23}/10^{-1}$	4.37	4.14 — 4.70	3.74 — 6.26
$\delta/180°$	1.39	1.12 — 1.77	0.00 — 2.00
Inverted neutrino mass hierarchy ($m_3 < m_1 < m_2$)			
$\Delta m^2_{21}/10^{-5}$ eV^2	7.54	7.32 — 7.80	6.99 — 8.18
$\Delta m^2_{31}/10^{-3}$ eV^2	2.34	2.28 — 2.40	2.15 — 2.52
$\sin^2\theta_{12}/10^{-1}$	3.08	2.91 — 3.25	2.59 — 3.59
$\sin^2\theta_{13}/10^{-2}$	2.40	2.18 — 2.59	1.78 — 2.98
$\sin^2\theta_{23}/10^{-1}$	4.55	4.24 — 5.94	3.80 — 6.41
$\delta/180°$	1.31	0.98 — 1.60	0.00 — 2.00

1.2 JUNO Experiment

The Jiangmen Underground Neutrino Observatory (JUNO) is a multi-purpose neutrino experiment. It was proposed in 2008 for neutrino mass hierarchy (MH) determination by detecting reactor antineutrinos from nuclear power plants (NPPs) [7, 8, 9]. The site location is optimized to have the best sensitivity for mass hierarchy determination, which is at 53 km from both the Yangjiang and Taishan NPPs. The neutrino detector is a liquid scintillator (LS) detector with a 20 kton fiducial mass, deployed in a laboratory 700 meters underground. The JUNO experiment is located in Jinji town, Kaiping city, Jiangmen city, Guangdong province which is shown in Fig. 1.1. The thermal power and baselines are listed in Table 1.2.

Cores	YJ-C1	YJ-C2	YJ-C3	YJ-C4	YJ-C5	YJ-C6
Power (GW)	2.9	2.9	2.9	2.9	2.9	2.9
Baseline(km)	52.75	52.84	52.42	52.51	52.12	52.21
Cores	TS-C1	TS-C2	TS-C3	TS-C4	DYB	HZ
Power (GW)	4.6	4.6	4.6	4.6	17.4	17.4
Baseline(km)	52.76	52.63	52.32	52.20	215	265

Table 1.2: Summary of the thermal power and baseline to the JUNO detector for the Yangjiang (YJ) and Taishan (TS) reactor cores, as well as the remote reactors of Daya Bay (DYB) and Huizhou (HZ).

JUNO consists of a central detector, a water Cherenkov detector and a muon tracker (shown in Fig. 1.2). The central detector is a LS detector of 20 kton fiducial mass and $3\%/\sqrt{E(\text{MeV})}$ energy resolution. The central detector is submerged in a water pool to

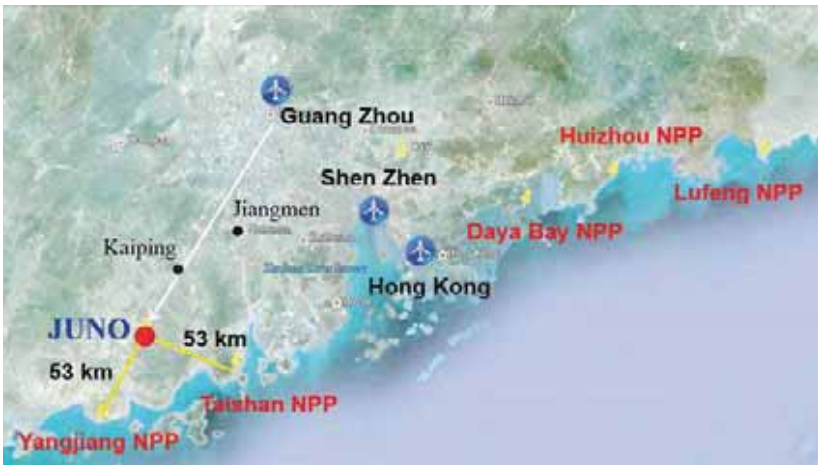

Figure 1.1: Location of the JUNO site. The distances to the nearby Yangjiang NPP and Taishan NPP are both 53 km. Daya Bay NPP is 215 km away. Huizhou and Lufeng NPPs have not been approved yet. Three metropolises, Hong Kong, Shenzhen, and Guangzhou, are also shown.

be shielded from natural radioactivities from the surrounding rock and air. The water pool is equipped with PMTs to detect the Cherenkov light from muons. On top of the water pool, there is another muon detector to accurately measure the muon track.

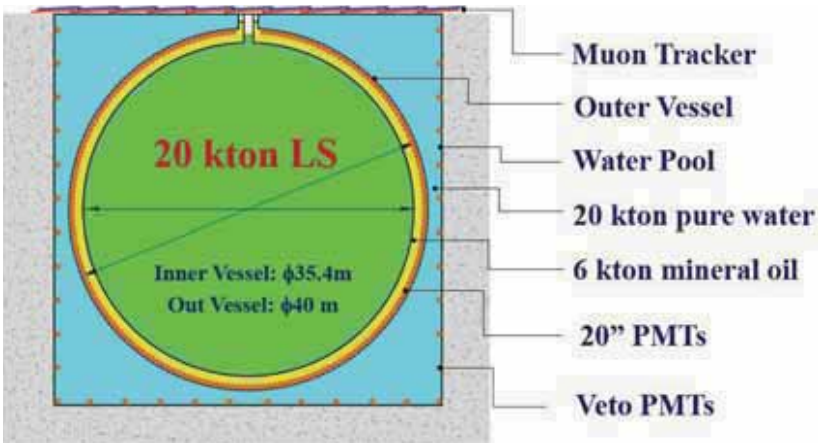

Figure 1.2: A schematic view of the JUNO detector.

It is crucial to achieve a $3\%/\sqrt{E(\mathrm{MeV})}$ energy resolution for the determination of the MH. A Monte Carlo simulation has been developed based on the Daya Bay Monte Carlo. The photoelectron yield has been tuned according to the real data of Daya Bay. The required energy resolution can be reached with the following improvements from Daya Bay [11]:

- The PMT photocathode covergage $\geq 75\%$.
- The PMT photocathode quantum efficiency $\geq 35\%$.
- The attenuation length of the liquid scintillator ≥ 20 m at 430 nm, which corresponds to an absorption length of 60 m with a Rayleigh scattering length of 30 m.

For the real experimental environments, there are many other factors beyond the photoelectron statistics that can alter the energy resolution, including the dark noise from the PMTs and electronics, the detector non-uniformity and vertex resolution, and the PMT charge resolution. A generic parametrization for the detector energy resolution is defined as

$$\frac{\sigma_E}{E} = \sqrt{\left(\frac{a}{\sqrt{E}}\right)^2 + b^2 + \left(\frac{c}{E}\right)^2} \ , \tag{1.6}$$

where the visible energy E is in MeV.

Based on the numerical simulation as shown in the next section, a requirement for the resolution of $a/\sqrt{E}$ better than 3% is approximately equivalent to the following requirement,

$$\sqrt{(a)^2 + (1.6 \times b)^2 + \left(\frac{c}{1.6}\right)^2} \leq 3\% \ . \tag{1.7}$$

1.3 Physics Potentials

1.3.1 Mass Hierarchy

The neutrino mass hierarchy (MH) answers the question whether the third generation (ν_3 mass eigenstate) is heavier or lighter than the first two generations (ν_1 and ν_2). The normal mass hierarchy (NH) refers to $m_3 > m_1$ and the inverted mass hierarchy (IH) refers to $m_3 < m_1$. JUNO is designed to resolve the neutrino MH using precision spectral measurements of reactor antineutrino oscillations, where the general principle is shown in Fig. 1.3.

In the JUNO simulation, we assume a 20 kton LS detector and a total thermal power of two reactor complexes of 36 GW. We assume nominal running time of six years, 300 effective days per year, 80% detection efficiency and a detector energy resolution $3\%/\sqrt{E(\mathrm{MeV})}$ as a benchmark. The simulation details can be found in Ref. [10]. In Fig. 1.3, the expected neutrino energy spectrum of the true normal MH, and best-fit neutrino spectrum of the wrong inverted MH are shown in the upper panel, and the ratio of two spectra is illustrated in the lower panel. One can observe that the distinct feature of two MHs lies in the fine structures of the neutrino spectrum.

To quantify the sensitivity of MH determination, we define the following quantity as the MH discriminator,

$$\Delta\chi^2_{\mathrm{MH}} = |\chi^2_{\mathrm{min}}(\mathrm{NH}) - \chi^2_{\mathrm{min}}(\mathrm{IH})|, \tag{1.8}$$

where the minimization process is implemented for the oscillation parameters and systematics.

The discriminator defined in Eq. (1.8) can be used to obtain the optimal baseline, which is shown in the left panel of Fig. 1.4. An optimal sensitivity of $\Delta\chi^2_{\mathrm{MH}} \simeq 16$ can be obtained for the ideal case with identical baseline at around 50 km, where the oscillation effect of δm^2_{21} is maximal. The impact of the baseline difference due to multiple reactor cores is shown in the right panel of Fig. 1.4, by keeping the baseline of one reactor unchanged and varying that of the other. A rapid oscillatory behavior is observed, which demonstrates the importance of baseline differences for the reactor

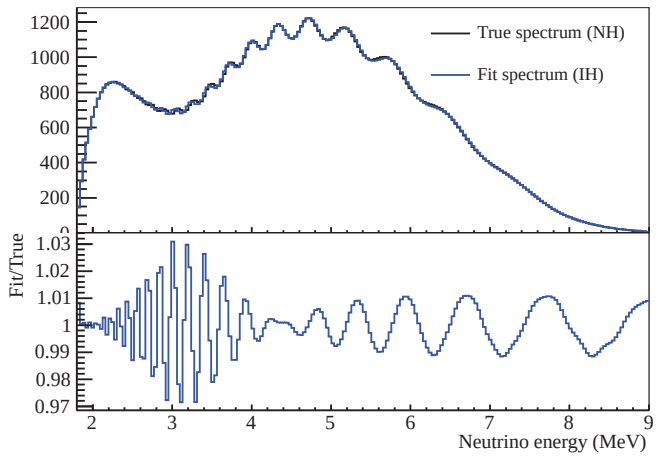

Figure 1.3: Neutrino energy spectra (upper panel) and their ratio (lower panel) with the true (NH) and fit (IH) MHs.

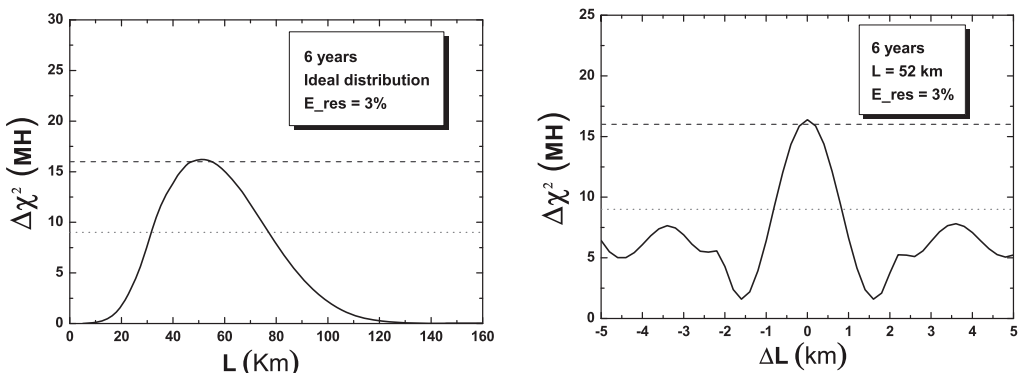

Figure 1.4: The MH discrimination ability as the function of the baseline (left panel) and as the function of the baseline difference of two reactors (right panel).

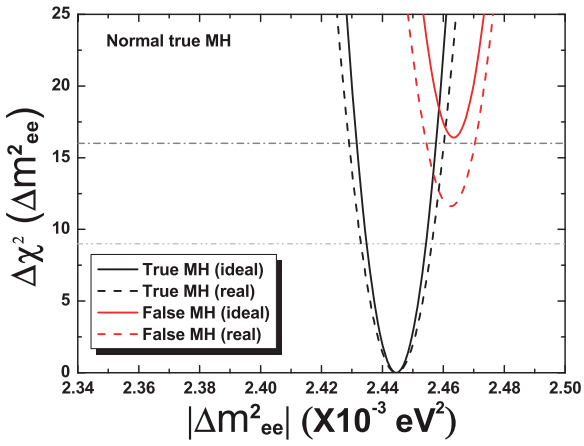

Figure 1.5: The comparison of the MH sensitivity for the ideal and actual distributions of the reactor cores and baselines. The real distribution gives a degradation of $\Delta\chi^2_{\rm MH} \simeq 5$.

cores. The worst case is at $\Delta L \sim 1.7$ km, where the $|\Delta m^2_{ee}|$ related oscillation is canceled between the two reactors. Taking into account the reactor power and baseline distribution of the real experimental site of JUNO, we show the reduction of the MH sensitivity in Fig. 1.5, which gives a degradation of $\Delta\chi^2_{\rm MH} \simeq 5$.

There are also reactor and detector related uncertainties that affect the MH sensitivity. Rate uncertainties are negligible, because most of the MH sensitivity is derived from the spectral information. On the other hand, the energy-related uncertainties are important, including the reactor spectrum error, the detector bin-to-bin error, and the energy non-linearity error. By considering realistic spectral uncertainties and taking into account the self-calibration of oscillation patterns of reactor antineutrino oscillations, we obtain the nominal MH sensitivity of JUNO as shown with the dashed lines in Fig. 1.6. In addition, due to the difference between $|\Delta m^2_{ee}|$ and $|\Delta m^2_{\mu\mu}|$, precise measurements of the two mass-squared difference can provide additional sensitivity to MH, besides the sensitivity from the interference effects. In Fig. 1.6, we show with the solid lines the improvement by adding a $|\Delta m^2_{\mu\mu}|$ measurement of 1% precision, where an increase of $\Delta\chi^2_{\rm MH} \simeq 8$ is achieved for the MH sensitivity.

1.3.2 Precision Measurement of Mixing Parameters

JUNO is a precision experiment in terms of huge statistics ($\mathcal{O}$(100k) inverse beta decay (IBD) events), optimal baseline, unprecedented energy resolution ($3\%/\sqrt{E}$) and accurate energy response (better than 1%). Therefore, besides the determination of the neutrino mass hierarchy (MH) [10], the $\mathcal{O}$(100k) IBD events allow JUNO to probe the fundamental properties of neutrino oscillations and access four additional parameters θ_{12}, θ_{13}, Δm^2_{21}, and $|\Delta m^2_{ee}|$.

Current precision for the five known oscillation parameters is summarized in Table 1.3, where both the results from individual experiments and from global analyses [5] are presented. We notice that most of the oscillation parameters have been measured to better than 10%.

Among all the four parameters that are accessible in JUNO, the θ_{13} measurement

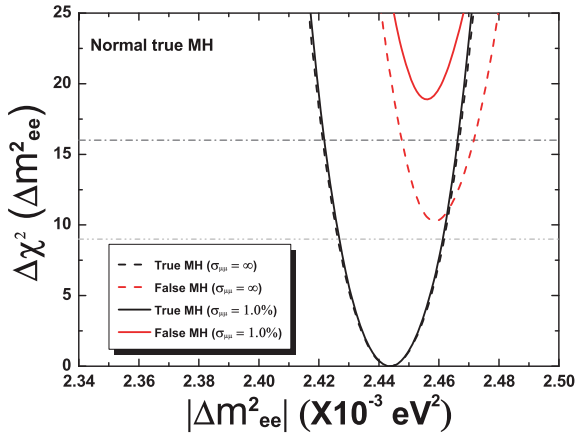

Figure 1.6: the reactor-only (dashed) and combined (solid) distributions of the $\Delta\chi^2$ function, where a 1% relative error of $\Delta m^2_{\mu\mu}$ is assumed and the CP-violating phase (δ) is assigned to be 90°/270° ($\cos\delta = 0$) for illustration. The black and red lines are for the true (normal) and false (inverted) neutrino MH, respectively.

	Δm^2_{21}	$\lvert\Delta m^2_{31}\rvert$	$\sin^2\theta_{12}$	$\sin^2\theta_{13}$	$\sin^2\theta_{23}$
Dominant Exps.	KamLAND	MINOS	SNO	Daya Bay	SK/T2K
Individual 1σ	2.7% [12]	4.1% [11]	6.7% [18]	6% [15]	14% [16, 17]
Global 1σ	2.6%	2.7%	4.1%	5%	11%

Table 1.3: Current precision for the five known oscillation parameters. The dominant experiments and their corresponding 1σ accuracy and global precision from global fitting groups [5] are shown in the first, second and third row, respectively.

	Nominal	+ B2B (1%)	+ BG	+ EL (1%)	+ NL (1%)
$\sin^2\theta_{12}$	0.54%	0.60%	0.62%	0.64%	0.67%
Δm^2_{21}	0.24%	0.27%	0.29%	0.44%	0.59%
$\lvert\Delta m^2_{ee}\rvert$	0.27%	0.31%	0.31%	0.35%	0.44%

Table 1.4: Precision of $\sin^2\theta_{12}$, Δm^2_{21} and $|\Delta m^2_{ee}|$ from the nominal setup to those with more systematic uncertainties. The systematics are added one by one from the left cell to right cell.

from JUNO is less accurate than that of Daya Bay because the designed baseline is much larger than the optimized one (~ 2 km) and only one single detector is considered in the design concept. The final $\sin^2 2\theta_{13}$ sensitivity of Daya Bay after five years of running will be about 4%, and would lead this precision level in the foreseeable future. Therefore, we shall consider the precision measurements of θ_{12}, Δm^2_{21} and $|\Delta m^2_{ee}|$[1].

With the nominal setup as in the study of the MH measurement [10], we estimate the precision of the three relevant parameters, $\sin^2\theta_{12}$, Δm^2_{21} and Δm^2_{ee}, can achieve

[1]There will be two degenerate solutions for $|\Delta m^2_{ee}|$ in case of undetermined MH. We consider the correct MH in the following studies.

the level of 0.54%, 0.24% and 0.27%, respectively.

Moreover, the effects of important systematic errors, such as the bin-to-bin (B2B) energy uncorrelated uncertainty, the energy linear scale (EL) uncertainty and the energy non-linear (NL) uncertainty, and the influence of background (BG) are presented. As a benchmark, a 1% precision for all the systematic errors considered is assumed. The background level and uncertainties are the same as in the previous chapter for the MH determination. In Table 1.4, we show the precision of $\sin^2\theta_{12}$, Δm^2_{21} and $|\Delta m^2_{ee}|$ from the nominal setup to those with more systematic uncertainties. We can see that the energy-related uncertainties are more important because most of the sensitivity is derived from the spectrum distortion due to neutrino oscillations.

In summary, we can achieve the precision of $0.5\% - 0.7\%$ for the three oscillation parameters $\sin^2\theta_{12}$, Δm^2_{21} and $|\Delta m^2_{ee}|$. Precision tests of the unitarity of the lepton mixing matrix and mass sum rule are possible with the unprecedented precision of these measurements.

1.3.3 Supernova Neutrinos

Measuring the neutrino burst from the next nearby supernova (SN) is a premier goal of low-energy neutrino physics and astrophysics. According to current understanding and numerical simulation, one expects a neutrino signal with three characteristic phases as shown in Fig. 1.7. In a high-statistics observation one should consider these essentially as three different experiments, each holding different and characteristic lessons for particle and astrophysics.

1. *Infall, Bounce and Shock Propagation.*—Few tens of ms after bounce. Prompt ν_e burst, emission of $\bar{\nu}_e$ at first suppressed and emission of other flavors begins.

2. *Accretion Phase (Shock Stagnation).*—Few tens to few hundreds of ms, depending on progenitor properties and other parameters. Neutrino emission is powered by accretion flow. Luminosity in ν_e and $\bar{\nu}_e$ perhaps as much as a factor of two larger than each of the ν_x fluxes.

3. *Neutron-star cooling.*—Lasts until 10–20 s, powered by cooling and deleptonization of the inner core on a diffusion time scale. No strong asymmetries. Details depend on final neutron-star mass and nuclear equation of state.

In order to estimate the expected neutrino signals at JUNO, we assume a fiducial mass of 20 kton LS. For a typical galactic SN at 10 kpc, we take the time-integrated neutrino spectra as $f_\nu(E_\nu) \propto E_\nu^\alpha \exp[-(1+\alpha)E_\nu/\langle E_\nu\rangle]$ with a nominal index $\alpha = 3$ and $\langle E_\nu\rangle$ being the average neutrino energy. Furthermore, a total neutrino energy of $E_{\rm tot} = 3\times10^{53}$ erg is assumed to be equally distributed among neutrinos and antineutrinos of three flavors. As average neutrino energies are both flavor- and time-dependent, we calculate the event rates for three representative values $\langle E_\nu\rangle = 12$ MeV, 14 MeV and 16 MeV, and in each case the average energy is assumed to be equal for all flavors. The total numbers of neutrino events in JUNO are summarized in Table 1.5. Some comments on the detection channels are presented as follows.

(1) The inverse beta decay (IBD) is the dominant channel for supernova neutrino detection at both scintillator and water-Cherenkov detectors. In the IBD reaction

$$\overline{\nu}_e + p \to e^+ + n \ , \tag{1.9}$$

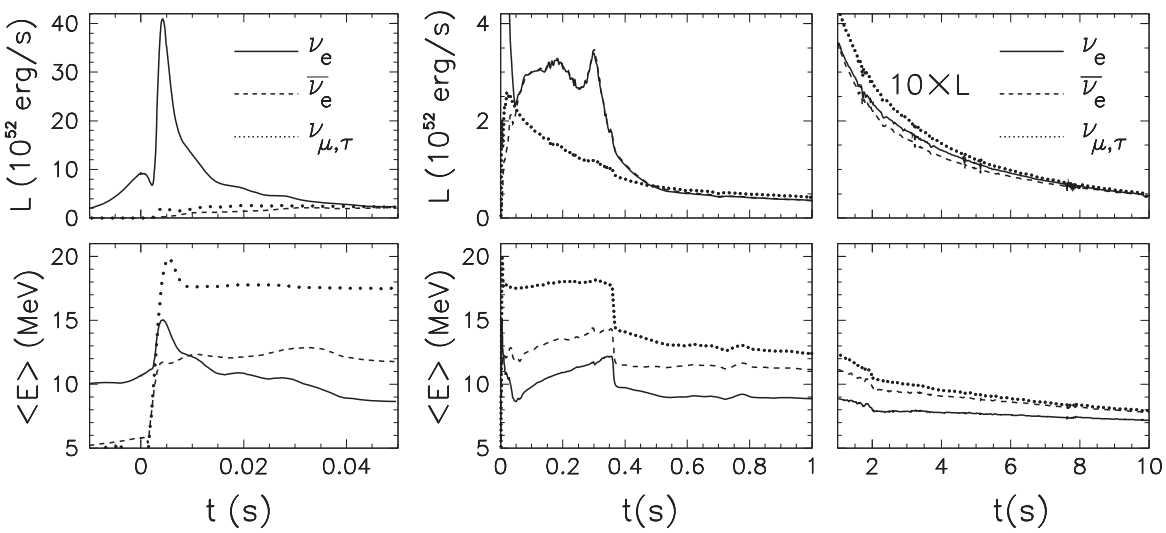

Figure 1.7: Three phases of neutrino emission from a core-collapse SN, from left to right: (1) Infall, bounce and initial shock-wave propagation, including prompt ν_e burst. (2) Accretion phase with significant flavor differences of fluxes and spectra and time variations of the signal. (3) Cooling of the newly formed neutron star, only small flavor differences between fluxes and spectra.

Channel	Type	Events for different $\langle E_\nu \rangle$ values		
		12 MeV	14 MeV	16 MeV
$\overline{\nu}_e + p \to e^+ + n$	CC	4.3×10^3	5.0×10^3	5.7×10^3
$\nu + p \to \nu + p$	NC	6.0×10^2	1.2×10^3	2.0×10^3
$\nu + e \to \nu + e$	NC	3.6×10^2	3.6×10^2	3.6×10^2
$\nu + {}^{12}\mathrm{C} \to \nu + {}^{12}\mathrm{C}^*$	NC	1.7×10^2	3.2×10^2	5.2×10^2
$\nu_e + {}^{12}\mathrm{C} \to e^- + {}^{12}\mathrm{N}$	CC	4.7×10^1	9.4×10^1	1.6×10^2
$\overline{\nu}_e + {}^{12}\mathrm{C} \to e^+ + {}^{12}\mathrm{B}$	CC	6.0×10^1	1.1×10^2	1.6×10^2

Table 1.5: Numbers of neutrino events in JUNO for a SN at a galactic distance of 10 kpc.

the neutrino energy threshold is $E_\nu^{\mathrm{th}} \approx 1.8$ MeV. The deposition of positron kinetic energy and the annihilation of the positron give rise to a prompt signal. In addition, the neutron is captured on free protons with a lifetime of about 200 μs, producing a 2.2 MeV γ. Hence the coincidence of prompt and delayed signals increases greatly the power of background rejection.

(2) As an advantage of the LS detector, the charged-current interaction on ^{12}C takes place for both ν_e and $\overline{\nu}_e$ via

$$\nu_e + {}^{12}\mathrm{C} \to e^- + {}^{12}\mathrm{B}\,, \tag{1.10}$$

$$\overline{\nu}_e + {}^{12}\mathrm{C} \to e^+ + {}^{12}\mathrm{N}\,. \tag{1.11}$$

The energy threshold for ν_e is 17.34 MeV, while that for $\overline{\nu}_e$ is 14.39 MeV. The subsequent beta decays of ^{12}B and ^{12}N with a 20.2 ms and 11 ms half-life, respectively, lead to a prompt-delayed coincident signal. Hence the charged-current reactions in Eqs. (1.10) and (1.11) provide a possibility to detect separately ν_e and $\overline{\nu}_e$.

(3) Neutral-current interaction on ^{12}C is of crucial importance to probe neutrinos of non-electron flavors, i.e.,

$$\nu + {}^{12}\mathrm{C} \rightarrow \nu + {}^{12}\mathrm{C}^{*} \ , \tag{1.12}$$

where ν stands for neutrinos or antineutrinos of all three flavors. A 15.11 MeV γ from the deexcitation of ^{12}C* to its ground state is a clear signal of SN neutrinos. Since neutrinos of non-electron flavors ν_x have higher average energies, the neutral-current interaction is more sensitive to ν_x, providing a possibility to pin down the flavor content of supernova neutrinos. However, it is impossible to reconstruct the neutrino energy in this channel.

(4) Elastic scattering of neutrinos on electrons will carry the directional information of incident neutrinos, and thus can be used to locate the SN. This is extremely important if a SN is hidden by other stars and the optical signal is obscured by galactic dust. The elastic scattering

$$\nu + e^{-} \rightarrow \nu + e^{-} \tag{1.13}$$

is most sensitive to ν_e because of the larger cross section. However, it is difficult to determine the direction of the scattered electron in the scintillator detector. At this point, large water-Cherenkov detectors, such as Super-Kamiokande, are complementary to scintillator detectors.

(5) Elastic scattering of neutrinos on protons has been proposed as a promising channel to measure supernova neutrinos of non-electron flavors [18, 19]:

$$\nu + p \rightarrow \nu + p \ . \tag{1.14}$$

Although the total cross section is about four times smaller than that of IBD reaction, the contributions from all the neutrinos and antineutrinos of three flavors will compensate for the reduction of cross section. As shown in Refs. [18, 19], it is possible to reconstruct the energy spectrum of ν_x at a large scintillator detector, which is very important to establish flavor conversions or spectral splits of SN neutrinos. For a realistic measurement of ν_x spectrum, a low-energy threshold and a satisfactory reconstruction of proton recoil energy are required. Taking into account the quenching effect, the total number of events is about 2240 above a threshold 0.2 MeV.

In summary, we show the time-integrated neutrino event spectra of SN neutrinos with respect to the visible energy E_{d} in the JUNO detector for a SN at 10 kpc, where no neutrino flavor conversions are assumed for illustration and the average neutrino energies are $\langle E_{\nu_e} \rangle = 12$ MeV, $\langle E_{\overline{\nu}_e} \rangle = 14$ MeV and $\langle E_{\nu_x} \rangle = 16$ MeV. The main reaction channels are shown together with the threshold of neutrino energies: (1) IBD (black and solid curve), $E_{\mathrm{d}} = E_{\nu} - 0.8$ MeV; (2) Elastic ν-p scattering (red and dashed curve), E_{d} stands for the recoil energy of proton; (3) Elastic ν-e scattering (blue and double-dotted-dashed curve), E_{d} denotes the recoil energy of electron; (4) Neutral-current reaction $^{12}\mathrm{C}(\nu, \nu')^{12}\mathrm{C}^{*}$ (orange and dotted curve), $E_{\mathrm{d}} \approx 15.1$ MeV; (5) Charged-current reaction $^{12}\mathrm{C}(\nu_e, e^{-})^{12}\mathrm{N}$ (green and dotted-dashed curve), $E_{\mathrm{d}} = E_{\nu} - 17.3$ MeV; (6) Charged-current reaction $^{12}\mathrm{C}(\overline{\nu}_e, e^{+})^{12}\mathrm{B}$ (magenta and double-dotted curve), $E_{\mathrm{d}} = E_{\nu} - 13.9$ MeV.

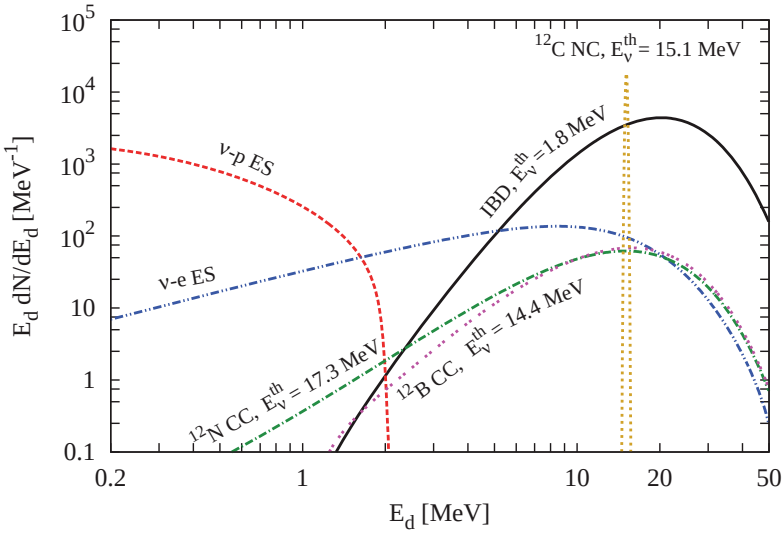

Figure 1.8: The neutrino event spectra with respect to the visible energy E_d in the JUNO detector for a SN at 10 kpc, where no neutrino flavor conversions are assumed for illustration and the average neutrino energies are $\langle E_{\nu_e} \rangle = 12$ MeV, $\langle E_{\bar{\nu}_e} \rangle = 14$ MeV and $\langle E_{\nu_x} \rangle = 16$ MeV. (See the text for details)

1.3.4 Diffuse Supernova Neutrino Background

The integrated neutrino flux from all past core-collapse events in the visible universe forms the diffuse supernova neutrino background (DSNB), holding information on the cosmic star-formation rate, the average core-collapse neutrino spectrum, and the rate of failed supernovae. The Super-Kamiokande water Cherenkov detector has provided the first limits [20, 21] and eventually may achieve a measurement at the rate of a few events per year, depending on the implementation of its gadolinium upgrade.

The JUNO detector has the potential to achieve a measurement comparable to Super-Kamiokande, benefiting from the excellent intrinsic capabilities of liquid scintillator detectors for antineutrino tagging and background rejection. Sources of correlated background events must be taken into account when defining the energy window, fiducial volume and pulse shape selection criteria for the DSNB detection. Reactor and atmospheric neutrino IBD signals define an observational window reaching from 11 to ∼30 MeV. Taking into account the JUNO detector simulation of the expected signal and background rates, a 3σ signal is conceivable after 10 years of running for typical assumptions of DSNB parameters. A non-detection would strongly improve current limits and exclude a significant range of the DSNB parameter space.

Following the method described in Ref. [22], we show in Tab. 1.6 the expected detection significance after 10 years of data taking for different DSNB models with $\langle E_{\bar{\nu}_e} \rangle$ ranging from 12 MeV to 21 MeV. Results are given based on either a rate-only or spectral fit analysis and assuming 5% or 20% for the background uncertainty. For each DSNB model it was assumed that the number of detected events equals the sum of the expected signal and background events. After 10 years the DSNB can be detected with $> 3\,\sigma$ significance if $\langle \mathrm{E}_{\bar{\nu}_\mathrm{e}} \rangle \geq 15$ MeV.

If there is no positive detection of the DSNB, the current limit can be significantly improved. Assuming that the detected event spectrum equals the background

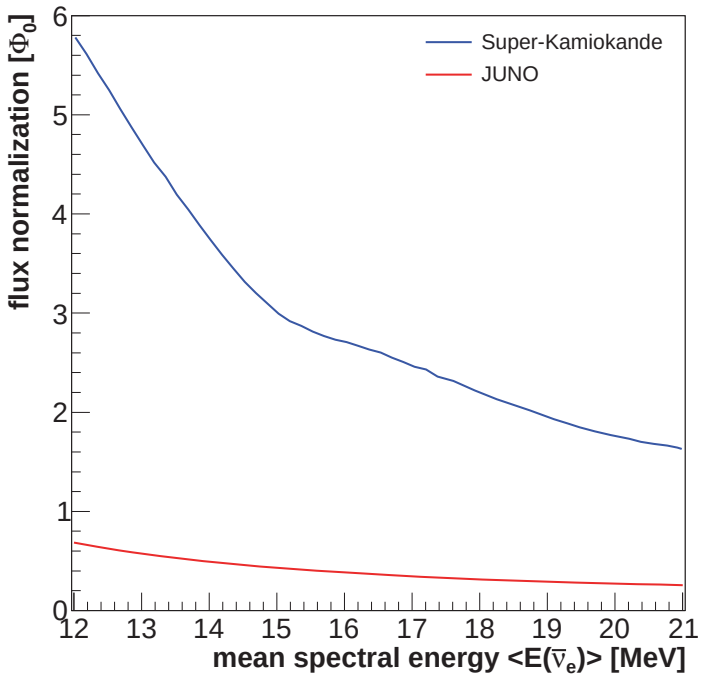

Figure 1.9: Exclusion contour at 90% C.L. as a function of the mean energy of the SN spectrum $\langle E_{\bar{\nu}_e} \rangle$ and the flux amplitude (SN rate times total emitted energy per SN). We assume 5% background uncertainty and no DSNB signal detection ($N_{\rm det} = \langle N_{\rm bg} \rangle$) after 10 yrs.

Syst. uncertainty BG	5 %		20 %	
$\langle E_{\bar{\nu}_e} \rangle$	rate only	spectral fit	rate only	spectral fit
12 MeV	$2.3\,\sigma$	$2.5\,\sigma$	$2.0\,\sigma$	$2.3\,\sigma$
15 MeV	$3.5\,\sigma$	$3.7\,\sigma$	$3.2\,\sigma$	$3.3\,\sigma$
18 MeV	$4.6\,\sigma$	$4.8\,\sigma$	$4.1\,\sigma$	$4.3\,\sigma$
21 MeV	$5.5\,\sigma$	$5.8\,\sigma$	$4.9\,\sigma$	$5.1\,\sigma$

Table 1.6: The expected detection significance after 10 years of data taking for different DSNB models with $\langle E_{\bar{\nu}_e} \rangle$ ranging from 12 MeV to 21 MeV ($\Phi = \Phi_0$). Results are given based on either a rate-only or spectral fit analysis and assuming 5% or 20% for background uncertainty.

expectation in the overall normalization and shape, the upper limit on the DSNB flux above 17.3 MeV would be $\sim 0.2\,\mathrm{cm}^{-2}\mathrm{s}^{-1}$ (90% C.L.) after 10 years for $\langle E_{\bar{\nu}_e} \rangle = 18\,\mathrm{MeV}$. This limit is almost an order of magnitude better than the current value from Super-Kamiokande [21]. In Fig. 1.9 we show the corresponding exclusion contour at 90% C.L. as a function of the mean energy with $\langle E_{\bar{\nu}_e} \rangle$ ranging from 12 MeV to 21 MeV.

1.3.5 Solar Neutrinos

More than forty years of experiments and phenomenological analyses brought to a crystal clear solution of the Solar neutrino problem in terms of oscillating massive neutrinos interacting with matter, with only the LMA region surviving in the mixing parameter space. The rather coherent picture emerging from all of these solar neutrino experiments is in general agreement with the values of the mixing parameters extracted from KamLAND data [23]. A global three flavor analysis, including all the solar neutrino experiments and KamLAND data and assuming CPT invariance, gives the following values for the mixing angles and the differences of the squared mass eigenvalues [24]: $\tan^2\theta_{12} = 0.457^{+0.038}_{-0.025}\,; \sin^2\theta_{13} = 0.023^{+0.014}_{-0.018}\,; \Delta m^2_{21} = 7.50^{+0.18}_{-0.21} \times 10^{-5}\,\mathrm{eV}^2$.

The measured values of the neutrino fluxes produced in different phases of the *pp* chain and of the CNO cycle are consistent with the Standard Solar Model (SSM). But they are not accurate enough to solve the metallicity problem [25], discriminating between the different (high Z versus low Z) versions of the SSM. Because most of the experimental results fall somehow in the middle between the high and the low Z predictions and the uncertainties are still too high. In order to operate this discrimination, a future experimental challenge would be an even more accurate determination of the ^{8}B and ^{7}Be fluxes, combined with the measurement of CNO neutrinos.

We present in Fig. 1.10(a) the expected singles spectra at JUNO with the radio purity assumption of 10^{-16}g/g for ^{238}U and ^{232}Th, 10^{-17}g/g for ^{40}K and ^{14}C, and Fig. 1.10(b) the expected singles spectra at JUNO with an ideal radio purity assumption of 10^{-17}g/g for ^{238}U and ^{232}Th, 10^{-18}g/g for ^{40}K and ^{14}C. The ^{7}Be spectrum clearly stands out all backgrounds. More studies on the capability sensitivity deserve further simulations.

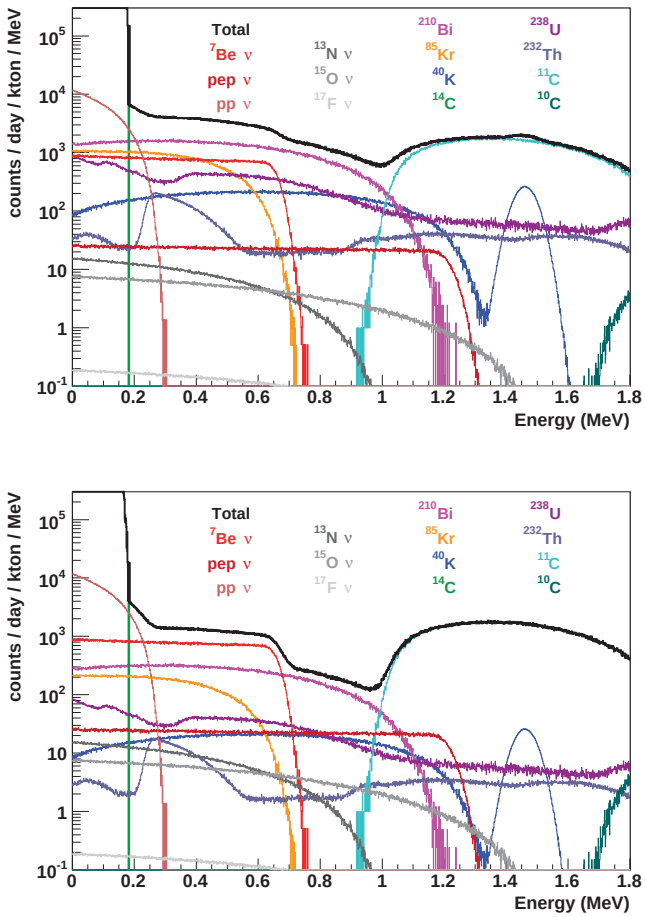

Figure 1.10: (a)On the top, the expected singles spectra at JUNO with the radio purity assumption 10^{-16}g/g for ^{238}U and ^{232}Th, 10^{-17}g/g for ^{40}K and ^{14}C. (b) On the bottom, assuming a background level one order of magnitude better for ^{238}U, ^{232}Th and for ^{40}K, ^{14}C.

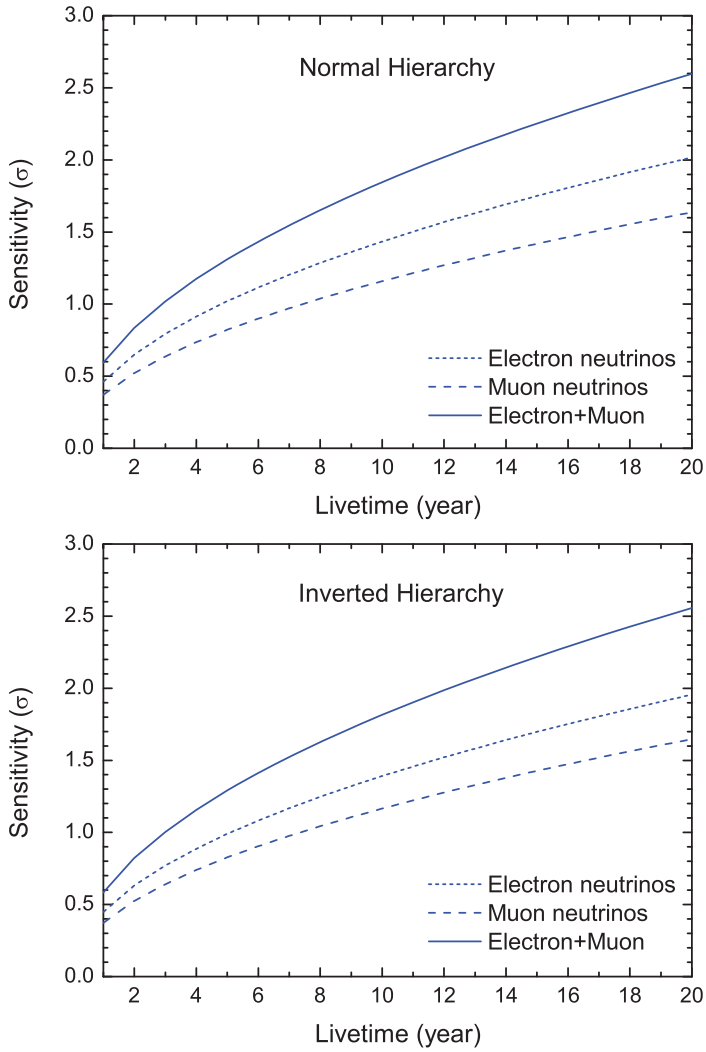

Figure 1.11: The MH sensitivities of atmospheric neutrinos as a function of livetime for the true NH (upper panel) and IH (lower panel) cases.

1.3.6 Atmospheric Neutrinos

Atmospheric neutrinos are one of the most important neutrino sources for neutrino oscillation studies. Atmospheric neutrinos have broad ranges in the baseline length (15 km $\sim$ 13000 km) and energy (0.1 GeV $\sim$ 10 TeV). When atmospheric neutrinos pass through the Earth, the matter effect will affect the oscillations of the neutrinos. The Mikheyev-Smirnov-Wolfenstein resonance enhancement may occur in the normal mass hierarchy (NH) for neutrinos and inverted mass hierarchy (IH) for antineutrinos. Therefore, JUNO has the capability to measure the neutrino MH through detecting the upward atmospheric neutrinos. This is complementary to the JUNO reactor antineutrino results. JUNO's ability in MH determination is at the 1σ-2σ level for 10 years of data taking. An optimistic estimation of the MH sensitivity is obtained based on several reasonable assumptions:

- An angular resolution of 10° for the neutrino direction and $\sigma_{E_{vis}} = 0.01\sqrt{E_{\rm vis}/{\rm GeV}}$ for the visible energy of neutrino events are assumed.
- The $\nu_e/\bar{\nu}_e$ CC events are identified and reconstructed in the $e^\pm$ visible energy range with $E^e_{\rm vis} > 1$ GeV and $Y_{\rm vis} < 0.5$, where $Y_{\rm vis}$ is defined as the ratio of the hadron visible energy in the visible energy of an atmospheric neutrino event.
- The selected $\nu_e/\bar{\nu}_e$ events are divided into two samples in terms of the numbers of Michael electrons with $N_e = 0$ ($\bar{\nu}_e$-like events) or $N_e \geq 1$ (ν_e-like events).
- The $\nu_\mu/\bar{\nu}_\mu$ CC events are selected with $L_\mu > 3$ m, where L_μ is the track length inside the LS region for the charge lepton $\mu^\pm$.
- The selected $\nu_\mu/\bar{\nu}_\mu$ events are divided into four samples. First, these events are grouped as partially contained (PC) and fully contained (FC) events depending on whether $\mu^\pm$ can escape from the LS region or not. Second, FC events with $N_e \geq 2$ or μ^- capture on ^{12}C or $Y_{\rm vis} > 0.5$ are defined as FC ν_μ-like events, and the residual FC events are defined as FC $\bar{\nu}_\mu$-like events. Finally, PC events with $N_e \geq 1$ or $Y_{\rm vis} > 0.5$ are classified as PC ν_μ-like events, and all the other PC events are PC $\bar{\nu}_\mu$-like events.

The MH sensitivity of the separate contribution of muon and electron neutrino events and their combinations in the cases of both normal and inverted MHs are presented in Fig. 1.11. We can observe from the figure that the $\nu_e/\bar{\nu}_e$ events have better sensitivity than $\nu_\mu/\bar{\nu}_\mu$ events because more $\nu_e/\bar{\nu}_e$ events with higher energies can deposit their whole visible energy in the LS region. The combined sensitivity can reach 1.8σ (2.6σ) after 10 (20) years of running. Finally, we want to mention that atmospheric neutrinos can also be used to search for CP violation effects and precisely measure the atmospheric mixing angle θ_{23}.

1.3.7 Geo-Neutrinos

For half a century we have established with considerable precision the Earth's surface heat flow 46 ± 3 TW (10^{12} watts), however we are vigorously debating what fraction of this power comes from primordial versus radioactive sources. This debate touches on the composition of the Earth, the question of chemical layering in the mantle, the

Source	Events/year
Geoneutrinos	408 ± 60
U chain	311 ± 55
Th chain	92 ± 37
Reactors	16100 ± 900
Fast neutrons	3.65 ± 3.65
^{9}Li - ^{8}He	657 ± 130
^{13}C$(\alpha, n)^{16}$O	18.2 ± 9.1
Accidental coincidences	401 ± 4

Table 1.7: Signal and backgrounds considered in the geoneutrino sensitivity study: the number of expected events for all components contributing to the IBD spectrum in the 0.7 - 12 MeV energy region of the prompt signal. We have assumed 80% antineutrino detection efficiency and 17.2 m radial cut (18.35 kton of liquid scintillator).

nature of mantle convection, the energy needed to drive Plate Tectonics, and the power source of the geodynamo, the magnetosphere that shields the Earth for the harmful cosmic ray flux.

Over the last decade particle physicists have detected the Earth's geoneutrino flux, the planetary emission of electron anti-neutrinos that are derived from naturally occurring, radioactive beta-decay events inside the Earth [26, 27]. Matter, including the Earth, is mostly transparent to these elusive messengers that reveal the sources of heat inside the Earth. By detecting a few events per years we are now measuring the geoneutrino flux from Thorium and Uranium inside the planet, which in turn allows us to determine the amount of radiogenic power driving the Earth's engine.

Predicting the geoneutrino signal at JUNO demands that we accumulate the basic geological, geochemical and geophysical data for the regional area surrounding the detector. Experience tells us that in the continents the closest 500 km to the detector contributes half of the signal and it is this region that needs to be critically evaluated [28]. This goal demands that the physical (density and structure) and chemical (abundance and distribution of Th and U) nature of the continent must be specified for the region. The main tasks include surveys and descriptions of the geology, seismology, heat flow, and geochemistry of the regional lithosphere.

The dominate background for the geo-neutrino observation is the reactor antineutrinos. In addition, other backgrounds include the cosmic-muons spallation products (^{9}Li-^{8}He isotopes, fast neutrons), accidental coincidences of non-correlated events, and backgrounds induced by radioactive contaminants of scintillator and detector materials (i.e., ^{13}C (α, n)^{16}O). In Tab. 1.7, we summarize the predicted geo-neutrino signal and backgrounds considered in the sensitivity study.

Precision of the reconstruction of geoneutrino signal is shown in Tab. 1.8, for the running time in 1, 3, 5, and 10 years. Different columns refer to the measurement of geo-neutrino signal with fixed Th/U ratio, and U and Th signals fit as free and independent components. The given numbers are the position and root meam square (RMS) of the Gaussian fit to the distribution of the ratios between the number of reconstructed and generated events. It can be seen that while RMS is decreasing with

Number of years	U + Th (fixed chondritic Th/U ratio)	U (free)	Th (free)
1	0.96 ± 0.17	1.01 ± 0.32	0.79 ± 0.66
3	0.96 ± 0.10	1.03 ± 0.19	0.80 ± 0.37
5	0.96 ± 0.08	1.03 ± 0.15	0.80 ± 0.30
10	0.96 ± 0.06	1.03 ± 0.11	0.80 ± 0.21

Table 1.8: Precision of the reconstruction of geoneutrino signal. See the text for details.

longer data acquisition time, there are some systematic effects which do not depend on the acquired statistics. With 1, 3, 5, and 10 years of data, the statistical error amounts to 17%, 10%, 8%, and 6% respectively with the fixed chondritic Th/U ratio.

1.3.8 Nucleon Decay

Being a large underground LS detector, JUNO is in an excellent position in search for nucleon decays. In particular, in the SUSY favored decay channel $p \to K^+ + \bar{\nu}$, JUNO will be competitive and complementary to other experiments using water Cherenkov and liquid argon detectors [29].

The protons in the JUNO detector are provided by both the hydrogen nuclei and the carbon nuclei. Using the Daya Bay liquid scintillator as a reference, the H to C molar ratio is 1.639. For a 20 kt fiducial volume detector, the number of protons from hydrogen (free protons) is 1.45×10^{33} and the number of protons from carbon (bound protons) is 5.30×10^{33}.

If the proton is from hydrogen, it decays at rest. The kinetic energy of the K^+ is fixed by kinematics to be 105 MeV, which gives a prompt signal in the liquid scintillator. The K^+ has a lifetime of 12.4 nanoseconds and would quickly decay into five different channels, $K^+ \to \mu^+\nu_\mu$ and $K^+ \to \pi^+\pi^0$ are two most probably decay modes. In either case, there is a short-delayed ($\sim$12 ns) signal from the K^+ daughters.

If the K^+ decays into $\mu^+\nu_\mu$, the delayed signal comes from the μ^+, which has a fixed kinetic energy of 152 MeV from the kinematics. The μ^+ itself decays 2.2 μs later into $e^+\nu_e\bar{\nu}_\mu$, which gives a third long-delayed signal with well known (Michel electron) energy spectrum. If the K^+ decays into $\pi^+\pi^0$, the π^+ deposits its kinetic energy (108 MeV) and the π^0 instantaneously decays ($\tau = 8.4 \times 10^{-17} s$) into primarily two gamma rays (98.80%) with the sum of deposited energy equal to the total energy of π^0 (246 MeV). The delayed signal includes all of the aforementioned deposited energy. Then, the π^+ decays ($\tau = 26$ ns) primarily into $\mu^+\nu_\mu$ (99.99%). The μ^+ itself has very low kinetic energy (4.1 MeV), but it decays 2.2 μs later into $e^+\nu_e\bar{\nu}_\mu$, which gives the third long-delayed decay positron signal.

The simulated hit time distribution of a $K^+ \to \mu^+\nu_\mu$ event is shown in Fig. 1.12, which displays a clear three-fold coincidence:

- A prompt signal from K^+ and a delayed signal from its decay daughters with a time coincidence of 12 ns.
- Both the prompt and delayed signals have well-defined energy.
- One and only one decay positron with a time coincidence of 2.2 μs from the prompt signals.

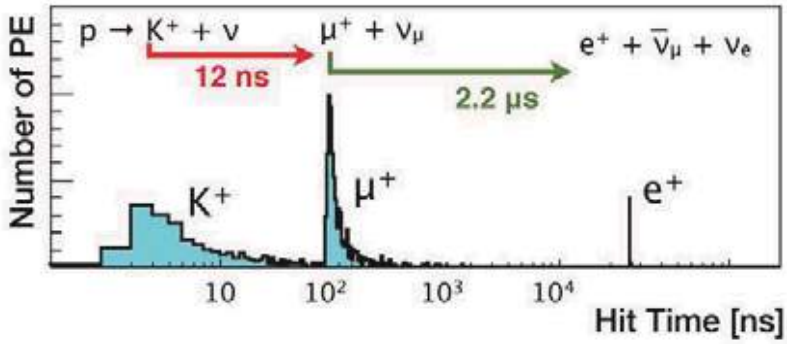

Figure 1.12: The simulated hit time distribution of photoelectrons (PEs) from a $K^+ \to \mu^+\nu_\mu$ event at JUNO.

The time coincidence and the well-defined energy provide a powerful tool to reject background, which is crucial in the proton decay search.

The sensitivity to proton lifetime, can be calculated as $\tau(p \to K^+ + \bar{\nu}) = N_p T R \epsilon / S$, where N_p (6.75×10^{33}) is the total number of protons, T is the measuring time where we assumed 10 years, R (84.5%) is the K^+ decay branching ratio included in the analysis, and ϵ (65%) is the total signal efficiency. S is the upper limit of number of signal events at certain confidence interval, which depends on the number of observed events as well as the expected number of background events. The expected background is 0.5 events in 10 years. If no event is observed, the 90% C.L upper limit is $S = 1.94$. The corresponding sensitivity to proton lifetime is $\tau > 1.9 \times 10^{34}$ yr. This represents a factor of three improvement over the current best limit from Super-Kamiokande, and starts to approach the region of interest predicted by various GUTs models. In a real experiment, the sensitivity may decrease if background fluctuates high. In the case that one event is observed (30% probability), the 90% C.L upper limit is $S = 3.86$. The corresponding sensitivity to proton lifetime is $\tau > 9.6 \times 10^{33}$ yrs. If two events are observed (7.6% probability), the sensitivity is further reduced to $\tau > 6.8 \times 10^{33}$ yrs. In Fig. 1.13 we plot the 90% C.L. sensitivity to the proton lifetime in the decay mode $p \to K^+ + \overline{\nu}$ at JUNO as a function of the running time. Due to the high efficiency in measuring this mode, JUNO's sensitivity will surpass Super-Kamiokande's after 3 yrs of data taking.

1.3.9 Light Sterile Neutrinos

Motivated from the anomalies of LSND [30], MiniBooNE [31], the reactor antineutrino anomaly [32], and Gallium anomaly [33], the light sterile neutrino [34, 35] is regarded as one of the most promising possibilities for new physics beyond the three neutrino oscillation paradigm. Therefore, future experimental oscillation searches at short baselines are required to test the light sterile neutrino hypothesis [36].

Several possible methods of sterile neutrino studies are considered at JUNO. The first one is the use of existing reactor antineutrinos, which can test the active-sterile mixing with the mass-squared difference ranging from 10^{-5} to 10^{-2} eV^2. This parameter space is irrelevant to the short baseline oscillation, but could be tested as the sub-leading effect of solar neutrino oscillations.

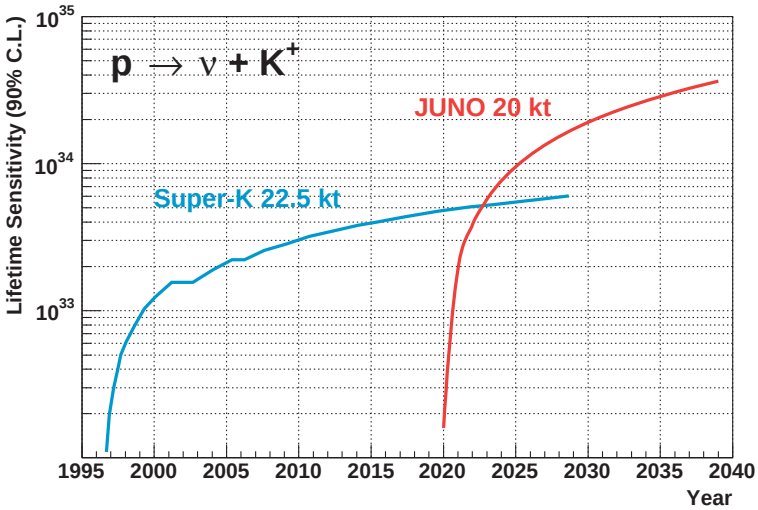

Figure 1.13: The 90% C.L. sensitivity to the proton lifetime in the decay mode $p \rightarrow K^+ + \overline{\nu}$ at JUNO as a function of time. In comparison, Super-Kamiokande's sensitivity is also projected [29].

The direct test of short baseline oscillations at JUNO requires additional neutrino sources placed near or inside the detector. Using 50 kCi ^{144}Ce-^{144}Pr as the antineutrino source at the detector center, JUNO can reach the 10^{-2} level of active-sterile mixing at 95% C.L. after 1.5 yrs of data taking. On the other hand, a cyclotron-driven ^{8}Li source can be employed as the decay-at-rest (DAR) neutrino source near the detector. The high DAR flux coupled with the large size of the JUNO detector allows us to make an extremely sensitive search for antineutrino disappearance in the region of short baseline oscillation anomalies. With a 60 MeV/amu cyclotron accelerator, JUNO can reach the 10^{-3} level of active-sterile mixing at 5σ C.L. after 5 yrs of data taking. IsoDAR@JUNO will be able to map out definitively the oscillation wave. There is no other planned experiment that matches this sensitivity.

1.3.10 Indirect Dark Matter Search

The existence of non-baryonic dark matter (DM) in the Universe has been well established by astronomical observations. DM can also be detected indirectly by looking for the neutrino signature from DM annihilation or decays in the Galactic halo, the Sun or the Earth. In particular, the search for the DM-induced neutrino signature from the Sun has given quite tight constraints on the spin-dependent (SD) DM-proton scattering cross section $\sigma_{\chi p}^{\rm SD}$ [37].

In general, DM inside the Sun can annihilate into leptons, quarks and gauge bosons. The neutrino flux results from the decays of such final-state particles. Here we consider two annihilation modes $\chi\chi \rightarrow \tau^+\tau^-$ and $\chi\chi \rightarrow \nu\bar{\nu}$ as a benchmark. The sensitivity calculations for $\sigma_{\chi p}^{\rm SD}$ are given in Fig. 1.14, where one can see that the JUNO sensitivity is much better than current direct detection constraints set by COUPP [38], SIMPLE [39] and PICASSO [40] experiments. Notice that the sensitivity for $m_\chi < 3$ GeV becomes poor due to the DM evaporation from the Sun.

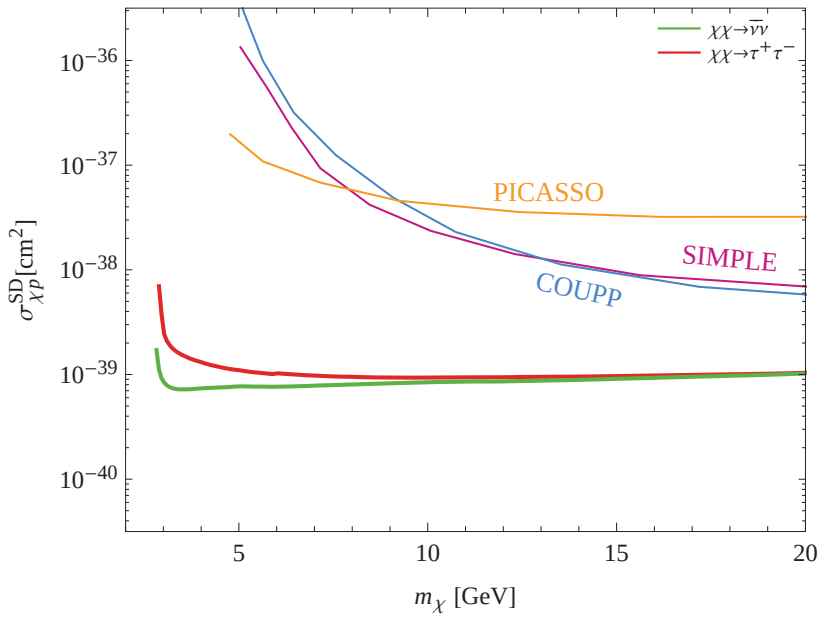

Figure 1.14: The JUNO 2σ sensitivity to the spin-dependent cross section $\sigma^{SD}_{\chi p}$ after 5 yrs of data taking. The constraints from the direct detection experiments are also shown for comparison.

1.3.11 Other Exotic Searches

The standard three-neutrino mixing paradigm can describe most of the phenomena in solar, atmospheric, reactor, and accelerator neutrino oscillations [4]. However, other new physics mechanisms can operate at a sub-leading level, and may appear at the stage of precision measurements of neutrino oscillations. Therefore, other exotic searches can be performed at JUNO using reactor neutrinos, solar neutrinos, atmospheric neutrinos and supernova neutrinos.

With the reactor neutrino oscillation, JUNO can:

- test the nonstandard neutrino interactions at the source and detector [41, 42];
- test the Lorentz and CPT invariance violation [43];
- test the mass-varying properties of neutrino propagation [44].

Meanwhile, using solar and atmospheric neutrino oscillations, JUNO can

- test the nonstandard neutrino interactions during the propagation [45, 46];
- test the long range forces [47];
- test the super light sterile neutrinos [48];
- test the anomalous magnetic moment [49, 50].

Therefore, with precision measurements JUNO will be a powerful playground to test different exotic phenomena of new physics beyond the Standard Model.

Bibliography

[1] S. Weinberg, Phys. Rev. Lett. **19**, 1264 (1967).

[2] Z. Maki, M. Nakagawa, and S. Sakata, Prog. Theor. Phys. **28**, 870 (1962); B. Pontecorvo, Sov. Phys. JETP **26**, 984 (1968).

[3] N. Cabibbo, Phys. Rev. Lett. **10**, 531 (1963); M. Kobayashi and T. Maskawa, Prog. Theor. Phys. **49**, 652 (1973).

[4] J. Beringer *et al.* (Particle Data Group), Phys. Rev. D **86**, 010001 (2012).

[5] F. Capozzi, G. L. Fogli, E. Lisi, A. Marrone, D. Montanino and A. Palazzo, Phys. Rev. D **89**, 093018 (2014); D. V. Forero, M. Tortola and J. W. F. Valle, Phys. Rev. D **90**, 093006 (2014); M. C. Gonzalez-Garcia, M. Maltoni and T. Schwetz, JHEP **1411**, 052 (2014).

[6] Z.Z. Xing and S. Zhou, *Neutrinos in Particle Physics, Astronomy and Cosmology* (Zhejiang University Press and Springer-Verlag, 2011).

[7] L. Zhan, Y.F. Wang, J. Cao, and L.J. Wen, Phys. Rev. D **78**, 111103 (2008); Phys. Rev. D **79**, 073007 (2009).

[8] Yifang Wang, talk at ICFA seminar, 2008, `http://www-conf.slac.stanford.edu/icfa2008/Yifang_Wang_102808.pdf`

[9] Jun Cao, talk at Neutrino Telescope, 2009, `http://neutrino.pd.infn.it/NEUTEL09/Talks/Cao.pdf`

[10] Y. F. Li, J. Cao, Y. F. Wang and L. Zhan, Phys. Rev. D **88**, 013008 (2013).

[11] F.P. An *et al.* (Daya Bay Collaboration), Phys. Rev. Lett. **108**, 171803 (2012); Chin. Phys. C **37**, 011001 (2013); Phys. Rev. Lett. **112**, 061801 (2014).

[12] A. Gando *et al.*, [KamLAND Collaboration], Phys. Rev. D **83**, 052002 (2011).

[13] P. Adamson *et al.*, [MINOS Collaboration], Phys. Rev. Lett. **110**, 251801 (2013).

[14] B. Aharmim *et al.*, [SNO Collaboration], Phys. Rev. C **88**, 025501 (2013).

[15] F. P. An *et al.* [Daya Bay Collaboration], arXiv:1505.03456 [hep-ex]; F. P. An *et al.*, [Daya Bay Collaboration], Phys. Rev. Lett. **112**, 061801 (2014).

[16] R. Wendell *et al.*, [Super-Kamiokande Collaboration], Phys. Rev. D **81**, 092004 (2010).

[17] K. Abe *et al.*, [T2K Collaboration], Phys. Rev. Lett. **111**, 211803 (2013); for the latest update see arXiv:1403.1532 [hep-ex].

[18] J. F. Beacom, W. M. Farr and P. Vogel, Phys. Rev. D **66**, 033001 (2002), [hep-ph/0205220].

[19] B. Dasgupta and J. F. Beacom, Phys. Rev. D **83**, 113006 (2011), [arXiv:1103.2768 [hep-ph]].

[20] M. Malek *et al.* (Super-Kamiokande Collaboration), Phys. Rev. Lett. **90**, 061101 (2003).

[21] K. Bays *et al.* (Super-Kamiokande Collaboration), Phys. Rev. D **85**, 052007 (2012).

[22] W. A. Rolke, A. M. López and J. Conrad, Nucl. Instrum. Meth. A **551**, 493 (2005).

[23] S. Abe *et al.* [KamLAND Collaboration], Phys. Rev. Lett. **100**, 221803 (2008).

[24] G. Bellini *et al.* [Borexino Collaboration], Phys. Rev. D **89** 112007 (2014).

[25] F. L. Villante, A. M. Serenelli, F. Delahaye and M. H. Pinsonneault, Astrophys. J. **787**, 13 (2014).

[26] L. M. Krauss, S. L. Glashow, and D. N. Schramm, Nature, **310**, 5974 (1984).

[27] W. F. McDonough, J. G. Learned, S. T. Dye, Physics Today **65**, 46 (2012).

[28] T. Araki *et al.*, Nature **436**, 499 (2005).

[29] E. Kearns, talk presented at the ISOUP Symposium (2013).

[30] A. Aguilar-Arevalo *et al.* [LSND Collaboration], Phys. Rev. D **64**, 112007 (2001) [hep-ex/0104049].

[31] A. A. Aguilar-Arevalo *et al.* [MiniBooNE Collaboration], Phys. Rev. Lett. **110**, 161801 (2013) [arXiv:1207.4809 [hep-ex], arXiv:1303.2588 [hep-ex]].

[32] G. Mention, M. Fechner, T. Lasserre, T. A. Mueller, D. Lhuillier, M. Cribier and A. Letourneau, Phys. Rev. D **83**, 073006 (2011) [arXiv:1101.2755 [hep-ex]].

[33] C. Giunti and M. Laveder, Phys. Rev. C **83**, 065504 (2011) [arXiv:1006.3244 [hep-ph]].

[34] C. Giunti, M. Laveder, Y. F. Li and H. W. Long, Phys. Rev. D **88**, 073008 (2013) [arXiv:1308.5288 [hep-ph]].

[35] J. Kopp, P. A. N. Machado, M. Maltoni and T. Schwetz, JHEP **1305**, 050 (2013) [arXiv:1303.3011 [hep-ph]].

[36] T. Lasserre, Phys. Dark Univ. **4**, 81 (2014) [arXiv:1404.7352 [hep-ex]].

[37] M. G. Aartsen *et al.* [IceCube Collaboration], Phys. Rev. Lett. **110**, 131302 (2013).

[38] E. Behnke *et al.* [COUPP Collaboration], Phys. Rev. D **86**, 052001 (2012) [arXiv:1204.3094 [astro-ph.CO]].

[39] M. Felizardo *et al.* (SIMPLE Collaboration), Phys. Rev. Lett. **108**, 201302 (2012) [arXiv:1106.3014 [astro-ph.CO]].

[40] S. Archambault *et al.* [PICASSO Collaboration], Phys. Lett. B **711**, 153 (2012) [arXiv:1202.1240 [hep-ex]].

[41] T. Ohlsson, H. Zhang, S. Zhou, Phys. Lett. B. **728**, 148 (2014).

[42] Y. F. Li and Y. L. Zhou, Nucl. Phys. B **888**, 137 (2014).

[43] Y. F. Li and Z. H. Zhao, Phys. Rev. D **90**, 113014 (2014).

[44] T. Schwetz and W. Winter, Phys. Lett. B **633**, 557 (2006).

[45] T. Ohlsson, Rept. Prog. Phys. **76**, 044201 (2013) [arXiv:1209.2710 [hep-ph]].

[46] A. Bolanos, O. G. Miranda, A. Palazzo, M. A. Tortola and J. W. F. Valle, Phys. Rev. D **79**, 113012 (2009).

[47] A. S. Joshipura and S. Mohanty, Phys. Lett. B **584**, 103 (2004) [hep-ph/0310210].

[48] P. C. de Holanda and A. Y. Smirnov, Phys. Rev. D **83**, 113011 (2011).

[49] C. Arpesella *et al.* [Borexino Collaboration], Phys. Rev. Lett. **101**, 091302 (2008).

[50] C. Giunti and A. Studenikin, arXiv:1403.6344 [hep-ph].

Chapter 2

Central Detector

2.1 Introduction and requirement of the central detector

The central detector of JUNO aims to measure the neutrino energy spectrum using 20 kt liquid scintillator (LS) and 17,000 PMTs. An inner sphere with a diameter of around 35 m is designed to contain the huge volume of LS, and an outer structure with a diameter of around 38 m is needed to support the inner sphere as well as PMTs. In order to get the $3\%/\sqrt{E}$ energy resolution, the central detector is required to maximize the collection of optical signals from LS meanwhile minimize the background from a variety of radioactive sources. Since it is not possible to repair during the operation, this detector must have a long life time and a high reliability.

Since the LS and PMTs are separately documented in Chapter 4 and Chapter 6, this chapter is mainly focused on the challenges:

1) Construction of the large structure of the sphere and its support;

2) Test and installation of the 17,000 PMTs;

3) Filling of LS and long term operation of the detector.

Throughout the design effort, the strength and stability of the structure is the drive. In addition, the working conditions in the underground hall, safety issues during the construction, cost, and the overall time schedule should be taken into account. The ideal design of the JUNO central detector is a stainless-steel tank plus an acrylic sphere, where the stainless-steel tank is used to separate the shielding liquid (mineral oil or LAB, to be decided) from the pure water in the water pool, and the acrylic sphere is to hold the 20 kt LS, as indicated in Fig. 2.1. Due to the limitation of space, it is very difficult to simultaneously construct the two spheres and there is also a high risk and significant schedule delay if the two spheres were constructed in series. As a result, alternative options could be:

1) the stainless-steel tank is replaced by an open space truss or other steel supporting structures;

2) the acrylic sphere is replaced by an off-site fabricated balloon.

Currently, the baseline is the first one, i.e. the so called acrylic sphere plus stainless-steel support option, which will be detailed in this document. The second option of the balloon plus stainless-steel sphere is a backup, and will be described also in this chapter.

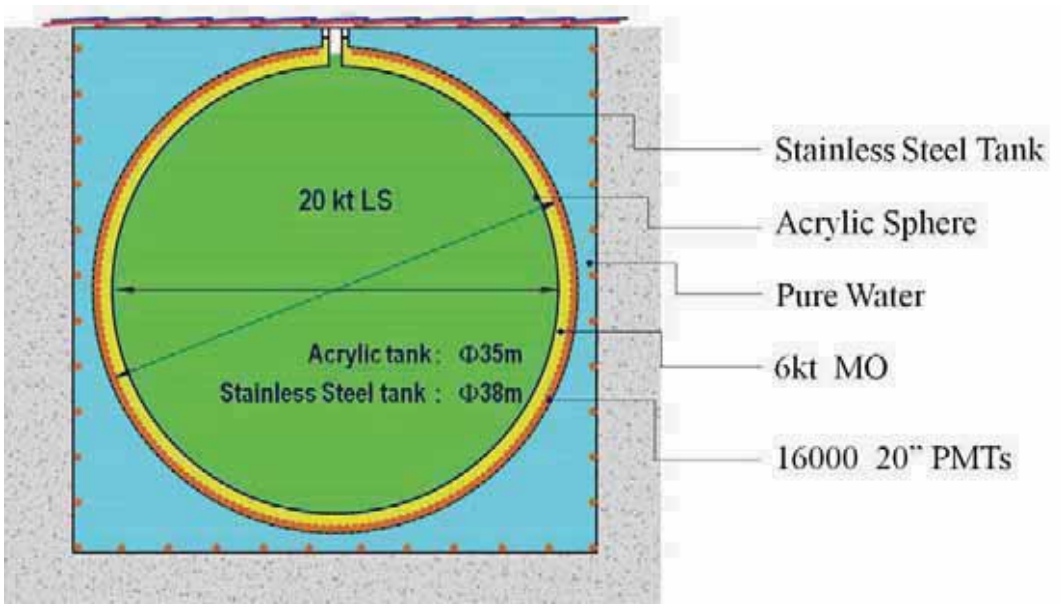

Figure 2.1: Traditional design of the central detector

The main requirements for the JUNO central detector are the following:

1) The detector should meet the physics requirements of the JUNO experiment, with 20 kt high purity LS and 16000 high Q.E. PMTs to reach an energy resolution of $3\%\sqrt{E}$;

2) The detector should minimize the radioactive background from different sources, including environment, structure, materials and the pollution from the construction process;

3) The detector structure should be reliable and its design should meet the standards in fields of large vessel, civil architecture and engineering. Leakage is not allowed between different spheres. The structure should be safe up to a seismic intensity of Richter scale 5.5, and should not be sensitive to temperature variation. The structure must have no single point of failure;

4) Materials used for the detector should have a long-term compatibility (about 30 years) with the liquid scintillator and pure water;

5) The central detector should provide a proper interface to other systems, i.e. VETO, calibration, electronics and so on;

6) The total construction duration should be reasonably short and not longer than 18 months;

7) The lifetime of the detector should be longer than 20 years, and during this period, no significant repair is needed;

8) The cost of the central detector should also be at a reasonable level.

2.2 Baseline option: Acrylic Sphere with Stainless-Steel Support

2.2.1 Introduction and the design requirements

In the baseline design the inner sphere is made of acrylic with a thickness of 12 cm and an inner diameter of 35.5 m. Surrounding the acrylic sphere there is a stainless-steel structure which supports the acrylic sphere and also the PMTs. Currently the stainless steel support structure has three options: the double layer truss, the single layer truss and the equator supporting method. For the first two options, the truss can also be used to fix the PMTs, but for the equator supporting method, an extra frame is needed for PMT installation. The inner diameter of the stainless-steel truss is 38 m in the present design, supported by a number of columns which are built on the base of the water pool. For the acrylic sphere, a chimney with an inner diameter of 0.5 m will extend up from the top of the sphere, serving as the interface for the calibration system. The relative pressure between the LS and the water has a great effect on the sphere. The chimney will be a few meters higher than the water level in order to provide flexibility in setting the LS relative height and the resulting stress in the sphere. Due to the height of the chimney above the sphere, optical isolation is needed to block the background induced light from being detected by the PMTs. Between the acrylic sphere and the truss, there are about 16000 inward-facing PMTs to collect optical signals produced by the LS. There is an opaque layer behind the PMTs to separate the central detector from outside veto detector. As an example, Fig. 2.2 shows the acrylic sphere and the double layer stainless-steel truss.

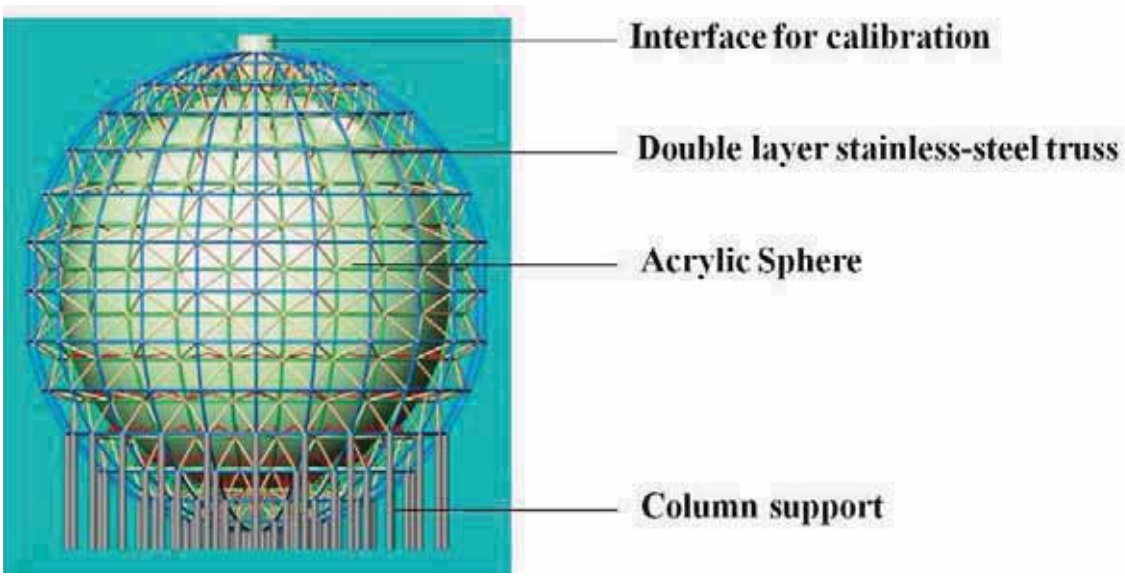

Figure 2.2: Schematic view of acrylic sphere plus stainless-steel double layer truss

Many factors need to be considered for the baseline design, such as:

• Stability and load status of the structure at different stages, such as during the construction, after the construction and installation of PMTs, during LS and water filling, and long-term operation of the detector.

• The acrylic sphere under different conditions such as earthquake, temperature variation and so on.

• The maximum stress on the sphere for long term operation < 5 MPa and for shorter durations < 10 MPa.

• Structure of the stainless-steel support should be reliable, and should meet the specifications of related fields.

• The joint of the acrylic and stainless steel should be reliable, and the impact induced by local failures should be minimal.

2.2.2 Stainless-steel Supporting Structure

The acrylic sphere is the most critical part of the whole central detector and is supported by the stainless-steel structure on its outer sphere. The design of the joint of the acrylic and stainless steel structure is critical and the ball head connection for flexibility and a rubber layer for buffering are adopted in the design. Currently, there are three design options under consideration for the stainless steel structure: double layer truss, single layer truss and equator support. The stainless steel is chosen to be the 316 type and the main parameters are the following: density of 8.0 g/cm^2, elastic modulus of 200 GPa, poisson ratio of 0.33 and the yield stress of 240 MPa.

2.2.2.1 Double Layer Stainless-Steel Truss

The space truss has been a popular choice in the civil construction domain given its properties of light-weight, small-size truss member, ease of handling and transportation, high rigidity, short construction time, low cost and good seismic resistance,etc. For the central detector, the truss is selected to be the outer structure which will not only support the acrylic sphere but also the PMTs. For the design of the truss, load-carrying capacity and stability were considered under different conditions. The truss will be the square pyramid space grid which is a multiple statically indeterminate structure. This type of truss can withstand the load coming from different directions, and has better load-carrying capability than the plane truss. The truss members have good regularity and high stiffness, and they are connected to each other by bolt-sphere joints which transmit only axial compression or tension, hence there are no moments or torsional resistance. Since the truss can be built up from simple, prefabricated units of standard size and shape which will be mass-produced industrially, the units can be assembled on-site easily and rapidly which greatly reduces the time for construction. With the present design, the diameter of the inner layer truss is 38.5 m, while that of the outer layer is 42.5 m at the two poles and 40.5 m at the equator. This shrinkage from poles to equator can significantly reduce the size of experimental hall hence the cost and time for civil construction. There are hundreds of supporting rods between the acrylic sphere and the inner layer of the truss. These rods will be connected to the truss at one end and inserted into the acrylic sphere at the other end. The acrylic sphere is supported by those rods directly. To reduce the axial load on each rod and hence the stress in acrylic, some other rods are added between the sphere and the outer layer of the truss. The truss itself will installed on the bottom of the water pool by supporting columns at the lower hemisphere. Fig. 2.3 shows the truss structure and some of its details.

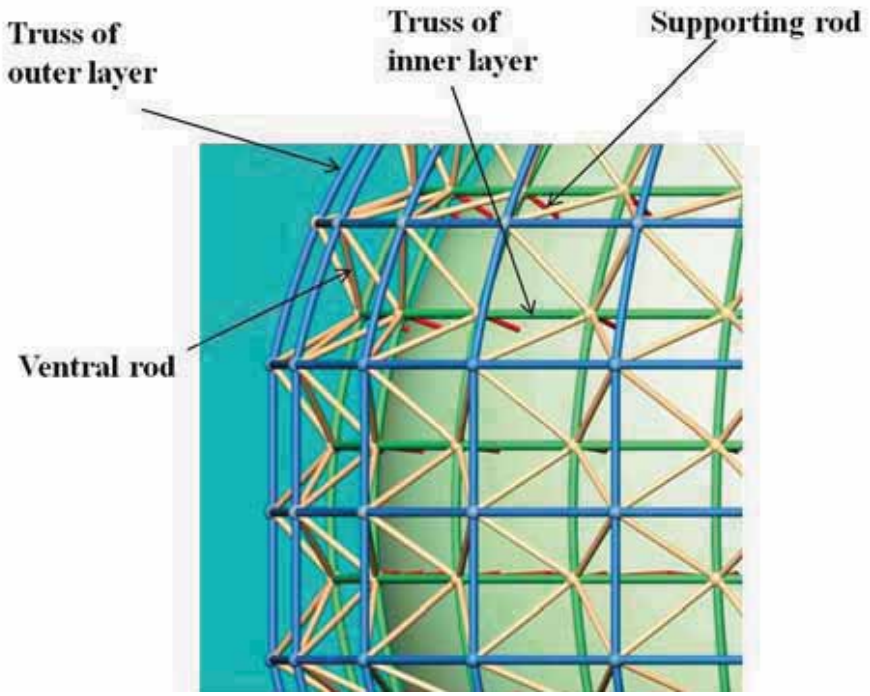

Figure 2.3: Double layer stainless-steel truss

According to JGJ7-2010, which is the technical specification for space frame structures, the truss members will be designed as the compression members and the slenderness ratio should be less than 150. Referring to the preliminary finite element analysis, the size of the chord members is selected to be ϕ273 mm x 8 mm, and the ventral members are ϕ219 mm x 8 mm. The supporting rods (brace members) between acrylic and truss are ϕ102 mm x 12 mm, and the columns for supporting truss are designed to be ϕ400 mm x 20 mm. The final size will be determined in engineering design after further stress analysis.

2.2.2.2 Single Layer Stainless-Steel Truss

As shown in Fig. 2.4 (a), this single layer truss is made of I-shaped unistrut in both longitudinal and latitudinal directions. Similar to the double layer truss, the supporting rods are also used to connect the sphere to the truss. The truss itself is supported on the base of the water pool by a number of columns. To improve the stability of the single layer truss and to avoid the possible torsion, a ring of spiral bracings are added in the truss grids to prevent any occurrence of torsional vibration shape. In addition, due to space limitation in the pole region of the truss, the square shaped structure is replaced by a triangle shaped one, so the number of truss members is reduced, as sketched in Fig. 2.4(b). This optimization gives more space for PMT installation and keeps the grid size of the truss in a reasonable range.

Compared to the double layer truss, the single layer truss can save a significant amount of space and hence the civil construction cost. Another advantage of this option is that PMT installation is much easier since there is no interference caused by the truss members.

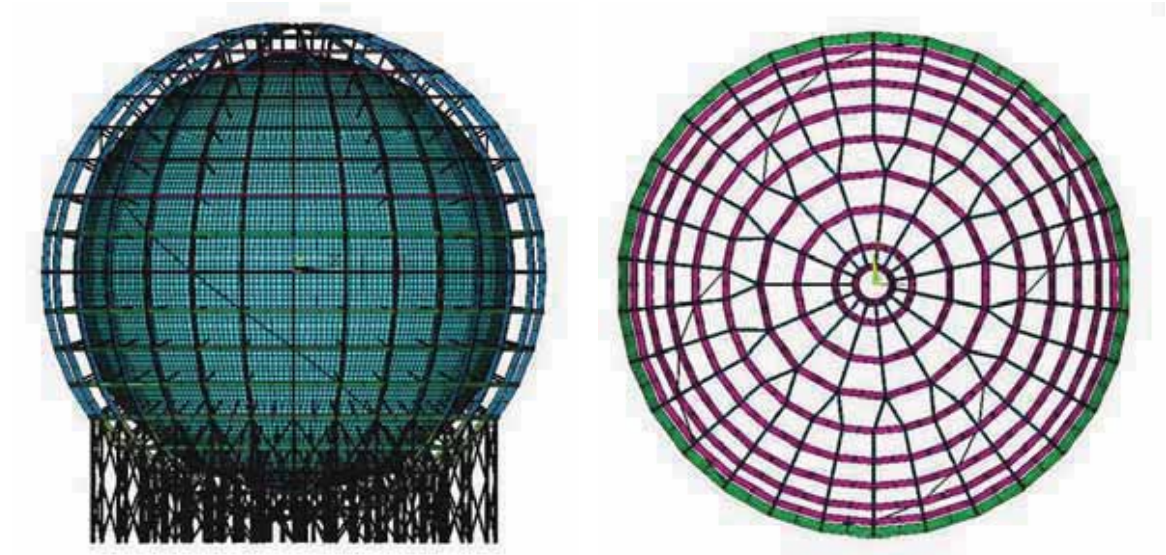

(a) Single layer stainless-steel truss with spiral support

(b) Reduction of the number of truss members in pole region

Figure 2.4: Single layer steel truss

2.2.2.3 Equator Supporting Method

This supporting structure is indicated in Fig. 2.5. The acrylic sphere is supported at the equator area with stainless-steel rings which connect to the wall or bottom of the water pool by rods. A radial extension growing from the sphere at the equator functions as supporting points where the stainless-steel rings are clamped to it. A rubber layer is used as buffer between the acrylic and steel ring to avoid any stress concentration, and this buffer layer is also very useful to improve the stability of the whole structure, especially under seismic conditions. The rings are separated into several parts along the circumference, each part anchored to the water pool by an H-shaped unistrut and a tilted rod.

To minimize the light blocking by the steel ring, another method is using a number of separated supporting points which are distributed at the equator. In this design there are 32 blocks cast into the sheets that are assembled at the equator. Into each of these blocks will be cast a steel plate. The sphere is supported at each of these steel plates so there is no direct bearing on the acrylic. Fig. 2.6 shows details of this concept. The 32 support points on the sphere will be supported by an external steel structure that is made of columns braced against the concrete wall. A beam will project forward from the columns and through the layer of PMTs which will surround the sphere. At the end of this beam a plate is welded to the profile. The height and depth of the “C” will be much larger than the plate that is cast into the acrylic sphere. The resulting gap between the plate and the “C” accommodates the assembly tolerances. The sphere will be built up from the bottom using temporary supports until the equator ring with the 32 support points is completed. The external steel structure will be in place and the “C” plate will be surrounding the plate cast into the sphere. At this point shims will be placed around the “C” which will lock the cast plate into place. Once shims have been installed on all 32 support points the bottom temporary supports can be

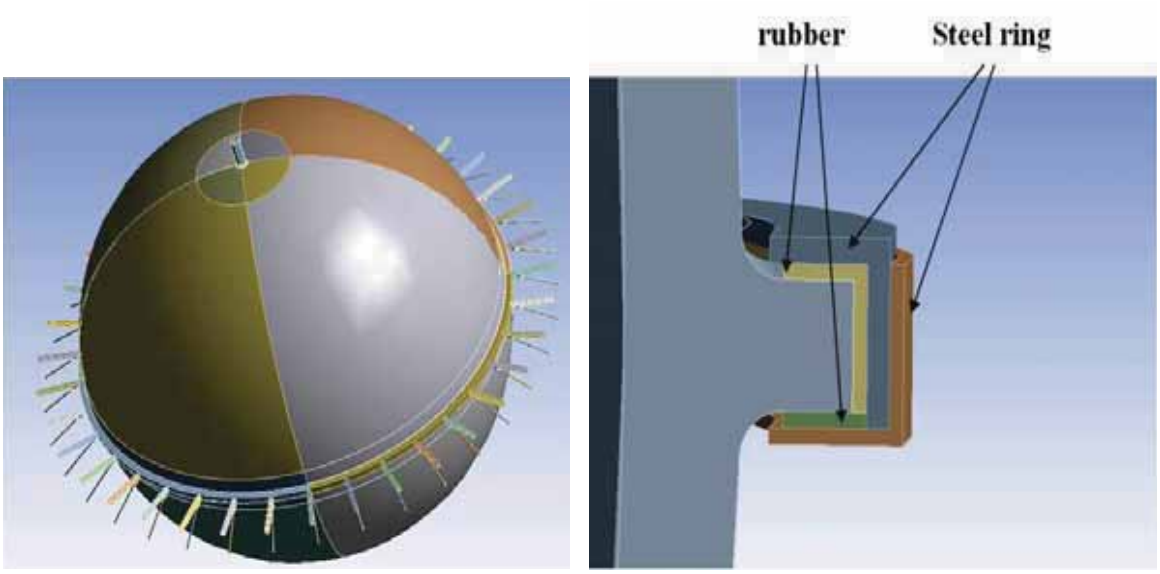

(a) Overall view of acrylic sphere supported at equator

(b) Detailed view of the support at equator by steel ring

Figure 2.5: Acrylic sphere supported at equator

removed and the entire load of the sphere will be transferred to the "C" plates and external steel structure. The top half of the sphere can then be assembled.

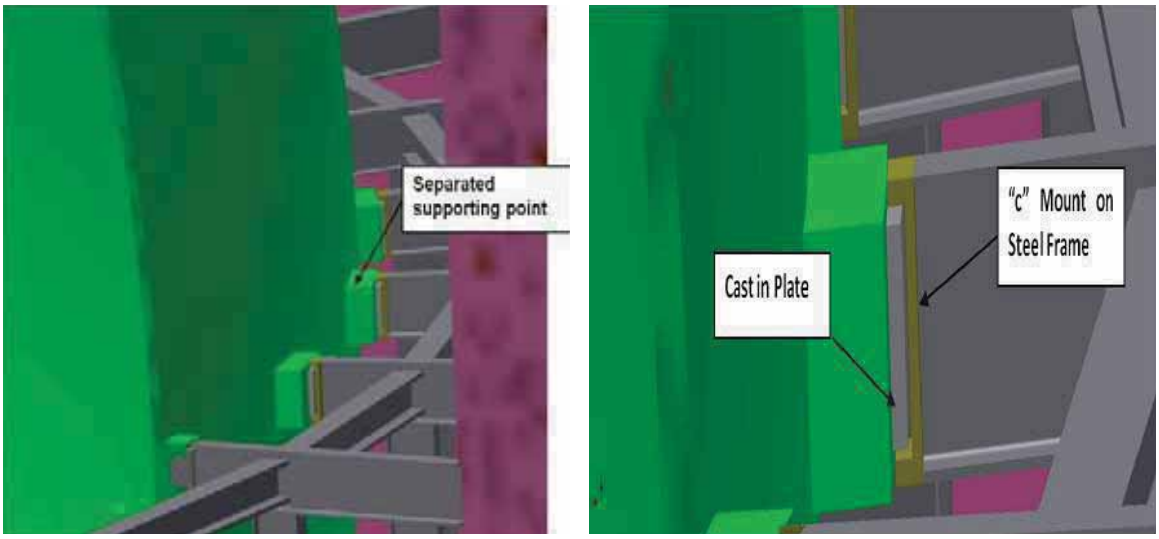

(a) (b)

Figure 2.6: Detailed view of the support at equator by separated points

2.2.3 The Acrylic Sphere

The inner structure of the central detector is a transparent acrylic sphere about 35.5 m in diameter and 120 mm in shell thickness. This acrylic sphere will be assembled and bonded with bulk polymerization by a number of acrylic sheets, as shown in Fig. 2.7.

Considering the production capacity and transportation limit, the acrylic shell will be divided into more than 100 sheets, each is about 3 m x 8 m in dimension. The final number and size of the sheet may be modified after further consideration and discussion with manufacturers. To reduce the stress on the sphere at the supporting points, some appended acrylic pieces will be bonded on top of the sheets. The supporting structure of the sphere will be connected to these appended acrylics. A chimney of about 0.5 m diameter is designed on top of the acrylic sphere, which will be used as the filling port and interface to the calibration system. An outlet may be designed on the bottom of the sphere for cleaning of the sphere and LS recycling during detector running.

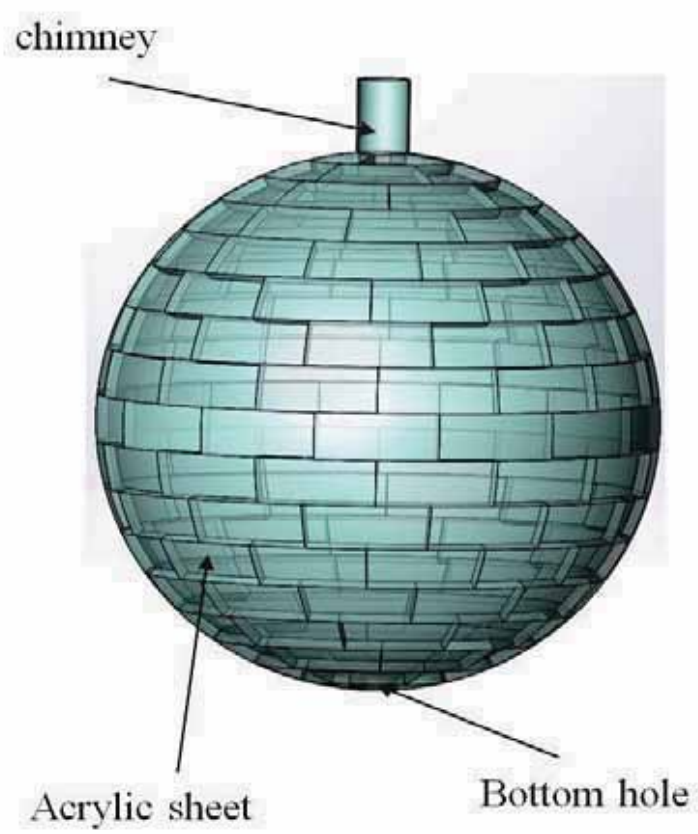

Figure 2.7: Schematic view of the acrylic sphere

2.2.4 Joint of the Acrylic and Truss

In the baseline design for the truss the concept of the joint between the acrylic sphere and the steel truss comes from the idea of the connecting structure used in the glass curtain wall. For each acrylic sheet, there will be one or two stainless steel disks which are embedded in it as a connecting structure, as shown in Fig. 2.8. At the location of each steel disk, there is an appended acrylic piece with 100 mm thickness on top of it and bonded to the sphere, and a rubber layer is placed between the acrylic and steel for buffering. The steel disk is designed to have a ball-type head, and a supporting rod will connect it to the truss. The load on the acrylic sphere will be transfered to the truss through these rods. The dimensions of the appended acrylic and the steel disk

may be changed according to a further analysis of the stress.

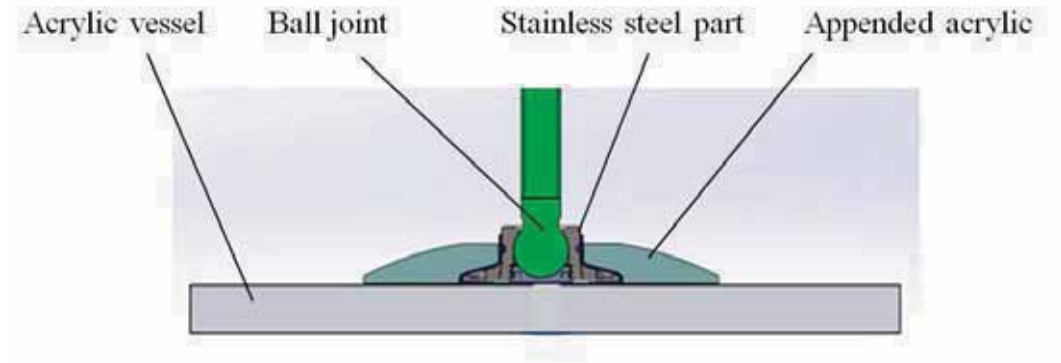

Figure 2.8: Supporting joint of the acrylic sphere and steel truss

In addition, there is another type of joint structure under design, as shown in Fig. 2.9. Instead of using the steel disk which is heavy and of large size, a steel ring is embedded into the acrylic, and connected to a steel plate on top of the appended acrylic by bolts. Rubber is placed in between the different components, and the bolt is surrounded by plastic bushing to avoid direct contact with the acrylic. This new structure is easier for construction and also can reduce the amount of stainless steel and hence the radioactive background.

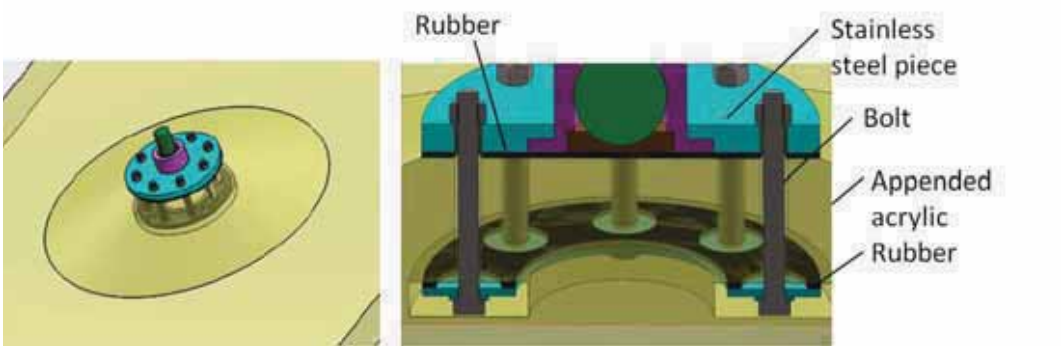

Figure 2.9: Structure of the joint with bolt

Currently the two design options are both under optimization, with a main goal of reducing the stress level to less than 5 MPa. Several prototype tests have been finished for the first option, and test for the second option will be done in the near future.

2.2.5 Finite Element Analysis and Testing

2.2.5.1 Global FEA

We have finished a global FEA for the central detector under the following conditions.

1) sphere is empty after the completion of acrylic sphere and steel truss: the load is just the self-weight of the structure.

2) All PMTs are installed on the truss: the weight of total 16000 PMTs is about 1600 KN, which will load on the truss.

3) Sphere is filled with liquid and running for long term: the linear liquid pressure will be loaded on the sphere, and the total buoyance of the sphere is about 3100 t; the PMT's buoyancy is about 1000 t, which will be distributed on the joint nodes of the truss.

During the analysis a load factor of 1.35 was used for the dead load. The FEA results include stress, deflection and stability for the three loading conditions. The effect caused by seismic load, temperature or relative liquid level difference has also been analyzed. Following are the main conclusions:

(1) Stress and deflection

From Table 2.1, Fig. 2.10 to Fig. 2.12, we can see that the maximum stress on the acrylic sphere is 8.502 MPa in condition (3). If the load factor of 1.35 is removed, the stress is 6.3 MPa. The maximum displacement is 35 mm, occurring at the bottom of the structure, which is only 1/1014 of the sphere span and meets the technical specification for space frame structures (JGJ7-2010).

Table 2.1: Maximum stress and deformation for each loading condition

Loading condition	Max. stress on sphere(MPa)	Max. stress on truss(MPa)	Max. general deflection (mm)
Condition 1	1.1	23.7	8.2
Condition 2	1.3	16.3	6.3
Condition 3	8.5	83.4	35.1

(2) Analysis of the seismic load

Based on the local geological condition, a seismic fortification intensity at Richter scale 5.5 was considered, and a seismic load of 0.1 g was taken in our analysis. Adding 0.1 g seismic load into the finite element model, the detector structure was analyzed for condition 3 and the result is shown in Fig. 2.13. We can see that the stress on the acrylic sphere is increased by only 1.6% and on the steel truss by only 4.4%. The small change shows that the structure of the detector is safe under the seismic load.

(3)Stability analysis

The safety factor for the buckling of the acrylic sphere is increased by the support from the steel truss. The double non-linearity of the material and the geometry were taken into account for the global stability analysis, and the first elastic buckling mode of the structure was taken as the initial imperfection in calculation. Fig. 2.14(a) shows the results of the instability mode. Fig. 2.14(b) shows the deflection-load coefficient curve and we can see from it the stability factor is 2.61, which meets the specification of JGJ7-2010.

(4) Effect of liquid level difference

Liquid level of the LS in the acrylic sphere will affect the stress status of the sphere. We did the analysis for several cases of the relative liquid level. A difference of -2 m, 1 m, 0 m, 1 m, 2 m and 3 m between the LS and water(LS level - water level) were taken into account. The results are shown in Table 2.2. We can see that the variation of the relative liquid level impacts stress significantly. If the LS level in the sphere is higher than the level of water outside, the stress will be reduced significantly. Raising the LS level may be considered in our final design.

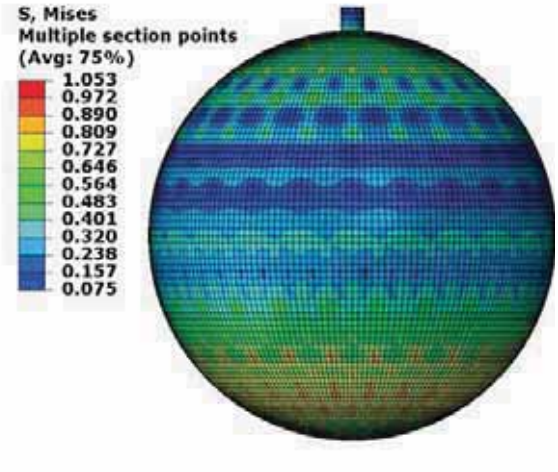

(a) condition 1

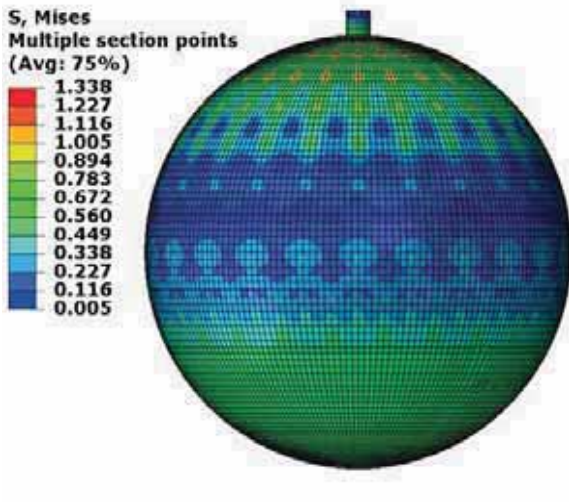

(b) condition 2

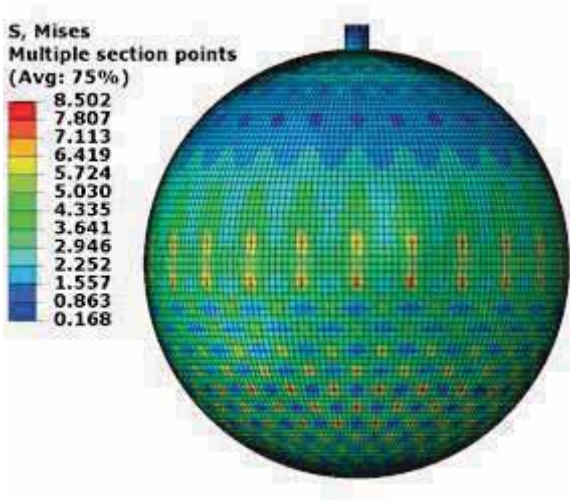

(c) condition 3

Figure 2.10: Stress distribution on the acrylic sphere

Table 2.2: Impact analysis of liquid level

Liquid level difference H(m)	Maximum stress on sphere (MPa)	Stress on supporting rod (MPa)
-2	10.2	67.7
-1	9.4	61.6
0	8.4	57.6
1	7.4	53.7
2	6.4	49.7
3	5.6	46.5

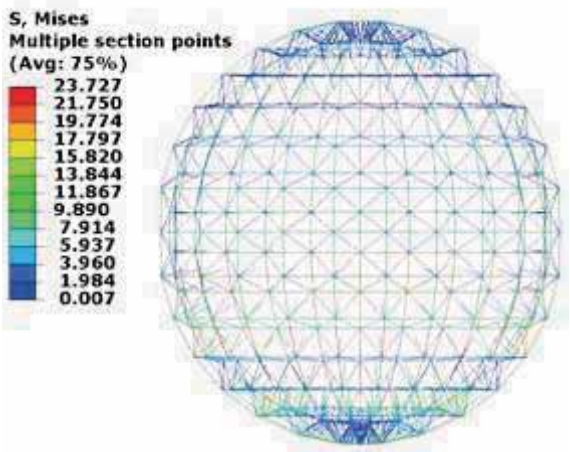

(a) condition 1

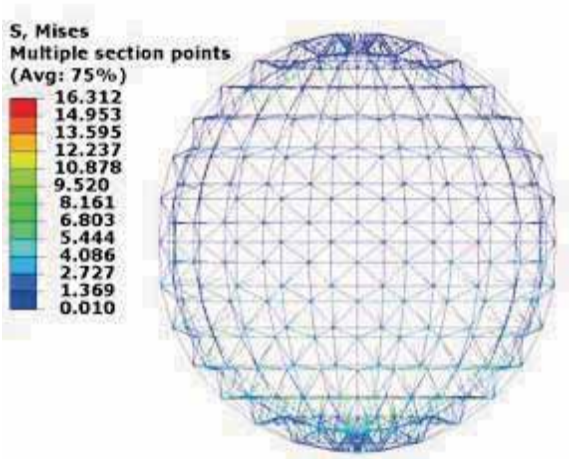

(b) condition 2

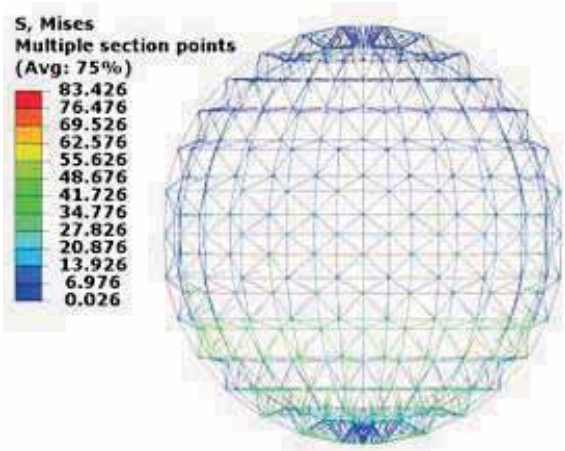

(c) condition 3

Figure 2.11: Stress distribution of the steel truss

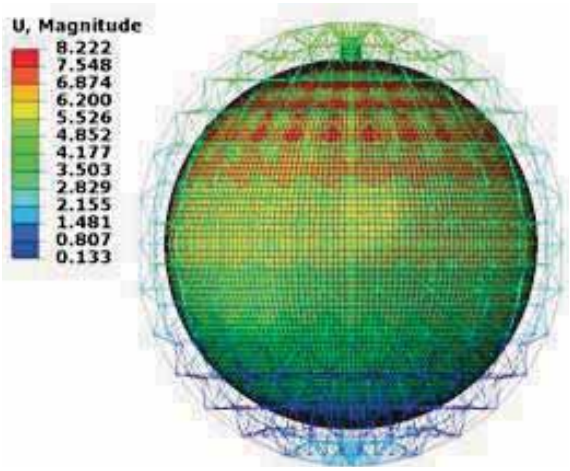

(a) condition 1

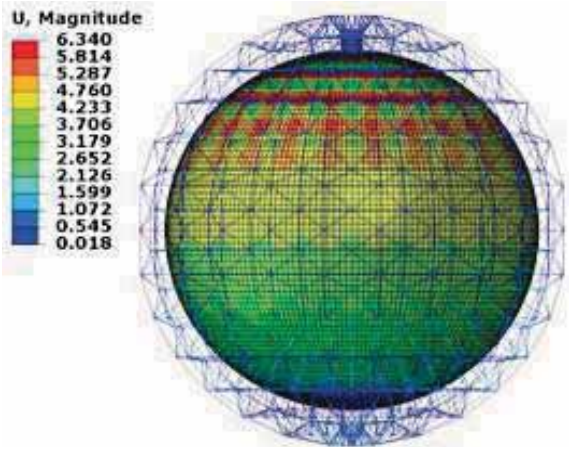

(b) condtion 2

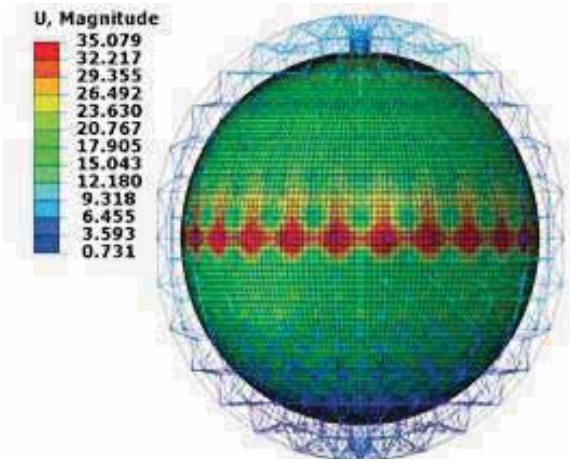

(c) condition 3

Figure 2.12: Deflection of the central detector

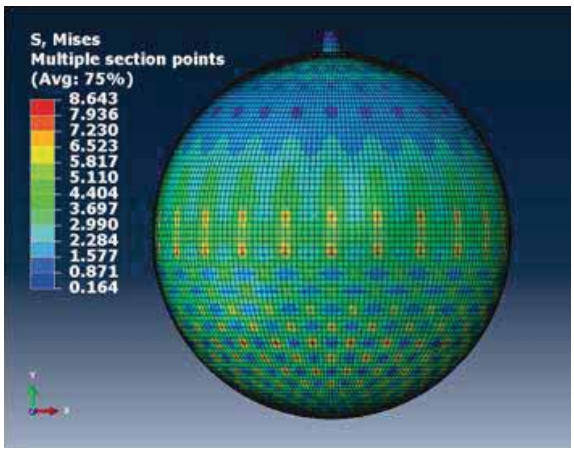

(a) Stress on the acrylic sphere under seismic condition

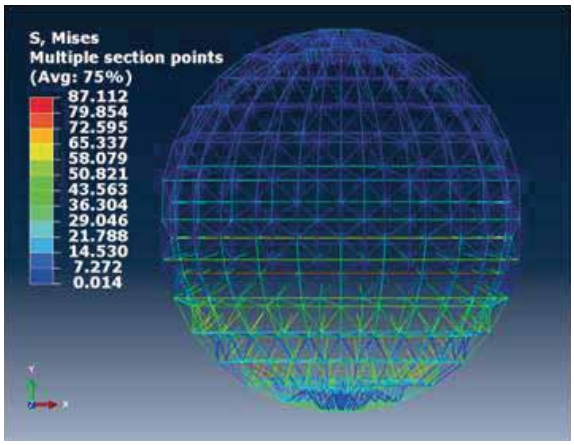

(b) Stress on the steel truss under seismic condition

Figure 2.13: Stress on the acrylic sphere and steel truss under seismic condition

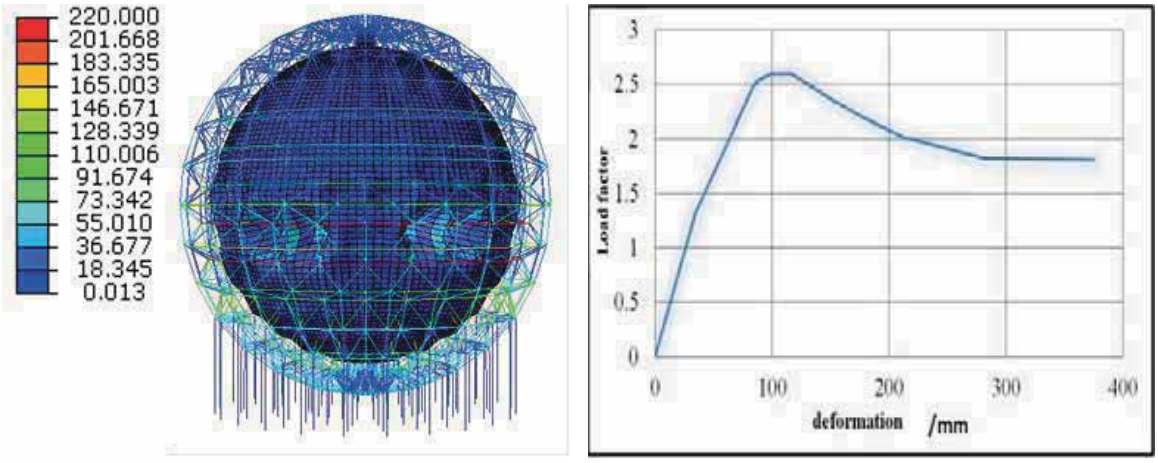

(a) Instability mode (b) Deflection-load coefficient curve

Figure 2.14: Stability analysis of the central detector

(5) Analysis of temperature impact

The detector will be constructed in a hall 700 m below the ground and the yearly temperature variation is rather small. Since the thermal expansion coefficients of the stainless steel and acrylic is different, the impact of temperature on the stress still needs to be considered. The impact of increasing or decreasing temperature by 10°C has been analyzed. Table 2.3 shows the results. For the stainless steel truss, the stress is always less than 100 MPa and the safety level will not be affected by temperature change. For the acrylic sphere, temperature elevation is helpful while decreasing of temperature will lead to a larger stress.So avoiding temperature decrease is necessary during detector running period.

Table 2.3: Temperature impact on stress

Condition	Maximum stress on sphere (MPa)	Maximum stress on truss (MPa)
Room temperature	8.5	83.4
Room temperature +10°C	8.0	77.5
Room temperature -10°C	10.1	95.0

(6) Failure analysis

The central detector is required to have a life-time of at least 20 years, and any crucial failure is not allowed during this period. For the acrylic sphere and steel truss, the key component is the support points on the sphere. The effect of one or more failure (for example, if a rod is broken) was evaluated. Four kinds of possible failures were analyzed, which are:

• condition 1: failure appeared at the maximum stress point;

• condition 2: failure appeared at all points on the same latitudinal circle where the maximum stress is located;

• condition 3: failure appeared at the points located in one longitudinal band in the lower hemisphere;

• condition 4. failure appeared at several points randomly distributed.

The analysis results of those cases are shown in Fig. 2.15.

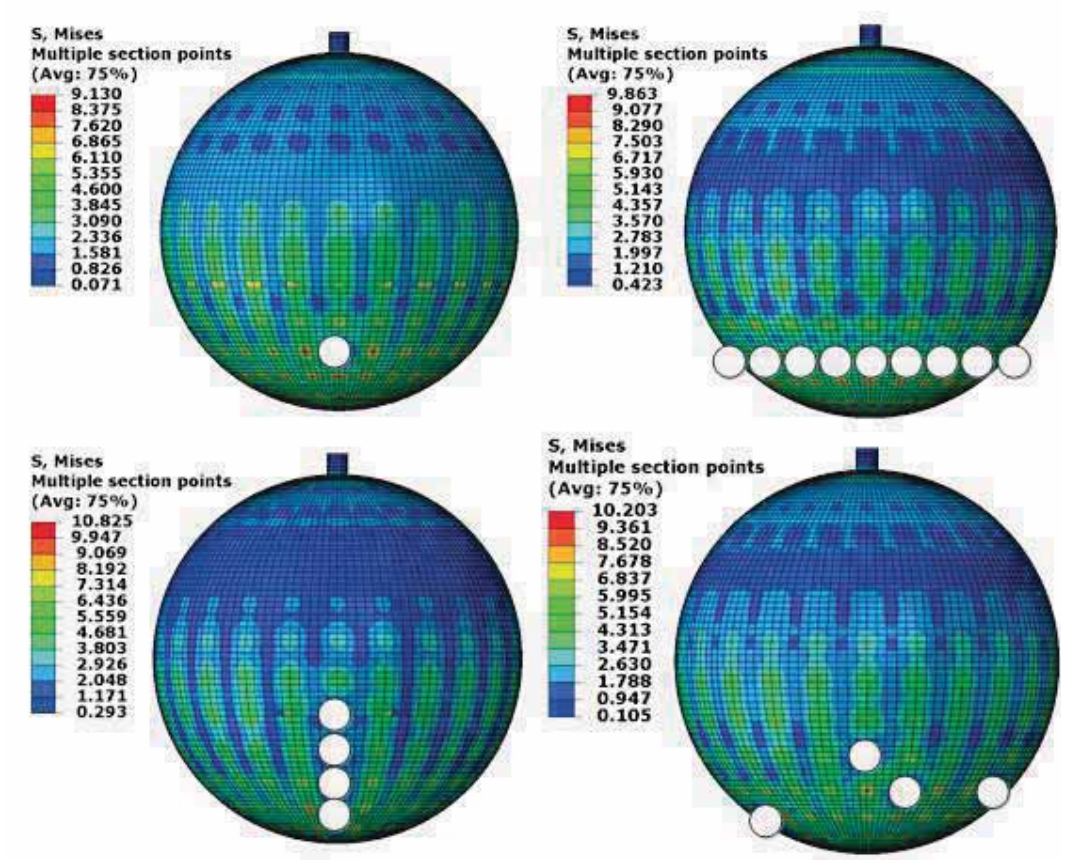

Figure 2.15: Failure analysis of the central detector for (a) condition 1, (b)condition 2, (c)condition 3 and (d)condition 4.

In the four failure cases, the maximum stress on the acrylic sphere is 10.8 Mpa (8 Mpa in dead load), an increase of 27.3% after failure. In fact, the possibility is very small for failures appearing at the same latitudinal or longitudinal band. One point failure is the most probable case and the stress variation is 7% in this case. The above analysis shows that the risk to the central detector is controllable.

2.2.5.2 Local FEA of the Supporting Point of the Acrylic Sphere

The grid size of the FEA model affects the accuracy of the calculation, especially for a singular point and the area around it. The above analysis shows that the maximum stress of the acrylic sphere appears at the joint of the stainless steel supporting rod and the acrylic sphere. Since this node is an intersection of the beam element and the shell element, it's a typical singular point. For FEA, a local fine model around the singular point is often employed in order to improve the accuracy. A validation test is necessary to check the analysis.

Fig. 2.16 shows the structure of the connecting point between the acrylic sphere and stainless steel truss. The structure at this joint involves the base acrylic shell, the appended acrylic piece and the stainless steel part.

For the local finite model with 3D solid elements, the base acrylic shell is 2.6 m x 2.6 m with a thickness of 120 mm, the appended acrylic is 100 mm in thickness

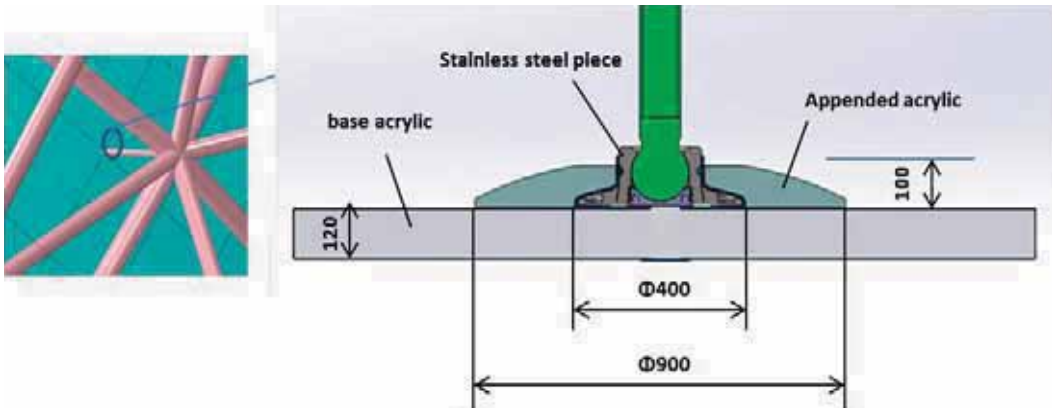

Figure 2.16: the structure of the connecting joint

and 900 mm in outer diameter, and the diameter of the stainless-steel disk is about 400 mm. The axial load of 14 t in the stainless-steel rod was taken into account for local FEA. Two different boundary conditions around the base acrylic were applied for analysis respectively, one being a fixed constraint and the other a simple constraint. Fig. 2.17 shows the analysis results of the fixed constraint and Fig. 2.18 the results of the simple constraint.

The results show that there is no large stress difference for the appended acrylic and stainless steel disk under the two boundary conditions for the base acrylic. The maximum stress in the simply supported model is 63.6% higher than that for the fixed constraint. The main reason for this is the stress concentration at boundary line due to the applied constraint. Removing these singular points, the stress difference for the two conditions is going to be small. For the central detector, the real loading status is between the fixed and simple constraint, so the maximum stress on the acrylic should be less than 10 Mpa.

2.2.5.3 Prototype and Testing of the Supporting Structure of the Acrylic Sphere

A prototype of the supporting structure was constructed to study the technique of fabricating the acrylic with steel built-in. Tests of the prototype were performed to understand the load-carrying capacity of the structure and to measure the stress and deformation to check FEA results. The prototype and the test can provide a reference and useful parameters for further design. Fig. 2.19 shows the prototype and some pictures taken during the test.

The stress and deformation on the measured points in this test are shown in Fig. 2.20. The measured points are distributed in the edge of the base acrylic, the border between the base acrylic and the appended acrylic, and the opening area of the appended acrylic. Fig. 2.21 is the load-strain curve of each measured point, which shows that all points have good elastic characteristics. All the measured strain data were analyzed to get the stress status of the prototype.

Under the axial load of 14 t, the maximum stress of the measured points is 8.6 Mpa which is located on the top of the appended acrylic. The measured stress was compared with the result from FEA as shown in Fig. 2.22. The deviation is less than 8%, which demonstrates that the FEA is reasonable and can simulate the real stress on the joint

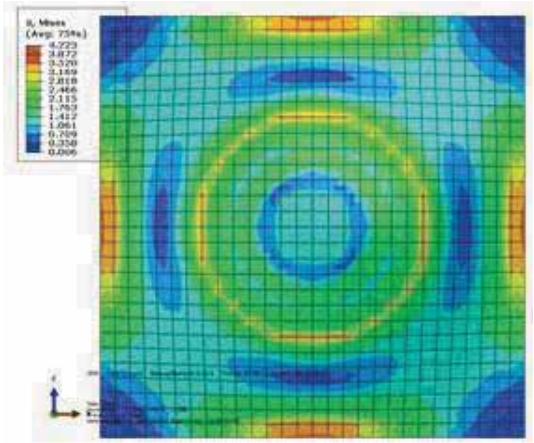

(a) stress distribution on the base acrylic. (Max: 4.2 MPa)

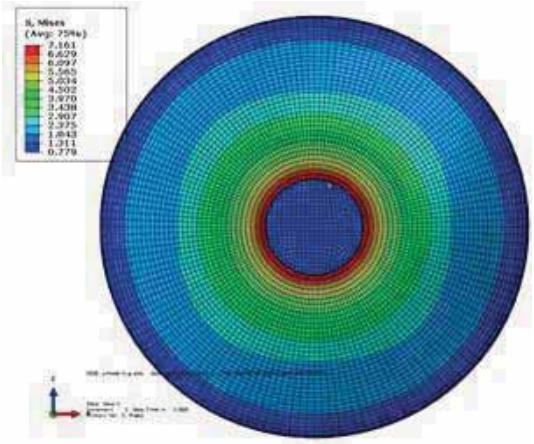

(b) stress distribution on the appended acrylic. (Max: 7.2 MPa)

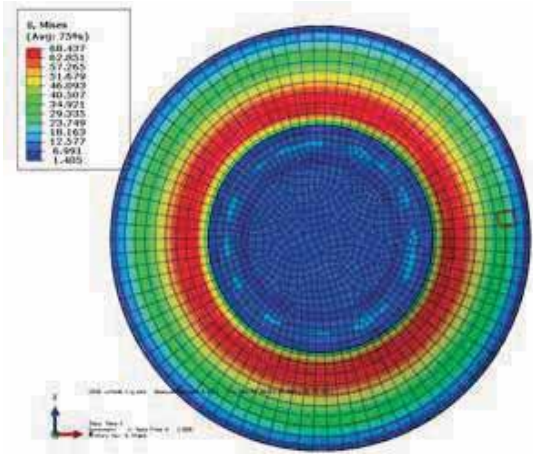

(c) stress distribution on the steel disk. (Max: 68.4 MPa)

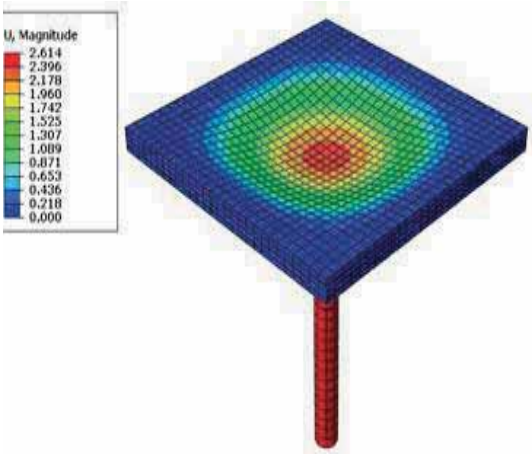

(d) deformation distribution on the whole prototype. (Max: 2.6 mm)

Figure 2.17: Analysis results for fixed constraint

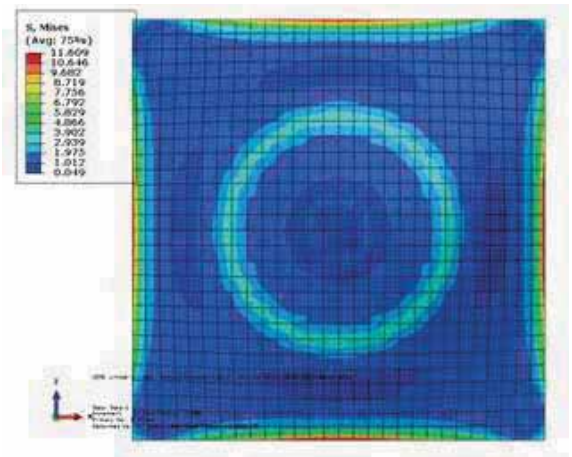

(a) stress distribution on the base acrylic. (Max: 11.6 MPa)

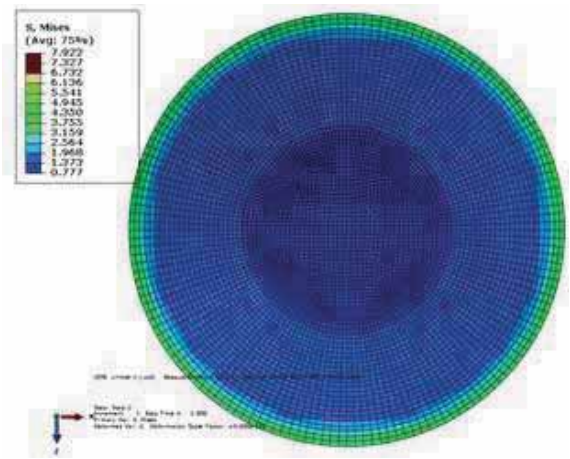

(b) stress distribution on the appended acrylic. (Max: 7.9 MPa)

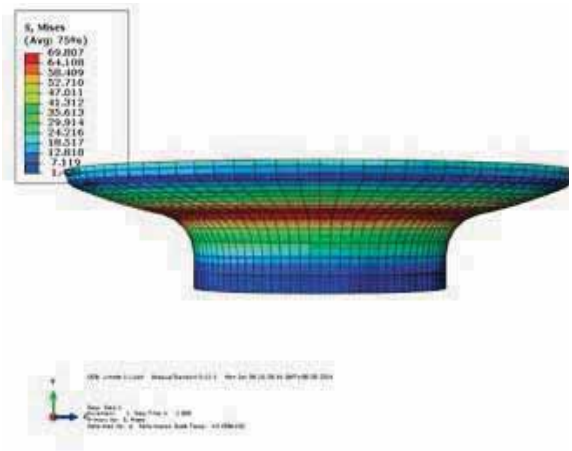

(c) stress distribution on the steel disk. (Max: 69.8 MPa)

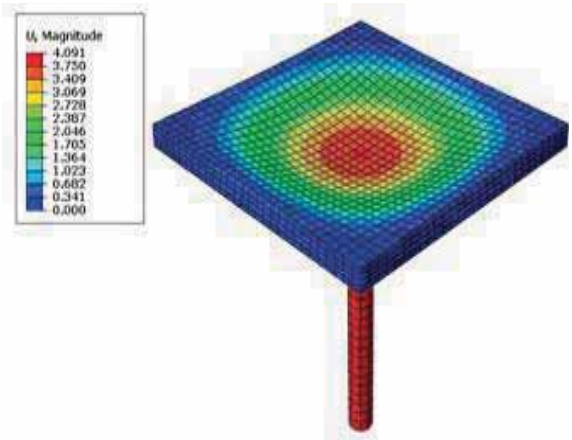

(d) deformation distribution on the whole prototype. (Max: 4.1 mm)

Figure 2.18: Analysis results for simple constraint

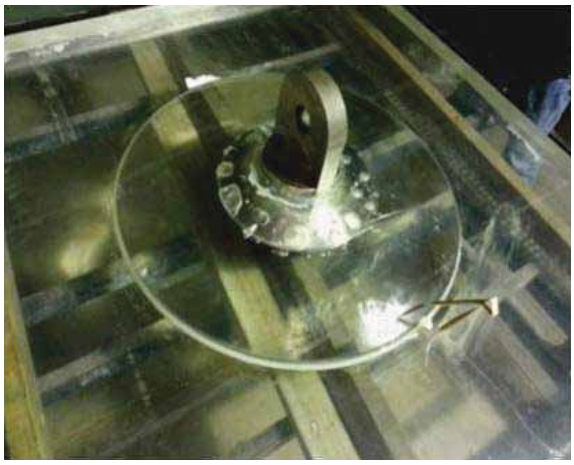

(a) the joint prototype

(b) Installation of the prototype

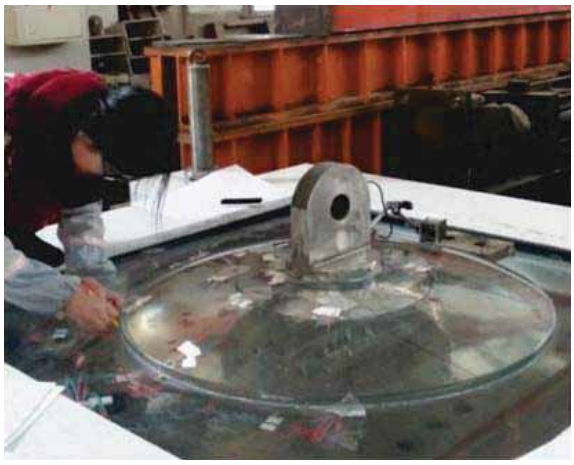

(c) Preparation of the prototype test

(d) load-carrying test of the prototype

Figure 2.19: the prototype and test

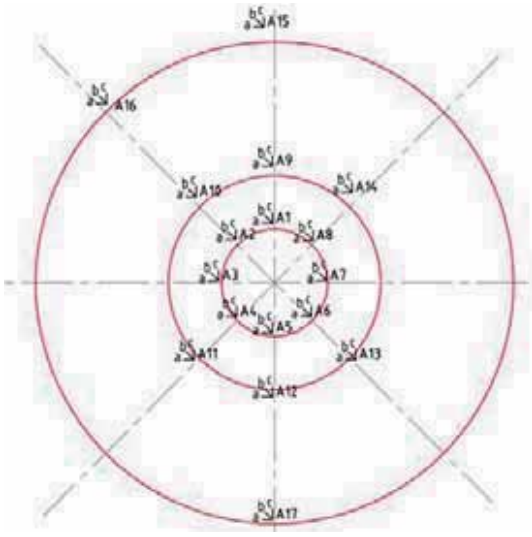

Figure 2.20: layout of the measuring points

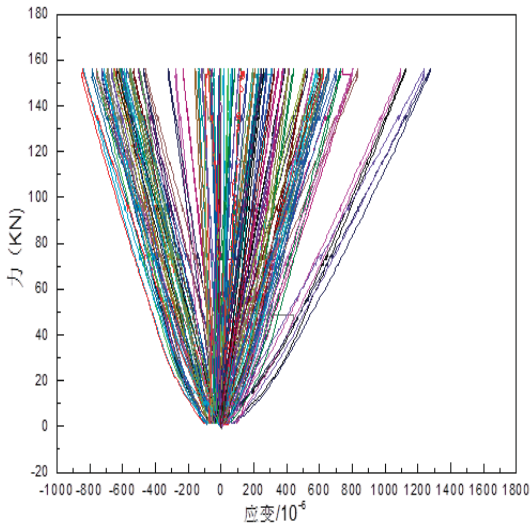

Figure 2.21: load-strain curve of the measurement points

by using the local refinement method.

point no.	A1	A5	A7	A2	A4	A6	A9	A12
stress(measured	7.8	8.51	9.07	8.06	9.02	8.73	4.14	4.43
average	8.46			8.6			4.29	
Stress (FEA)	7.84			7.96			4.38	

Figure 2.22: Comparison of stress between measurement and FEA

The above prototypes and tests have verified that the supporting structure of the sphere is safe under 14 t load as well as the reliability of FEA. Since defects existed in fabrication of those prototypes(such as polymerization not being completely finished due to the too low working temperature, the ball joint not working as expected due to being accidentally glued to the appended acrylic), a third prototype has been designed and tested with the known problems fixed. In addition, to test the maximum load-carrying capacity of the joint structure, an orthogonal load was applied to the prototype. The new prototype and test are shown in Fig. 2.23.

Given the improvements in the new prototype, the maximum load that the prototype can bear is up to 51 tons, which is significantly larger than the 28 tons obtained from the previous prototypes. Since the maximum design load is 14 tons, a 3.6 safety factor is reached by the third prototype. Additionally, the measurements confirm the FEA results, and the maximum stress is about 8.4 MPa, as shown in Table 2.4:

Table 2.4: Comparison of FEA and measurement for the third prototype

Load	Properties for comparison	Measured point	data	FEA
140KN	Stress/MPa	A7-3	8.467	8.392
		B7-3	3.479	2.963
		C1-3	3.262	3.093
	Displacement /mm	W4-3	0.512	0.630

Since we require that the maximum stress on the acrylic should not be larger than 5 MPa, optimization of the supporting structure is still needed to further reduce the stress level and get a larger safety factor.

2.2.5.4 Optimization of the Detector Structure

From the global and local FEA of the detector structure as well as the prototype test, we can see that the maximum stress in the acrylic shell (not including the appended acrylic) is less than 5 MPa and meet our requirement, but stress in the joints (on the appended acrylic) is still larger than 8 MPa and further optimization is needed. The optimization and modification can be done by:

- reducing the axial load on the connecting rod;
- raising the LS liquid level in the sphere;
- improving the uniformity of the whole structure to get a better loading status;
- reducing the number of connecting rods in the top and bottom area of the sphere to simplify the construction (see Fig. 2.24).

The results after those optimizations are shown in Table 2.5.

(a) the third prototype of joint

(b) Test of the third prototype

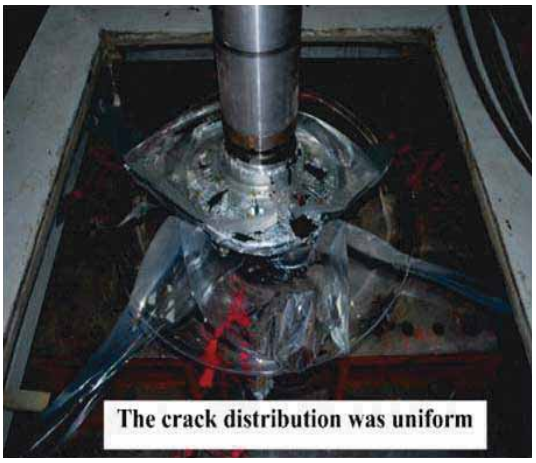

(c) The crack pattern of the third prototype

Figure 2.23: Third prototype test

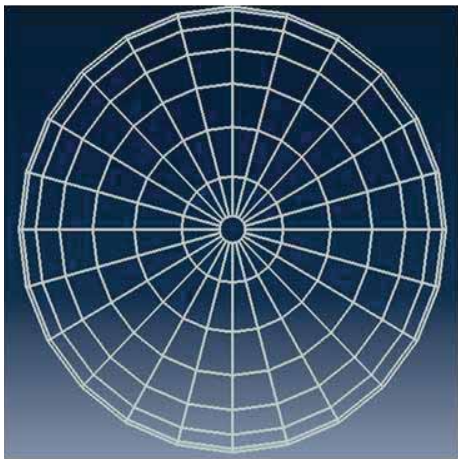

(a) Inner layer truss before sparsifying the truss members

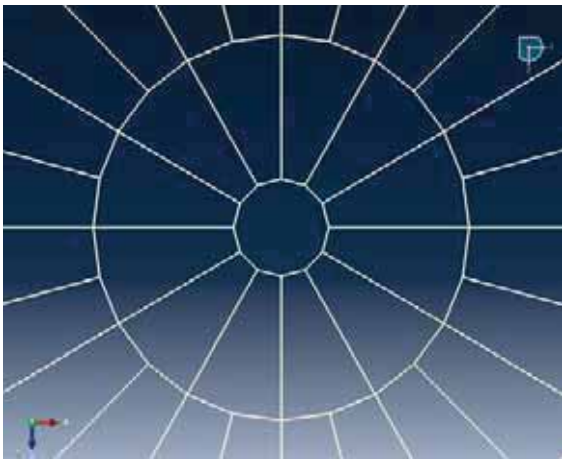

(b) Inner layer truss after sparsifying

Figure 2.24: Inner layer truss after sparsifying the truss members

Table 2.5: Results from FEA after optimization

Conditions	Max-stress on sphere(Singular point excluded) /MPa	Max-stress on sphere(Singular point included) /MPa	Max-stress on truss /MPa	Max-axial load /KN	Max-displacement /mm
Optimization 1	9.6	6.4	74.7	164.7	47.4
Optimization 2	6.9	5.2	115.1	135.9	27.3
Optimization 3	6.5	4.9	91.3	126.1	28.4
No 1.35 factor	4.8	3.6	67.6	93.4	21.0

Note that for Table 2.5:

• In all conditions, the liquid level difference is 3 m;

• Before optimization: the thickness of the upper acrylic hemisphere is 8 cm and the lower hemisphere is 12 cm. The number of supporting rods is 503 and no support comes from the outer layer of the truss to the upper hemisphere.

• Optimization step 1: the thickness of the sphere is changed to 10 cm. The number of the supporting rods is increased to 646 and symmetrically placed on the sphere;

• Optimization step 2: the supporting rods at both poles are sparsified, and the total number is 610.

From Table 2.5, we can see the stress in the acrylic is 3.6 MPa if the support point is excluded, and the maximum axial load in the supporting rods is only 93.4 KN. Since the stress is proportional to the load, it means that the stress should be also reduced a lot, and the FEA modeling to confirm this is currently underway.

2.2.6 Study of the Acrylic Properties

Acrylic is the main material used for the central detector construction. Since the detector will involve LS, LAB and high-purity water during long-time operation, the acrylic materials in the liquids should be studied. At present, a number of tests have been finished or are in progress.

(1) Normal mechanical properties test

Referring to the standards of ASTM-D638, ASTM-D695 and ASTM-D790, the tensile strength, compressive strength and flexural strength of the acrylic had been tested and the results are 68.2 MPa, 108.3 MPa and 88.0 MPa, respectively. Since the thickness of the acrylic sphere is 120 mm, it needs 2 or 3 layers of thinner sheet to be bonded together. In order to know the strength after bonding, we also did the test for the double-layer material. The test result is 66.8 MPa for the tensile strength and 101.7 MPa for the flexural strength.

(2) Aging test in LS

The acrylic samples were submerged into LS at temperatures of 50°C, 60°C, and 70°C. The testing time lasted 30, 60, 120, and 180 days for each temperature point. After that the mechanical properties of the aged acrylic was measured to compare with the fresh one. Results are shown in Fig. 2.25. Testing shows that the material has different aging behavior for different mechanical properties. Here, we mainly focus on the tensile strength since it is the weakest strength compared to others. It is known

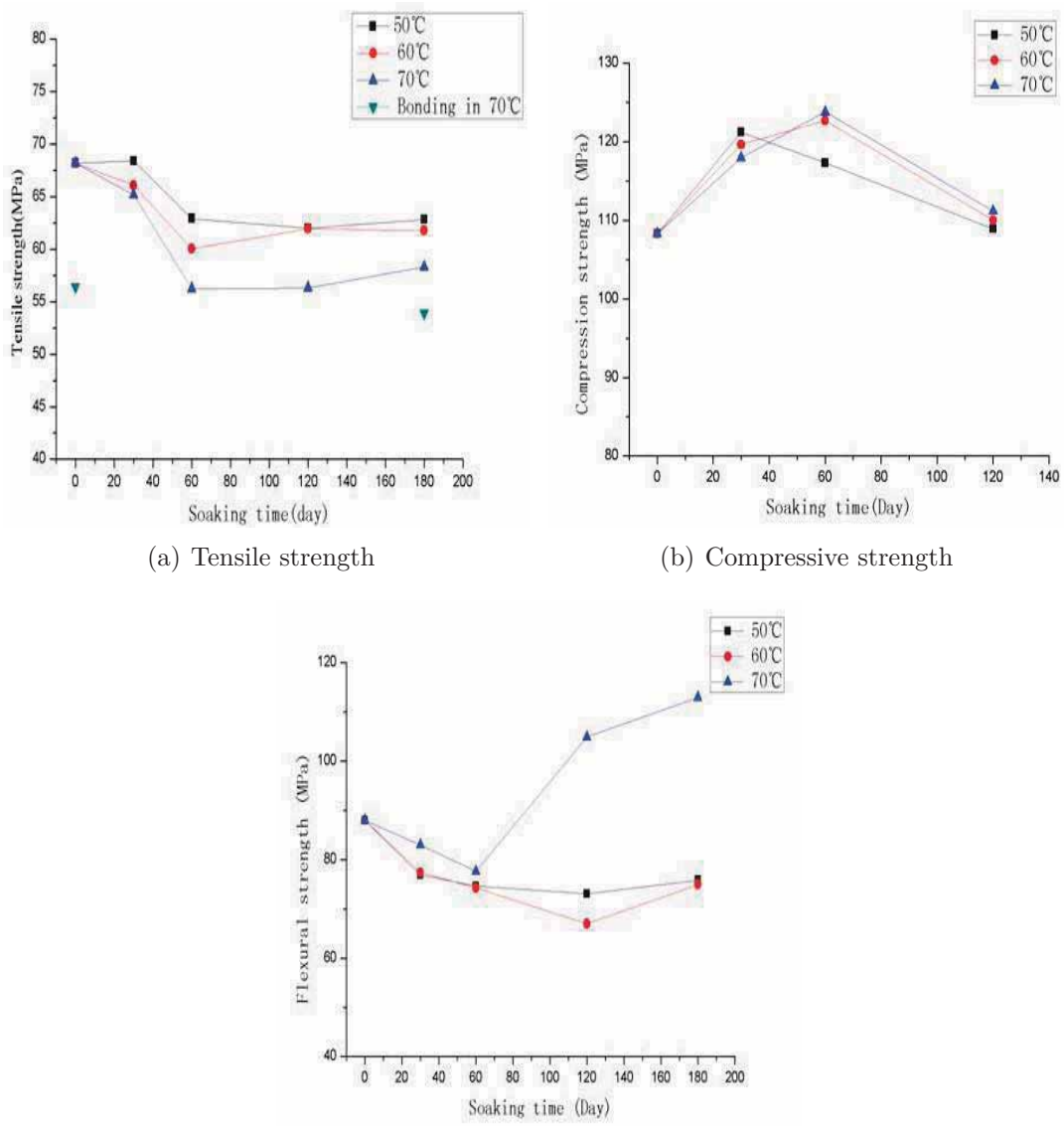

(a) Tensile strength

(b) Compressive strength

(c) Flextual strength

Figure 2.25: Performance of the acrylic after aging

that 60 days at 70 degrees corresponds to 16 years at 20 degrees, so we can predict that the tensile strength will drop by 18% after 16 years of running. To validate this conclusion, further tests are in progress.

(3) Test of the old acrylic pieces

To study the influence of the surrounding environment such as ultraviolet radiation, sunlight, temperature and humidity, measurements have been made for old acrylic pieces after 14 and 17 years in outdoor. Results are shown in Table 2.6.

The tensile strength of the normal acrylics is about 68 MPa. From the table, we can see that it drops by 17% and 21% respectively, for 14 years and 17 years in outerdoor.

(4) Test for the new bonding techniques

The construction of the acrylic sphere will require a large amount of bonding. Since the normal bonding technique needs a long time for curing, and therefore a very long construction time, the manufacturers are studying two new bonding tech-

Table 2.6: Strength of the acrylic after outdoor exposure

Explosure time	14 years	17 years
Elastic modulus /MPa	803	942
Poisson ration	0.405	0.405
Tensile strength	56.6	53.57

niques(ultraviolet irradiation and fast bonding) to reduce the curing time. The tensile strength with those new techniques has been tested and compared with the normal ones. The strength for ultraviolet irradiation is 46.5 MPa and for fast bonding is 55.3 MPa. The latter corresponds to 80% of the full strength of the acrylic. Details are shown in Table 2.7. Fig. 2.26 shows the cross-section where the break happens; it can be seen that the cross-section of normal bonding (A) and fast bonding (B) are similar, while for the other two (C and D) it has a very flat surface, indicating that the bonding syrup is not completely adhering with the original acrylic, hence giving a lower strength.

Table 2.7: Comparison of the different bonding techniques

Bonding techniques	time /hours	Tensile strength /MPa	Ratio
Without bonding		68.2	100%
Normal bonding	12	56.4	82.7%
Ultraviolet irradiation without annealing	3	37.2	54.5%
Ultraviolet irradiation with annealing	7	46.5	68.2%
Fast bonding	4	55.3	81.1%

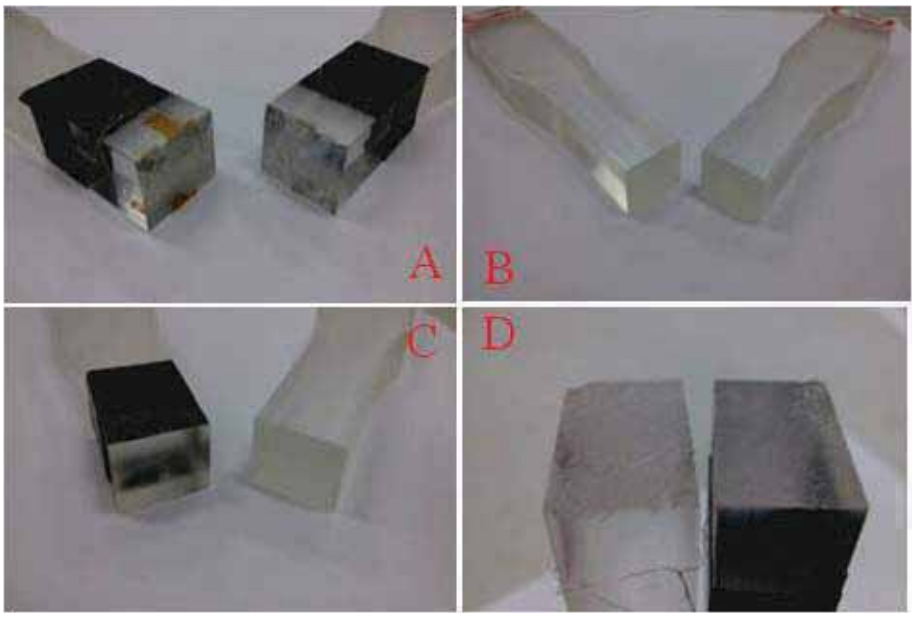

Figure 2.26: cross section of the broken acrylic

(5) Crazing test

Users and manufacturers of plastics have been aware of a phenomenon that glassy plastics will develop micro-cracks, which start at the surface of the material and grow perpendicularly to the direction of stress. Studies have shown that there are at least five factors which may cause glassy plastics to craze, as listed in the following:

• Applied or residual tensile stress;

• Stress generated on the surface of the acrylic due to differential temperature;

• Stress generated on the surface of the acrylic due to absorption and desorption of moisture;

• Weathering;

• Contact with organic solvents.

Crazes are initiated and propagated only when the tensile stress on the material surface exceeds some critical value. For the central detector of JUNO, the acrylic sphere will be immersed in LS and water under stress loading. The problems of crazing become important concerning the reliability and longevity of the structural parts manufactured from acrylic.

We did the following tests on acrylic samples in laboratory. Samples with 4.8 MPa stress applied were immersed in the LS and the liquid mixture of 80% LS+20% C_9H_{12}, at the room temperature and 60°C. The results are summarized as the following:

1) No crazing appeared by submerging in LS for 90 days at the room temperature;

2) No crazing appeared by submerging in the mixture of 80% LS+20% C_9H_{12} for 90 days at the room temperature;

3) By submerging samples in LS at 60°C, two of the samples showed initial crazing after 30 days, and the other two had no crazing. After 90 days, the initial crazing had grown along the direction of thickness. More tests and studies on crazing will be made in future.

(6) Test of light transmittance

The test results indicate that the light transmittance of the acrylic with 4 cm-8 cm thickness is over 96%, and the thickness has no significant effect on it. The measured attenuation length in air is 110.1 cm at 410 nm and 278 cm at 450 nm.

(7) Creep test

The creep test has been partially finished up to now for the acrylic submerged in LS at 20 degrees under a stress of 30 MPa, 25 MPa, 20 MPa, and 15 MPa. The results are shown in Fig. 2.27. This measured curve is consistent with the theoretical prediction, and the time before breaking increases dramatically at lower stress level. To understand the allowable maximum stress, more data are needed. Currently the creep tests are ongoing, including the test in pure water.

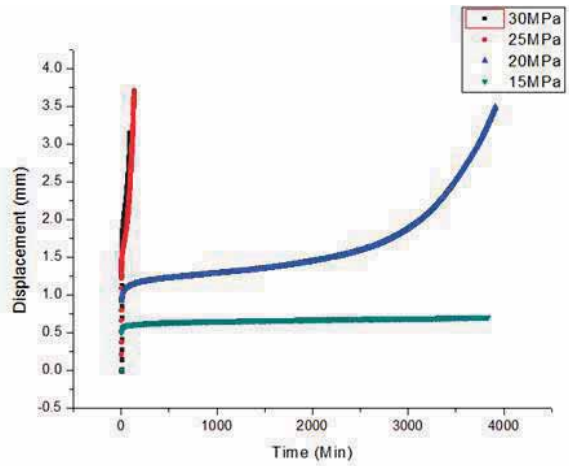

Figure 2.27: Creep curve of the acrylic under different stress

2.3 Backup option: Balloon in a steel tank

2.3.1 Introduction

The backup option of the central detector is a balloon with a stainless-steel tank. The tank, located in the center of the experimental hall, is about 38 m in diameter. A balloon of 35 m in diameter is installed in the steel tank. This balloon, welded from transparent films, is filled with 20 kt of LS as a target. The buffer liquid between the tank and balloon is LAB or MO. The density of LS in the balloon is 0.3-0.5% larger than the buffer liquid. The soft balloon needs a reliable supporting structure to keep it spherical and reduce the stress, so a thin acrylic layer surrounding the balloon is designed for this purpose. Both the balloon and the acrylic structure have the same diameter. The inner wall of the steel tank is covered by more than 16000 20 inch PMTs. Fig. 2.28 shows the structural sketch of this option.

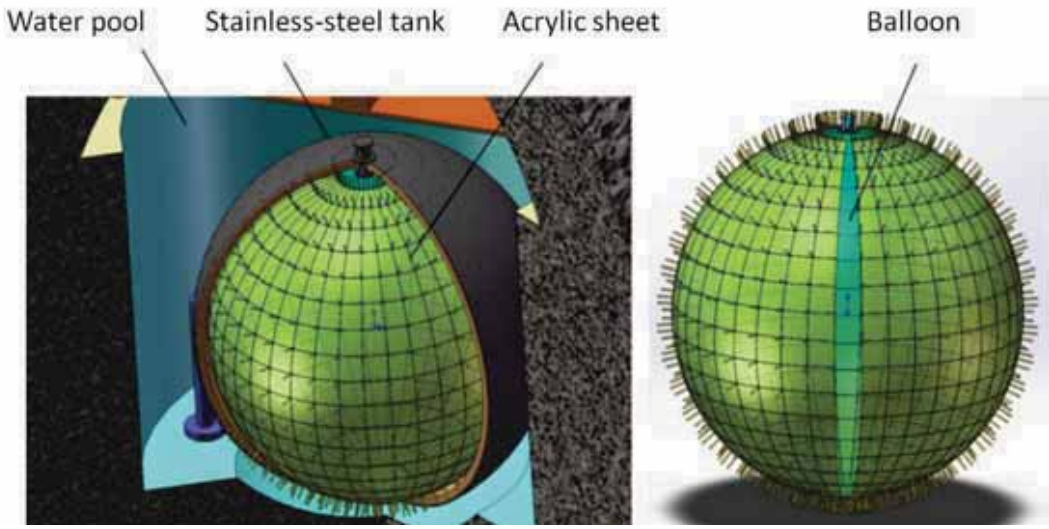

]

Figure 2.28: Schematic view of stainless-steel tank and the balloon

2.3.2 Balloon

The balloon is the most important structure in this option. The candidate materials for the balloon include ETFE, PET, PE/PA and FEP. There are two flanges with a pipe on the top and bottom of the balloon, which will provide the interface for filling and recycling. As the balloon is supported by the acrylic layer, the stress of the balloon is very small, and we do not have to worry about the balloon's shape. Therefore, the main study on the balloon is as follows:

- the compatibility of the balloon material in the liquid;
- the radioactivity of the material;
- the transparency and aging properties of the material;
- the cleanliness of the balloon during its production and installation;
- sealing of the balloon.

The primary task is to understand the material properties. Present studies show that the yield strength of ETFE film is about 18 MPa. This film has a good compatibility with all the liquids, good aging resistance, strength and impact resistance. It is self-cleaning, but its light transmittance is poor. For example, the transmittance of a 50 micron ETFE film is only 93%. The test result shows that PE/PA film is compatible with MO and the compatibility test with liquid scintillator is ongoing. PET film has good compatibility and light transmittance, but its flexibility is slightly worse. FEP film has good light transmittance, but there is no wide application for this film so far.

In order to keep the cleanness and minimize the dust, the balloon must be made and installed in a clean room. The cleanliness of the workshop in the factory should hopefully be at the 1000 level. Constant temperature and humidity are also needed during the production in the workshop. Providing clean gas to remove radon is necessary during the balloon production. The balloon should be carefully packaged, not only for safe transportation and ease of opening in the experimental hall, but also for avoiding contamination and damage.

Leak tests of the balloon should be done in the workshop and at the experimental site. Assuming that the concentration of PPO penetrating into the buffer liquid is less than 10 ppm in 10 years, the leakage of the balloon should be about 5 x 10^{-2} cc/s at 3 mbar hydrostatic pressure. In the workshop, the method of leak test can refer to that of the Borexino experiment based on SF6 gas [3].Sealed into another balloon, pumping the SF6 gas into the inner balloon and getting it into every corner, we can measure and obtain the curve of concentration-time of SF6 in the outer balloon and calculate the leakage. A vacuum leak test is also very useful. After the transportation to the underground hall, the balloon will be installed into the stainless-steel tank and the final leak test will be done onsite. The balloon can be filled with purified gas mixed with a certain concentration of SF6. The balloon's leakage is determined by testing the concentration of SF6 in the volume between tank and balloon. Further studies and tests should be done to get a detailed solution for the leak test.

2.3.3 Acrylic Structure for the Balloon Support

Acrylic here is designed as the supporting structure for the balloon. It is a sphere with 35 m diameter, fixed on the steel tank by supporting legs, as shown in Fig. 2.29. The acrylic layer is made up of many acrylic sheets and it is not necessary to seal it. In other words it will lower the difficulty and reduce the working time for installation

onsite. The thickness of acrylic sheets in this option is 30 mm, which allows us to have a wide choice from commercial products.

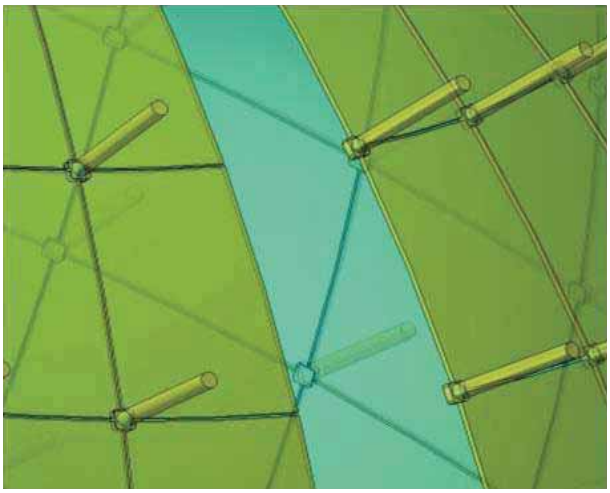

Figure 2.29: The acrylic supporting structure for the balloon

The density of liquid inside and outside the balloon has a small difference, expected to be 0.3-0.5%. In stress analysis, we set a 0.5% density difference as a starting condition, and the others conditions being hydrostatic pressure towards the internal surface of the balloon and external surface of the supporting structure. In this preliminary analysis, we used tetrahedral finite elements to analyze a 9° partial spherical layer with 25 mm thickness, and acrylic supporting legs were set as fixed ends. The results showed that the stress of the main part is below 2 MPa and the total displacement is about 9 mm, as shown in Fig. 2.30. Since the element density affects the local stress on the supporting points, further analysis with more detailed supporting structure will be done.

2.3.4 Stainless-steel Spherical Tank

In the backup option, the outer structure is a spherical stainless-steel tank. It will not only bear the weight of the liquid inside and support the balloon and the acrylic structure, but also provide an installation structure for the PMTs. The tank is not the same as a conventional pressure tank; its design should consider the installation process and on-site conditions as well as issues like cost and reliability. Based on the requirements above, the preliminary structure of the tank is designed as shown in Fig. 2.31.

The tank is supported by landing legs, which are welded to the tank at its equatorial belt. The tank has a chimney on the top, and its size should satisfy requirements such as the installation of a calibration facility, the entrance for lifting the PMTs, ventilation and lighting of the tank, arrangement of the cables, etc. The chimney reaches the liquid level, so it is easy to seal. At the bottom of the tank, there is a hole to be used to dispose the waste liquid from cleaning and as a manhole during the installation stage.

The tank is made of 170 welded steel plates, which are located in 9 belts of the spherical tank. These plates can be produced in the factory and then be assembled and welded after being transported to the site. Based on our investigation, there are

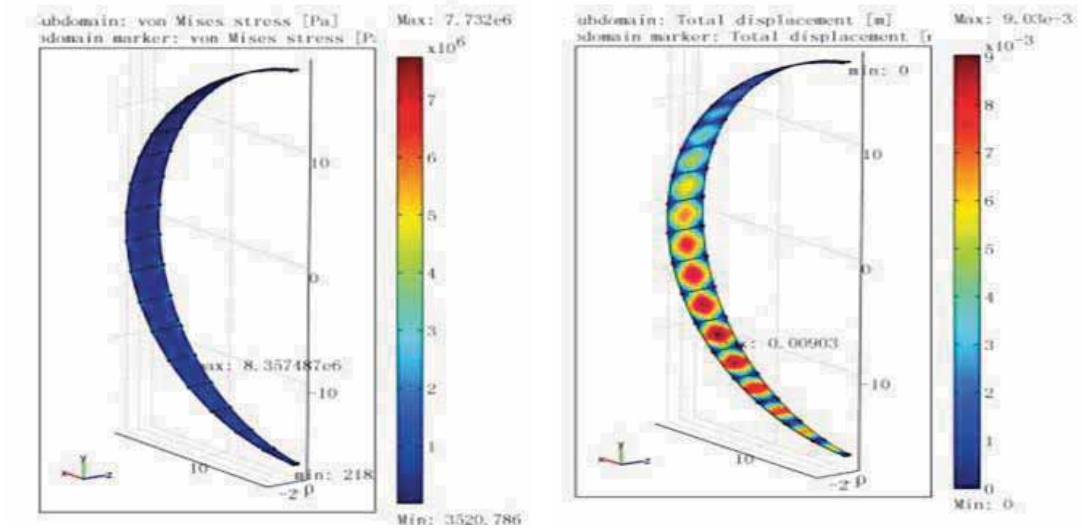

(a) the stress distribution (b) the deflection distribution

Figure 2.30: the stress and deformation of the acrylic support

]

Figure 2.31: A preliminary structure of the stainless-steel tank

many professional companies who have experience in making large spherical tanks. In addition, the largest spherical tank in China is up to 50 m in diameter, while the largest stainless-steel spherical tank is only 17 meters in diameter. Although there is a certain degree of difficulty and challenge for the ϕ38 m stainless-steel tank in this option, there are many examples to follow.

2.3.5 Installation Issues

After the construction of the stainless-steel tank in the experimental hall, the PMTs and acrylic support sheets will be installed. To reduce the time for installation, several PMTs will be pre-assembled as modules. The bottom of the PMT module is made of stainless steel plate and the PMTs can be mounted on it. The ribs on the bottom plate are designed to increase its rigidity, as each PMT suffers about 70 kg buoyancy. There has to be about 10 cm clearance between the bottom plate of the PMT module and the inner wall of the stainless-steel tank, which will provide space for cable arrangement.

During the installation, scaffolding will be installed in the stainless-steel tank. After the tank is completed, the scaffolding can be used to wash the tank from the top to the bottom. If the cable and PMT modules can be installed separately, the pre-layout of the cables can be finished in the inner wall of the tank before the PMT installation is started. A sling can also be hung along the inner wall of the tank for lifting the PMT module. After the tank cleaning and cable arrangement, the scaffolding can be removed. The pipe for filling the liquid scintillator and LAB will be installed outside the tank, and the pipe outlet, which is also the entrance into the steel tank, is at the bottom of the tank. The PMT modules will be installed from bottom to top one by one. The PMT modules can be moved by a manual chain which is hung by the sling. The cable can be connected to each PMT after it is installed. The PMTs in each module will be tested after the installation of each layer.

After the PMT modules are installed, acrylic rods will be installed at the back plate of each module, and the acrylic sheet will be mounted on the rod to support the balloon. Once PMTs are tested, water can be filled into the tank. When water reaches the top of that layer of PMTs, installation of the next layer of PMTs can be started. After installing all PMTs and acrylic sheets, the water can be drained from the bottom of the tank. During this process, it is necessary to guarantee that the air coming into the tank is clean. After all water is removed, the balloon will be lifted into the tank from the top, and the filling pipe can be connected to the bottom flange of the balloon through the manhole. The top hole and bottom manhole will then be sealed to prevent dust getting into the tank. The flange on the top of the balloon will be sealed, and the gas for the leak test will go through the pipeline for filling liquid scintillator into the balloon to replace the air in it. Once the balloon leak test completed, the manhole at the bottom will be sealed by the flange. After making sure that every part works well, liquid scintillator will be filled into the balloon. During the process, the filling speed of LS, LAB and water outside the tank should be controlled strictly to keep the level of different liquids the same.

2.3.6 Conclusions

Since the balloon can be made in the factory and then delivered to underground lab for the final installation and leak check, the time needed onsite is relatively low. The cost of fabricating a balloon is much lower compared to the acrylic sphere so more than one balloon can be made. If one balloon has trouble in the leak checking or any other damage, it can be replaced in a short time. On the other hand, the balloon is a soft structure and not easily damaged under a shock load (such as seismic load). The use of the acrylic layer as support for the balloon reduces the stress and greatly improves the safety. Since the acrylic sheets in this option do not need to be sealed, the difficulty and time needed for on-site construction is reduced. Because the detector construction in this option involves the tank welding onsite, installation of the acrylic sheets and the balloon in the tank, cleaning and leak test of the balloon, the procedure will be more complex. Therefore this option is considered to be a backup.

2.4 PMT assembly

2.4.1 PMT testing and validation

The JUNO central detector will use 20 inch PMTs with highest possible quantum efficiency and large photo-cathode. The main specifications of the PMT include:

- Response to single photoelectrons
- Quantum efficiency of photocathode
- Gain-HV function and gain nonlinearity
- Transit time spread, ratio of after pulse and time structure
- Dark noise rate
- Uniformity of detection efficiency

To precisely measure those parameters, a test bench integrated together with software and hardware needs to be setup. Based on the requirements, a dark room with shielding to earth's magnetic field is necessary. Efficient testing can be implemented by using a light source with multiple optical fiber coupling. Testing of PMTs consists of several steps: single sample test, test of a group of samples and batch test. Details will be finalized later.

2.4.2 High Voltage System of PMTs

A high voltage system is needed to provide stable power to the PMTs. This includes high voltage power supply, cable and water-proof structure. The three options below are under consideration:

1) One to one option: one HV channel supplies one PMT, and a divider is needed to produce different voltages for each electrode. This option can have a control to each PMT HV independently but a huge number of cables are needed.

2) Multi-core cable option: a group of HV channels are carried by a single cable with multiple cores, via an exchange box close to the PMTs, the HV supplies a bunch of PMTs. In this option: the number of cables are reduced, while each PMT is still powered independently. However, a dry box is needed for HV exchange and distribution, and a connector with water-proof design is needed.

3) Front-end HV module option: for this option, the low voltage is firstly delivered to the front end near the detector, then the low voltage is transformed to high voltage which is supplied to the PMTs. The advantage of this option is to save cost and significantly reduce the number of cables.

The voltage of the PMTs is provided by a Cockroft Walton capacitor diode, which converts the low voltage carried by a flat cable to high voltage and finally supplies the whole power grid. Compared to the traditional HV power based on dividers, this method of voltage multiplier has some clear advantages:

1) the expensive high voltage cable and connector is replaced by a cheap flex cable. This is an efficient way to save cost, reduce the number of cable and improve the overall quality.

2) the high efficiency of the voltage multiplier can reduce heat power consumption significantly. In general this kind of device will consume power less than 50 mW without light load, while under maximum light load, the power consumption is less than 200 mW. As a comparison, the option using dividers will consume 3.6 W in the form of heat loss.

3) the high voltage is very stable due to a deep negative feedback designed in the module, and complete load characters are provided.

4) the cost of the high voltage power supply with the multiplier itself is low, about 3-4 times lower than the other options.

The main parameters of the JUNO 20" PMT high voltage power supply are shown in Table 2.8, Table 2.9 and Table 2.10 below:

Table 2.8: USB bus adapter

Maximum number of channel	127
Power supply	computer USB port
BUS voltage/ V	LV - 5V,BV - 24
Interface	RS-485
Communication line to computer	USB-2.0
Working temperature/degree	(- 10) - (+40)
Working humidity/ %	0 - 80
size/ mm x mm x mm	70x50x22
Weight/ kg	0.15

Table 2.9: 20" PMT HV module

PMT connection, grounding	cathode
Range of HV for anode / V	1500-2500*
Operating voltage/ V	+2300*
Precision of anode HV/ V	0.25
Error of HV output	3%
Stability of HV / %	0.05%
Temperature coefficient/ ppm/degree	100

Table 2.10: HV value of PMT dynode

focus / V	+300
D1/ V	+400
D2/ V	+1200
D3/ V	+1300
D4/ V	+2100
Anode/ V	+2300
Up limit of anode current/ mA	100
Cross talk/ mV	20
Nominal voltage/ V	+5,+24
Power consumption of single module /W	0.1
Communication protocol	RS-485

2.4.3 PMT related Structure Design

PMT related structures include PMT voltage divider, implosion protection structure, potting structure and mechanical supporting structure. JUNO will use 20" PMTs, each one weighting about 10kg and the buoyancy in water of 70 kg. The PMTs are mounted on the stainless-steel truss.

A preliminary design and test of the MCP-PMT divider has been carried out. The method of positive HV powering has been adopted, to reduce the number of cables and connectors, and the signal is readout by a splitter.

A potting structure is needed since the PMTs are working in water, and a conceptual view is shown as Fig. 2.32. The potting will use a plastic cover and the water-proof adhesive to seal the PMT base, electronics and cable from contact with water. The waterproof design needs to consider long-term compatibility with high purity water and 4 atm hydrostatic pressure. After finishing the design and related tests, we will set up a batch test system to test each of the PMTs before installation.

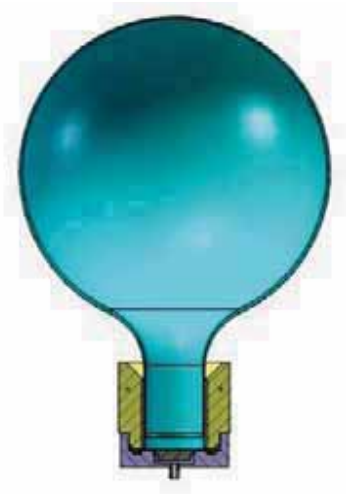

Figure 2.32: conceptual view of PMT potting structure

The following sections will discuss the implosion protection structure of the PMTs. Currently there are three ideas under consideration to protect the PMTs from implo-

sion in 40 m depth of water:

1) the PMT is covered by an acrylic shell for the upper half sphere and the lower part by another shell made from FRP, PE or ABS. A few small holes are opened on the shell to allow air flow and liquid circulation. When the PMT collapses, the amount of ingoing water is minimized by those holes, hence the strength of the induced shock wave is suppressed;

2) an air chamber is placed around the lower half of the PMT. When collapse happens, the air chamber will quickly expand due to a sudden drop of the local water pressure, hence the amount of ingoing water is also reduced and the shock wave is weakened;

3) a thin layer of film is attached to the PMT surface, this film will prolong the PMT collapse time, and hence the intensity of inrushing water. The film is transparent so no light will be blocked.

(1) Study of PMT implosion mechanism

The shell of the PMT is made of fragile glass, so an implosion could happen when damaged glass shell is immersed in water. As was experienced in Super-K, implosion of one PMT could lead to a cascaded implosion and eventually all the PMTs would be destroyed. A simulation of the PMT implosion is shown in Fig. 2.33. The PMT glass shell crashes in 5 ms due to an outer pressure of 5 atm, the water then rushes inward suddenly. After about 40 ms, due to the collision of inrushing water, the implosion happens, and a shock wave is produced which propagates outwards.

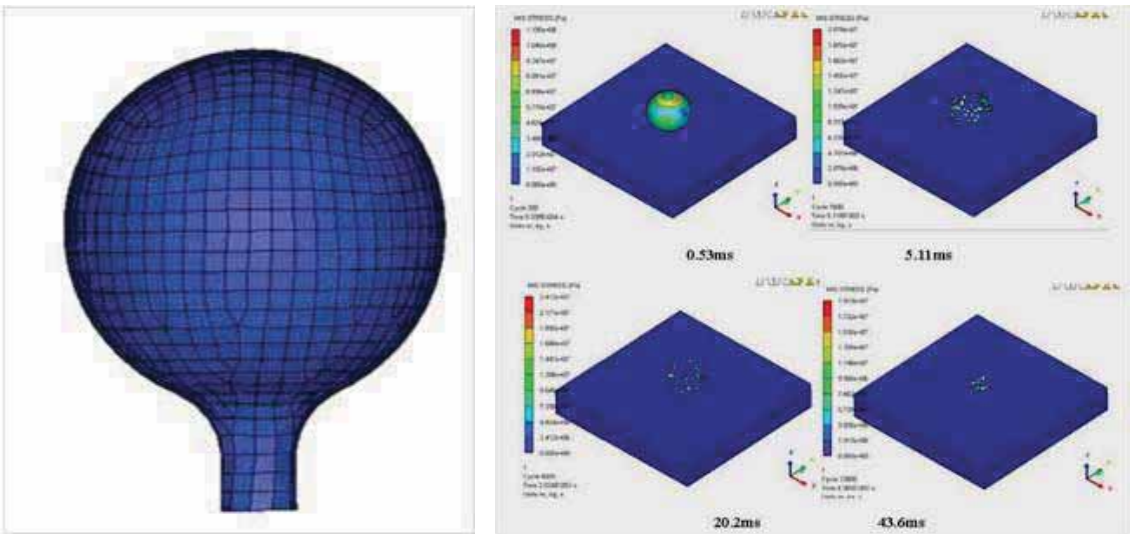

(a) (b)

Figure 2.33: Simulation of PMT implosion

A preliminary study of the implosion behaviors such as shock wave strength as a function of time, distance, PMT volume and water pressure has been performed. As shown in Fig. 2.34, the strength from simulation is consistent with the real test. The strength follows a 1/r relation to distance as seen from Fig. 2.35, and is proportional to PMT volume and water pressure as shown in Fig. 2.36 and Fig. 2.37, respectively.

(2) PMT implosion test and simulation

The purpose of the PMT implosion test is to measure the shock wave parameters,

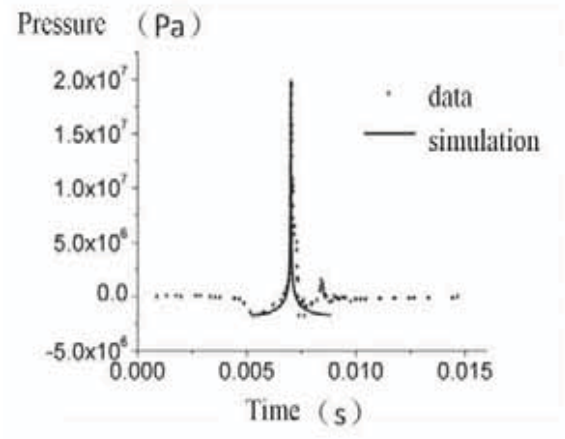

Figure 2.34: Peak pressure of the shock wave

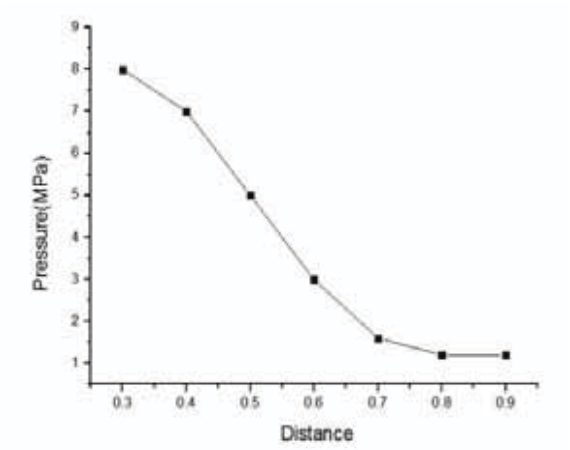

Figure 2.35: strength of the shock wave as a function of distance

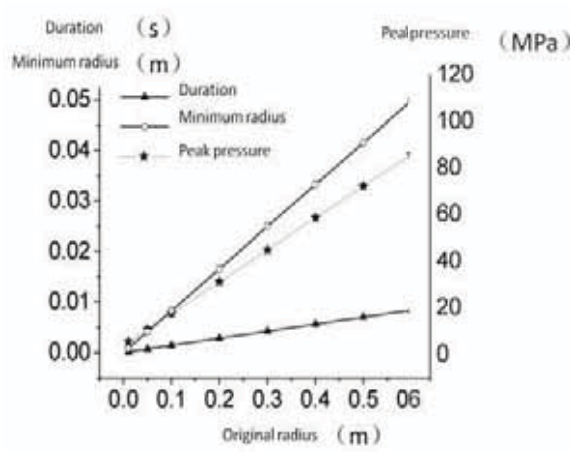

Figure 2.36: strength of the shock wave as a function of PMT volume

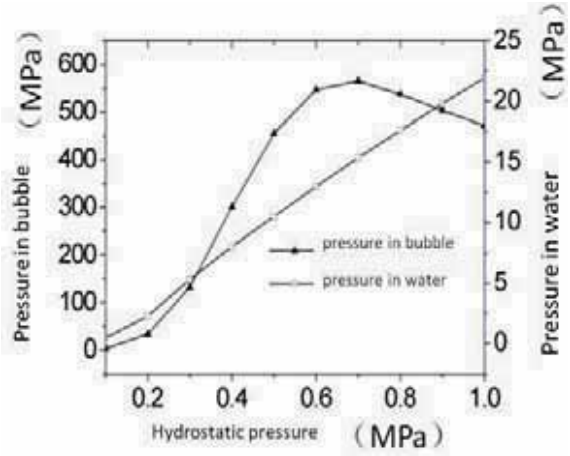

Figure 2.37: strength of the shock wave as a function of pressure

including production, propagation and relation to space and time. In addition, the test can verify the function of the acrylic cover. Fig. 2.38 shows the schematic view of the implosion test and the pressurized tank. The tests are currently underway.

(a) Schematic view of the implosion test (b) the pressure tank for implosion test

Figure 2.38: the setup for implosion test

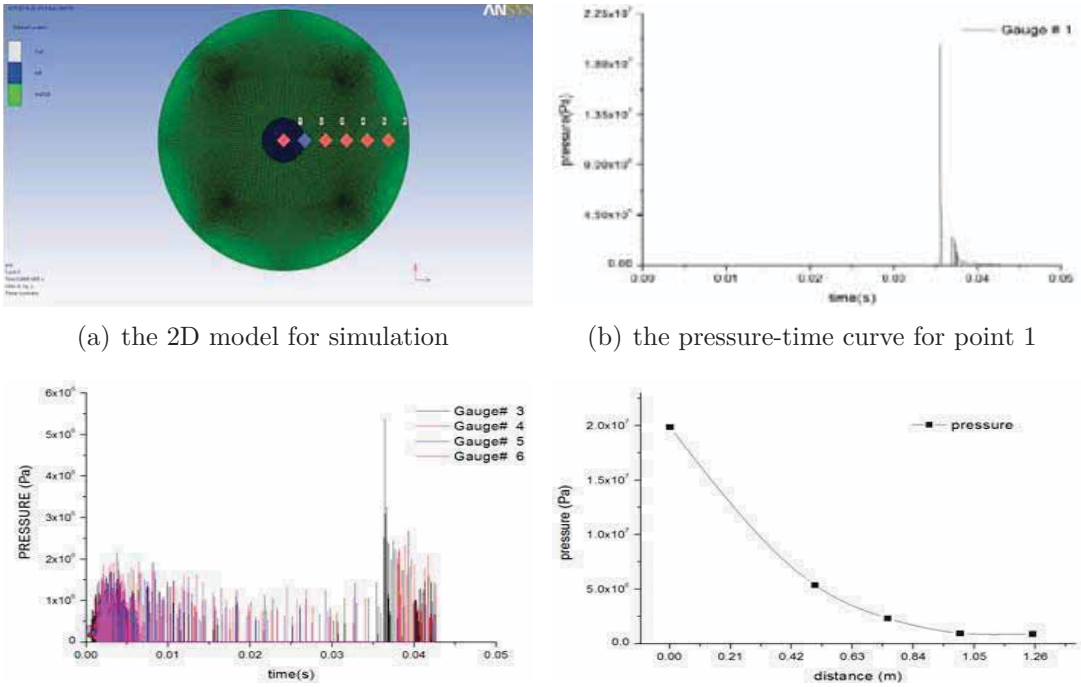

(a) the 2D model for simulation (b) the pressure-time curve for point 1

(c) Pressure-time curve of different points (d) Peak pressure as a function of distance

Figure 2.39: Simulation of the PMT implosion

To get the correct implosion model, simulation have been done following the real boundary conditions in the test. Fig. 2.39(a) shows a 2D simulation of single PMT without protection enclosure, in which the diameter of the water tank is 1.5 m, the diameter of the air bubble (PMT volume) is 0.5 m, the hydrostatic pressure is 4 atms, and the gas pressure in PMT is about 10^{-5} Pa. The boundary is set as a rigid border.

There are 6 points in simulation which are uniformly distributed from the center to the border, in which point 2 is floating and movable to measure the size variation of the air bubble, and the other 5 points are fixed to measure the dynamic pressure induced by the shock wave. Fig. 2.39(b) shows that the peak pressure appears at t=35.2 ms. From Fig. 2.39(c), multiple shock waves are emitted during the process of compression and rebound of the air bubble, and the waves frequently happen at beginning or the end of the compression. The air bubble is finally compressed to a minimum size with the pressure reaching a maximum value of 20 MPa inside of the bubble, then the strongest shock wave is initiated. Fig. 2.39(d) shows the pressure for different points, where the pressure drops along with the distance. At the border of the PMT (d=25cm), the strength of the shock wave is about 11 MPa.

The data from the real test will validate the simulation described above. Tests of multiple PMT implosion, and simulation of the effect of the acrylic cover are also in progress.

2.5 Prototype

2.5.1 Motivations of the Prototype Detector

Following the progress and schedule of the JUNO experiment, considering the requirements of each sub-system, a prototype detector was proposed to test key technical issues:

1) Test and study of the PMT candidates:

The JUNO experiment is designed to use large area, high quantum efficiency PMTs to realize the highest photo-cathode coverage. Candidate PMTs include Hamamatsu, Hainan Zhan Chuang (HZC), and a newly developed MCP-PMT. It is necessary to compare their performance in a real scintillator detector. From the prototype, we expect to extract the effective PMT parameters and compare them.

2) Test and study of the liquid scintillator:

Liquid scintillator is another key component of the JUNO detector, a lot of experiences show that the final LS parameters in a detector, such as light yield, attenuation length, stability (or aging) and background level, are different from what were measured in the lab. With the prototype, many of those parameters can be extracted and optimized.

3) Test and study of electronics:

The planned PMT waveform readout electronics will be very flexible for different physics requirements. The electronics system should be tested in a real LS detector.

4) Waveform data analysis algorithms and detector performance study:

With the prototype, algorithms of PMT waveform readout scheme will be developed and detector performances will be understood.

2.5.2 Prototype Design

The prototype detector is shown in Fig. 2.40, which re-uses the Daya Bay prototype as the main container. An acrylic sphere locates at the center of the stainless-steel tank (SST) as a LS vessel, and is viewed by 51 PMTs dipped in the pure water. The expected photo-cathode coverage is 55%. The water tankand the PP/Lead layer is

designed to have 1 m.w.e. shielding, aiming to reduce the radioactivity coming from the outside of SST. The expected trigger rate is less than 100Hz@0.7MeV, and the energy resolution is 4%@1MeV.

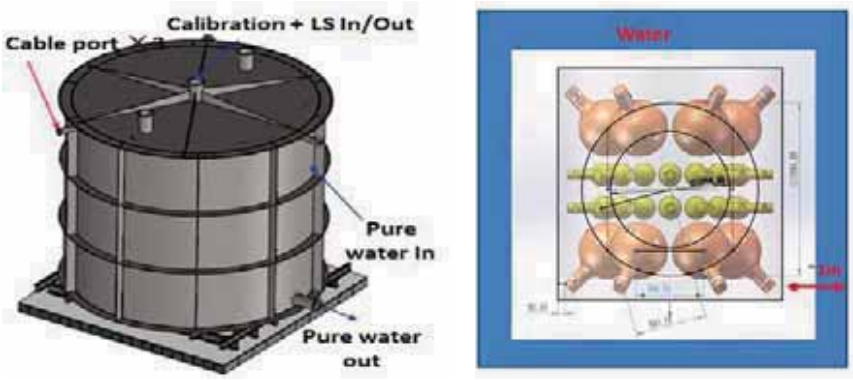

(a) (b)

Figure 2.40: the prototype design

As shown in Fig. 2.41, the diameter of the acrylic sphere is 50 cm with a thickness of 1 cm, and a tube with a diameter of 5 cm and a length of 70 cm is located at the top of the acrylic sphere for filling and calibration. The 51 high quantum efficiency PMTs, in the diameter of 8”, 9” and 20”, are uniformly arrayed in 4 layers facing to the center of the acrylic sphere. As follows is the detailed arrangement of the PMTs:

• Top layer: which includes 4 MCP-PMTs of 20” and 2 Hamamatsu PMTs of 20”;

• Middle layers: which are divided into two layers and each layer including 8 MCP-PMTs of 8”, 4 HZC-PMTs of 9” and 4 Hamamatsu PMTs of 8”;

• Bottom layers: which are divided into two rings, the inner ring includes 3 MCP-PMTs of 8”, 2 HZC-PMTs of 9”and 2 Hamamatsu PMTs of 8”, and the outer ring has the same arrangement as the top layer.

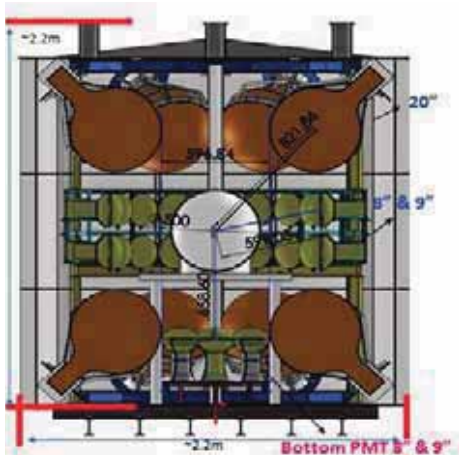

Figure 2.41: The side view of the prototype detector

Fig. 2.42 is the shielding system. The bottom and top of this system are covered by 10 cm thick lead plus 10 cm thick pp plate, while each of the other 4 sides is shielded by a customized water tank in 1m x 5m x 3m dimension constructed by standard

stainless-steel elements which are widely used by water and conditioning system. One of the 4 sides is movable to allow the internal detector installation.

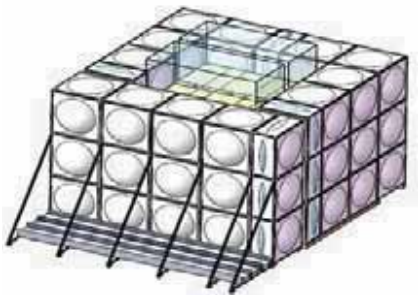

(a) schematics of the shielding structure

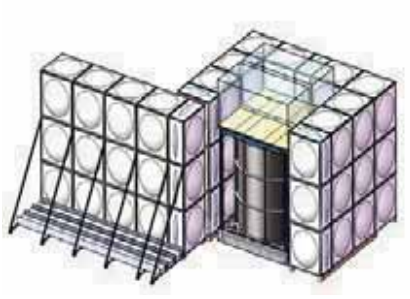

(b) one side of the water tank opened

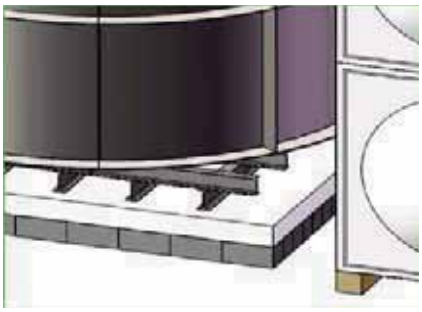

(c) bottom and top shielding design with lead and pp plate

Figure 2.42: the shielding system

2.5.3 Expected Performance

With preliminary Geant4 simulation (simulation geometry is shown in Fig. 2.43), we confirm that the detector will have a good measurement of electron and alpha for LS study. Gammas have a large energy leakage due to the limited detector dimension, we will need a spectral fitting to extract more parameters. Measurements of Muon and calibration will provide more opportunities for detailed study. According to the prototype design, we expect to measure PMTs' parameters, liquid scintillator, electronics and background, to achieve the goals.

The prototype is now under preparation and will be operational soon.

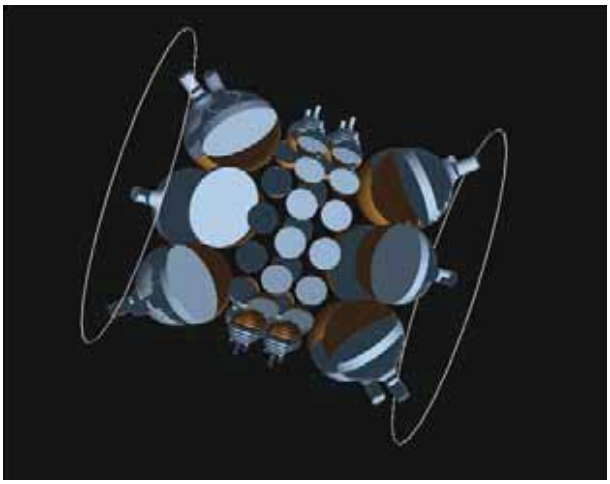

]

Figure 2.43: Geant4 simulation geometry

2.6 Construction of the central detector

2.6.1 Assembly of the Stainless-steel Truss

The stainless-steel truss used in the central detector has a bolted connection, which makes the on-site assembly easy and safe without any welding. The design and the construction of the truss should follow the technical standards, design specifications and procedures. In China, the space truss technique is very popular for building construction. Many companies have capability and rich experience in design and production of steel trusses.

There are two main stages for the construction of the stainless-steel truss. The first stage is the off-site preparation in the factory, and the second stage is assembly onsite. All the truss members, bolts and joints will be finished for the machining and production in factory before transportation, and the machining precision and quality should be ensured at this stage. When all parts are transported to the experimental hall, some important tests need to be done onsite to make sure that all conditions meet the requirements for construction before truss assembly. Theses tests include: checking the foundation of the truss area; double checking the parts of the truss; checking the height mark, axial and gradient of the embedded part, and so on. Since the complexity of truss assembly depends on the accuracy and roundness of the first three circles, the beginning preparation of axis positioning and height level is more important for the whole assembly of the truss. To control and check the coordinate position of each truss joint, some reference and checking points should be installed at different areas of the hall. When all conditions for the construction meets the requirements of design and standards, the truss assembly can be started following the detailed construction procedure. Theodolites or other survey instruments will be used during the truss assembly to control the error.

For the central detector, the stainless-steel truss and acrylic sphere are not independent and need overall consideration of the construction sequence and procedure. It should be better to make the truss and acrylic sphere layer by layer alternately. The detailed procedure needs further discussion with the factory. In general, the whole procedure needs to ensure the safety and reliability of the sphere and truss.

2.6.2 Construction of the Acrylic Sphere

As Fig. 2.6 shows, the acrylic sphere is made up of many acrylic sheets which are bonded together to form the sphere. Satisfying the production capacity and transportation limit, the size of each acrylic sheet should be as big as possible to reduce the total bonding length onsite. For the preliminary consideration and design of the sphere, there are a total of 170 acrylic sheets and divided into 17 layers. Each sheet is less than 3 m x 8 m in size. The total bonding length of the sphere is about 1.8 km.

Production and machining of the acrylic sheets will be finished in the factory before construction onsite. In the factory, the first step is to produce a flat sheet of acrylic with 120 mm thickness. The next step is to thermoform the flat acrylic into a spherical sheet with 35.5 m inner diameter in a concave spherical mold, and these thermo-formed sheets should be stored carefully to prevent damage to the acrylic surface. After that are the steps of machining, milling, polishing and annealing. Some measurements should be done for each step to control the quality in the factory. One such step is the thickness measurement of each flat sheet used as the thermoforming blank. The second measurement is for the thickness of the sheet after thermoforming. In general, the acrylic blank increases in thickness around its border and decreases in thickness at the center after the thermoforming operation in the female mold. The third measurement is the acrylic thickness after annealing. The curvature of the acrylic blank should also be measured to ensure the assembly requirement [2]. In the factory, the fixtures for positioning and assembly should be machined.

After all the part production and fixture preparation is finished by the manufacturer, they will be delivered to the underground to do the construction of the acrylic sphere onsite. The acrylic sphere can be constructed with the help of the truss. The acrylic sectors can be supported by the truss joints during assembling, positioning and bonding layer by layer. The truss can also be used as the scaffolding or platform for sphere construction. The acrylic sphere will be built from the bottom to the top, layer by layer. The quality control and check of dimension, positioning, roundness, bonding status and annealing need to be ensured for each layer throughout the period of construction. Inspections of the finished spherical sphere consist of careful visual checks, dimensional measurements, and stress checking.

For the construction of the detector, two cranes will be needed in the hall. One is to carry and lift the components of the detector, and the other is a lift to carry people to access the working area in the pool. The working platforms should be designed and installed inside and outside the acrylic sphere for the processes of positioning, assembly, sanding and polishing. Safety nets should be installed surrounding the sphere during construction to prevent any dropping of objects which will damage the detector or people. Special requirements may be needed for the ventilation system of the assembly cavern. There are special rules and regulations governing working underground to which the project must conform.

2.6.3 PMT Installation

When the acrylic sphere and stainless-steel truss are finished, about 16000 PMTs need to be installed on the truss facing inwards to receive signal from the LS. These PMTs should be arranged as close to each other as possible to provide more than 75% optical coverage. The PMT support structure must provide a stable and accurate platform

for the mounting and positioning of the PMT assemblies to view the active detector regions. The PMT support structure should also provide a mechanism to protect adjacent PMTs from the risks of cascaded implosion and permit the replacement of the PMT assemblies. To reduce the installation time, PMTs will be installed by PMT module. Several PMTs are assembled to be one module in the surface assembly building. The PMT modules will then be delivered underground for on-site installation. At present, two options for PMT installation are considered.

One option is to use stainless steel as the support panel of the PMT module, and each PMT with its protecting cover will be mounted using a clamp on the panel as Fig. 2.44 shows. Some slots on the truss should be left for the lifting and installation of the PMT module. The circular rails along the latitude will be installed on the joint of the inner layer of the truss. There are pulleys at the back of the stainless-steel panel to allow the PMT element to slide to the expected location and finish the mounting. Fig. 2.45 shows the sketch of this option. The design of the module size and shape should consider the location and number of the joints and supporting rods between acrylic sphere and truss to get the maximum optical coverage for the central detector.

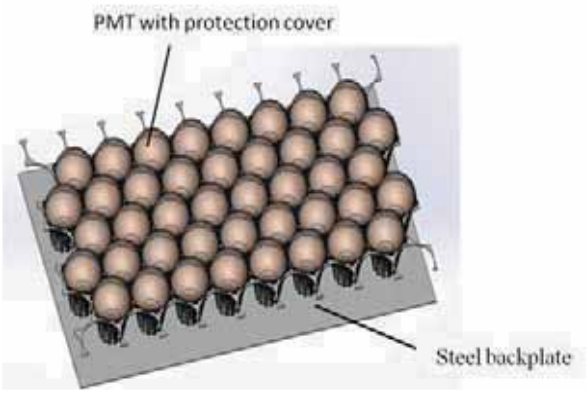

Figure 2.44: PMT module with the stainless-steel backplate

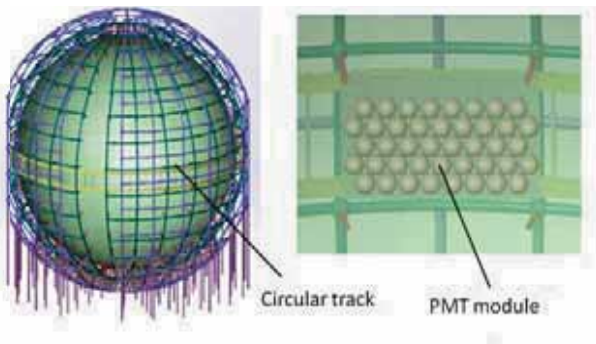

Figure 2.45: Installation of the PMT module

The other option is to use profile stainless steel as the supporting structure. PMTs will be mounted on the profile steel one by one. This profile steel will be pre-installed on the inner layer of the truss. Fig. 2.46 shows the sketch of this option. This option allows many work groups to do the installation at different working areas simultaneously.

2.6.4 Filling system for the Liquid Scintillator

Filling will start when the construction of central detector is finished. The filling liquid involves LS and water for the main option and LAB needs to be considered for the backup option. The veto system will be responsible for water filling and the central detector system is responsible for LS and LAB filling. The two systems should coordinate their filling speed to balance the pressure. During filling, cleanness, background, temperature, liquid storage tank, pipe design and process monitoring should be considered and controlled.

1) Controlling the Cleanness and low background

During filling, the detector and LS need to be kept clean, especially to prevent the radioactive background and radon gas from pollution. The central detector will be

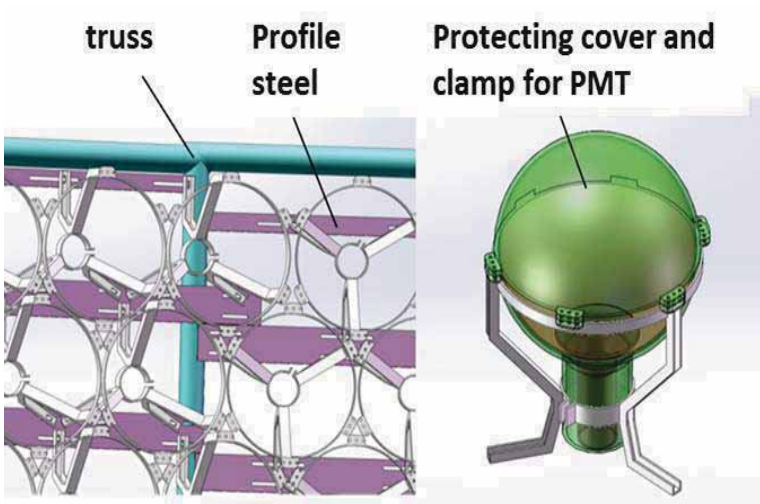

Figure 2.46: Using profile steel for PMT installation

cleaned using purified water before filling. For the acrylic sphere plus stainless-steel option, a special cleaning robot will be designed and used for cleaning the acrylic sphere and the other parts such as the steel truss. The PMTs will be washed first. The acrylic sphere can be washed with LS at the end. For the backup option, the inner wall of the stainless-steel tank and the outer surface of balloon will be water flushed and the inner surface of the balloon can be cleaned by filling and pumping water repeatedly. The filling pipes and pump, which will come into contact with LS, need special care and cleaning, and they should be compatible with LS. Before filling, the whole filling system will be cleaned with LS several times and the used LS will be disposed of. Spaces where the LS is exposed to air, such as inside the acrylic or balloon and the LS storage tank, will be filled with nitrogen to prevent radon pollution and contact with oxygen.

2) Pure water exchange or nitrogen exchange for filling

Pure water exchange means we need to firstly fill the acrylic sphere or balloon with water and then fill LS into the vessel while draining the water out. Because of its lower density, the LS will be float at the top of the water. This process filters the LS and is helpful to remove the background. The other method is exchanging with pure nitrogen, which means filling the acrylic sphere or balloon with nitrogen first and then putting pure LS into the vessel to replace the nitrogen.

3) Controlling the liquid temperature

The LS temperature will be high if it is produced and stored on the ground. Since we hope the liquid for filling can be kept at 20°C, the liquid needs to be cooled before filling the detector. The place for cooling should be selected on ground or underground according to the general deployment of the civil construction, and the cooling method can be water cooling or air-conditioning.

4) The preliminary plan for the LS pipe, storage tank, overflow tank and LS cycling system.

As shown in Fig. 2.47, the filling port of the central detector is designed at the bottom of the sphere. The filling pipe comes from the LS storage tank which sits in the storage room, and goes down along the water pool wall to connect to the filling port. When the LS filling is finished, the pipes between the storage tank and central

detector make them communicating vessels and then the storage tank can be used as the overflow tank. If the LS needs recycling during running, we will remove the LS from top of the detector and transport it to the LS recycling equipment, and then pump it back into LS storage tank. Finally the LS will be filled back into the central detector through filling pipes from the storage tank.

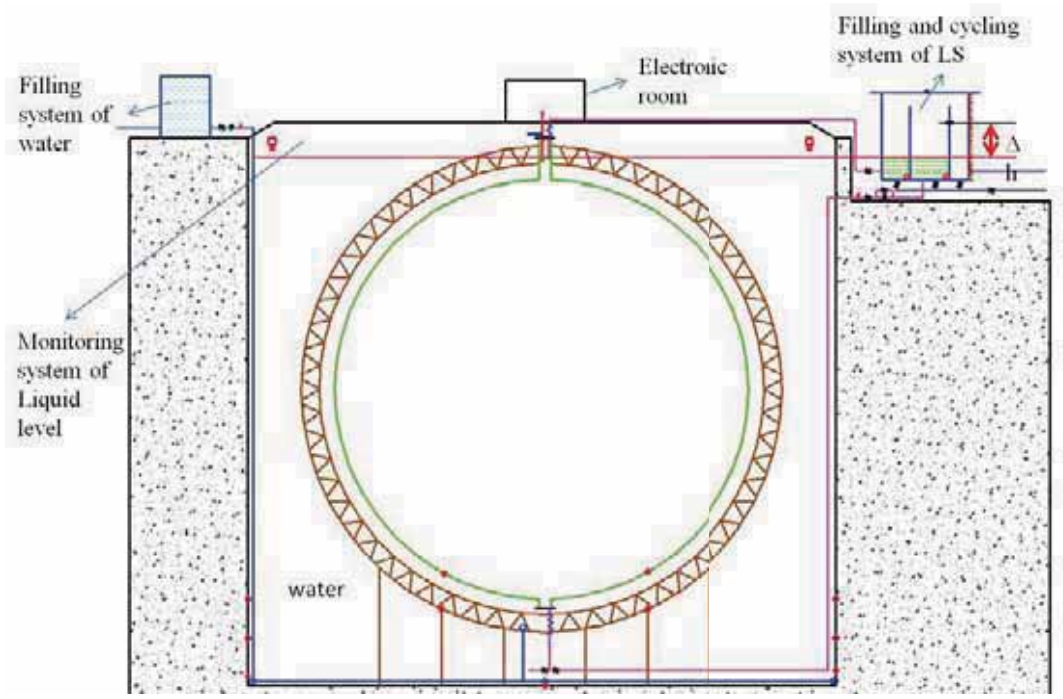

Figure 2.47: Sketch of the LS filling system

5) Filling process control

Filling process control involves the speed control, monitoring of liquid levels, monitoring of stress and deformation of the detector, monitoring of stress, temperature, and so on. The design of filling speed and capacity of the filling system should consider the requirements of total filling time, the capacity of LS storage and production, and cost. The design of the relative liquid level difference should consider the load stress on the detector.

2.7 Reliability and Risk analysis

• Structural reliability analysis

The baseline option takes large glass buildings and techniques used for glass curtain walls as an important reference, given that those buildings and techniques have been matured for long time in the field of architecture. In our case, the material of glass is replaced by acrylic, and the crucial parts include bulk-polymerization of the acrylic sheets, different liquid located inside and outside of the acrylic and long term water pressure and buoyancy. Reliability of the stainless-steel structure is less important than that of the acrylic sphere in this option. We should consider:

1) The aging properties of acrylic under stress and submersion in organic or inorganic liquid needs further tests, to make sure it will be stable during the 20-year

running.

2) Acrylic is a brittle material, if there is a crack it will grow under stress. Cracks can be repaired during the construction but will be fatal after the liquid filling is finished.

3) The stress is generally larger in the joints of the acrylic and truss than other areas, so needs to be controlled to keep it low enough.

4) As for the requirements of the SNO and Daya Bay, the stress on the acrylic should be less than 5 MPa, and more work is needed to reach this goal.

• Construction reliability

Fabrication of a thick acrylic sheet in a spherical shape is not a mature technique, and on-site construction of the large acrylic sphere also needs more R&D effort.

• The reliability of FEA

The analysis needs to be compared with test results, and the accuracy of analysis should be verified by joint tests and small prototype tests. Maximum errors should be taken as the input parameters for the analysis.

• Construction risk

Construction of the truss should be under control since there is a mature specification. For construction of the acrylic sphere, since there will be a large mount of work done onsite, a standard procedure should be followed and strict quality control should be applied especially on the key parameters of the structure such as stress, deformation and stability.

• Local failure

Local failure means a failure of the joint between the acrylic sphere and truss, so the stress of the whole structure would need to be re-analysed. According to the current analysis, if the failure happens on the truss, it will not be too serious. If it happens on the acrylic, however it will result in severe damage, especially when the acrylic sphere has been filled with liquid scintillator. This kind of failure should be avoided at all costs.

• Long term compatibility and leakage problem

It has been proved that acrylic is compatible with liquid scintillator, and bulk-polymerization will not lead to leakage problems.

• Long term performance

The lifetime of acrylic is up to 30 years and the acrylic sphere for the SNO [18] experiment has already been running for nearly 20 years. In our case, however the aging effect of the acrylic still needs more study.

2.8 Schedule

The schedules of the central detector are the following:

• 2013

1) Conceptual design of the detector, including FEA and prototype test

2) Consideration of the central detector schedule, budget, manpower related issues.

• 2014

1) Review existing options, select one main option and one candidate option. Perform extensive study on the two options, solve the key design parameters by analysis and prototype.

2) Preliminary design and test of implosion-proof structure of PMT.
3) Start to study PMT potting and LS filling.
4) Start to study batch test for PMT.
• 2015
1) Optimize the detector design, conduct prototype design, fabrication and test. Start to consider on-site construction of the detector.
2) Further study the water-proof of PMT
3) Finish a preliminary design of the implosion-proof structure of PMT
4) Study the batch test system of PMT, including electronics performance test, water-proof and pressure test.
5) Determine the final central detector structure.
• 2016
1) Continue detector structure design and on-site construction study
2) Determination of the batch test design for PMT
3) Start to design the liquid filling system and monitoring system.
4) Determination of the high voltage option for PMT
5) Start to manufacture the implosion-proof structure for PMT
6) Finish the engineering design of central detector.
• 2017
1) Finish bidding for the central detector structure, determine the construction company and start to produce the components.
2) Determine the high voltage option and water-proof design of PMT.
3) Start PMT batch test.
4) Determine liquid filling option, bidding for the system.
5) Design of nitrogen protection system for liquid scintillator.
• 2018
1) Start to construct the central detector.
2) Continue PMT batch test.
3) Start to install detector monitor and other necessary devices.
• 2019
1) Finish central detector structure construction.
2) Finish PMT installation.
3) Finish detector monitor installation.
4) Finish installation of liquid filling system, start to fill the liquid.
• 2020
1) Finish liquid filling.
2) Finish detector commissioning and start data taking.

The total time for the central detector construction is estimated about 18 months, as follows:

• Construction of the stainless-steel truss: 3 months (January 2018 - April 2018). This includes interface(column supports on the base of the water pool), fixtures, hoisting, measurement, fixing, surveys etc.

• Construction of the acrylic sphere: 8 months (May 2018 - November 2018). This includes acrylic sheet hoisting, positioning, fixture installation, joint connection and adjustment, bulk-polymerization, sanding, stress monitoring, installation of the LS filling device and the interface of calibration.

• Survey of the acrylic sphere and leak test: about 1 month (December 2018)

• Cleaning of the acrylic sphere. The total area of the inner and outer surface of the sphere is about 8000 m^2. A high cleanliness level is needed for the inner surface and it is hard for humans to clean, so a robot cleaner is under consideration. An outlet need to be reserved in the bottom of the sphere. It will be closed after cleaning.

• Installation of PMTs and monitors: 5.5 months (February 2019 - June 2019). A number of work groups are considered to work in parallel at a rate of 2 PMTs/hour and 8 working hours/day, so 128 PMTs can be installed in one day. In total this requires about 120 working days, meaning 5.5 months, for the 16000 PMTs.

• Cleaning of the whole detector after installation. This is not included in the timetable of the central detector since it can be done together with VETO.

Bibliography

[1] J. Boger et al. Nuclear Instruments and Methods in Physics Research A 449 (2000) 172-207

[2] Jerry D. Stachiw Handbook of acrylics for submersibles hyperrodic chambers and aquaria,2003

[3] J. Benziger et al. Nuclear Instruments and Methods in Physics Research A 582 (2007) 509-534

Chapter 3

Liquid Scintillator

3.1 Introduction

The innermost part of the JUNO detector is formed by 20,000 tons of liquid scintillator (LS) contained inside an acrylic sphere of 35 m diameter. The LS serves as target medium for the detection of neutrinos and antineutrinos. The primary reactions for reactor electron antineutrinos ($\bar{\nu}_e$) is the inverse beta decay on free protons, $\bar{\nu}_e + p \rightarrow n + e^+$, resulting in a prompt positron and a delayed signal from the neutron capture on hydrogen ($\tau \sim 250\,\mu$s).

The scintillator itself is a specific organic material containing molecules featuring benzene rings that can be excited by ionizing particles. Compared to other materials, this process is very efficient: About 10^4 photons in the near UV and blue are emitted per MeV of deposited energy. The time profile of the light emission is dictated by the decay constants of the excited states of the organic molecules but also depends on the type and energy of the incident particle.

The LS is composed of several materials: The solvent liquid, linear alkyl benzene (LAB), forms the bulk of the target material and is excited by the ionizing particles. This passes on the excitation to a two-component system of a fluor (PPO) and a wavelength-shifter (Bis-MSB), that are added at low concentration (a few g/l resp. mg/l) and by subsequent Stokes' shifts increase the wavelength of the emitted photons to ~ 430 nm. This shift is crucial as the long wavelength avoids spectral self-absorption by the solvent and allows the photons generated by a reaction at the very center of the target volume to reach the photosensors (PMTs) mounted on a scaffolding outside the target volume. At 430 nm, the transparency of the compound liquid will be largely governed by the Rayleigh scattering of photons on the solvent molecules. It can be reduced by the presence of unwanted organic molecules featuring absorption bands in the wavelength region of interest.

The energy resolution of JUNO is specified with 3 % at 1 MeV, corresponding to at least 1,100 photoelectrons (pe) per MeV of deposited energy. Compared to Borexino, this corresponds to more than twice the pe yield. To meet this demanding requirements, both the initial light yield and the transparency of the liquid have to be optimized simultaneously.

In spite of the large number of neutrinos crossing the detector and the huge target mass, the minuscule cross-section of weak interaction allows the detection of only a few tens of neutrino events per day. Low-background conditions are therefore abso-

lutely crucial. From the point of view of the LS, this means that the concentration of radioactive impurities inside the liquid should result in an activity on the same level or below the rate of neutrino events. This is less critical in case of the inverse beta decay channel for $\bar{\nu}_e$ detection. The reaction provides a fast coincidence signature that can be used to suppress single-event background.

As a consequence, light yield, fluorescence time profile, transparency and radiopurity are the key features of the LS. These quantities will be mainly defined by the original materials, but as well by the presence of organic and radioactive impurities, temperature and aging effects. For the next years, we foresee a broad spectrum of laboratory measurements to characterize different brands of LAB and wavelength shifters. Multiple experimental methods will be used, like GC-MS, LS-MS, UV-VIS, and ICP-MS, amongst others. A close contact with the producing companies has been established which will allow the optimization of the production quality within certain limits. Moreover, we will study a variety of purification techniques to optimize both optical performance and radiopurity of the LS. Finally, a large-scale test will be conducted in one of the Antineutrino Detectors (ADs) of the Daya-Bay experiment, which will allow a to study the effect of purification on a sample of about 20 tons of LS.

The final aim is to set up a scheme for the mass production of 20,000 tons of LS. This study will comprise all steps from the initial production, the transport on site, the local facilities for liquid-handling, plants for purification and instrumentation for quality control as well as safety and cleaning methods.Ref [1]

3.2 Specifications

The basic specifications and requirements for the liquid scintillator are:

- **Total mass:** 20,000 tons.

- **Composition:**
  Scintillator solvent: Linear alkyl benzene (LAB)
  Scintillating fluor: PPO (2,5- diphenyloxazole) at 3 g/L
  Wavelength shifter: Bis-MSB at 15 mg/L

- **Light yield:**
  Minimum of 1,100 photoelectrons (pe) per MeV

- **Transparency:**
  Attenuation length @ 430 nm: > 22 m
  Absorption coefficient of less than 3×10^{-3} in spectral range 430−600 nm

- **Radiopurity:**
  $\bar{\nu}_e$ detection: Concentrations of ^{238}U, ^{232}Th $\leq 10^{-15}$ g/g, ^{40}K $\leq 10^{-16}$ g/g.
  ν_e detection: Concentrations of ^{238}U, ^{232}Th $\leq 10^{-17}$ g/g, ^{40}K $\leq 10^{-18}$ g/g.

3.3 Study of Optical Properties

3.3.1 Light Yield

The light yield and emission time profile of the LS are key aspects of JUNO. For a given solvent (LAB), they depend mainly on the the concentrations of the fluor PPO and the wavelength-shifter Bis-MSB. The resulting light yield and fluorescence times of the composite LS will be measured as a function of these concentrations. While for both quantities higher concentrations will in general increase the performance, the optimum concentration of PPO and Bis-MSB will be determined taking into regard the detrimental effects of self-absorption on the attenuation length and the radioimpurities introduced into the scintillator.

The studies presented in the following section mainly concentrate on the characterization of the light yield as a function of fluor concentration and temperature. Moreover, the non-linearity of the light yield as a function of the energy of incident electrons will be studied as it has implications on the linearity in the energy response of positrons. Beyond the setups described here, first studies of the fluorescence properties in laboratory experiments have already been performed at the INFN institutes in Milano and Perugia and will be intensified in the future.

3.3.1.1 Effect of Fluor Concentrations

The light yield (LY) of an LS sample depends greatly on the concentration of fluor(s) added to the solvent. At low concentrations, it will increase almost linearly with the fluor concentration. However, the increase will become less steep once a concentration of $1-2\,\mathrm{g/L}$ is reached. To optimize the amount of collected light with regard to self-absorption effects which are expected to play a role for concentrations of several g/L and more, the LY of a variety of LAB samples featuring varying concentrations of PPO and Bis-MSB will be studied. This will be done by a setup based on a Compton coincidence detector, an established technique for a comparative measurement of the LY of LS samples.

Figure 3.1 shows the basic principle of the experimental setup: A PMT is attached to a vessel containing the LS sample that is excited by gamma-rays from a nearby source. Without a coincidence detector, the pulse height spectrum observed by the PMT will correspond to a Compton shoulder, which will require a relatively complicated fit to evaluate the light out. Adding a coincidence detector to record the scattered gamma-rays allows to define a fixed energy deposition in the LS sample by fixing the scattering geometry. In these circumstances, the pulse height spectrum can be fitted by a simple Gaussian, providing a more accurate result.

The experimental setup shown in Fig. 3.2 has been designed to determine the LY with less than 2 % uncertainty. The panels on the right display the pulse-height spectra obtained in a sample measurement and demonstrate the impact of the coincidence measurement. Beyond fluor concentrations, this setup will be used in the long term to test the effects of purification techniques, LS temperature and aging.

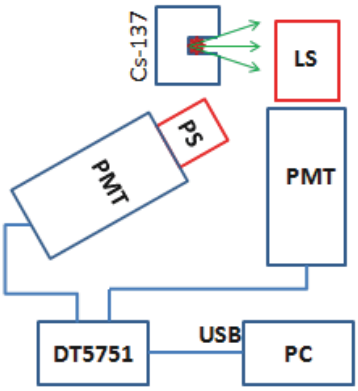

Figure 3.1: Schematic setup for the relative determination of the light out

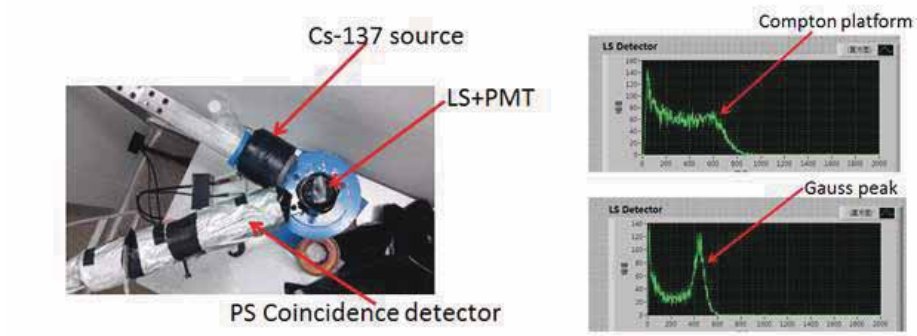

Figure 3.2: Setup for measuring the LS light out and preliminary result

3.3.1.2 Temperature Dependence

An increase in scintillation LY has been observed when lowering the temperature of the LS. This will be studied in a somewhat modified setup shown in Fig. 3.3 that has been adjusted for the application of different temperature levels to the LS sample. The ^{137}Cs γ-source, the LS vessel, the PMT and the coincidence detector are put into an enclosed thermostat, allowing to vary the temperature from -40 °C to 30 °C. The signals from the PMT and the coincidence detector are recorded by a CAEN DT5751 FADC unit. A temperature-resistant optical fiber is used to monitor the temperature response of the PMT.

3.3.1.3 Energy Non-linearity of Electron Signals

While the light output of LS is an almost linear function of the deposited energy, additional small non-linear terms will introduce an additional systematic uncertainty for the energy reconstruction in JUNO. Of special relevance is the non-linearity in case of positron signals that might affect the sensitivity of the mass hierarchy measurement. To take these effects correctly into account, it is important to study the energy response in small-scale laboratory setups. For practical reasons, these experiments will rely on electrons instead of positrons.

A corresponding experimental setup has been realized at IHEP, designed to mea-

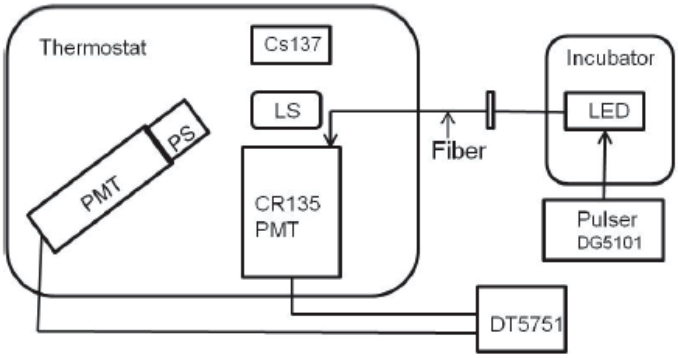

Figure 3.3: Experimental setup to determine the temperature dependence of the LY

sure the energy non-linearity of electron signals below 1 MeV at a precision of better than 1 %. The measurement is performed by inducing low-energy recoil electrons by Compton scattering of γ-quanta in a small LS sample. As the incident energy E_γ is known, a specific electron energy E_e can be selected by fixing the scattering angle θ (see above). It holds

$$E_e = E_\gamma \left[1 - \frac{1}{1 + \alpha(1 - \cos\theta)} \right], \tag{3.1}$$

where $\alpha = \frac{E\gamma}{m_e}$, with m_e the electron mass. The non-linearity of the energy response is obtained by determining the ratio of observed light output and computed electron energy as a function of θ.

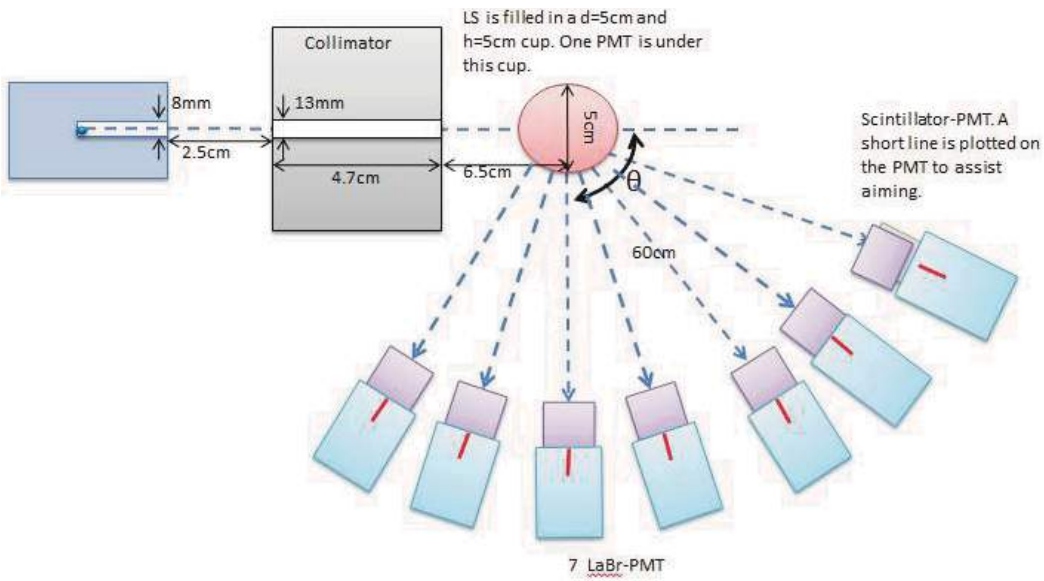

Figure 3.4: Conceptual drawing of the electron energy non-linearity setup

Figure 3.4 shows a conceptual drawing of the experiment, while Fig. 3.5 displays the actual laboratory setup.The gamma source used in the setup is ^{22}Na with an activity of 0.3 mCi. From β^+ decay to an excited state, it provides two γ-rays of 0.511

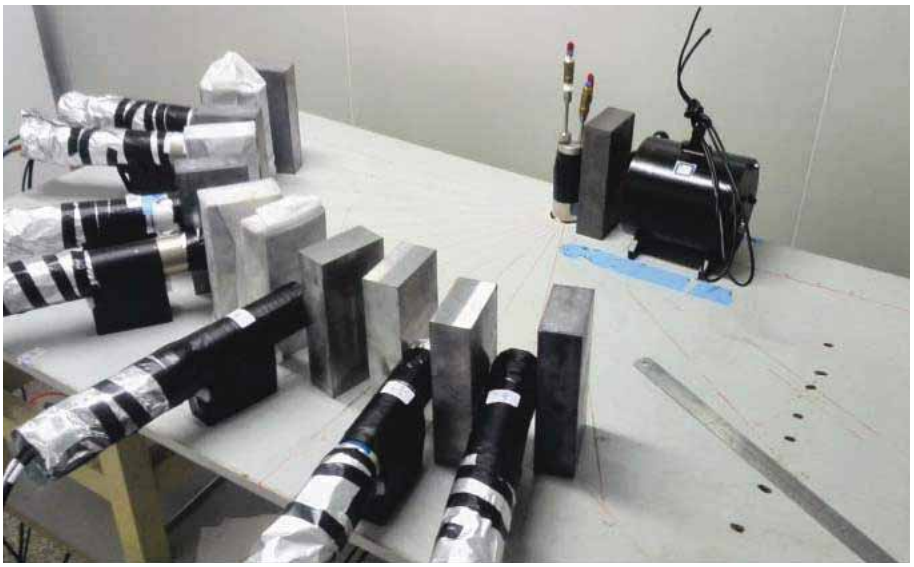

Figure 3.5: Photograph of the electron energy non-linearity setup

MeV and one at 1.275 MeV. After passing through a lead collimator of 9 mm diameter, the γ-rays scatter in the LS sample, which is held in a cylindrical silica cup of 5 cm diameter and height. The light generated by the recoil electron is collected by a PMT (XP2020) attached to the LS cup. Seven coincidence detectors are placed at various angles (20°, 30°, 50°, 60°, 80°, 100°, 110°) at 60 cm distance from the LS cup.These coincidence detectors consist of an inorganic crystal scintillator (LaBr) and a PMT (XP2020). The signals acquired simultaneously by all PMTs pass a Fan-In-Fan-Out unit (CAEN N625) before being sent to a trigger board (CAENN405) and a FADC (CAEN N6742). Using an array of PMTs rather than a single PMT mounted to a rotatable arm is reducing the required acquisition time and avoids variations of the PMT response induced by the rotation of the dynode chain in magnetic stray fields.

Preliminary results are expected for late 2015. At the present state, the uncertainty on electron energy non-linearity is estimated to be smaller than 2 %. The results will be used as well in the data analysis of the Daya Bay experiment.

3.3.2 Optical Transparency

Compared with other neutrino experiments, the optical transparency of the LS in JUNO is absolutely crucial. By scaling up the target volume from several hundreds to 20,000 tons, the diameter of the target volume in JUNO will be 35.4 m. If light transmission in the liquid scintillator is too low, scintillation photons from a neutrino interaction in the center of the detector will be absorbed by the liquid itself before reaching the photomultipliers positioned at the verge of the volume.

The light transmission is described by the attenuation length which quantifies the distance over which the original light intensity is reduced to a fraction of $1/e$. This attenuation is due to two kind of processes: Light absorption on organic impurities, in which case the photon can either be fully absorbed or re-emitted, and light scattering off the solvent molecules. In the latter case, light is not lost but merely re-directed

and may still be detected. Several laboratory scale experiments will be conducted to characterize LS samples regarding their transparency: Measurements include the wavelength-dependent attenuation spectrum of LS in relatively short cells (10 cm), precise measurements of the LS attenuation length over large samples (several meters) and independent measurements of the scattering length of LS. Moreover, the fraction of organic impurities of different samples will be determined and the long-term stability of LS samples tested.

3.3.2.1 Characterization of Attenuation Spectrum

The attenuation spectrum of a material corresponds to the fraction of incident radiation absorbed by the sample over a certain thickness as a function of the wavelength of the incident light. The measurement is performed by commercial UV-Vis spectrometers that usually are sensitive to a wavelength range from 190 to 900 nm. These measurements require only a low amount of time and a relatively small amount of LS as typical sample cells contain only 30 ml or less. Therefore, this method is very suitable for the real-time monitoring of solvent or LS samples. Periodic measurements can be used to study the long-term stability of LS samples.

A first characterization of samples can be done based only on the solvent LAB (without adding the fluors). It is found that the resulting UV-Vis spectra vary for LAB samples from different providers. Fig. 3.6 shows the attenuation curves of LAB samples produced by several companies that apply different manufacturing technologies. Substantial divergences are present in the wavelength region below 500 nm which is most important for the propagation of scintillation light.

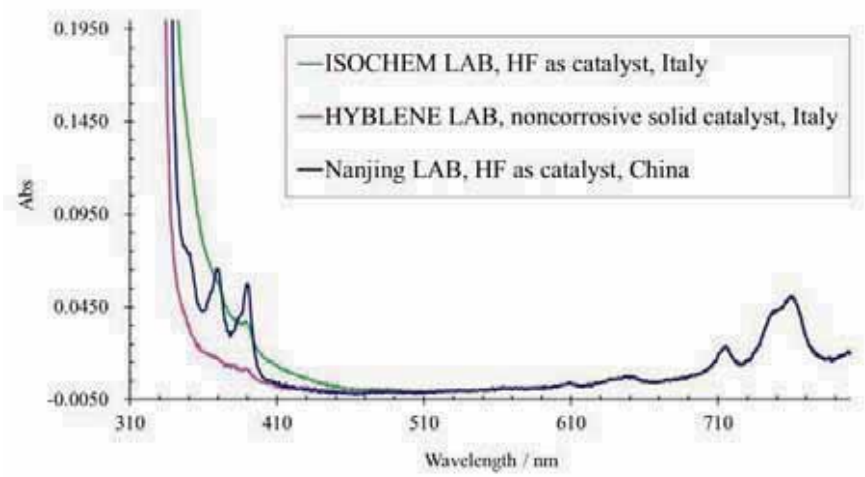

Figure 3.6: The UV-Vis attenuation spectra of LAB from different manufacturers

When loading the solvent with the fluors necessary to form the liquid scintillator, the attenuation spectrum changes. The shift of the absorption band to longer wavelengths is illustrated in Fig. 3.7.

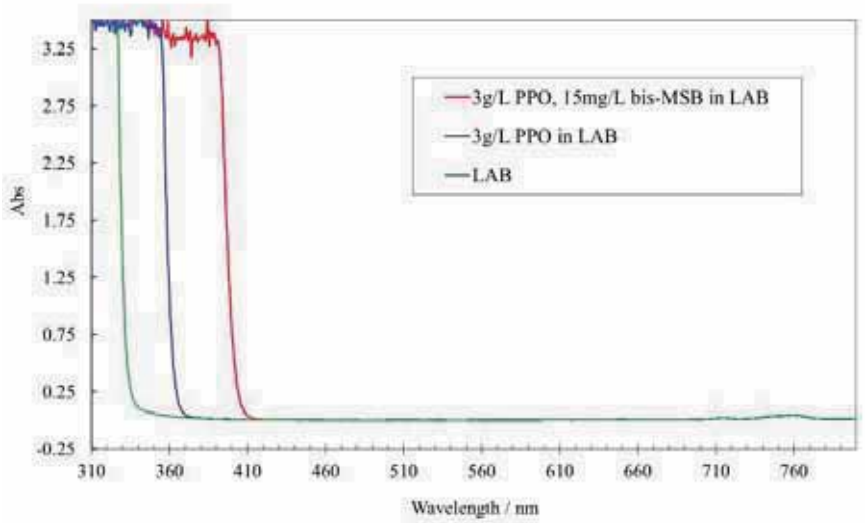

Figure 3.7: The UV-Vis spectra of LAB and LAB-based liquid scintillators

3.3.2.2 Long-range Measurement of Attenuation Length

As stated above, the light intensity generated by particle interactions in the bulk of the LS volume will be attenuated by scattering and absorption before reaching the PMTs. The relation between the intensity $I(d)$ remaining after propagation by a distance d in the LS and the initial light intensity I_0 can be expressed by

$$I(d) = I_0 \exp(-d/\ell_{\text{att}}). \tag{3.2}$$

The length scale ℓ_{att} quantifying the distance after which $I(d)$ is reduced to $1/e$ of the initial value I_0 is the attenuation length.

The accuracy that can be reached by UV-vis spectrometers on the attenuation length is limited if $\ell_{\text{att}} \geq 10\,\text{m}$. This is due to the very small decrease of the light intensity when passing through a sample cell of less than 10 cm in length and thus considerably shorter than the expected attenuation length of the LS ($\ell_{\text{att}} > 20\,\text{m}$). Considering the importance of exact knowledge of ℓ_{att} for light propagation in the large LS volume, dedicated measurements are performed in the wavelength range around 430 nm which corresponds to the emission band of Bis-MSB and at the same time represents the optimum intersection of scintillator transparency and PMT photosensitivity. Figure 3.8 shows the corresponding laboratory device at IHEP and a schematic sketch of the setup. A similar device with an even longer sample cell is currently developed at TU Munich (Germany). Measurements of this kind will be especially valuable to assess the effect of purification techniques on the optical transparency of the LS.

3.3.2.3 Determination of Scattering Lengths

The attenuation of the initial scintillation light can be caused by a variety of processes: Absorption by organic impurities, self-absorption by the fluors (primarily Bis-MSB), Mie scattering off dust or particulates in suspension in the LS, or Rayleigh scattering of the solvent molecules. In general, the relation between the corresponding optical

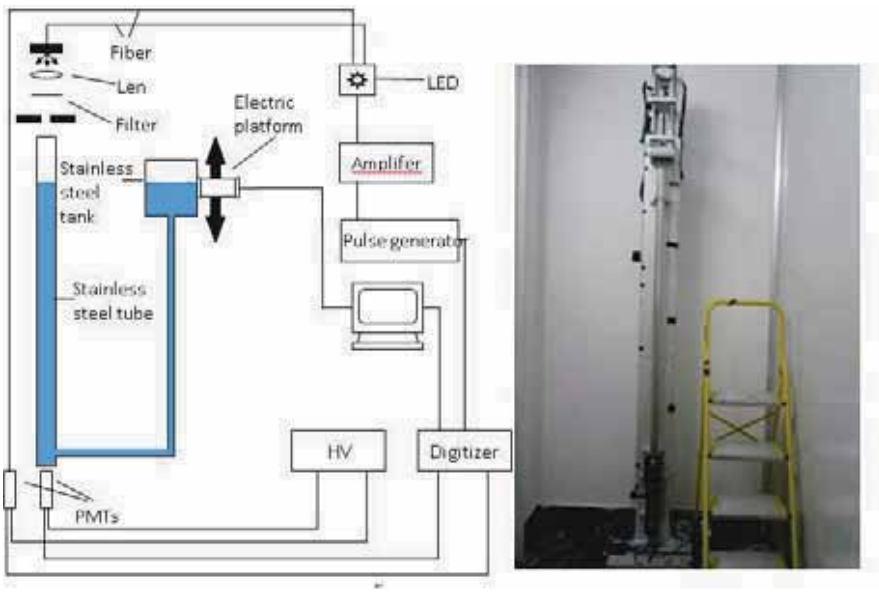

Figure 3.8: Setup for a long-range measurement of the attenuation length

length scales can be given as:

$$\frac{1}{\ell_{\text{att}}} = \frac{1}{\ell_{\text{abs}}} + \frac{1}{\ell_{\text{are}}} + \frac{1}{\ell_{\text{scat}}}, \tag{3.3}$$

where ℓ_{abs} describes the absorption length without re-emission, ℓ_{are} means absorption followed by re-emission, and ℓ_{scat} is the Rayleigh scattering length. Only the light absorbed without re-emission will be fully lost for event reconstruction. All other processes merely divert a photon from its original path so that it can still be detected by a PMT.

For an ideal scintillator without impurities, $\ell_{\text{att}} \approx \ell_{\text{Ray}}$ as Rayleigh scattering is the only irreducible process. In comparison, a conceivable contribution from Mie scattering on dust particles is expected to be negligible because the LS will be virtually dust-free after purification. Absorption-reemission might play a role as the long-wavelength tail of the Bis-MSB absorption band reaches into its emission spectrum centered around 430 nm and might thus be relevant for light propagation.

The physics requirements of JUNO necessitate to come at least close to this ideal state in order to maximize the light output of the target LS. On the other hand, light emitted in a neutrino interaction and scattered while traveling to the PMTs will be deflected from a straight line of sight, influencing both spatial reconstruction and pulse-shaping capabilities of the experiment. Therefore, a precise measurement of the Rayleigh scattering length will allow to determine the ultimate transparency limit for an LS based on the given solvent (LAB in case of JUNO), and at the same time provide valuable input for MC simulations that study the expected detector performance. Moreover, the impact of different purification techniques on the composition of the scintillator can be monitored by studying the combined results of attenuation and scattering lengths measurements (see below).

The Rayleigh scattering length expected for a given material can be calculated

based on the Einstein-Smoluchowski-Cabannes (ESC) formula,

$$\frac{1}{l_{ray}} = \frac{8\pi^3}{3\lambda^4} kT \left[\rho \left(\frac{\partial \epsilon}{\partial \rho} \right)_T \right] \beta_T \left(\frac{6+3\delta}{6-7\delta} \right) \tag{3.4}$$

where λ is the wavelength of scattered light, ρ is the density and ϵ the average dielectric constant of the liquid, k is the Boltzmann constant, T is the temperature, β_T is the isothermal compressibility and δ is the depolarization ratio. Based on the ESC formula, the Rayleigh scattering of LAB can be obtained by measuring the reflectivity, isothermal compressibility, and the depolarization. Comparing to direct measurements of the scattered intensity (see below), this relative measurement can lower the systematic error on the depolarization ratio and directly derive the scattering length as a function of the incident wavelengths λ of the scattered lights. Figure 3.9 shows a schematic drawing of the setup located at Wuhan University.

Complementarily to the described measurements, a direct measurement of the amount of scattered light will be performed at the University of Mainz (Germany). By investigating the dependence of the scattered intensity on the incident wavelength, polarization and scattering angle, contributions from different scattering processes as well as absorption/re-emission can be resolved. On the one hand, this will provide an important cross-check of the Rayleigh scattering length measurement. On the other hand, it will allow to scrutinize purified samples for residual dust particles and organic impurities and, more importantly, to assess the impact of Bis-MSB self-absorption on light propagation. Measurements of this kind have been already performed in Ref. [9].

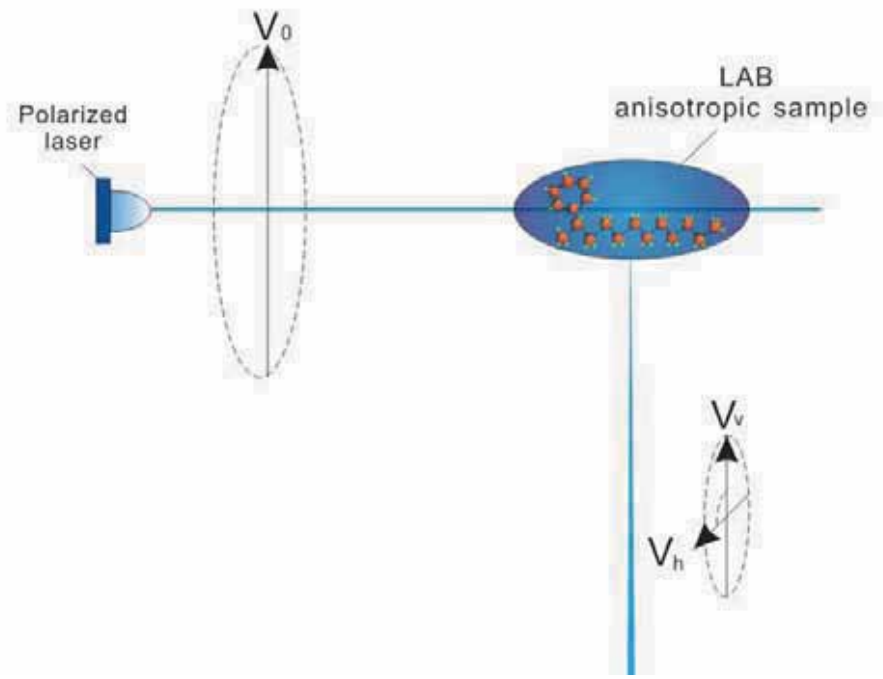

Figure 3.9: Schematic diagram of Rayleigh scattering measuremens

3.3.2.4 Organic Impurities from GC-MS Measurements

Gas chromatography combined with mass spectrometry (GC-MS) is a commonly used technique to analyze the composition of complex organic mixtures. GC-MS analysis combines the high resolution of gas chromatography with the high sensitivity of mass spectrometry. Type and concentration of impurities in LAB as well as the primary LAB components can be resolved and identified by the GC-MS method. The results will provide useful information for improving the purification scheme.

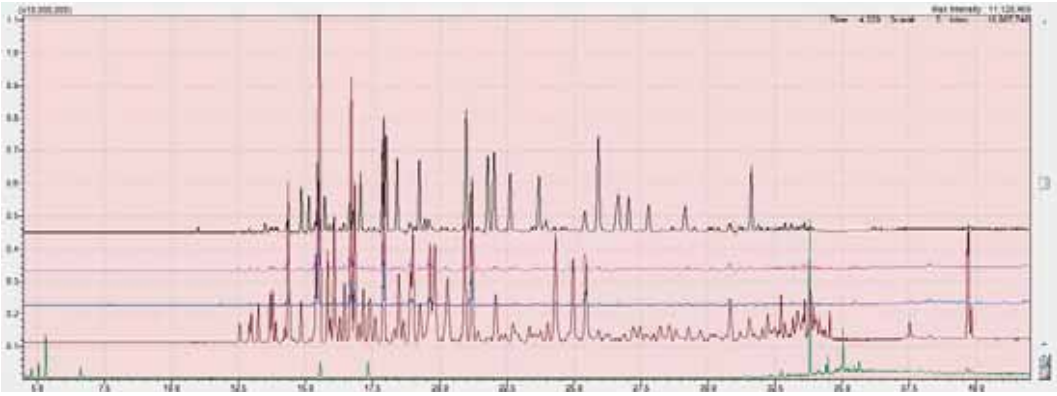

Figure 3.10: Total ion chromatogram of LAB and impurities in LAB from GC-MS measurements

We have analyzed a sample of commercially available LAB produced by the Nanjing LAB factory. In Fig. 3.10, the black curve indicates the components of LAB. The remaining curves stem from the impurities. The result suggests that

1. There are many impurities in LAB, which can be divided into several categories: fluorene, naphathelene derivatives, biphenyl derivatives, diphenyl alkane, and small amounts of alcohol, ketone, and ester.

2. The retention times of impurities coincide with LAB components. The impurities in LAB must be separated and enriched before GC-MS analysis.

3. The resolution of the chromatogram is not satisfying. The analytical conditions of GC-MS must be optimized in order to perform precise qualitative and quantitative analyses.

Therefore, both the LAB pre-treatment methods and instrumental conditions have to be optimized in order to establish the GC-MS method for studying type and level of impurities in LAB samples.

GC-MS is an important addition to the characterization of the LS as it provides data on the chemical composition complementary to the optical measurements. We expect that following the adaptation of the method we will be able to clearly identify the main organic impurities in different brands of LAB. This will allow us to cooperate with the LAB manufacturers in order to achieve an optimization of the chemical purity of the LS raw materials.

3.3.3 Long-term Stability

JUNO is supposed to be in operation for at least 10 years. This poses the question of the long-term stability of the composite liquid and especially of its scintillation and optical properties. A common method of investigation often applied in chemistry are aging tests relying on heating the samples. According to the Van't Hoff equation, the rate of possible deteriorating processes will increase by a factor 2 to 4 for every 10 C° over room temperature (25 °C). Therefore, a 6-months aging test performed at 40 °C is equivalent to five years at 25 °C. The temperature-treated samples will be characterized by their light out, attenuation length and absorption spectrum.

During the tests, the LS samples will be filled into containers of stainless steel. This will allow the performance of a material compatibility test with the LS at the same time. Different types of stainless steel (SS316 or SS304) will be investigated. Some ageing experiments are being conducted on LS. Figure 3.11 shows two 15-liter stainless steel vessels.

Figure 3.11: Laboratory setup for LS aging tests

3.3.4 Selection of Raw Materials

3.3.4.1 Solvent

LAB is a family of organic compounds with the formula $C_6H_5C_nH_{2n+1}$. When used as a detergent, n lies typically between 10 and 16. For JUNO, a specific product selected for $n = 10 - 13$ will be chosen as it shows better optical properties.

In China, the list of LAB manufacturers includes the Nanjing LAB factories of Jinling Petrochemical Company, the Fushun wash & chemical factory of the Fushun Petrochemical Company, and the Jintung Petrochemical Corporation Ltd. The annual output of each factory is very large. Only several months will be needed to produce 20 ktons of LAB for JUNO.

In general, LAB production in China is based on a HF catalyst (HF-acid method). Outside China, an alternative technology based on a non-corrosive solid acid catalyst

(Solid-acid method) is more common. The advantages of the HF acid method are the high conversion efficiency and the long-term stability in operation. The disadvantage is that it generates more by-products because the syntheisizing reaction is more violent than in case of the solid acid method. Therefore, the general expectation is that production by the solid-acid method should result in better optical properties of LAB.

Instead, our investigations based on the attenuation spectra of LAB samples suggest that the method of synthesis is not the critical factor for the resulting optical properties. Figure 3.12 compiles the attenuation spectra of LAB samples produced both by the HF-acid method in the Nanjing LAB factory (specially ordered by optimizing production flow, not commercially available) and by the solid-acid method in an Egyptian plant (Helm AG). The sample from Nanjing shows much lower absorption for the spectral range below 410 nm. As the spectral measurement is not sufficiently sensitive at the most interesting wavelength of 430 nm, the sample was also tested in the long cell at IHEP. Again, the Nanjing sample showed a much longer attenuation length $\ell_{\mathrm{att}} \approx 20\,\mathrm{m}$, while the LAB by Helm featured only $\ell_{\mathrm{att}} \approx 12\,\mathrm{m}$.

Based on these results, it seems that Chinese manufacturers using the HF-acid method should be able to provide LAB of sufficient quality for JUNO as long as the quality of the raw materials is assured and the production flow is optimized. For this, we foresee a cooperation with domestic LAB factories. In addition, we will further investigate samples of LAB from foreign companies.

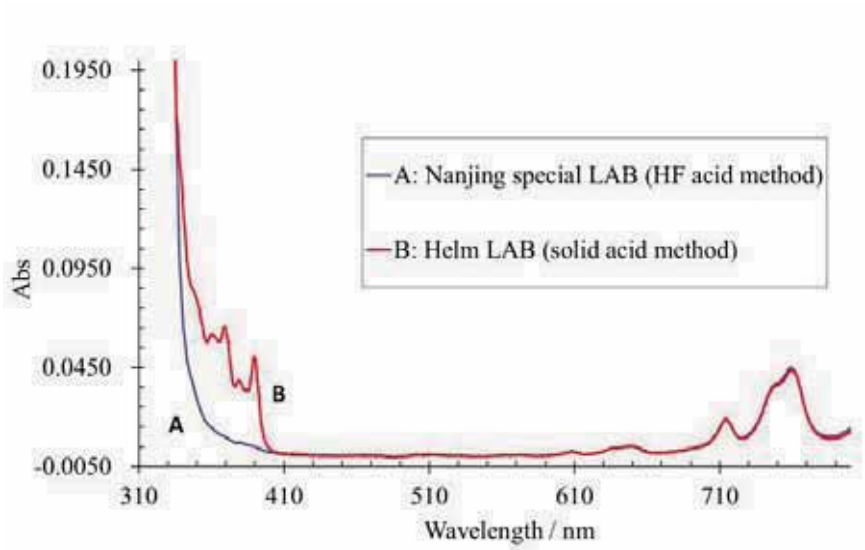

Figure 3.12: UV-Vis attenuation spectra of LAB produced by HF acid method and solid acid method

3.3.4.2 Fluor (PPO) and Wavelength Shifter (bis-MSB)

As described above, a system of two fluors will be used in JUNO: LAB will non-radiatively pass on the excitations to the primary fluor PPO, which will in turn perform a mainly non-radiative transfer to the secondary wavelength shifter Bis-MSB. As a consequence, the effective light emission (including optical propagation effects) will be shifted to 430 nm.

Due to the self-absorption of the fluors, the absorption spectra of the complete LS will differ significantly from pure LAB. This might be further enhanced by optical impurities introduced along with the fluors. Figure 3.13 illustrates the influence of PPO on the absorption spectrum of LS. If PPO concentration is increased from the baseline value of 3 g/L to 10 g/L, an effect induced by the tails of the absorption band of PPO becomes visible that extends up to 460 nm. This clearly demonstrates that the optimum PPO concentration must be balanced between light yield and optical transparency in the 430 nm range, taking re-emission processes into account.

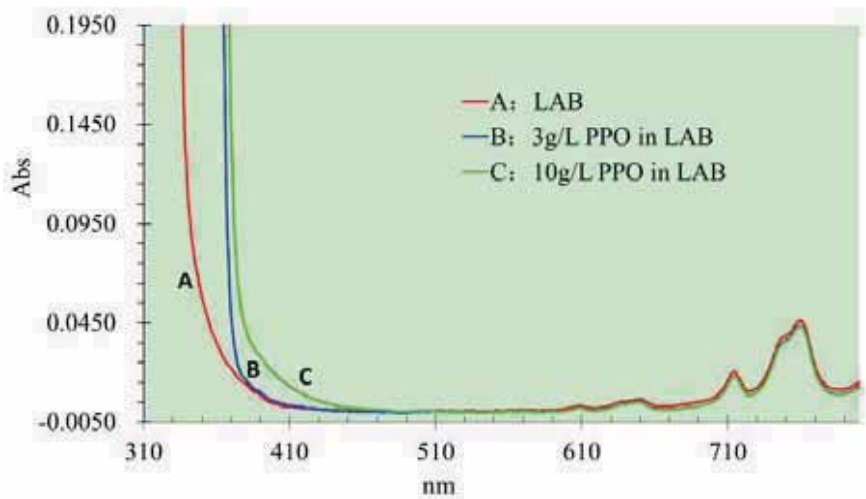

Figure 3.13: UV-Vis attenuation spectra of LAB doped with PPO

Organic impurities introduced with PPO will as well have an impact on attenuation. Figure 3.14 shows the attenuation spectra of LAB samples containing 10 g/L PPO. The PPO was obtained from two different sources: one from rpi (Research Products International Corp), one from the Ukraine. For the latter, spectra for both the original and purified PPO (by Haiso pharmaceutical chemical Co., Ltd., Hubei, China) are shown separately. The positive impact of purification on transparency is clearly visible. The original quality of PPO from rpi seems to be comparable to purified PPO from Ukraine.

A similar or greater impact on the attenuation spectra is expected from the addition of the secondary fluor Bis-MSB. Like in the case of PPO, the chosen concentration has to be optimized and the impact of impurities studied. Two measured attenuation spectra of Bis-MSB in LAB are given in Fig. 3.15. While the same concentration of Bis-MSB was realized and the effective light yield of both solutions is identical, the absorption spectra differ.

3.3.5 Purification Techniques

Beyond the choice of suitable raw materials, optical properties can be further improved by dedicated purification methods. Several methods of purification have been investigated at IHEP, including distillation, column purification, water extraction and

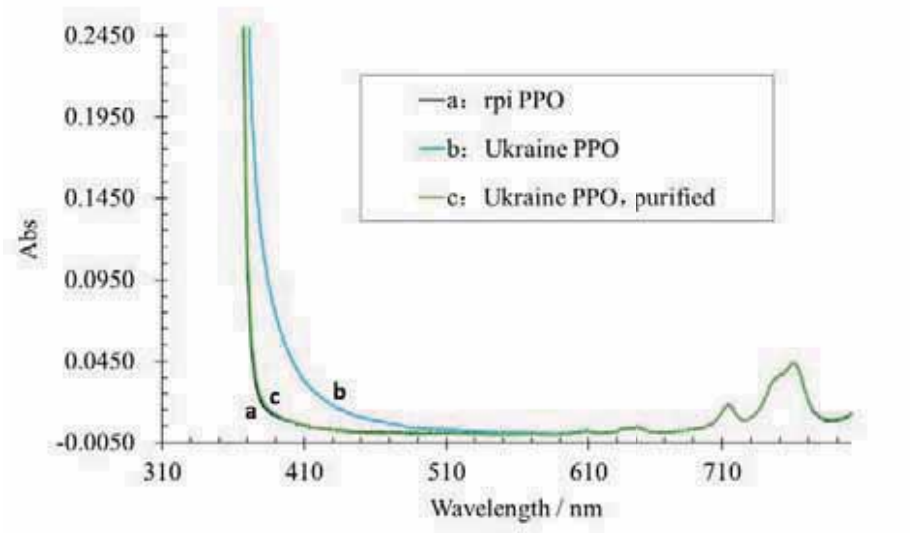

Figure 3.14: UV-vis attenuation spectra of LAB with PPO from selected providers

nitrogen stripping. Figure 3.16 displays a compilation of attenuation spectra of LAB samples by different manufacturers. For comparison, the spectrum of Nanjing LAB after purification in an aluminum column is shown. It clearly shows the best performance in the wavelength region of interest. Similar studies are currently performed at INFN and German institutes.Ref [8]

3.3.5.1 Fractional Distillation of LAB

Distillation relies on the (partial) evaporation of the initial liquid to separate its constituents during vapor condensation. However, simple one-stage distillation usually does not meet the requirements for separating complex mixtures. This is usually achieved by multi-stage or fractional distillation: The technique relies on a heat exchange between upward-streaming vapor and downward-streaming condensate inside the distillation column. By this re-heating, the concentration of volatile components in the upper vapor increases, while less volatile components are enriched in the lower condensate. As the vapor keeps rising and the condensate keeps falling, several equilibrium states between gas and liquid are established along the column. Therefore, distillation occurs in multiple stages. If the fractional column is sufficiently long, an efficient separation of volatile from solid components is achieved.

In a first step, a setup including a single-stage distillation column was built up at IHEP. However, the resulting purification efficiency shown in Fig. 3.17 proved insufficient. Therefore, the setup was upgraded to fractional distillation by the addition of a Vigreux column. This resulted in a substantial improvement due to the increased number of theoretical plates.

Compared to single-stage distillation, fractional distillation is much more efficient in the removal of the impurities causing absorption lines in the region from 330 to 410 nm. However, in case of the IHEP setup, neither method provides a visible improvement in region around 430 nm. Possible explanation comprise:

- The boiling points of the organic impurities influencing absorption at 430 nm are

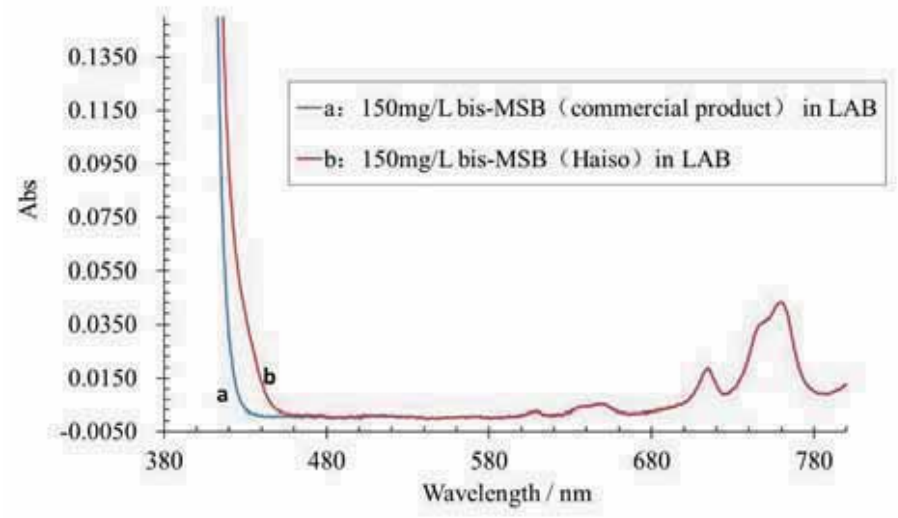

Figure 3.15: UV-vis attenuation spectra of Bis-MSB in LAB solutions

too close to LAB to be removed by distillation.

- New organic impurities are generated by distillation, e.g. by the break-up of LAB molecules.
- UV-vis spectroscopy is not sufficiently accurate to resolve an improvement.

While the unexpected absence of a beneficial affect of distillation in the 430-nm range requires further exploration, this method clearly improves transparency in the wavelength region below 410 nm. However, First results from a similar test setup at INFN Perugia in fact show an increase of the attenuation length in the region of interest.

The Vigreux column proved to be simple and easy to operate for laboratory-scale operations. However, a system based on fractional columns will be necessary for the distillation of large amounts of LAB for JUNO.

3.3.5.2 Purification of LAB by Aluminum Columns

The impact of purification in an aluminum (Al_2O_3) column on the optical properties of LAB has been studied in detail at IHEP. The results show that column chromatography is very effective in removing optical impurities.

The attenuation spectra of Fig. 3.18 clearly demonstrate that column purification does not only remove the impurities featuring absorption in the region from 330 to 410 nm, but also improves transparency in the critical range around 430 nm. These findings have been confirmed by long-range attenuation length measurements. Column purification increased the attenuation length of an LAB sample originally featuring $\ell_{\mathrm{att}} \approx 9\,\mathrm{m}$ to 20 m. Moreover, the most transparent raw product, Nanjing special LAB, featured an attenuation length of 25 m after purification. Provided the manufacturer can produce this high-quality LAB in large quantities, aluminum column purification will be sufficient to obtain a LS meeting the experimental specifications.

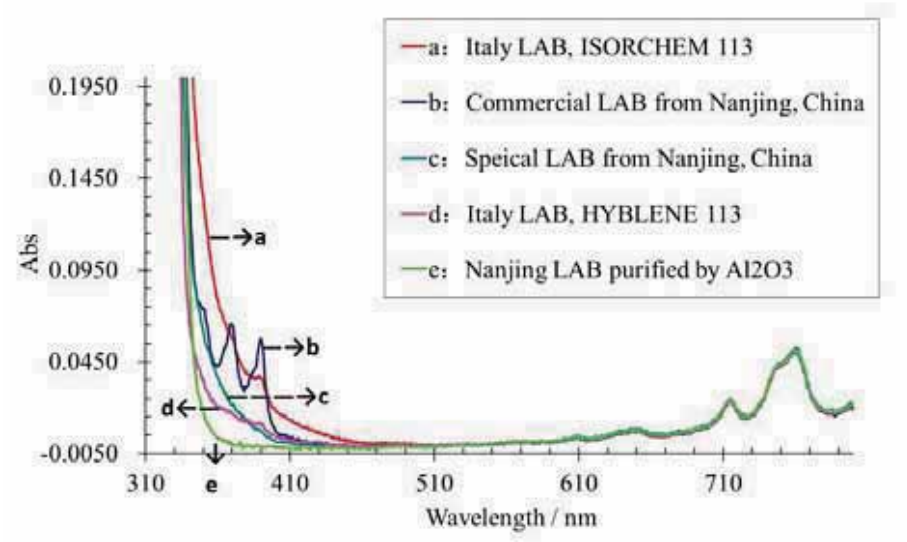

Figure 3.16: UV-vis attenuation spectra of LAB samples from different providers. In case of Nanjing LAB spectra taken before and after purification in an aluminum column are shown.

Further laboratory studies are foreseen for the future:

1. Optimization of the Al_2O_3 column purification
2. Study of alternative column packings, such as a molecular sieve
3. Regeneration of the used Al_2O_3
4. Types and concentration of impurities in LAB which are removed by the Al_2O_3 column.

3.3.5.3 Further Purification Techniques Applied to LS

Distillation cannot completely remove the radioactive contaminants dissolved in LAB. Thus, water extraction and nitrogen stripping are applied after mixing of distilled LAB, PPO and Bis-MSB.

Water extraction utilizes the polarity of water molecules to extract polarized impurities and radioactive free-state metal ions from LAB. The method efficiently removes metallic radionuclides such as ^{238}Th, ^{232}U, ^{210}Bi and ^{40}K.

Gas stripping is used for purging the LS from radioactive gases, mainly ^{85}Kr and ^{39}Ar, oxygen (which will decrease the light yield due to photon quenching) and water (introduced by water extraction).

3.3.5.4 Purification of Fluors

The purification of the fluors has to be carefully considered for the JUNO experiment. In the Daya Bay experiment, purification of PPO was performed in cooperation with

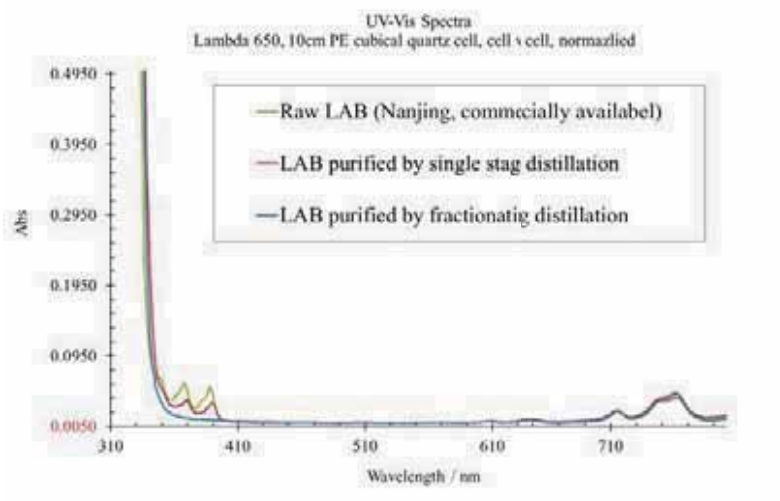

Figure 3.17: UV-Vis spectra of LAB before and after distillation

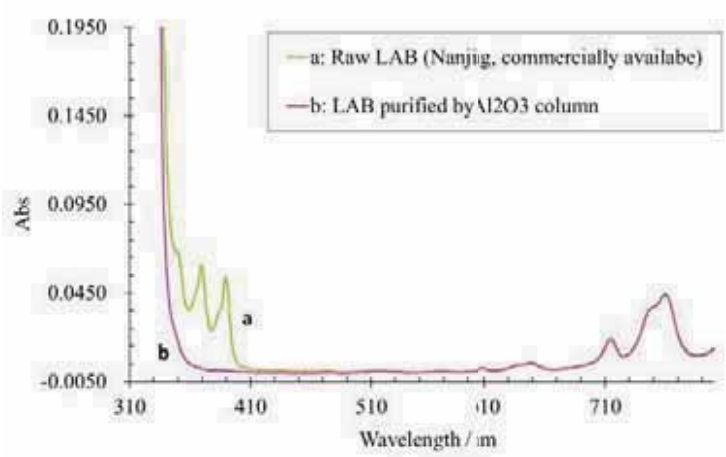

Figure 3.18: UV-Vis spectra of LAB before and after purification in an aluminum column

a domestic chemical company. A domestic producer has also been identified for Bis-MSB: The provided sample meets the requirements concerning light yield, while it will have to be purified to obtain the necessary optical transparency. Moreover, experience from Borexino suggests that the radiopurity of the fluors is an important issue that has to be studied by laboratory experiments.

3.4 Radiopurity Studies

An important prerequisite for the detection of low-energy neutrinos is the radiopurity of the detector and especially the target material, i.e. the LS. The residual contamination aimed for is on the level of the neutrino event rate, so in the order of hundreds of counts per day within the target volume. In case of antineutrino detection, the inverse beta decay coincidence signal somewhat relaxes the requirement on radiopurity as the

Isotope	Antineutrinos	Solar neutrinos
^{232}Th	$\leq 10^{-15}$ g/g	$\leq 10^{-17}$ g/g
^{238}U	$\leq 10^{-15}$ g/g	$\leq 10^{-17}$ g/g
^{40}K	$\leq 10^{-16}$ g/g	$\leq 10^{-18}$ g/g

Table 3.1: Requirements for LS radiopurity concerning uranium, thorium and potassium, listed both for antineutrino and for solar neutrino detection.

fast double signature allows to discriminate most of the single event backgrounds.

Radiopurity levels are usually specified by the concentration of ^{232}Th, ^{238}U and ^{40}K in the LS. The basic requirements for the JUNO LS are listed in Tab. 3.1: The baseline scenario assumes a contamination on the level of 10^{-15} gram of U/Th and 10^{-16} gram of ^{40}K per gram of LS, which will be sufficient for the detection of reactor antineutrinos. More stringent limits have to be met for the detection of solar neutrinos by elastic neutrino-electron scattering. Here, 10^{-17} g/g resp. 10^{-18} g/g should be reached. These requirements are more than a factor 1000 resp. 10 above the current world-record held by the LS of the Borexino experiment. However, due to the scale of the project, achieving these radiopurity levels is a demanding task and will have to be studied and planned in considerate detail.

While members of the natural ^{232}Th and ^{238}U decay chains are the most common contaminants, also other sources of radioactive impurities for the LS have to be taken into account. Moreover, the contamination may arise from different sources that have to be avoided or at least controlled:

- **Dust particles** containing elements of the natural U/Th decay chains as well as radioactive potassium ^{40}K.
- **Radon emanation**, especially the more long-lived ^{222}Rn that is released from building materials (such as granite, brick sand, cement, gypsum, etc.) but also plastics, cables etc.
- The **radioactive noble gases ^{85}Kr and ^{39}Ar** can be introduced as residual contamination of the nitrogen used to create an inert atmosphere in the liquid handling system or by exposure to the ambient air
- **Surface depositions of ^{210}Pb:** ^{222}Rn will settle on surfaces exposed to air and decay to the long-lived isotope ^{210}Pb ($\tau \sim 30$ yrs), which in turn decays into ^{210}Po and ^{210}Bi.
- **^{210}Po** from surface contaminations, distilled water or other unknown sources.
- **Radioimpurities of the fluors**, mostly ^{40}K.
- **Radioactive carbon ^{14}C** intrinsic to the hydrocarbons of the LS.

While the majority of these studies is currently carried out at Chinese institutes, the European collaborators and especially the fraction that is involved in the Borexino experiment has a considerable experience in radio-purification. Several lab-scale studies are foreseen for the immediate future.

3.4.1 Experimental Setups

The aimed-for radiopurity levels of the JUNO specifications are too low to be measured by standard laboratory-scale experiments. Gamma spectrometers can only establish upper limits on the level of contamination. However, the effectiveness of purification techniques can be tested by artificially loading LS samples with greater amounts of radioactive elements and measuring the activity before and after applying a purification step. Moreover, the close relations with the Daya Bay experiment will allow a test of LS radiopurity by filling a large sample of LS (∼20 tons) into one of the subvolumes of a Daya Bay Antineutrino Detector (AD). The AD will both offer the necessary capacity to hold a significant quantity of LS and a suitable low-background environment to test radiopurity to the level of the specifications.Ref [8],Ref [6],Ref [7].

3.4.1.1 Low-background Gamma Spectrometer

A standard laboratory technique to measure level and type of radioactive impurities inside a LS sample are gamma spectrometers. The device currently in use has been employed to measure LS samples before purification. Corresponding to the minimum sensitivity of the setup, only an upper limit can be set on the sample activity, which is smaller than 0.1 Bq/kg. The corresponding concentration of ^{238}U should be smaller than $8.1 \cdot 10^{-9}$ g/g, so 6−7 orders of magnitude above the JUNO specification levels. The activity corresponding to the specified level of 10^{-15} g/g is on the order of 10^{-8} Bq/kg and thus clearly beyond the sensitivity of this and comparable setups.

3.4.1.2 Assays with Loaded Scintillator Samples

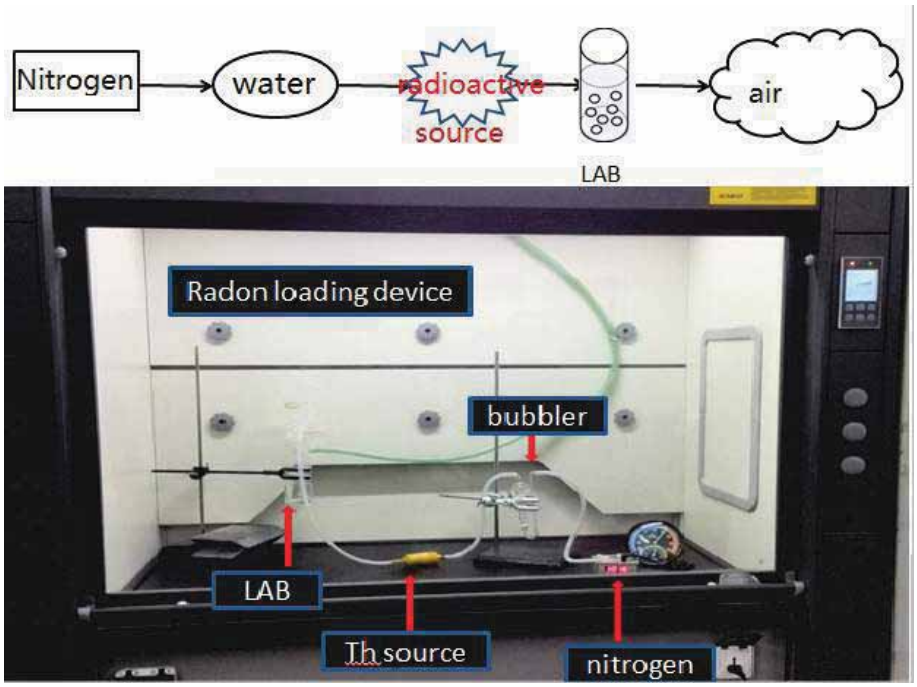

Figure 3.19: Laboratory setup for radon-loading of LS samples

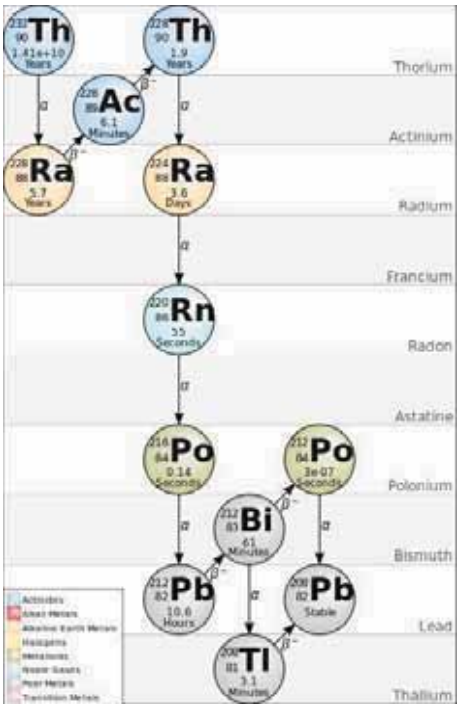

Figure 3.20: The natural decay chain of ^{232}Th

In order to investigate the effect of purification schemes on LS in laboratory experiments, the only solution is an artificial pollution of the samples with radioactivity, bringing the activity to a level accessible by small-scale counting experiments. This is achieved by loading the LS with suitable radioisotopes.

The experience gained in the purification campaigns carried out in Borexino suggests that the radioisotope most difficult to remove from the LS is the long-lived ^{210}Pb. Therefore, it is crucial that purification tests will be carried out using^{212}Pb as a tracer. While easier to tag in lab experiments, its chemical properties correspond to ^{210}Pb. However, direct deposition of lead in LS is difficult as metallic powders will not dissolve in the organic liquid. Instead, the method commonly chosen for loading is the exposition of an LS sample to radon which will in turn decay into lead.

The corresponding setup inside a glove box is shown in Fig. 3.19: A solid ^{232}Th source contained in a small box is used to produce the noble gas ^{220}Rn ($T_{1/2} = 56\,\mathrm{sec}$) by emanation (cf. Fig. 3.20). This box is constantly ventilated by an air pump, creating a stream of radon-enriched air that is lead by a hose to a further container holding the LS sample. As a noble gas, radon is easily dissolved into the LS by purging the sample. It rapidly decays to ^{216}Po and then ^{212}Pb, which is β-unstable with a half-life of $T_{1/2} = 10.6\,\mathrm{h}$ and is thus well-adjusted for performing purification tests. Its daughters ^{212}Bi and ^{212}Po decay in a fast coincidence that provides a further experimental tag.

The activity is measured by the experimental setup depicted in Fig. 3.21. In a light-tight box, a pair of 2” PMTs is placed on both sides of an LS sample cell to detect the light produced by the ^{212}Pb decays. Gamma rays from ambient radioactivity are attenuated by a shielding of low-activity lead bricks. Thus, the background rate for the ^{212}Pb measurement is $0.5\,\mathrm{s}^{-1}$. If the fast coincidence of ^{212}Bi and ^{212}Po is used, the background rate is further reduced to only $2\,\mathrm{d}^{-1}$. A sample waveform of a Bi-Po event

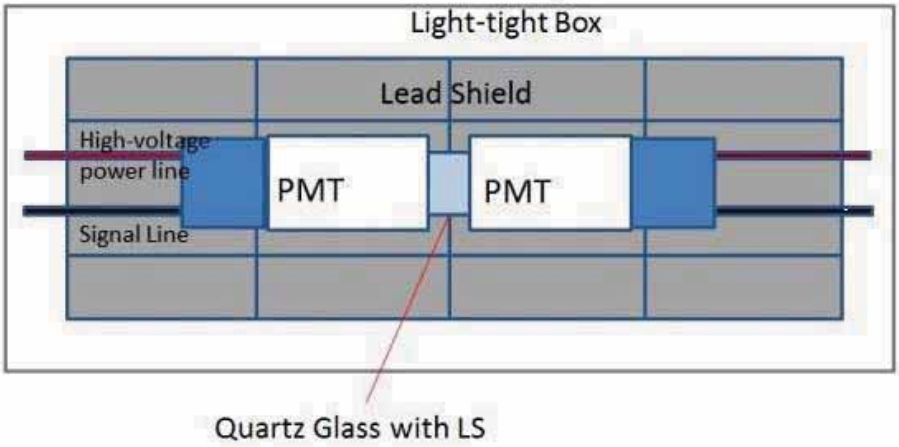

Figure 3.21: Laboratory setup for measuring the efficiency of radio-purification

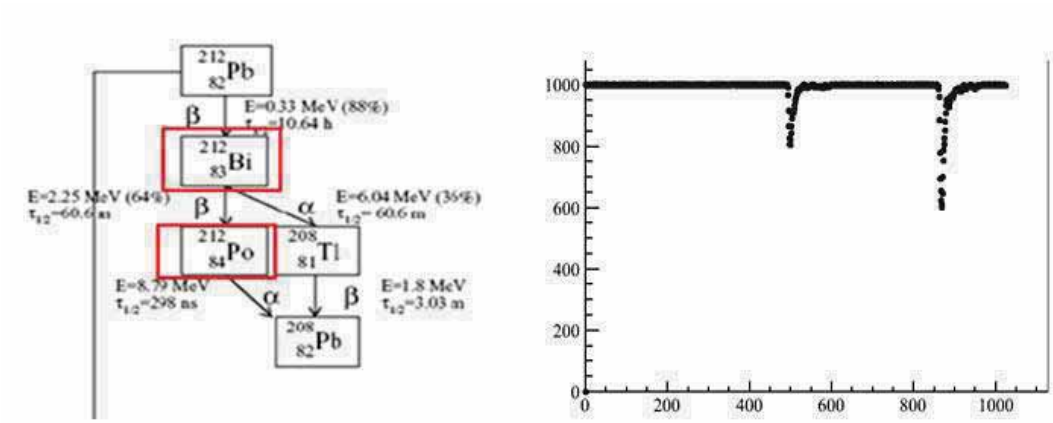

Figure 3.22: Sampel pulse of a fast ^{212}Bi-^{212}Po coincidence.

acquired in this setup is shown in Fig. 3.22.

3.4.1.3 Purification Test with a Daya Bay AD

Once different purification schemes have been tested on the laboratory scale, the test in a medium-sized setup containing several tons of LS will be an important next step to assure that purification techniques are efficient down to the extremely low radiopurity levels of the JUNO specifications. The Antineutrino Detectors (ADs) of the Daya Bay Experiment are ideally suited to do such a study. The low-background conditions provided by the underground labs (the Daya Bay Near Experimental Halls are more than 100 meters underground) as well as the low-background material used in constructing the ADs themselves provide favorable conditions to measure the residual radioactivity of up to 20 tons of LS filled into one of the acrylic volumes of the AD in question.

Moreover, an AD test setup allows the practicability of the purification scheme on the scale of a system able to handle ∼100 liters of LS per hour. For this purpose, a circular system will be set up. After initial filling with an LAB-based LS replacing the

original LS in the AD, purification techniques will be probed in loop mode by monitoring the change in radiopurity levels. This setup will provide important information for the design of a system able to handle the 20,000 tons of LS for the filling of the JUNO detector.

Beyond radiopurity, the filled AD will also provide information on the scintillation and optical properties of the LS. The large-scale setup allows to study the effect of purification on both the light yield and the light attenuation in the scintillator under realistic conditions.

3.4.2 Purification Methods

For the moment, the methods investigated for their purification efficiency concerning radioactive contaminants comprise aluminum columns, distillation, water extraction, and nitrogen stripping (cf. Sec. 3.3.5).

3.4.2.1 Aluminum Columns

Purification in aluminum Al_2O_3 columns proves to be very efficient in removing organic impurities from LAB, resulting in increased transparency. Beyond this, laboratory studies also show a decrease in radioactive impurities by adsorption on Al_2O_3.

The Al_2O_3 best suited for radio-purification was selected by gamma spectroscopy. Results of a comparative study are shown in Table 3.2. The Al_2O_3 featuring the lowest activity levels in ^{238}U, ^{232}Th, and ^{40}K is produced by the Zibo Juteng chemical company (γ-type).

Nuclide	energy (keV)	XP-type Al2O3 (Bq/kg)	γ-type Al2O3 (Bq/kg)	(GY) Al2O3 specific activity (Bq/kg)	~~hamamatsu low background glass~~ (Bq/kg)
Th-232	583.1	3.94	0.07	0.52	2.02
U-238	609.4	3.93	0.16	0.60	5.46
K-40	1460.8	5.49	0.54	4.30	24.14

the lowest

Table 3.2: Comparison of Al_2O_3 radioactivity levels.

The radiopurity assay was based on a ^{220}Rn-loaded LAB sample of 211 ml volume. Measurements based on counting of ^{212}Bi/Po coincidences were performed before and after column purification. A spin-type column was used, with a fill height of 20 cm of Al_2O_3. Based on the ^{212}Bi/Po count rate, a radio-purification efficiency of 99.4 % could be determined. Figure 3.23 shows the corresponding event spectra and count numbers before and after purification.

For the future, an extension of these studies is foreseen at European institutes, especially INFN and JINR Dubna, which will also comprise adsorbants other than aluminum oxide.

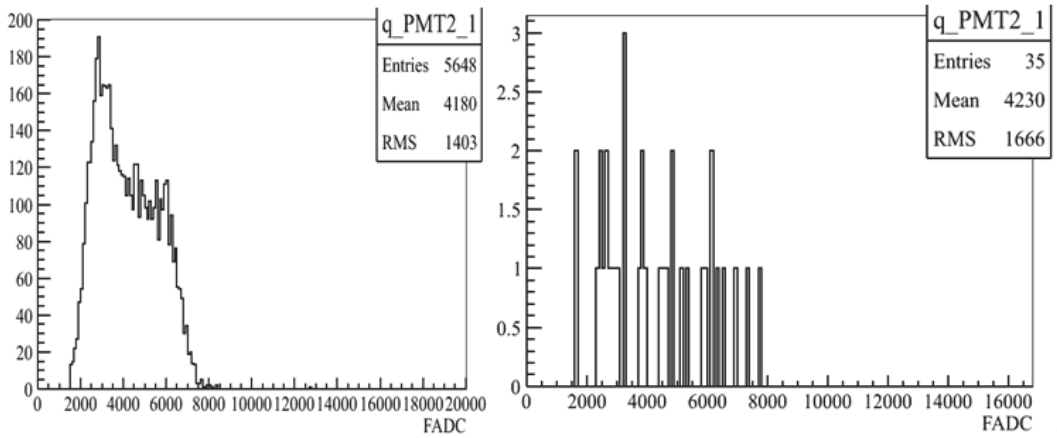

Figure 3.23: Event spectra from ^{212}Bi/Po coincidences acquired before and after column purification.

3.4.2.2 Distillation of LAB

Distillation relies on the difference in boiling points and volatility of the LS components and possible impurities (see above). In particular, excellent efficiency is expected for the removal of radioactive metal ions because of the vast difference in boiling points compared to LS components. However, there are also large differences between the boiling points of the solvent LAB and the solutes PPO and Bis-MSB, which make the application of this technique very demanding once the three components are mixed for forming the LS. Thus, distillation is most suited for a purifications stage before mixing.

The effectiveness of distillation regarding radio-purification has been tested in the laboratory setup depicted in Fig. 3.24. Radioactivity levels of a ^{220}Rn-loaded LAB sample have been determined before and after distillation. Based on ^{212}Bi/Po coincidence counting the efficiency has been determined to 98.4 %. Further tests will be performed after adding a reflux unit that should further improve the purification efficiency.

In the current setup, we find that after distillation with high temperatures or long heating times the LS samples feature a reduced attenuation length, change color and release a strong smell. A possible reason is the chemical break-up of organic impurities by the heating process. Possible solutions are an optimization of the distillation process or a reduction of heat-sensitive impurities in the LAB raw materials. It should be noted that similar laboratory-scale distillation tests at INFN Perugia did not show a degradation of the LS.

In the final large-scale setup for JUNO, vacuum distillation will be used for a reduction of the necessary heating temperature and the related energy consumption. To reduce the energy consumption on the experimental site, the distillation plant could be realized directly at the LAB factory. The preliminary design of the installation comprises multistage plates and a vacuum distillation tower for LAB with a processing capacity of up to 12,000 liters per hour, operated at a temperature of 220 °C. These preliminary working parameters will be refined by further studies carried out at INFN institutes.

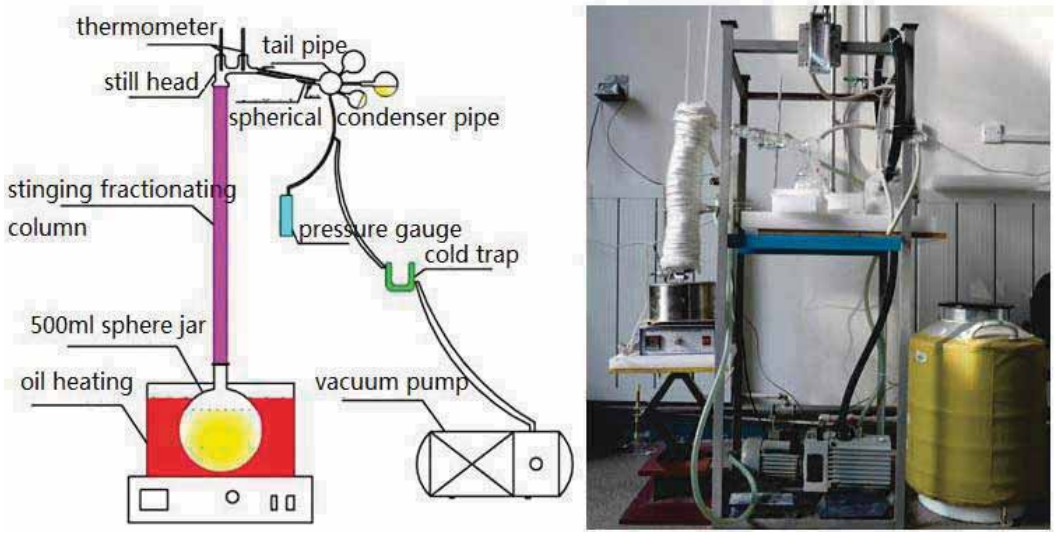

Figure 3.24: Laboratory setup for distillation tests

3.4.2.3 Water Extraction

Purification by water extraction relies on the polarity of water molecules to separate polarized impurities, e.g. free-state ions of radioactive metals, from the non-polar LAB and fluor molecules. Mixing of water and LS is performed in a purification tower that contains a counter-current water extraction column. Pure water is filled at the top while LS enters at the bottom of extraction column. The mixing of the two liquids is supported by a porous filling. As soon as a state of full mixing has been reached, the LS leaves at the top of the column while the waste water is collected by the drainage system at the bottom.

The water extraction method is highly efficient for removing metal ions: Radium is removed at the level of 96.5%. For lead and polonium, the purification efficiency of 82−87 % is somewhat lower as both can form chemical bonds with the organic molecules of the solvent that are fairly stable at room temperature.

3.4.2.4 Nitrogen Stripping

Purging the LS by nitrogen aims both at the removal of dissolved radioactive noble gases (argon, krypton, xenon, and radon) in the liquid and the removal of oxygen, which acts as a quencher lowering the light yield by oxidation of the fluor molecules. Beyond active purification by purging, ultrapure nitrogen will be used for establishing a nitrogen atmosphere or blanket inside the liquid handling system and in the final detector to avoid gas contamination of the LS.

For laboratory purposes, industrial-grade high-purity nitrogen is mostly sufficient. However, the high solubility of noble gases in the LS makes it necessary to add a further purification step for the nitrogen before bringing it in contact with the liquid. For this, high-purity nitrogen of grade 6.0 (99.9999 % pure nitrogen) is passing through a cold trap at liquid argon temperatures. The resulting ultrapure nitrogen can reach radioactive background levels of 10^{-17} g/g, corresponding to 0.36 ppm of ^{39}Ar and 0.16 ppt of ^{85}Kr. Figure 3.25 shows a schematic drawing of a laboratory-scale setup for the

production of ultrapure nitrogen based on an active carbon absorber submerged in a bath of liquid argon. The resulting radiopurity will be tested by GC-MS measurements (Agilent 7890A/5975, cf. Sec. 3.3.2.4).

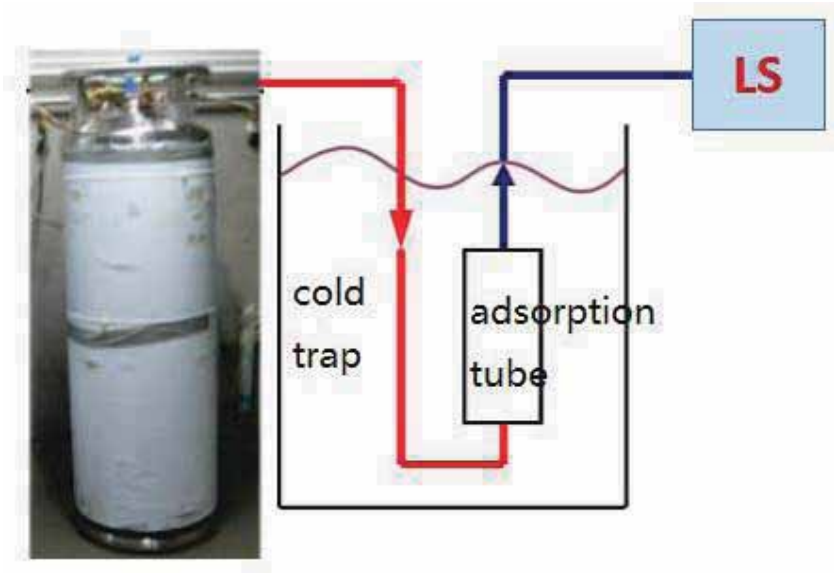

Figure 3.25: Schematic setup of the production unit for ultrapure nitrogen.

3.5 Mass Production of 20 kton LS

Production. The production of 20 kilotons of LS will be achieved in three or four cycles over a period of 1−2 years. Based on the current status of laboratory studies (see above), the solvent LAB will most likely be provided by the company from Nanjing. Criteria for quality control will be developed jointly by IHEP and the company. Similar arrangements will be made for the solutes PPO and Bis-MSB.

Transport. A professional logistics company will take care of the transport of the LAB from the production line at Nanjing to the JUNO experimental site. Suitable transport containers will be manufactured by a company specifically for this purpose, meeting specifications set by IHEP concerning radiopurity, air tightness and material compatibility with LAB.

The on-site LS handling system is depicted in Fig. 3.26. The facilities include:

Storage tanks. Since the LAB will arrive in 3 to 4 batches of 5 kt each, the foreseen storage area comprises about 5,000 square meters, featuring several tanks with a volume of 3 ktons and another set of smaller tanks on the scale of several hundred tons. This includes not only tanks for LAB, but also for white oil and temporal containers needed during unloading. In addition, an area of 30 m^2 is to be reserved for storage of the fluors.

Surface purification plants. Fig. 3.26 depicts the basic scheme for the on-site system of purification plants: The current design mainly relies on an initial purification of

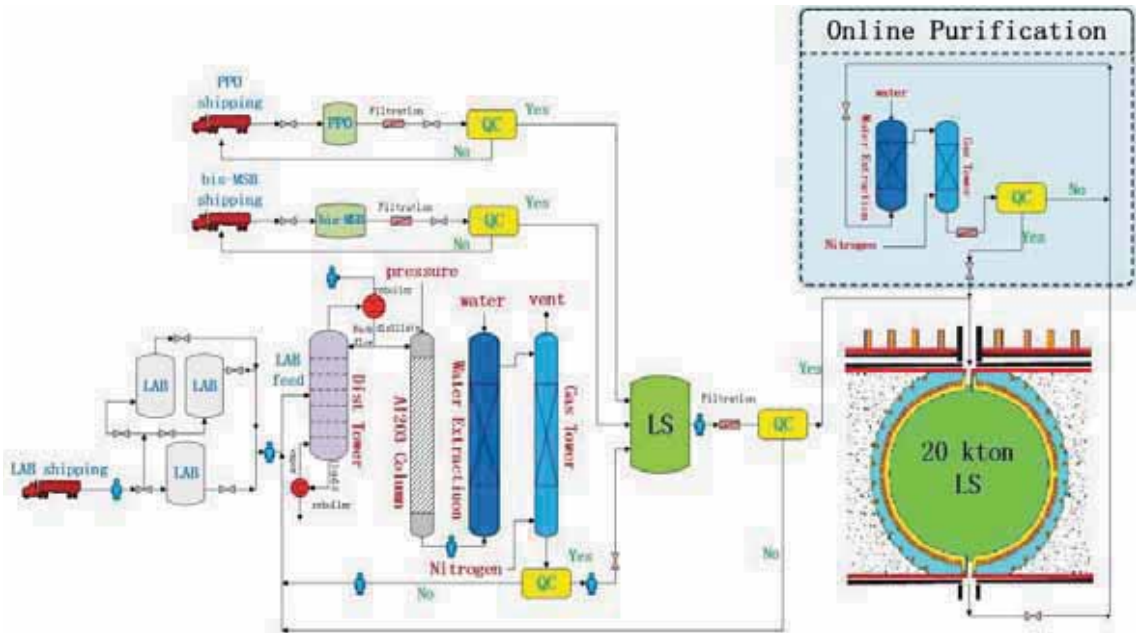

Figure 3.26: Schematic drawing of the system of LS purification plants

the individual LS components (solvents and solutes) before mixing them to obtain the final LS. The major task of purifying LAB is to be performed on surface. The foreseen purification steps include distillation, adsorption in an aluminum oxide column, water extraction and nitrogen purging (cf. sec. 3.4.2).

Assuming a total mass of 20 kt of LS and a period of 200 days reserved for continuous purification and detector filling, the required processing capacity of the purification plants is 100 tons per day. Based on the power consumption of similar (but smaller-scale) purification plants realized for the Borexino, KamLAND and SNO+ experiments, the corresponding power consumption is about 2 MW. In addition, a supply of ultrapure nitrogen on a rate of 200 m^3/h as well as ultrapure water of 6 tons per hour has to be assured. The system will require a surface clean room of 200 m^2 area and 10 m height for its installation. In addition, rooms for the production plants of ultrapure water and nitrogen are needed (30 m^2 each).

LS mixing plants. After purification of the individual components, LS mixing will be performed. A complication arises from the low solubility of Bis-MSB on LAB. To reduce the processing time and assure a constant amount of the fluor in the LS, batches of highly concentrated LAB-Bis-MSB solution (150 mg/l) will be prepared beforehand and then watered down with pure LAB during mixing.

The mixing tanks will be made from organic glass to ensure both the material compatibility of the LS and to allow for a visual inspection of the mixing product. The mixing system will be housed in a room of 300 m^2.

Quality assurance and control. Constant control of the LS leaving the purification and mixing plants is of uttermost importance for the success of JUNO. As the LS is produced in cycles, even a single low-quality batch passing the controls unnoticed and filled into the detector could potentially spoil the high-quality of all LS produced up to this point. Therefore, a careful program of QA/QC measures before and after pu-

rification and mixing has to be developed. Separate teams of operators and inspectors should be formed and be supervised by an on-site manager, following a strict protocol.

Two inspection rooms of a total area of 60 m^2 will house systems for QC, including GC-MS for detection of organic impurities and small-scale experiments to monitor attenuation length and spectrum as well as light out of the LS.

Underground installations. Approved batches of LS will be sent by a pipeline to an underground storage area where it remains until detector filling. The pipe system should allow the flow of LS in both directions and feature high-pressure resistance to allow for a safe transport of the LS. Two storage tanks of 200 tons for LS and white oil are foreseen close to the detector cavern.

Beyond the surface plants for the initial purification of the LS, a secondary system is foreseen underground to perform loop-mode purification of the LS while the experiment is running. This online purification system will rely on water extraction and nitrogen stripping. The system will require two underground halls of 500 m^2 area and 10 m in height. The necessary supply of water, electricity and gas will be roughly equivalent to the requirements of the surface system.

Cleanliness conditions. Ensuring the cleanliness and purity of all materials in contact with the LS and its raw materials will be decisive for meeting the radiopurity requirements of JUNO. All pipes, pumps storage and processing vessels through which the LS passes from arrival on-site until filling of the detector will have to meet the requirements for chemical compatibility, cleanliness of all surfaces and air-tightness.

All surfaces have to be thoroughly cleaned and probably rinsed with LAB before being brought into contact with the LS. Removal of dust on surfaces is mandatory: At an average activity of 200 Bq/kg in U and Th, not more than 10 g of dust are allowed to be dissolved in the total mass of 20 kt of LS. What is more, piping and tank materials will be containing U and Th themselves and thus will potentially emanate radon that will diffuse into the liquid. This process can be mitigated by applying suitable surface liners stopping the diffusion.

The expected radon level in the underground air is about 100 Bq/m^3. Contact of LS and process water to air has to be strictly avoided as the solubility of radon in LS is far greater than in water. To reach this goal, all the liquid handling system must be absolutely air-tight, and an atmosphere of ultrapure nitrogen will be established inside the system.

All surface and underground facilities will be equipped with cameras, fire protection, monitors for oxygen and radon as well as alarm systems for poisonous gases.

3.6 Risk Assessment

The JUNO detector will contain both LS and and mineral oil. Material properties are listed in Table 3.3.

LAB. The main component of LS is linear alkyl benzene (LAB), of which 20 ktons are required. In industry, it is mainly used in the production of detergents. For this, LAB is sulfonated to form linear alkylbenzene sulfonate (LAS), which in turn serves as raw material for washing powders, liquid detergents, pesticide emulsifiers, lubricants and dispersants. It is non-poisonous and odorless. For use in JUNO, the only safety

Properties	LAB	Mineral Oil
Quantity	20 kt	7 kt
Appearance	odorless, colorless, transparent	odorless, colorless, transparent
Flammable	yes	yes
Toxic	no	no
Corrosive	no	no
Chemical formula	$C_6H_5C_nH_{2n+1}$ ($n = 10 - 13$)	C_nH_{2n+2}
Density [g/cm^3]	0.855−0.870	0.815−0.840
Freezing point	-50 °C	
Flash point	135 °C	145 °C
Vapor pressure (20°C)	0.1 mmHg	0.1 mmHg

Table 3.3: Table of material properties

concern is its flammability.

Mineral oil. The buffer volume surrounding the acrylic sphere might be filled with 7,000 tons of mineral oil. The foreseen type is food grade mineral oil 10#. It is a liquid by-product of the distillation of crude oil which is performed during the production of gasoline or other petroleum-based products. Again, the only safety concern is flammability. Mineral oil is widely used in biomedicine, cell cultures, veterinary uses, cosmetics, mechanical, electrical and industrial engineering, food preparation etc.

Due to the flammability of both liquids, the main risk to be taken into account is fire safety. The necessary precautions have to be taken into account during transport, on-site storage, purification and mixing of the LS components as well as during detector operation.

From an experimental point of view, the intactness of the LS poses additional constraints on all operations. Cleanliness and tightness of the liquid handling system have to be considered carefully.

Further risks will be induced by the installation of the LS purification plants and storage tanks in an underground cavern at a depth of 700 m. This will result in complicated hoisting equipment, high-altitude operations, and a need for accurate positioning. Purification underground will pose additional risks because a possible spillage of nitrogen are more serious under these confined conditions. All operations of this kind will have to be carefully planned beforehand.

3.7 Schedule

2013 Realization of laboratory setups for LS properties.

First explorative measurements of LS properties.

Measurement of the depolarization ratio to determine the Rayleigh scattering length.

2014 Realization of laboratory-scale setups for testing different purification method: Low-pressure distillation, aluminum-oxide column, nitrogen stripping and water extraction.

First steps towards the optimization of the purification scheme:

Tests of optical purification: Measurements of light out, attenuation length and spectrum, and water content of the purified LAB.

Tests of radio-purification: Establish the technology for injecting ^{212}Pb and ^{224}Ra in LS samples and setup of the corresponding measurement device to study the effect of purification on radioactive contamination levels.

Start of joint research programs with companies providing LAB.

2015 Design and realization of a purification system.

Final determination of purification parameters.

Start of measurements for electron energy non-linearity.

Design and setup of the quality control devices.

Start of joint research activities with providers of PPO and Bis-MSB.

Conception and setup of devices for quality testing.

2016 Jan−Jun: Setup and testing of purification plants at Daya Bay.

Jul−Dec: Installation and debugging the purification system.

2017 Determination of the final recipe of LS production based on the experimental data and the purification methods.

Final measurement of light out and attenuation length of the LS.

Signing of contracts with the companies providing the purification plants and start of the design.

Signing of contracts with the providers for PPO and Bis-MSB.

Start of the batch production at the end of the year.

Finalization of the design of storage tanks for LAB. Design and build the LS purificaiton hall on the ground.

2018 Signing of all contracts for LAB storage area.

Setup of the large storage tanks before the middle of the year:
3−5 of 3000−1000 m^3 tanks for LAB, LS and white oil

Installation of the purification system until end of the year.

Setup of two 200-ton underground buffer tank.

Setup and testing of the LS QA/QC systems.

2019 Testing of all purification plants.

Setup and testing of ultrapure water and nitrogen plants.

Design and build the LS mixture system.

Production of 8 ktons of LS of sufficient quality for the central detector.

Bibliography

[1] An, F.P. *et al.* (DAYA-BAY), Phys.Rev.Lett. **108**, 171803 (2012), arXiv:1203.1669 .

[2] G. Alimonti *et al.* (Borexino), Nucl. Instrum. Meth. **A600**, 568 (2009), arXiv:0806.2400 [physics].

[3] http://astronu.jinr.ru/wiki/upload/3/36/Seminar_Ianni_15_12_2008.pdf

[4] http://phys.msu.ru/rus/about/virtual/mtg-lomonosov-13/PDF/24.08.07/Morning/Fujikawa.pdf

[5] http://hcpl.knu.ac.kr/detector/internal/Documents/LSc/KamLand_1KiloTon.pdf

[6] http://www.ipp.ca/pdfs/SNOp_chen.pdf

[7] Mike Leung, PhD. Thesis Princeton University

[8] R. Ford, M. Chen, O. Chkvorets, D. Hallman, E. Vazquez-Jauregui, AIP Conf.Proc. **1338**, 183 (2011).

[9] Michael Wurm *et al.*, Rev. Sci. Instrum. **81**, 053301 (2010), arXiv:1004.0811 [physics].

Chapter 4

Veto Detector

4.1 Experiment Requirements

The main goal of JUNO is to determine the neutrino mass hierarchy, which is one of the most important unsolved problems related to neutrinos.

The neutrinos are detected via the inverse beta decay by measuring the correlated positron and neutron signals. With a careful design of the detector, the neutrino spectrum can be measured precisely, and we are looking for the distortion of the spectrum for the sign of neutrino mass ordering. Compared to the small number of signal events (60/day), the number of background events is still very high due to the large volume of detector (20 kton). The cosmic ray muon induced backgrounds are the main backgrounds and they are hard to remove. The cosmic ray generated backgrounds are:

1. ^{9}Li/^{8}He background from muon spallation and muon shower particles.

2. Fast neutron background in the detector from muon induced high energy neutrons.

The cosmic ray induced backgrounds also effect the study of the diffuse supernova neutrino flux.

In order to reduce the experimental backgrounds, the neutrino detector must be placed in deep underground and a veto system is used to tag muons. The muons should be detected with high efficiency for the purpose of background reduction. This chapter is mainly about research and design of the veto system.

Due to the strict requirements on background suppression, larger overburden of rocks on top of the detector is needed to reduce the cosmic ray muon flux. The experiment is located at a site of about 53 km equal distance to the Yangjiang and Taishan nuclear power plants. The height of the mountains is 270 meters and the experimental hall is located underground at the depth of 460 meters. Therefore, there is about 700-meter rock on top of the experimental hall. Muon rate is estimated at about 0.003 Hz/m^2 and the average muon energy at about 214 GeV from simulation. The cosmic ray muon flux is reduced by ~60000 times compared to that at the ground surface. The remaining energetic cosmic ray muons can still produce a large number of neutrons in the rocks and other detector materials surrounding the central detector. These neutrons can produce fast neutron background in the central detector which mimics the inverse beta decay signal. This kind of background cannot be ignored. In order to shield the neutrons and the natural radioactivities from the surrounding rocks, at least 2 meters of water surrounding the central detector is needed. The water is effective for

shielding against neutrons and gamma (Fig. 4.1). And when being instrumented with photomultiplier tubes (PMTs), the water pool can serve as a water Cherenkov detector to tag muons. The Daya Bay experiment shows that the veto system utilizing water Cherenkov detector can be very successful [1]. From simulation, muons with relatively long track in the detector can be detected with very high efficiency, and the undetected muons are mainly of short track lengths, which would induce less background because they are relatively away from central detector. Based on the Daya Bay experimental results (fast neutron background about ~0.2%), if the water shield thickness is at least 2.5 meters in JUNO, fast neutron background to signal ratio is ~0.3%, after taking into consideration the large detector volume and geometry effects.

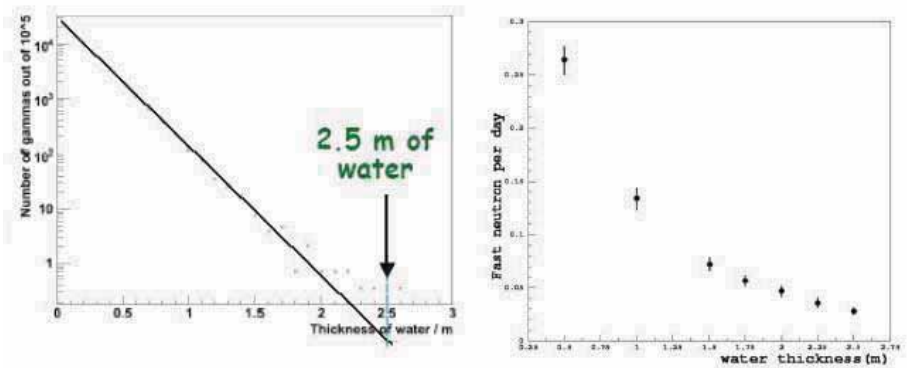

Figure 4.1: Left: Gamma attenuation vs thickness of water shield; Right: Neutron attenuation vs thickness of water shield.

Another background is produced from ^{9}Li/^{8}He resulting from muon spallation in the scintillator and muon shower particles. The beta-n decay of ^{9}Li/^{8}He would mimic inverse beta events. This kind of background can not be reduced from increasing the thickness of the water shield. The number of ^{9}Li/^{8}He background events is estimated to be ~80/day. Their existence would greatly reduce JUNO's capability to determine the neutrino mass hierarchy. To reduced the ^{9}Li/^{8}He background, we need precise muon track information. The ^{9}Li/^{8}He background is reduced by excluding a certain cylindrical region along the muon track within a certain period of time after the muon had passed through the detector. Therefore, the ^{9}Li/^{8}He background reduction depends on precise muon track reconstruction. We will build a tracking detector on top of the water Cherenkov detector to help muon tagging as well as track reconstruction. The top tracker can tag muons and reconstruct muon tracks, independent of the central detector and water Cherenkov detector. The tracking results from the top tracker can be extrapolated to the central detector. Therefore, it can provide an independent measurement of the ^{9}Li/^{8}He background. The muons which pass through the water pool but not the central detector can also produce high energy particles (pions, gamma, neutrons, etc.), which could migrate into the central detector and produce ^{9}Li/^{8}He there. A simple simulation shows that this kind of background which cannot be detected by the central detector is ~1.2/day. A top tracker covering a large area can help directly measure such background. Through optimization of the top detector area and its layout, the detector placed at the top with a long strip structure provides better results. This configuration can identify up to 1/4 of this kind of background, which

would be helpful for the study of such background. It can also be used to measure the rock neutron related background. Also the top tracker and water Cherenkov detector can help identify multi-muon events for the central detector to reduce the ^{9}Li/^{8}He background.

4.2 Detector Design

The JUNO veto system is shown in Fig. 4.2. The system consists of the following components:

1. Water Cherenkov detector system, a pool filled with purified water and instrumented with PMTs. When energetic muons pass through the water, they can produce Cherenkov light. The Cherenkov photons can be detected by PMTs. The arrangements of the PMTs as well as the number of PMTs needed in the water pool is currently under study to facilitate the high efficiency detection of muons as well as good muon track reconstruction. One of the options is to have the water pool surface and central detector outer surface covered with reflective Tyvek to increase the light detection by PMTs without using a large number of PMTs.

2. Water circulation system. There will be 20000-30000 tons of water in the pool depending on the different central detector designs. This system will include a water production system on the ground and a purification/circulation system underground in the experimental hall.

3. Top tracker system. It can provide independent muon information to help muon tagging and track reconstruction. The OPERA top tracker are going to be transported and installed in JUNO.

4. Geomagnetic field shielding system. Though small, the Earth's magnetic filed can affect the performance of PMTs. Either compensation coils or magnetic shields will be used to reduce the effect on PMTs.

5. Mechanical system. The system includes top tracker support structure, water pool PMT support structure as well as a light and air tight cover for the water pool.

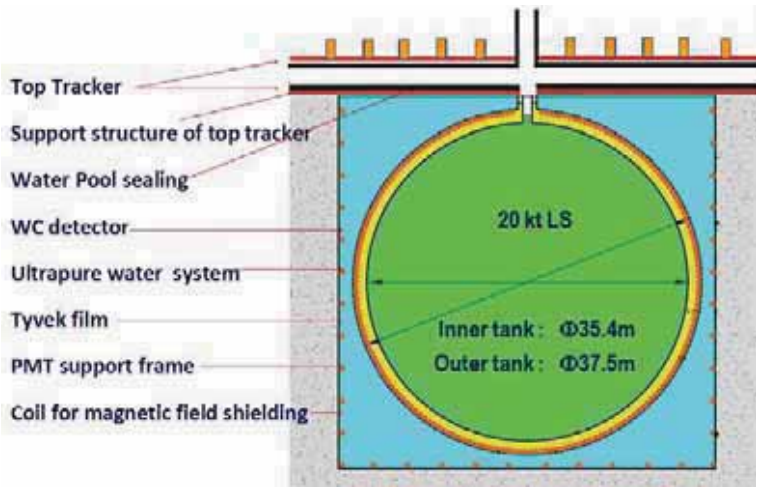

Figure 4.2: Veto systems of JUNO.

4.2.1 The Central Detector as a Muon Tracker

The large liquid scintillator central detector itself is one of the most important muon trackers in the veto system. The muon rate for the central detector is about 3 Hz due to 700-meter rock overburden above. A minimum-ionizing muon deposits about 2 MeV cm^2/g. On average, a muon will pass through 23 m of LAB based liquid scintillator (density of about 0.85 g/cm^3) inside of the central detector, resulting in about 3.9 GeV energy deposition.

A muon generates Cherenkov photons and scintillation photons along its track in the detector. The Cherenkov photons are emitted in a cone with an opening angle $\theta = \cos^{-1}(1/n)$ relative to the muon track trajectory, where n is the index of refraction for liquid scintillator ≈ 1.45. Although the scintillation photons are emitted isotropically, the path for the fastest photon arriving at any PMT follows the same angle as that of the Chrenkov light angle θ when the velocity of the muon is nearly the speed of light. Based on the earliest hit time from each PMT, it is straightforward to reconstruct the muon track. Such a method, called the "Fastest-Light" muon reconstruction, has been proved to be very successful in reconstructing more than 99% of the non-showering muons in the KamLAND experiment. Based a preliminary muon tracking study on the simulated JUNO muon tracks, the bias of this method on the zenith angle is less than 5° and the distance to the detector center bias is less than 20 cm. Although the current study has not considered many real detector effects, such as the resolution of PMT transition time, given the much better energy resolution and comparable or better PMT transition time resolution for JUNO detector compared with KamLAND, the fitting quality is expected to be further improved.

However, the fitting quality of this algorithm becomes worse for the corner clipping muons, which are close to the edge of the detector. And more importantly, this reconstruciton method is also not appropriate for multiple muons or showering muons inside the detector, which is estimated to be about 10-20% of all muons. Since the muon rate for the JUNO central detector is about 10 times higher than that of the KamLAND detector, it is not acceptable to veto the whole detector for a few ms, which will significant reduce the detector live time. In order to reduce the ^{9}Li/^{8}He background introduced by those muons, we have to rely on the other veto system, such as the water Cherekov detector and the top tracker to track those muons.

4.2.2 Water Cherenkov Detector

PMTs are placed in the water pool to tag cosmic ray muons by detecting water Cherenkov light that is produced. The number of photons produced is proportional to the muon track length in the water. Due to the limited thickness of water as well as the presence of the central detector, the majority of the muon tracks going through the water pool are not very long. Therefore, a large photo-coverage in the water pool is desired to detect muons with high efficiency. For the purpose of tagging muon, normally the pool surface would be covered with high reflectivity Tyvek film to help collect the photons without using a large number of PMTs. Based on the experience of the Daya Bay experiment and with Geant4 for simulation, muon detection efficiency is about 98% in (Fig. 4.4) by using 1600 8 inch PMTs with at least 2.5 meter thickness of water in the pool, if we can keep the noise level as low as that of the Daya Bay experiment. The long track muons can be detected with extremely high efficiency, as

shown in Fig. 4.3. Since the central detector size is larger than that of the Daya Bay detector, the large surface area of stainless steel tank might have a big effect on light transmission. We carried out a simulation and found that there is no major impact on detector performance if the surface of the steel tank is covered with reflective Tyvek.

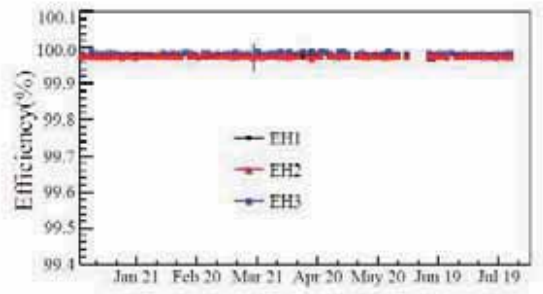

Figure 4.3: Detection efficiency (vs time) for long track muons going through antineutrino detector of Daya Bay.

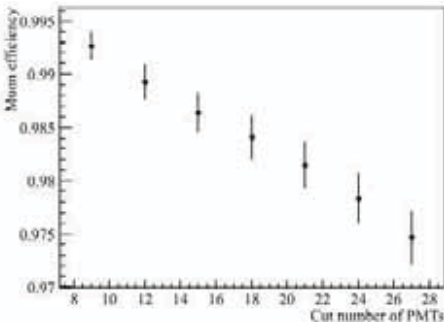

Figure 4.4: Muon detection efficiency vs threshold in number of PMT (1600 PMTs, with a number of PMTs threshold at 20, the efficiency is larger than 97%).

The challenge for the JUNO water Cherenkov detector is that we not only need to tag the muon with high efficiency but also want to reconstruct the tracks of those muons. Ideally full photo-coverage on the water pool surface would be the best choice. Yet the budget constraint limit the number of PMTs available for the water pool. Considering the directional nature of the Cherenkov light and that all muons are coming from outside, it would be natural to have PMTs installed on the central detector. Only few clipping muons at certain particular incident angles would not have direct photons projected on the central detector if not utilizing reflective water pool surface. Some of these clipping muons would be detected by the top tracker. Most of these clipping muons are further away from central detector (> 2 m) which would less likely to produce cosmogenic backgrounds in the central detector. The possibilities of different configurations of the central detector as well as the uncertainty to utilize the outer surface of the central detector, require careful study on PMT arrangements, placement as well as the number of PMTs in the water pool. Large photo coverage enhances the muon detection but also drives the cost high. Therefore, it needs study

of utilizing larger size PMTs or wavelength shifting plates around the PMTs as done in the Super-Kamiokande experiment [2] and find the optimal solution.

Since the muon track reconstruction is important for ^{9}Li/^{8}He background reduction, we would consider to increase the water pool muon track reconstruction capability for the purpose of background reduction. For JUNO, the shower muons will induce non-negligible dead time if the central detector can't reconstruct the shower muon tracks due to detector saturation. If the water Cherenkov detector can help reconstruct those muon tracks, it would reduce the central detector dead time. Reflective surfaces can enhance the Cherenkov photon detection, and therefore help tag muons. But the reflection would smear out the position information. We can use more PMTs to build optically segmented water Cherenkov detectors to improve muon reconstruction resolution. But these segmented detectors could normally provide only one point along the muon track, therefore it might need to have multiple layers of these kind of detectors installed to reconstruct the muon tracks, which would pose engineering as well as installation challenges. In the mean time, developing better algorithms for track reconstruction utilizing both the PMT charge and timing information would be useful. For this purpose, a better water pool PMT calibration system is essential to not only calibrate the PMT gains but also the PMT timing. Now, all these options are under study.

The simplest option would be to have a single water Cherenkov detector by installing PMTs on the surface of the water pool. There are other options, such as having multiple layers of PMTs or modular PMT boxes installed. Since there is not much space in the water pool and there will be structures for the central detector in the pool, therefore from the engineering point of view, a simple water Cherenkov detector is desired. A simulation was performed to study the muon reconstruction capability of the simple water Cherenkov detector. PMTs are uniformly distributed on the surface of the water pool as well as the outer surface of the central detector (Figure 4.5). Of the 2000 PMTs, 200 PMTs are on the top facing toward the outside of the pool, 200 PMTs are at the bottom and 800 PMTs are on the barrel all facing inward. Another 800 PMTs are on the outer surface of the central detector. This gives roughly 2.5 m distance between PMTs. All the surfaces are covered by Tyvek with reflectivity of 95%. Figure 4.6 shows various muon tracks with points on different kinds of surface where the PMTs are installed

Table 4.1: Resolution of reconstructed points on the muon tracks.

	X	Y	Z
Points on the top of the pool			
Resolution	~1.5 m	~1.5 m	
Points on the bottom of the pool			
Resolution	~0.8 m	~0.75 m	
Points on the barrel of the pool			
Resolution	~0.3 m	~0.4 m	~0.8 m
Points on the surface of CD			
Resolution	~0.4 m	~0.4 m	~0.4 m

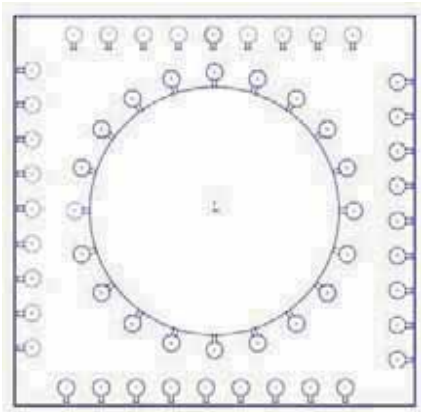

Figure 4.5: Simple water Cherenkov detector option. Uniformed distribution of PMTs. PMTs at the top of water pool are facing outward. PMTs at the bottom and on the barrel are facing inward.

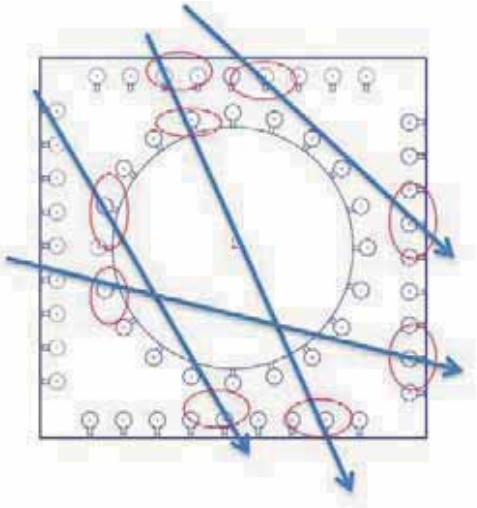

Figure 4.6: Various muon tracks with reconstructed points at pool surface or central detector.

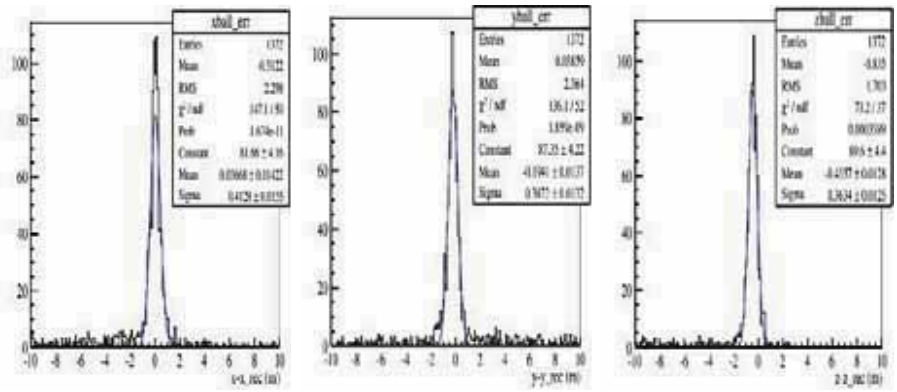

Figure 4.7: Resolution of the reconstructed points on the central detector

The muon tracks are represented by the interceptive points on either the top, barrel, bottom of the pool or on the central detector. The points are obtained using charge center method. The reconstructed points on the barrel and bottom are the exit points of the muon track. And the reconstructed points on the top and central detector are the entry points. Table 4.1 shows the resolution of the reconstructed points at various location. The reconstructed points on the top are poor due to thin water the muons going through and thus having fewer photons for PMTs. The reconstructed points on the barrel are good for X and Y and average with a bias of ~0.5 m for Z, this could be the results of all the tracks are going downward. The reconstructed points are very good on the central detector for all coordinates. It might be possible to use the reconstructed points from top tracker for muons passing through the top of the pool.

It is essential to have good reconstructed muon track in central detector. Though the central detector can be excellent muon tracker when the muon path is close to the center of the central detector, the muon track reconstruction gets worse when the muon is close to edge of the central detector. Therefore, the presence of good reconstructed points from the water Cherenkov detector would definitely help and cross check with the central detector muon track reconstruction. Optimizing the number of PMTs, the PMT arrangement as well as taking into account the PMT hit timing information in reconstruction definitely warrant further study.

Of all the muons, about 10% are multiple muons. For double muons, it was estimated that the central detector could distinguish the muons with distance greater than 4 m. Water Cherenkov detector with good resolution of muon entry points on the central detector has the potential to be able to separate multiple muon tracks by looking for clusters of hit PMTs. This would be helpful to reduce the dead time caused by multiple muons.

4.2.2.1 Tyvek Reflector Film

As proved in the Daya Bay experiment, reflective surface is effective in tagging muons without larger number of PMTs. Tyvek film as a reflective material has the merits of high reflectivity and stable performance, therefore it is widely used in water Cherenkov detectors. The Daya Bay experiment uses Tyvek film as to make reflective surface in the water Cherenkov detector. In JUNO, the Tyvek reflective film could be used to cover the inner wall of the pool and the outer surface of the central detector. The Cherenkov photons produced in the pool can be detected by the PMTs after multiple reflections to improve the detection efficiency. Figure 4.8 shows the process of making reflective Tyvek. Tyvek pieces with a width of 1 meter and short lengths can be welded together to form a larger piece of reflector for large detector installation. The performance of various Tyvek reflective films is shown in Fig. 4.9.

The reflectivity of the Tyvek depends on the thickness of Tyvek. The Daya Bay experiment uses two layers of thick Tyvek (1082 D) with PE between them to form a multi-layer Tyvek. The reflectivity of the multilayer Tyvek is shown as the red points in Fig. 4.9. The reflectivity is >95% when the wavelength > 300 nm.

Figure 4.8: The process of making the tyvek reflector.

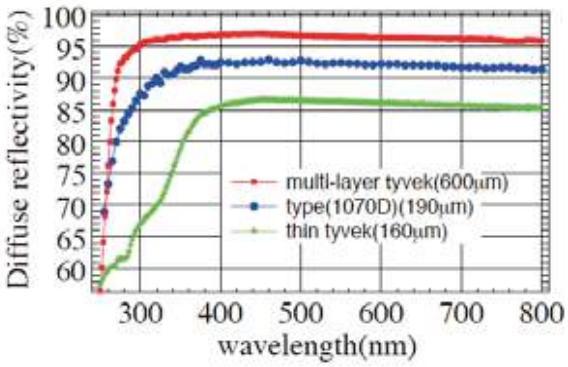

Figure 4.9: Reflectivity of different type Tyvek films .

4.2.2.2 Calibration system

The gain and the timing calibration of the PMTs will be monitored by a LED system. No radioactive sources will be required. As Fig. 4.10 shows, we will use LED or diffuse ball by LED for the PMT calibration. LED flashing is triggered by pluse generator. The diffuse balls could be put at differnt positions of water pool. So every PMT can receive the photons from diffuse ball. PMTs gain and timing calibration could be done once a week.

4.2.3 Top Tracker

The JUNO cosmic muon tracker will help enormously to evaluate the contamination of the cosmogenic background to the signal. The OPERA detector has to be dismounted soon and the OPERA TT [3]($\sim$ 4.5M EUR) will become available by mid–2016. It will be placed on top of the JUNO water Cherenkov detector to be used as a cosmic muon tracker.

Figure 4.10: LED and diffuse ball for PMT calibration.

4.2.3.1 OPERA Target Tracker

The TT is a plastic scintillating detector which had several critical roles in OPERA: it was used to trigger the neutrino events, to identify the brick in which the neutrino interaction took place and to reconstruct muons therefore reducing the Charm background. Its performances well met the expectations: only limited aging was observed over the 2007 - 2012 data taking period, and the detector understanding was well demonstrated by showing very good data/MC agreement in particular on the muon identification and energy reconstruction [4].

The TT is composed of 62 walls with a sensitive area of 6.7×6.7 m^2. Each wall is formed by four vertical (x) and four horizontal (y) modules (Fig. 4.11). The TT module is composed of 64 scintillating strips, 6.7 m length and 26.4 mm wide. Each strip is read on both sides by a Hamamatsu 64-channel multi-anode PMT. The total surface which could be covered by the 62 x-y walls is 2783 m^2. All TT walls in OPERA are hanged by the top part of the detector and are thus in vertical position (Fig. 4.12). In the case of JUNO, all TT modules have to be placed in horizontal position, in which case more supportive mechanical structure is needed.

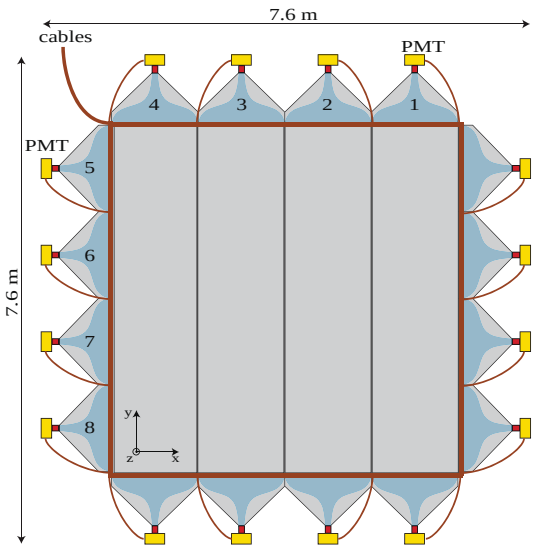

Figure 4.11: Schematic view of a plastic scintillator strip wall.

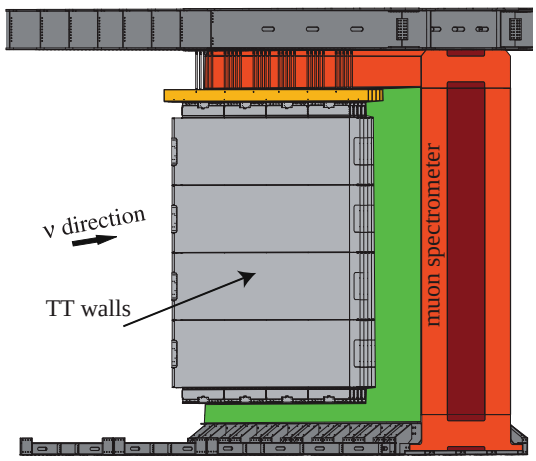

Figure 4.12: Target Tracker walls hanging in between two brick walls inside the OPERA detector.

The particle detection principle used by the TT is depicted by Fig. 4.13. The scintillator strips have been produced by extrusion, with a TiO_2 co-extruded reflective and diffusing coating for better light collection. A long groove running on the whole length

and at the center of the scintillating strips, houses the wavelength shifting (WLS) fiber which is glued inside the groove using a high transparency glue. This technology is very reliable due to the robustness of its components. Delicate elements, like electronics and PMTs are located outside the sensitive area where they are accessible (Fig. 4.14).

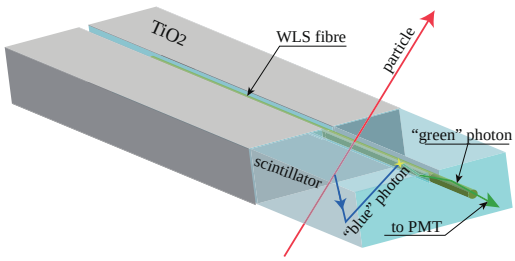

Figure 4.13: Particle detection principle in a scintillating strip.

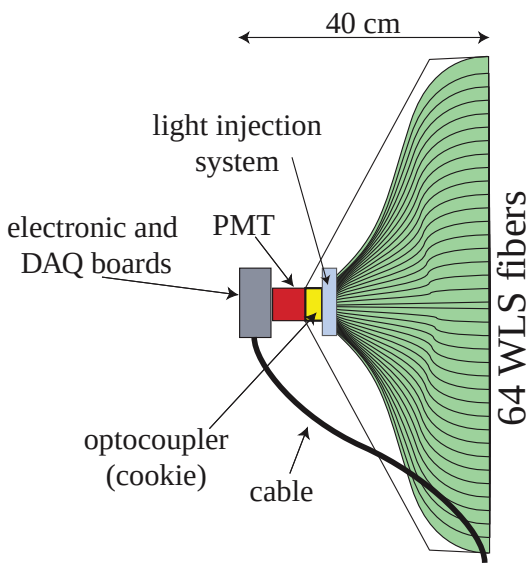

Figure 4.14: Schematic view of an end–cap of a scintillator strip module.

Figure 4.15 presents details about the end-caps of the TT modules hosting all electronics, front end and acquisition. These electronics are composed of:

- a front end card located just behind the multi-anode Hamamatsu PMT, hosting the two OPERA ROC chips (32 channels each, BiCMOS 0.8 microns) [5],
- an acquisition card (DAQ) [6], also hosting an ADC for charge digitization,
- a light injection card located on the DAQ card,
- two LEDs able to inject light at the level of the WLS fibers near the PMT and driven by the light injection card, this system is used to regularly calibrate the detector (PMT gain, stability etc.),
- an ISEG High Voltage module located on the DAQ card.

The TT electronics record the triggered channels and their charge, thanks to the OPERA-ROC chip. A schematic view of this chip is given by Fig. 4.16. Each channel has a low noise variable gain preamplifier that feeds both a trigger and a charge measurement arms. The adjustable gain allows an equalization of all PMT channel gains which can vary from channel to channel by a factor 3. The auto-trigger (lower part) includes a fast shaper followed by a comparator. The trigger decision is provided by the logical "OR" of all 32 comparator outputs, with a threshold set externally. A mask register allows disabling externally any malfunctioning channel. The charge measurement arm (upper part) consists of a slow shaper followed by a Track & Hold buffer. Upon a trigger decision, charges are stored in 2 pF capacitors and the 32

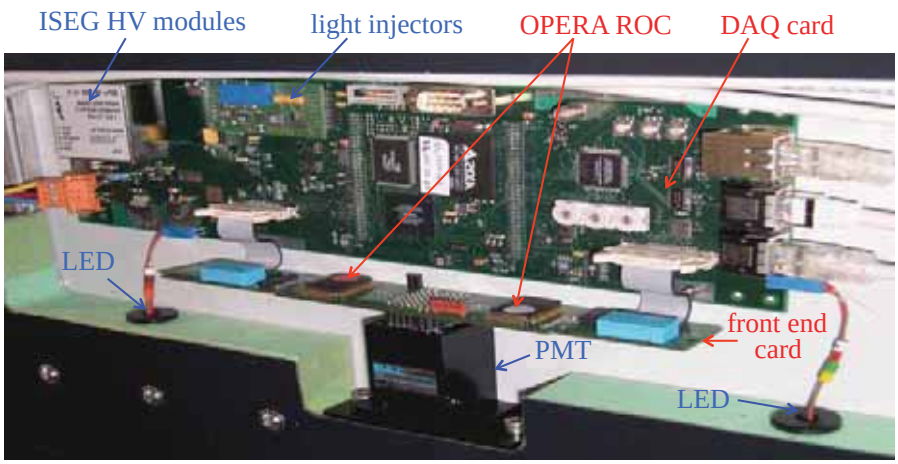

Figure 4.15: TT electronics including DAQ card. All elements in red will be replaced.

channels outputs are readout sequentially at a 5 MHz frequency, in a period of 6.4 μs. All charges are digitized by an external ADC (12–bit AD9220) placed on the DAQ cards.

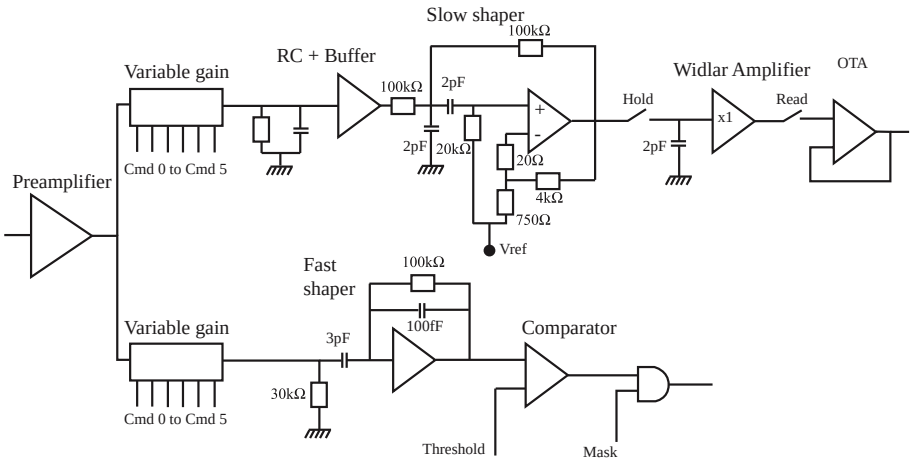

Figure 4.16: Architecture of a single channel of the OPERA–ROC chip.

TT dismounting in Gran Sasso

The TT dismounting in Gran Sasso underground laboratory will start in summer 2015 (first OPERA Super Module) and will end in Spring 2016 (second OPERA Super Module). The OPERA detector dismounting and cost sharing among the funding agencies are defined in a special MoU. The cost of the TT dismounting up to its storage area is part of this MoU and thus it is not considered in the IN2P3 JUNO requests.

All TT modules will be stored in Gran Sasso in 10 containers before sending them to China. The shipping of the containers will be done when storage halls will be ready near the JUNO underground laboratory. This is expected to take place in 2016. In all the cases the TT will not be mounted on top of JUNO detector before 2019. This implies that the TT containers will be stored somewhere for about three years. The best place, in order to avoid big temperature variations and scintillator aging, is the

Gran Sasso underground laboratory. Negotiations are engaged with LNGS on this possibility. If this is not possible, the TT will be temporarily stored in a hall in the surface LNGS laboratory waiting to be shipped to China.

TT in JUNO

This muon tracker, called now Top Tracker (again TT), will be needed in JUNO in order to well study the cosmogenic background production. The most dangerous background is induced by cosmic muons generating ^{9}Li and ^{8}He unstable elements, and fast neutrons, which could fake an IBD interaction inside the central detector. Figure 4.17 presents schematically the most important noise configurations. The first two, (a) and (b), mainly concern ^{9}Li and ^{8}He production directly in the central detector (a) and in the veto water pool (b) while the last one (c) concerns the neutron production in the surrounding rock.

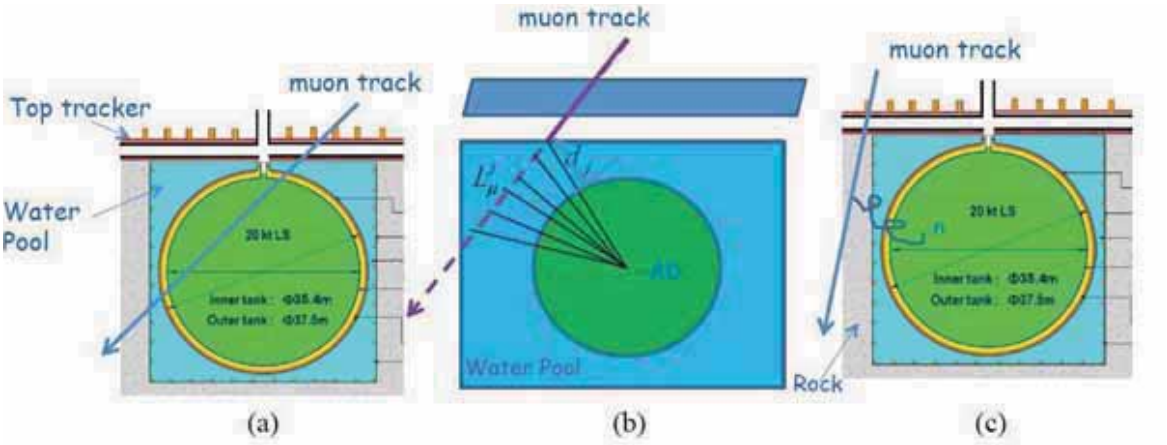

Figure 4.17: Configurations considered for the induced noise.

The surface on the top of the JUNO detector is of the order of 40×40 m^2. The total surface that the TT could cover depends on the number of superimposed $x - y$ layers (composed by consecutive TT walls). In any case it will never be able to cover the entire surface, half of cosmic muons crossing the JUNO detector can pass by the sides. The number of layers will depend on several parameters:

- the minimum statistics needed to well measure the cosmogenic background (^{9}Li and ^{8}He production),
- the muon tracking accuracy needed up to the bottom part of the central detector (of the order of the one induced by the multiple scattering),
- the noise rate reduction using coincidences (affordable by the acquisition system),
- the rate reduction of fake tracks.

First studies show that 3 to 4 layers will be needed that means that the total surface on top of JUNO liquid scintillator detector will be 690 m^2 to 920 m^2, respectively.

The noise rate in JUNO underground laboratory is expected to be significantly higher than that in Gran Sasso. During OPERA operation the noise rate for 1/3 p.e. threshold was of the order of 10 Hz. This low rate was mainly due to the low PMT

dark current (2.5 Hz) and the fact that the TT walls were shielded by the OPERA lead/emulsion bricks. Before the insertion of the bricks the noise rate was of the order of 25 Hz/channel. In JUNO this rate is expected to be significantly higher for several reasons:

- The JUNO overburden is lower (2000 m.w.e.) than for Gran Sasso (4200 m.w.e.) implying more cosmic muons crossing the detector.
- There will be no shielding between the TT walls.
- The radioactivity of the rock, measured by the Daya Bay experiment 200 km away, is expected to be significantly higher than the one observed in the Gran Sasso underground laboratory.
- There will be no concrete on the walls surrounding the JUNO underground laboratory (contrary to the Gran Sasso underground laboratory), concrete that could absorb part of the γ's emitted by the rock.

In the case of 4-layers cover, the configurations of Fig. 4.18 have been considered. The first configuration has the advantage compared to the others of covering the maximum surface of the central detector region. The second one is more representative of all detector configurations and noise measurements could be extrapolated to the total detector top surface. The third configuration is best for rock muon production estimation but is not very representative of the rest of the detector. Finally, as baseline it has been defined the second configuration. In all the cases, the TT has to well cover the chimney region (central region not covered by the veto water Cherenkov) from where radioactive sources will be introduced to calibrate the detector.

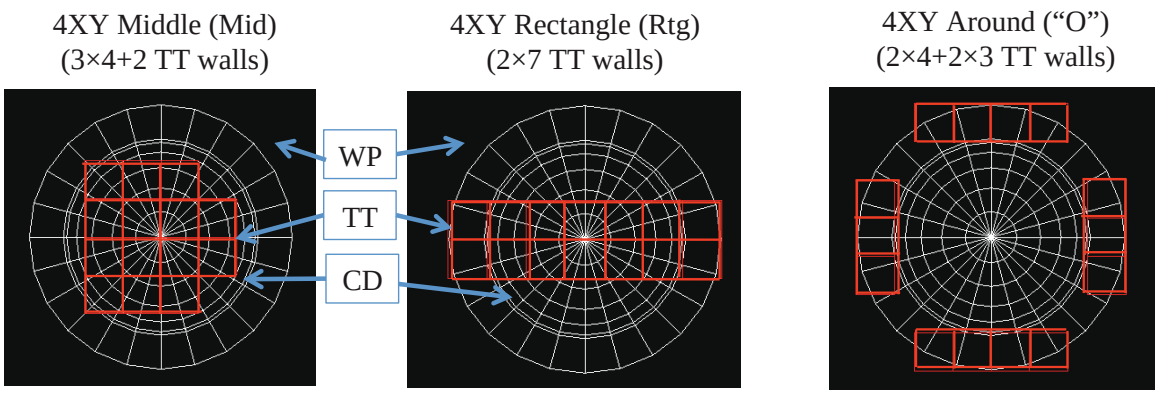

Figure 4.18: Configurations considered for the Top Tracker coverage.

Noise rate estimations

Table 4.2 presents the rock noise rate for one x layer on the top, for one y layer just below and for the case of one $x-y$ coincidence of these two layers ($x-y$ correlated coincidence). For the $x-y$ correlated coincidences the x and y hits must come from the same radioactivity event while for the $x-y$ accidental coincidences come from different events occurring during 200 ns time–window. The slight noise reduction from the x layer to the y one is due to the fact that the top layer shields a bit the layer above. A strong noise rate reduction is observed when an $x-y$ coincidence is required.

For all the cases a threshold of one and two photoelectrons is considered. The results are shown considering no concrete on the JUNO cavern walls and with 10 cm concrete. The presence of concrete would reduce the radioactivity noise by about a factor 4.

Table 4.2: Noise rate for several TT conditions. (a) is under 1 p.e. threshold and (b) is under 2 p.e. threshold. (1)no concrete; (2)10 cm concrete.

Config.	Rate (Hz/m^2),(a)		Rate (Hz/m^2),(b)	
	(1)	(2)	(1)	(2)
$1-x$ layer (top)	6800	1780	2700	710
$1-y$ layer (bottom)	6500	1780	1200	310
$x-y$ layer (correlated)	540	150	29	7
$x-y$ layer (accidentals)	400	29	29	2

The noise rate per channel is not the only parameter to take care during the design of the new TT configuration. The number of $x-y$ layers will mainly be determined by the number of "fake" muons (virtual tracks due to many hits in a time–window of 200 ns) produced by the environmental radioactivity. Table 4.3 presents the "fake" muons' rate estimation considering two and three TT $x-y$ layers. For the case of the two layers, the distance between is considered to be 2 m, while for the case of three layers the third layer is inserted at the middle between the two considered layers. It can be observed that the rate is considerably reduced for the case of three layers compared to the one of only two layers. From this table the case of two layers can be excluded. The rate being of the order of few Hz and less for the case of three layers, the case of four layers initially considered probably will not be necessary. A fourth layer would provide some redundancy in case of inefficiencies due to scintillator aging, dead time or dead zones. It has also to be noted that each "fake" muon will bias the cosmogenic ^{9}Li and ^{8}He production and thus this rate has to be very low.

Table 4.3: Rate of "fake" tracks for several TT conditions.(a) is under 1 p.e. threshold and (b) is under 2 p.e. threshold. (1)no concrete; (2)10 cm concrete.

Config.	Fake muon rate (Hz), (a)		Fake muon rate (Hz), (b)	
	(1)	(2)	(1)	(2)
2 TT $x-y$ layers	340000	12500	1300	31
3 TT $x-y$ layers	2.6	0.02	6×10^{-4}	2×10^{-6}

In order to study the noise induced by ^{9}Li, ^{8}He and fast neutrons, enough statistics has to be collected using the TT. To estimate the noise rate induced by these three source for the three configurations of Fig. 4.17, the following parameters have been considered:

- E_μ: the muon energy,
- L_μ: the average track length of muons in the liquid scintillator (case a),

- R_μ: the muon rate in the liquid scintillator (case a),
- F_{nCap}: the neutron capture ratio (1 for JUNO, case a),
- N: the muon number (case b),
- L_{att}: the attenuation length of ^{9}Li/^{8}He in water pool (0.5 m, case b),
- S_{wp}: surface of water pool (case c).

The following formulas give the noise rate of the three considered configurations:

- $R_{Li,He} \propto E_\mu^{0.74} \cdot L_\mu \cdot R_\mu \cdot f_{nCap}$ for case (a),
- $R_{Li,He} \propto \frac{\sum_{i=1}^{N} E_{\mu^i}^{0.74} (\sum_{j=1}^{M} L_{\mu^i}^{j} e^{-\frac{d_j}{L_{att}}}) f_{nCap}}{N} \cdot R_{wp}$ for case (b),
- $R_n^{rock} \propto E_{\mu^i}^{0.74} \cdot R_\mu \cdot S_{wp} \cdot f_{nCap}$ for case (c)

Table 4.4 presents the expected noise rate from ^{9}Li and ^{8}He for all three TT coverage configurations of Fig. 4.18. From these results, the TT configuration (4XY, "O") can be excluded because of the poor rate observed of the ^{9}Li and ^{8}He induced noise. It has to be noted that in absence of the TT the ^9Li and ^8He rate per day is of the order of 90 to be compared to ∼50 IBD interactions induced by nuclear reactors. Obviously, this background has to be reduced or at least its rate must be well known.

Table 4.4: Noise rate induced by ^{9}Li and ^{8}He for case (a) of Fig. 4.17.

	L_μ (m)	R_μ (Hz)	^{9}Li/^{8}He rate/day
all muons	22.5	3.5	90
TT (4XY, Mid)	23.5	0.94	27
TT (4XY, Rtg)	23.4	0.80	23
TT (4XY, "O")	21.8	0.30	9

Table 4.5 presents the expected noise rate from ^{9}Li and ^{8}He for all three TT coverage configurations of Fig. 4.18 where the muons only cross the water pool without passing through the central detector. As already said, the TT configuration (4XY, Rtg) is the most representative of all parts of the detector and, not seen a significant difference between this configuration and the configuration (4XY, Mid), the configuration (4XY, Rtg) has been considered as baseline.

Table 4.6 presents the expected noise rate from fast neutrons obtained by extrapolations for Daya Bay observations for case (c) of Fig. 4.17 and for the baseline configuration of TT (4XY, Rtg) of Fig. 4.18. It is expected to have a fast neutron induced noise rate of the order of 0.13 per day which represents 0.3% of the expected signal.

The noise measured with the help of the TT will be extrapolated to the whole detector and will be introduced in the simulations in order to well estimated the related systematic errors.

Table 4.5: Noise rate induced by ^{9}Li and ^{8}He for case (b) of Fig. 4.17.

	^{9}Li/^{8}He rate/day	Back./signal (%)
all muons	1.2	3.0
TT (4XY, Mid)	0.35	0.9
TT (4XY, Rtg)	0.3	0.7
TT (4XY, "O")	0.16	0.4

Table 4.6: Expected noise rate from fast neutrons for case (c) of Fig. 4.17 and for the configuration of TT (4XY, Rtg) of Fig. 4.18.

	Daya Bay	Far detector	JUNO
E_μ (GeV)	57	137	215
R_μ (Hz)	1.2	0.055	0.003
S_{wp} (m^2)	724	1032	3740
f_{nCap} (%)	45	45	100
Rock neutron bkg. rate/day	1.7	0.22	0.13 (B/S$\sim$0.3%)

Modifications to the Target Tracker

The present OPERA TT acquisition system can afford up to 20–25 Hz trigger rate per channel. For higher rates (as those expected in JUNO) this system would have severe limitations inducing huge dead time and thus significantly reducing the TT efficiency. Even if the $x-y$ coincidences already reduce the noise rate (see above), the acquisition system specifically developed for OPERA needs will not be able to be used for the TT installed in JUNO cavern.

The high noise rate expected in JUNO obliges the replacement of the acquisition system (DAQ) by a new one. By the same way, the front end electronics based on OPERA-ROC [5] chip will be replaced. Indeed, this chip is now obsolete and not enough spares are available. The new generation chip MAROC3 [7] (AMS SiGe 0.35 μm technology, developed by IN2P3 Omega laboratory) disposing of more functionalities can replace the OPERA-ROC chip. On OPERA-ROC the word registering the triggered channels was not functioning properly while on MAROC3 this has been corrected. This gives the possibility to only read the triggered channels and not all of them as it was done in OPERA TT, thereby gaining in readout speed. The MAROC3 chip has a similar architecture (Fig. 4.19) than the OPERA–ROC (fast part for triggering and slow one for charge measurement). The difference is that in MAROC3 the ADC is already integrated in the chip while for OPERA–ROC the ADC was externally implemented on the DAQ cards. The MAROC3 chip has two "OR"s, one could be used for the timestamp while the second one could be used for fast coincidences with other sensors. This would allow to do fast coincidences with at least x and y strips to reduce the DAQ trigger rate. For all coincidences among TT sensors a dedicate electronics card has to be developed receiving the "OR" of all sensors and making coincidences. The timestamp can be provided by a special clock card to be developed.

OPERA institutes participating now in JUNO have expressed a strong interest to

develop the DAQ cards which will be located just behind the multi–anode PMTs, as done in OPERA. The front end card where the MAROC3 chip will be located could be produced by the same institutes, which would also have the responsibility to check and characterize all MAROC3 chips produced for this application (992 plus spares). These institutes could also develop the clock card and the coincidence card.

The drawings for the installation of the TT in JUNO will be produced by IN2P3 and IHEP–Beijing. It is already agreed with IHEP that the TT supporting structure will be financed and produced by Chinese institutes. This structure, very different from the one used in OPERA due to the fact that in JUNO all modules will be in horizontal position instead of vertical position in OPERA, has to be drawn with care and in a close collaboration between IN2P3 and IHEP. A special care has also to be taken in order to leave accessibility to all electronics of all TT modules.

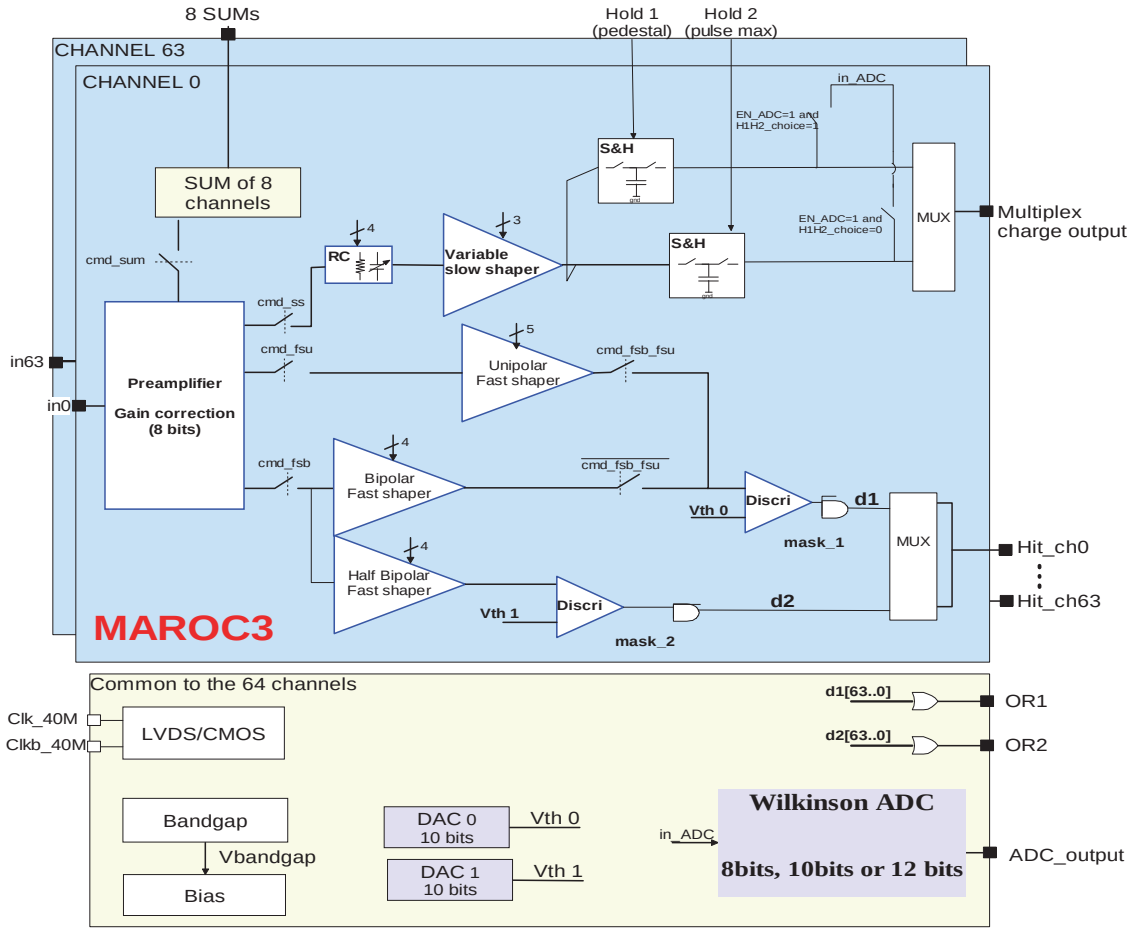

Figure 4.19: Architecture of the MAROC3 chip.

4.3 Water System

For the JUNO water Cherenkov detector, it requires ultrapure water for high muon detection efficiency. There will be different kinds of materials submerged in the water, including stainless steel, Tyvek, PMT glass, cables, etc. The complexity of the

underground environment makes it difficult to seal the pool completely and almost impossible to passively keep the water quality good for a long period of time. Therefore, it is necessary to build a reliable ultrapure water production, purification and circulation system.

Another important function of the water system is to keep the overall detector temperature stable. The stability of the temperature of the central detector is critical for the entire experiment. JUNO is located in southern China, and the temperature of the surrounding rocks can reach 32 degrees Celsius. We intend to maintain the temperature of the central detector at 20 degrees Celsius. Water is a good conductor of heat. Lowering the temperature of the water flowing into the pool is a natural choice to offset the heat from the surrounding rocks.

The Daya Bay experiment has 1300 tons of water in the near experimental hall water pool and 2000 tons of water in the far experimental hall water pool. The water production rate is 8 tons/hour and the purification rate is 5∼8 tons/hour. It can circulate one volume of water in two weeks. The water Cherenkov detector's muon detection efficiency is high to 99.9% and its long-term performance is stable. The designed water purification system satisfies the experiment requirements [13].

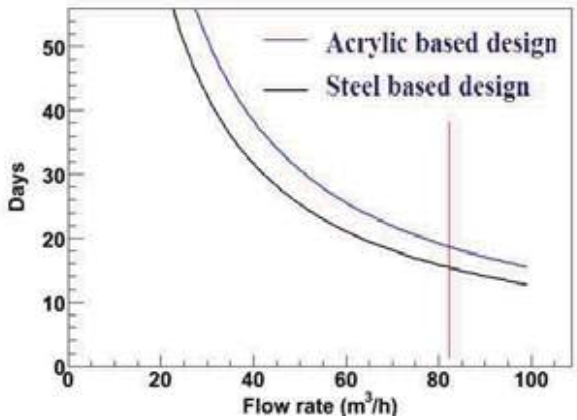

Figure 4.20: Flow rate vs one cycle time.

The JUNO water Cherenkov detector will have 20000 - 30000 tons of ultrapure water. Based on the experience of Daya Bay experiment, circulating one volume of water in two weeks requires a flow rate of about 80 tons/hour at JUNO. With this flow rate, we can keep good water quality as well as maintain pool water at stable temperature. Fig. 4.20 shows the number of days to circulate one volume of water as function of the flow rates of the proposed water system for the two candidate designs of the central detector. The red line indicates the flow rate at 80 tons/hour. It would take about 16 to 20 days to circulate one volume of water and this would satisfy the experiment requirements.

In the proposed design, we divide the water system into two parts. One part is for the production of ultrapure water and the other part is for the circulation/purification of water. For the water production system, one part of the system would be on the surface ground and the other part of the system would be underground. The reason for this design is that there is a strict requirement of waste water rate to be less than 5 tons/hour at 500 meters underground. Therefore, we have the part of the water

production system which generates the most waste water on the surface ground.

4.3.1 Water Production on Surface

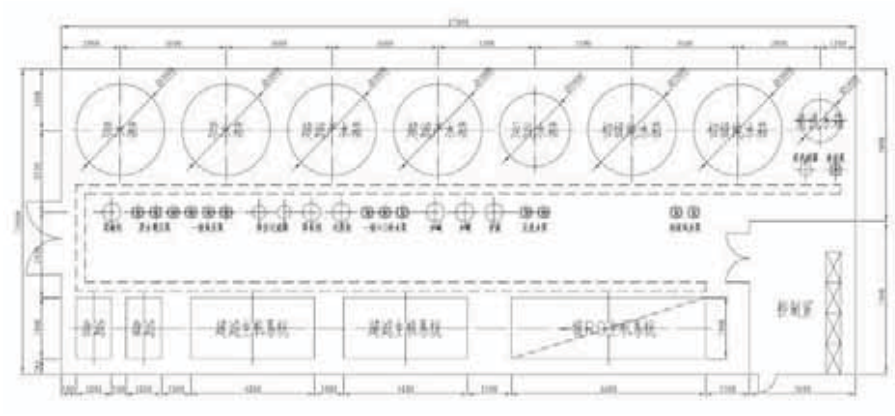

Figure 4.21: General view of water production system on surface ground.

As Fig. 4.21 shows, water flows through the disk filter first, which can block solid sediments and other large particles from flowing into the raw tank before goes through the ultrafiltration hosts. The ultrafiltration hosts can filter out small particles of insoluble material in the water before it goes into ultrafiltration tank. The water then passes through a reverse osmosis (RO) system, which can remove most of the ions in the water. Finally the water flows into the primary pure water tank. After the RO process, a third of the original water is produced as waste water with high ion concentration at a rate of 15 tons/hour. The waste water is of no harm to the environment and can be directly drained.

4.3.2 Water Production Underground

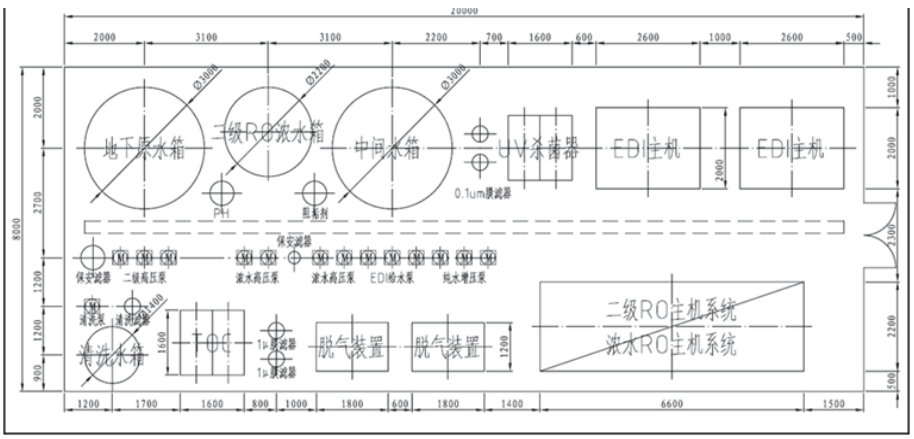

Figure 4.22: General view of water production system underground.

From primary pure water tank on the surface ground, the water is pumped through pipes at about 85 tons/hour going down a height of 500 meters into the underground raw water tank. From there the water will go through another RO system as well as other water treatment systems, like reduction of Total Organic Carbons (TOC) and Electrodeionization (EDI) systems. The resulted ultrapure water with resistance greater than 16 MOhm flows into experiment hall at a rate of 80 tons/hour.

4.3.3 Water Circulation/Purification Underground

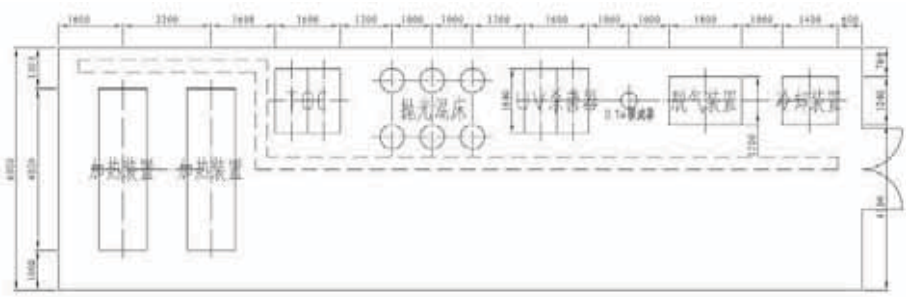

Figure 4.23: General view of water circulation/purification system on ground.

We would start the circulation process after the pool is fully filled with water. The water will be drawn from the pool at 80 tons/hour. The water will first go through the heat/cooling equipment . Then the water will flow through the TOC system (to remove organic carbon), the polishing mixed bed (to remove ions in the water to improve water quality), UV sterilization system, membrane filters, the degassing apparatus (to remove oxygen and other gases in water), and finally a cooling device (to control the water temperature). In the end, the purified water will return to the pool.

For the whole water production, purification and circulation system, we will use a water control system to automate the running of the system. The people on duty will only need to replace filters and other supplies on a regular basis.

4.4 Geomagnetic Field Shielding System

At the experimental site, the horizontal component of the geomagnetic field is about 40 μT and vertical component is about 24 μT. Since JUNO will use 20 inch PMTs as the main device for central detector, the geomagnetic field will have a big effect on large size PMT. It will deteriorate the whole detector performance. Figure 4.25 shows the relationship between the PMT collection efficiency and the external magnetic field intensity. We need to establish an effective magnetic shielding system to ensure good performance of central detector.

We intend to ensure that a spherical region with a radius of 37.5 m would be well shielded from geomagnetic field. We plan to use coils with current flowing through them to compensate the geomagnetic field. The residual field intensity could be reduced to be below 10 μT. The baseline design is of one coil system. We can perform accurate measurement of the geomagnetic field to determine its main direction (mapping the

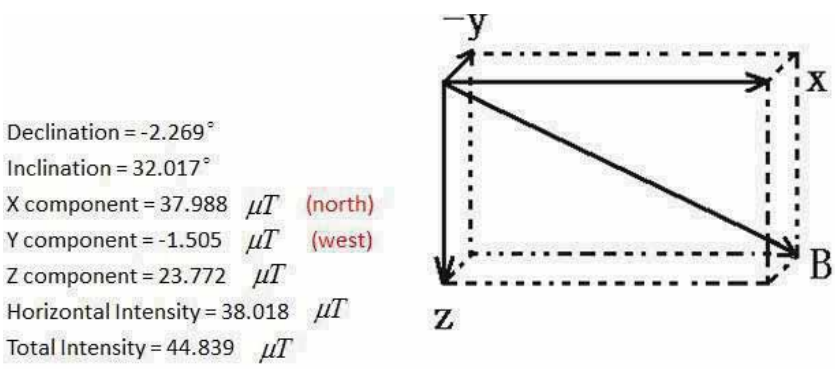

Figure 4.24: Earth magentic in Jiangmen.

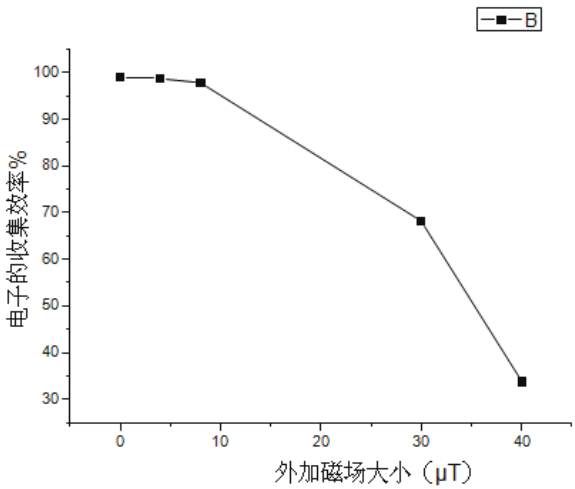

Figure 4.25: PMT collection efficiency vs the external magnetic field.

geomagnetic field in the pool) and then do compensation along its main direction. As Fig. 4.26 shows, this system is easy to control. Figure 4.27 is the magnetic field distribution in the sphere from one coil system. It can have a good shielding. The uniformity within the 37.5 m volume is 1.8%. The PMTs in central detector will not be effected by the Earth's magnetic field after compensation.

Careful selection of non-magnetized materials used in the detector for parts such as the supporting structure for PMTs as well as stainless steel for the detector, etc. is also important. They could cause an additional local magnetic field in additional to the Earth's field, which could affect the performance of the PMTs. The compensation coils would be installed on the central detector which means the PMTs of the water Cherenkov detector would still be subject to the Earth's magnetic field plus some additional field generated from the coils. Therefore, it needs to have the pool PMTs shielded against magnetic field with passive magnetic shield like the one used in the Daya Bay experiment [12].

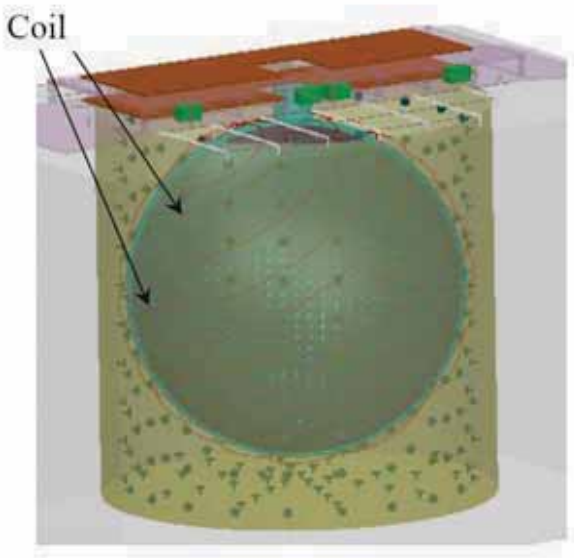

Figure 4.26: One group earth magnetic shield system.

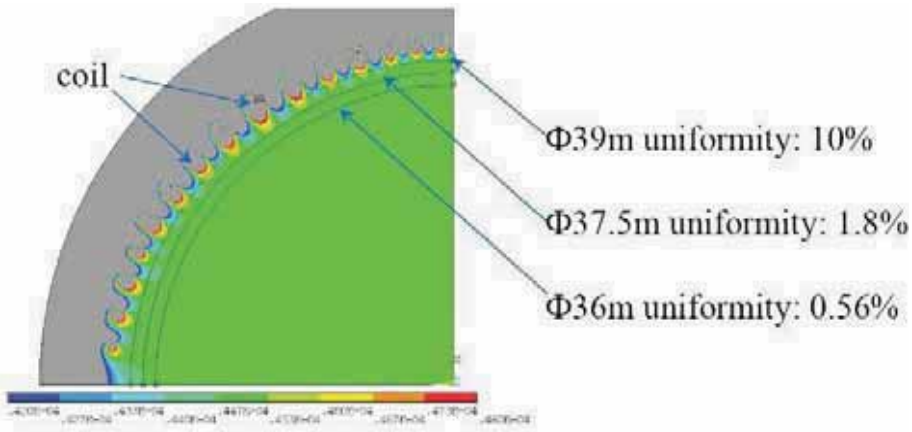

Figure 4.27: Magnetic field distribution with one group system.

4.5 Mechanical Structures and Installation

4.5.1 Support Structure over the Pool

The tracking detectors over the pool are divided into two groups, each consisting of several layers of detectors stacked together. One group is placed on the steel bridge, while the other is put three meters above the first group. Hence a two-story bridge is needed, as shown in Fig. 4.28. The parameters of the two-story bridge are as follows: bridge width is between 17 m and 20 m and the distance between two layers of the bridge is 3 meters. The support structure has three functions:

(1) supporting the tracking detectors;

(2) supporting the scale systems of the central detector;

(3) possibly supporting the electronics rooms.

The diameter of pool is 42 meters and the supports of bridge are located at both ends of the bridge. Considering the height limit of the underground space and the structure stiffness, a box structure is adopted for the bridge. Two columns of tracking detectors, whose width is about 15 m, are placed on the bridge. Considering the passageway and the width of the electronics room (about 3 meters), the bridge width is between 17 m and 20 m. The load of the bridge includes the weight of the central detector cable and electronics rooms (about 100 tons), weight of the tracking detectors (about 70 tons), weight of the electronics room (20 tons) and weight of the supports of the tracking detectors.

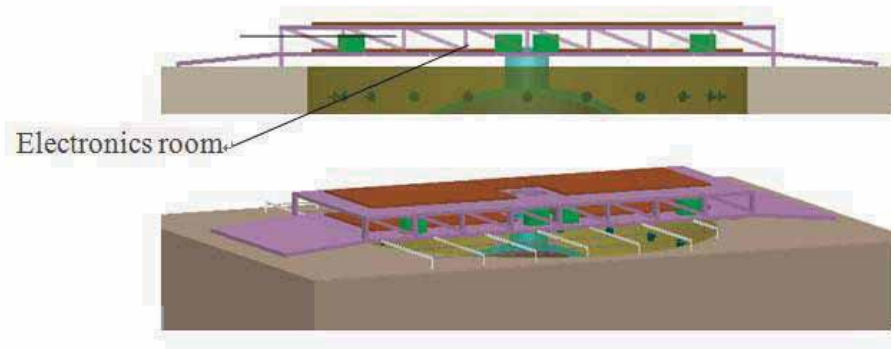

Figure 4.28: The top support structure.

Figure 4.29: PMT support structure of DayaBay.

Figure 4.30: The cover design of Daya Bay. a) gastight zipper b) Th connection between pool cover and pool dege

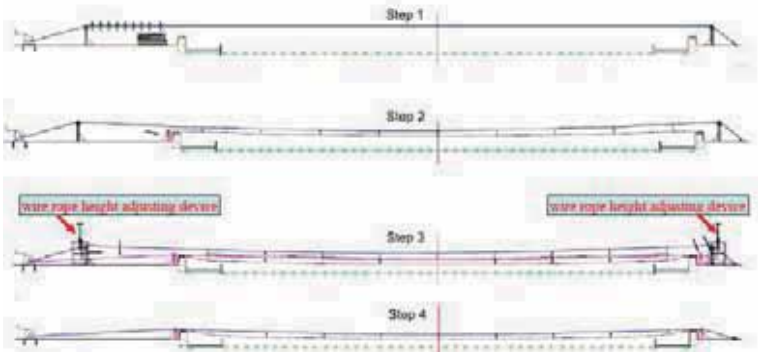

Figure 4.31: The wire design option for cover installation of Daya Bay experiment.

4.5.2 Support Structure for PMTs

The support structure of PMT adopts the design for the Daya Bay veto PMTs, as shown in Fig. 4.29. The PMT support structure is then attached to a steel-frame fixed on the waterpool wall. The design of the steel-frame structure will be similar to that for the central detector. The tyvek film will also be fixed to the steel frame.

4.5.3 Sealing of the Pool

A black rubber cloth served as the pool cover in the Daya Bay experiment. The pool cover is connected to the pool edge through an air-tight zipper which shields the pool from the external air and light, as shown in Fig. 4.30. With the seal zipper, the pool is easily accessible for routine maintenance, such as replacing the liquidometer. We will adopt the same technique for JUNO's pool seal.

As the JUNO pool is very large with a 40-meter span, it is difficult to unfold the black rubber cloth. Therefore, we propose two solutions: the first is the tight-wire

scheme used in the Daya Bay experiment; the second is a slide-guide scheme. The two schemes are similiar. For the slide-guide scheme shown in Fig. 4.30, the cloth is unfolded along the guide, instead of the tight-wire in the tight-wire scheme shown in Fig.4.31. For comparison, the tight-wire scheme is more difficult to operate. In order to prevent the cloth from touching the ground, we will adjust the height of the wire rope pillar. The adjustment process is shown in Fig.4.31. Firstly, wire is put on the higher rope pillar and pulled tight; secondly, unfold the black rubber cloth and fix the edge of the cloth; finally, put the tight-wire on the lower pillar slowly.

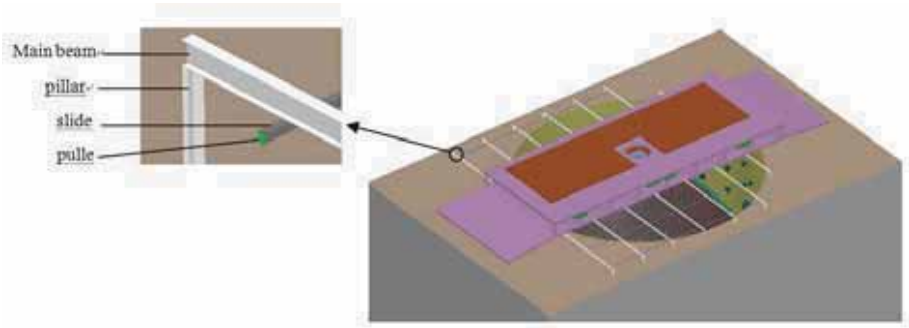

Figure 4.32: Lead rail for rubberized fabric cover option installation.

The slide-guide scheme costs more, but is more easily implemented. The main structure contains the main beams, columns, slide guides and pulleys. A couple of slide guides is fixed on the main beams under bridge. One end of the main beam is supported on the bridge, and the other end is connected to the pillar fixed on the ground.

Each of the two schemes have advantages and disadvantages, and the final design choice is still under discussion.

4.5.4 Lining and Thermal Insulation Layer of the Pool

The cylindrical pool with 42-meter diameter and height will be filled with 2300 tons of ultra-pure water. Since the laboratory is located 400 meters underground, the pressure of underground water is high. A powerful lining is needed to prevent water from the surrounding rock seeping into the pool. We propose to adopt high-density polyethylene (HDPE) material as the waterproof lining between rock and pool. HDPE has good corrosion resistance, high strength, good ductility, and does not pollute ultrapure water. The design can be similar to that for landfill, but the lining for the JUNO water pool contains many through holes and further studies are needed.

The operating temperature of the JUNO detector system is 20 degrees, while the temperature near the laboratory rock is around 32 degrees, significantly higher than the operating temperature. The granites surrounding the pool have poor permeability, which has certain heat preservation effect. The concrete wall of the pool is a poor heat conductor with a heat transfer coefficient of only 1.63 W/(mK).

According to an independent heat transfer calculation and the example of calculation for the Daya Bay experiment, the pool thermal insulation may not require additional insulating layer. However, to reduce operating costs, it is proposed to add an insulating layer.

4.5.5 Installation

The detector installation includes the assembling of PMT and bracket, and the fixation of PMT bracket. The assembling of PMT and bracket is shown in Fig. 4.29. To make full use of the embedded parts in concrete pool wall, the PMT bracket is considered to be fixed on the embedded parts. In addition, special tools and operation management are needed to ensure safe and smooth detector installation.

4.6 Prototype

4.6.1 Geomagnetic Shielding Prototype

Through numerical calculation, we provide an option for the geomagnetic shielding system for JUNO. A prototype of coil system is required for validation and material property study. After the prototype study, we will have a more accurate estimate for the shielding effect and can then optimize the design of the geomagnetic shielding system.

4.7 Detector Construction and Transportation

The veto system mainly consists of the water Cherenkov detector and the tracking detector. For the water Cherenkov detector, the most important tasks are PMT test and transportation, water purification system construction and transportation, and support structure manufacturing and transportation. The veto PMT test and transportation will be done together with the central detector PMTs. Water system manufacturing and transportation and support structure construction await the final design decisions before the bidding and other processes can be started. The option for the top trackers also needs to be finalized before the detailed plans for the constructions and transporting can be made.

4.8 Risk and Safety Issues

The large size of the JUNO detector limits the available space in the experimental hall. For the veto system, it is important to carefully coordinate the installations of various detectors and hardwares. If the assembly coordination is not optimal, it could influence the whole veto systems installation. To avoid this risk, a careful coordination and strict schedule should be performed for various assembly tasks. Any potential conflicts in the installation schedule should be discussed and resolved among the detector coordinators to ensure a smooth installation process.

Most of the safty issues occur during the detector installation stage. The safety procedure must be strictly followed when the large JUNO detector is installed.

4.9 Schedule

The plan for the period 2014-2020 is as follows:

- 2014: Setup the following two kinds of veto detector prototypes and take data with cosmic muons:

  1) liquid scintillator + fiber prototype;

  2) a multilayer resistive plate chamber (RPC).

- 2015: Finalize the top tracker option.

- 2016: Determine the pool liner design and begin to prepare lining installation;

  Complete the design of water pool insulating layer design and start installation preparation;

  Determine geomagnetic shielding design and start the installation preparation.

- 2017: Start to install water pool insulating layer;

  Start to install water pool lining;

  Start to install the geomagnetic shielding system.

- 2018: Complete the production of water Cherenkov detector PMT support structure and top track detector supporting structure;

  Start the installation of the top track detector and water Cherenkov detector PMT installation.

- 2019: Complete water Cherenkov detector installation and top track detector installation;

  Start pump ultra pure water into water pool.

- 2020: Complete pump process and start veto system commissioning.

Bibliography

[1] F. P. An *et al.* [Daya Bay Collaboration], “The Muon System of the Daya Bay Reactor Antineutrino Experiment", Nucl. Instrum. Meth. A **773** (2015) 8-20.

[2] S. Fukuda *et al.* [Super-Kamiokande Collaboration], “The Super-Kamiokande Detector", Nucl. Instrum. Meth. A **501** (2003) 418-462.

[3] T. Adam *et al.*, "The OPERA experiment Target Tracker", Nucl.Instrum.Meth. **A577** (2007) 523, arXiv:physics/0701153.

[4] N. Agafonova *et al.* [OPERA Collaboration], “Study of neutrino interactions with the electronic detectors of the OPERA experiment,” New J. Phys. **13** (2011) 053051 [arXiv:1102.1882 [hep-ex]].

[5] A. Lucotte, S. Bondil, K. Borer, J. E. Campagne, A. Cazes, M. Hess, C. de La Taille and G. Martin-Chassard *et al.*, “A front-end read out chip for the OPERA scintillator tracker,” Nucl. Instrum. Meth. A **521** (2004) 378.

[6] J. Marteau [OPERA Collaboration], “The OPERA global readout and GPS distribution system,” Nucl. Instrum. Meth. A **617** (2010) 291 [arXiv:0906.1494 [physics.ins-det]].

[7] S. Blin, P. Barrillon and C. de La Taille, “MAROC, a generic photomultiplier readout chip,” IEEE Nucl. Sci. Symp. Conf. Rec. **2010** (2010) 1690.

[8] M. Ageron *et al.* [ANTARES Collaboration], Nucl. Instrum. Meth. A **656** (2011) 11 [arXiv:1104.1607 [astro-ph.IM]].

[9] http://www.km3net.org/TDR/KM3NeT-TDR.pdf (ISBN 978-90-6488-033-9)

[10] Physics 37 (Procedia 2012) 1201 - 1208, 2 NOvA Technical Design Report, Oct 8, 2007

[11] Nucl. Instrum. Meth. A **463** (2001) 194-204

[12] P. DeVore *et al.*, “Light-weight Flexible Magnetic Shield For Large-Aperture Photomultiplier Tubes", Nucl. Instrum. Meth. A **737** (2014) 222-228.

[13] J. Wilhelmi, R. Bopp, R. Brown, J. Cherwinka, J. Cummings, E. Dale, M. Diwan and J. Goett *et al.*, arXiv:1408.1302 [physics.ins-det].

Chapter 5

PMT

5.1 Design Goals and Specifications

5.1.1 Introduction

Photon detectors measure the scintillation light created by interactions of the neutrinos with liquid scintillator and are key components for accomplishing the physics goals of JUNO. Important requirements for photon detectors used in JUNO include high detection efficiency for scintillation photons, large area, low cost, low noise, high gain, stable and reliable, long lifetime. JUNO plans to use approximately 20,000 tons or 23175 m^3 liquid scintillator hosted in a spherical container of diameter 35.4 m. Photon detectors will be mounted on a sphere 37.5 m in diameter covering at least 75% of the 4654 m^2 surface area of the sphere according to the reference design of the central detector. Large area vacuum photomultipliers are the only viable choice for the JUNO photon detectors. Table 5.1 shows the numbers and sizes of PMTs required for JUNO in two scenarios with photocathode coverage ratio of 75% and 70%. Assuming 508 mm (20 inch) diameter PMTs with a photocathode diameter 500 mm are used, 16875 such PMTs are required by the central detector of JUNO to cover 75% of the detector surface.

Table 5.1: PMTs required by JUNO

PMT mounting diameter	photocathode coverage	508 mm
37.5 m	70%	15750
37.5 m	75%	16875

5.1.2 PMT Spectications

The main specifications for the 508 mm PMTs in JUNO are given in Fig. 5.1. Bialkali (BA) photocathode will be used. The spectral response of the BA photocathode matches the light emission spectrum of the liquid scintillator well. One of the most critical requirements for JUNO PMTs is high photon detection efficiency (PDE), which is equal to the photocathode quantum efficiency (QE) multiplied by the efficiency of photoelectron collection efficiency (PCE) in the PMT vacuum. In order to achieve the required peak PDE of 35%, the peak photocathode QE is set to 38% by assuming the

PCE to be 93%. We hope the average PDE for scintillation photons, which have a rather broad spectrum, can be $> 30\%$.

Note that PMTs are measured by manufacturers in air and with incident light beams perpendicular to the surface of the glass entrance while PMTs are submerged either in water or in oil when used in JUNO, and the scintillation light can penetrate the curved glass window of a PMT at any angle. Small discrepancies regarding the photocathode QE between the manufacturers, measurements and those experimentally observed can occur as a result of differences in light reflections at the medium/glass interface.

JUNO PMTs will work in photon counting mode and the typical gain required is 10^7. The PMT noise pulse level must be low so that the single photoelectron peak can be clearly separated from the PMT noise. In JUNO cosmic events the minimum momentum of cosmic ray muons is 218 GeV and the penetrating muons' rate is 3.8 Hz. Energy deposition by muons that do not generate showers would be as high as 7 GeV and a total of 7×10^7 scintillation photons would be produced. The required dynamic range of JUNO PMTs is given as 0.1-4000 pe's. The photocathode noise rate, rate of prepulse and after-pulses are given in Fig. 5.1. The radioactivity levels of the PMTs, which mostly comes from the glass, are also given.

In addition to the 508 mm diameter PMTs for measuring scintillation light generated by neutrino reactions in the detector, approximately 2000 of 203 mm (8 inch) diameter PMTs are needed for cosmic ray muon veto by detecting Cherenkov light generated by cosmic muons. These PMTs will be mounted on the outside surface of the stainless steel structure that supports the liquid scintillator vessel. The total area to be covered is approximately 5000 m^2. The requirements for these PMTs are similar to those used in the Daya Bay neutrino detector.

Specifications of PMTs for JUNO

Parameters	Specs	Comments
Diameter (mm)	508	20 inches
Photocathode diameter (mm)	500	Glass thickness 4 mm
Peak quantum efficiency (QE)	≥ 38%	Prefer at wavelength ~420 nm
Photoelectron Collection efficiency (PCE)	≥ 93%	Average over entire photocathode
Photon detection efficiency (PDE)	≥ 35%	PDE ≅ QE ×PCE
Spectral response (nm)	300 - 650	Scintillation 380 – 550 nm
Transition time spread（ns）	5 ns	FWHM
Gain	$> 10^7$	
Single pe peak/valley（P/V）	> 2	
Dark noise pulse rate (kHz)	30	Based on Hamamatsu R3600-2 (25°C, >0.25 pe)
Linear range（pe）	0.1 - 1000	
Dynamic range （pe）	0.1 - 4000	
Pre-pulse	< 1%	
Fast after pulse	< 1%	< 1 μs
Slow after pulse	< 5%	< 200 μs
Maximum hydraulic pressure (atm)	9	4.2 atm in JUNO
^{238}U content (g/g)	1×10^{-8}	PMT weight ~ 10 kg
^{232}TH content (g/g)	2×10^{-8}	PMT weight ~ 10 kg
^{40}K content (g/g)	10^{-5}	PMT weight ~ 10 kg
Lifetime (year)	> 20	

Figure 5.1: Specifications of PMTs for JUNO

5.2 MCP-PMT R&D

In order to ensure optimum performance of the detector, the PDE of PMTs in the detector is preferred to be $\geq 35\%$, averaging over the entire photocathode and scintillation spectrum. No commercial large PMTs can achieve this. A R&D effort intended to accomplish such an ambitious goal was started in early 2009. This effort was led by IHEP (Beijing) and joined by research institutes, university groups and related companies in China, and a formal R&D group was established in early 2011. Significant progress in all aspects of PMT R&D has been made. The goal of the design and manufacturing 508 mm PMTs that meet the requirements listed in Table 5.2 and in particular to achieve the 35% PDE is not easy and cannot be taken for granted. If we are unable to accomplish our stated goal in time, we will make corresponding adjustments to the design of the experiment. Depending on the status of our R&D effort by the time of the decision on the PMT choice, commercially available PMTs that may or may not have the desired photon detection efficiency can be considered.

It is worth noting that in early 2009, a team from IHEP lead by Yifang Wang, then the deputy director of IHEP visited a former PMT manufacturer, the No. 741 factory of the Chinese Electronics Administration in Nanjing, China. The manager of that factory became interested after hearing of our effort to develop large PMTs for JUNO (then Daya bay II). He made an effort to line up financial support from two entrepreneurs in Beijing and successfully negotiated a deal with PHOTONIS France S.A.S. and bought their stalled PMT production line and all related technologies. A Chinese PMT company, SCZ PHOTONIS, was established in 2011 and have now started to make 12 inch PMTs, with a plan in place to make 20 inch PMT samples soon.

Meanwhile, IHEP representatives have been in contact with Hamamatsu, Japan, which have been developing high efficiency 20 inch PMTs for the future Hyper Kamiokande experiment in Japan and made good progress in the last few years. Hamamatsu has agreed to deliver 20 inch PMT samples to IHEP for testing.

We will discuss the R&D effort for JUNO PMTs by the collaboration led by IHEP (Beijing) in this section. Options provided by the two commercial companies will be discussed in section 6.4.2.

5.2.1 MCP-PMT R&D at IHEP

The R&D effort to develop PMTs for JUNO started in early 2009 when the Daya bay II experiment was in the very early conceptual development stage. The main obstacle for achieving the physics goals of the experiment was the lack of commercially available PMTs that can reach the photon detection efficiency (PDE) required. Of the two major PMT manufacturers in China, the aforementioned No. 741 Factory in Nanjing had stopped PMT production for a number of years and another PMT manufacturer, the No. 261 Factory in Beijing was bought by Hamamatsu and the resulted Hamamatsu Photonics (Beijing) produced only low-end small PMTs. The R&D work on PMT related technologies such as Bialkali photocathode had ceased for more than a decade in China.

The quantum efficiency (QE) of a vacuum PMT is conventionally defined as the number of photoelectrons emitted from the photocathode layer into vacuum by the

number of incident photons. When the QE of a PMT is measured, the device is placed in air and the incident light beam is perpendicular to its glass window action. Typically 4% of photons are reflected by the glass surface and more light is reflected at the interface of the glass substrate and the photocathode layer, which has a high index of refraction. The cathode sensitivity and QE as functions of wavelength of the incident photons are plotted in Fig. 5.2 (taken from the PMT manual published by Philips Photonics). The blue curve is QE of conventional bialkali photocathode (SbK2Cs) with a peak value of about 30%. The spectral response of the conventional BA photocathode matches the spectrum of scintillation light from the liquid scintillators well and the estimated average QE for the entire scintillation light emission spectrum is about 25% based on this plot. However for large PMTs, the QE is normally lower than the values shown in Fig. 5.2.

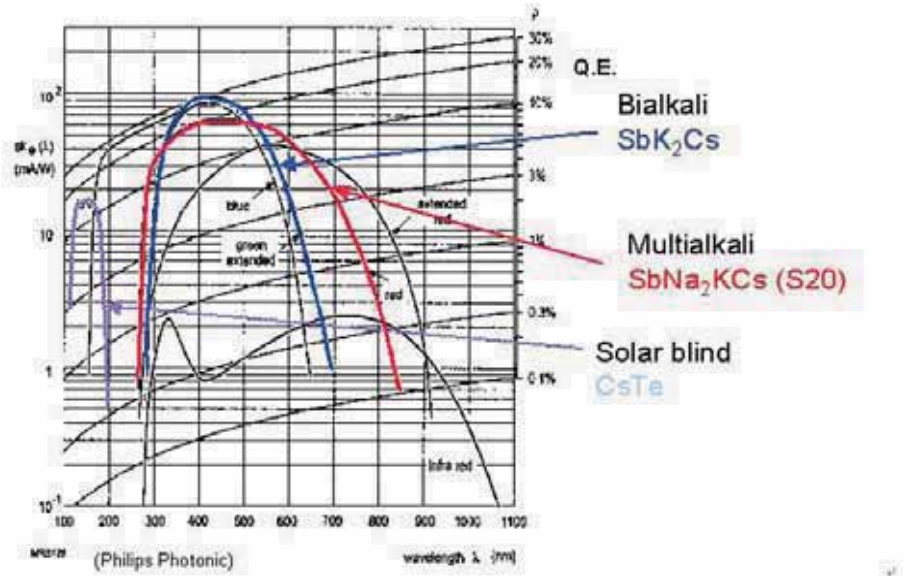

Figure 5.2: The photocathode sensitivity and quantum efficiencies of various photocathodes

For the 20 inch Hamamatsu R3600-02 used in the KamLand experiment, the peak QE is about 20% and the peak photon detection efficiency (PDE) is only about 16% since the photoelectron collection efficiency is 80% as stated by Hamamatsu for the R3600-02. The 16% peak PDE is far lower than the desired 35% PDE for JUNO. Another factor that also needs to be considered is the effective photocathode area. The R3600-02 PMT has an outside diameter of 508 mm and its effective photocathode diameter is only 460 mm. This factor puts a limit on the capability for JUNO to maximize its photocathode coverage. Given these factors, it became apparent that we need to start our own large PMT R&D program mainly to improve the photon detection efficiency. Note that new 20 inch PMT (R12860 Under development) samples with super bialkali photocathode from Hamamatsu have shown great improvement for the PDE.

Our PMT R&D was based on a concept proposed by IHEP (Beijing) in early 2009. The conceptual schematic is shown in Fig. 5.3. The concept calls for a spherical PMT with top hemisphere, as shown in the figure, used as transmission photocathode and

its bottom hemisphere used as reflective photocathode which converts the photons that passed through the transmission photocathode. It is hoped that by optimizing the thickness of the photocathode in the top and bottom halves, the QE of such a PMT can be significantly improved compared to the conventional design that has only the top transmission photocathode. This new design requires two back-to-back compact electron multipliers, since conventional dynode chains would be too bulky. The proposed electron multipliers are two back-to-back pairs of microchannel plates (MCPs), so that photoelectrons from the top and bottom photocathodes are focused on the two sets of MCPs facing left and right, as shown in Fig. 5.3.

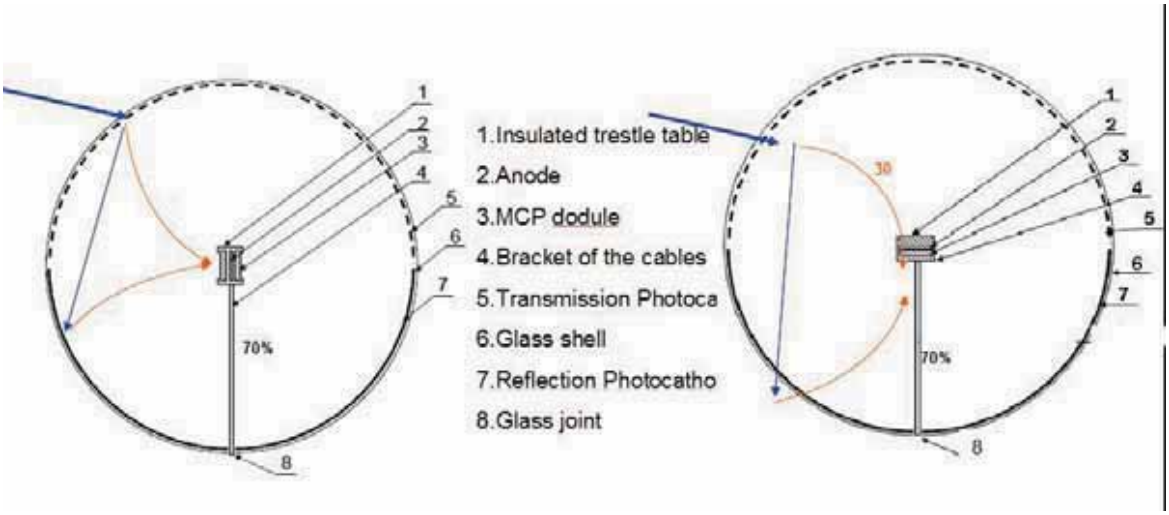

Figure 5.3: The conceptual drawing of the high efficient spherical PMT with two sets of MCP electron multipliers

As a starting point, a contract for a 5 inch MCP-PMT prototype was signed with the Nanjing Electronic Devices Institute, which was the only place in China that had made MCP PMTs. The progress was slow at the beginning and after about two years, working prototypes were successfully made. While working with the Nanjing Electronic Devices Institute, it became apparent that we needed to expand our efforts in order to broaden our technology bases to solve many complex and difficult technical issues. The Large Area MCP-PMT Development Collaboration was formally established in 2011. Coordinated by IHEP, the collaboration consists of the CNNC Beijing Nuclear Instrument Factory, the Xi'An Institute of Optics and Precision Mechanics (XIOPM) of the CAS, Shanxi Baoguang Vacuum Electric Device Co., Ltd., China North Industries Group Corporation (NORINCO GROUP), Nanjing University, and the PMT Division of the CNNC Beijing Nuclear Instrument Institute (formally No. 261 Factory). Great progress has been made since the start of the collaboration almost three years ago.

5.2.2 Large Area High Efficiency MCP-PMT Project

Many critical components and technologies need to be developed for the success of the Large Area High Efficiency MCP-PMT Project. First, the raw materials and methods to produce large glass bulbs with high strength, high optical quality and extremely low radioactivity must be identified. Among many requirements, the glass bulbs must

be able to work in pure water under high pressure. The technology for vacuum sealing between the glass and the Kovar metal leads must be developed. Technologies required for making large area high QE photocathodes are also needed. The alkali metals and Antimony sources and thin film deposition technologies necessary for photocathode fabrication also require development work. Fabricating MCP pairs as electron multipliers with low noise and gain exceeding 10^7 is very complex and requires a lot of development work. Other key technologies include electro-optic, mechanic and electric designs for MCP-PMTs and the testing of such PMTs. At the time when the collaboration was started, most of the required technologies did not exist in China. After three years of collective work, 8 inch and 20 inch MCP-PMT prototypes have been successfully made and evaluated.

5.2.2.1 Basic Concept of Large Area MCP-PMT

1) Effect of combining the transmission and reflection photocathodes

Conventional wisdom says that the QE of a reflective photocathode, that can be made thicker, has much higher QE than that of a transmission photocathode. Coating the lower half hemisphere of a spherical PMT bulb to convert the light that has passed through the transmission photocathode on the top hemisphere into photoelectrons can in principle improve the QE of the device. Scientists at XIOPM have done theoretical analysis and computer simulation, showing that by optimizing the thicknesses of transmission and reflection photocathodes, the QE of the spherical PMT can indeed be improved. Such improvement has also been seen in prototypes of MCP-PMTs.

2) Electro-optical Simulation

The shapes of photocathodes of the focusing electrodes required for effective photoelectron collections, and of the other structures inside the PMT bulb, require careful electro-optical calculations. Commercial computer software specially written for this purpose are extensively used by XIOPM and NORINCO to optimize the MCP-PMT design both for 8 inch and 20 inch MCP-PMTs. An example of the computer simulation results is given in Fig. 5.4. The simulation includes the photocathode, MCP assembly, its support structure and metal leads, focusing electrodes and the Earth's magnetic field. Electric potentials for various electrodes were optimized.

3) MCP computer simulation

XIOPM has performed computer simulations for photo-electron collection and amplification in the microchannels of MCPs. Electrode arrangement, gap size between two MCP plates, size of microchannels and inclination angles were studied. A diagram of such simulation is given in Fig. 5.5. The MCP assembly has several advantages such as compactness insensitivity of the electron amplification to the Earth's magnetic field, high dynamic range, etc. Additional concerns, including the photoelectron collection efficiency and lifetime, etc. still need to be addressed.

5.2.2.2 MCP and MCP Assembly

NORINCO has decades of extensive experience in MCP production and development. The company has organized a special group to develop the MCP and MCP assembly required for the MCP-PMT project. Large capital and manpower investments have been made. MCP parameters and processing procedures have been adjusted. High gain MCP assemblies with gain exceeding 10^7 for a pair of MCPs have been developed

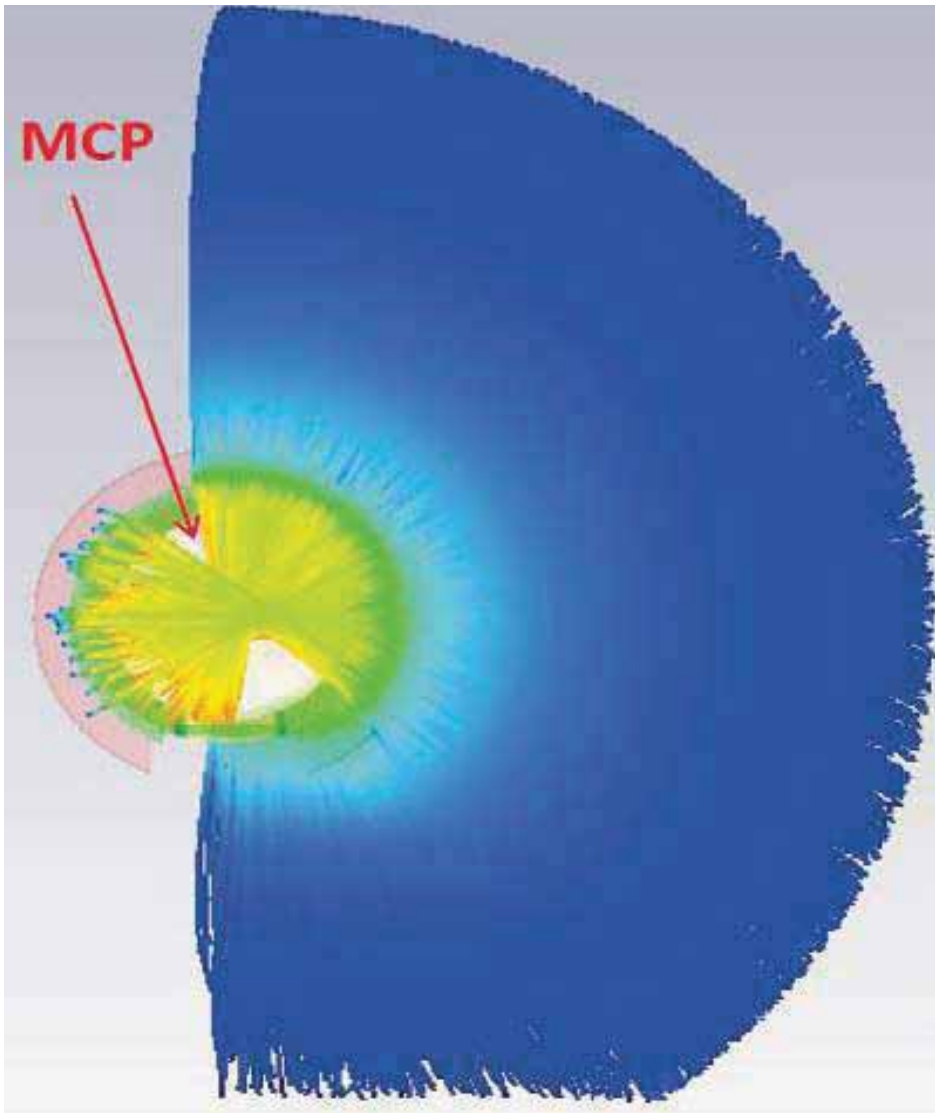

Figure 5.4: MCP-PMT electro-optic simulation with Earth magnetic field

after the design of the MCP assembly was optimized. This level of gain is critical for single photoelectron detection.

5.2.2.3 Glass Tube and Raw Materials

Our 8 inch MCP-PMTs use the traditional electro-vacuum glass, whose coefficient of thermal expansion (CTE) matches the CTE of Kovar, which is used for vacuum feedthrough pins. The vacuum seal is easy to make. However, the electro-vacuum glass is difficult to blow into 20 inch glass tubes due to its poor mechanical properties above the softening point. Also there are other issues that make the electro-vacuum glass unsuitable for 20 inch PMT tubes even if it can be used to make 20 inch glass tubes. Its mechanical strength is not good enough to withstanding the high hydraulic pressure, while oxides of alkaline metal in the glass can slow leach out and affect the optical transparency of the glass. Therefore, the Pyrex type of borosilicate glass that

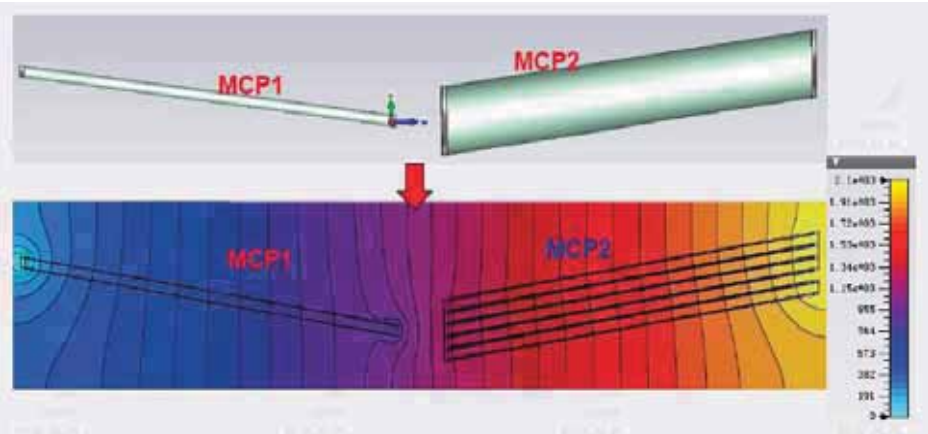

Figure 5.5: Simulation for MCP functionality

has the required mechanical strength and chemical stability is preferred for making 20 inch glass tubes. Unfortunately, the CTE of Pyrex glass does not match the CTE of Kovar so a section of glass tube that joins the Perex to electro-vacuum glass needs to be made by using glasses with different CTEs. Techniques and glass materials must be developed for making this multiple transition glass tube section. The aforementioned technical difficulties have been solved by the collaborative effort of our collaboration and industrial partners. The resulting 20 inch glass bulb has a good appearance and excellent quality. Its mechanical accuracy and thickness uniformity are also excellent. Some completed glass bulbs, including the Pyrex sphere and neck, multiple transient section and Kovar seal, as shown in Fig. 5.6, have been tested in a pressure test set-up with pressure up to 10 bars.

Since the neutrino event rate in JUNO is extremely low, radioactivity of the PMTs for JUNO must be tightly controlled. The radiative decay of radioactive materials in PMT can potentially be a major source of background for a low energy neutrino experiment. The radioactive elements ^{238}U, ^{232}TH, and ^{40}K in the glass are the major contributors of PMT radiation backgrounds. The glass of the Hamamatsu 8 inch R5912 used in Daya bay detector has rather high radioactivity level, which is acceptable for a relatively high rate experiment like Daya bay, but far exceeds the level that can be tolerated by JUNO. To control the radioactive level in the PMT glass tubes, care must be taken to select the raw materials and also to control the glass melting process preventing the radioactive materials contained in the crucibles to be dissolved into the molten glass.

The main component of Pyrex glass is SiO2. We have identified sources of high purity quartz sand in China and indeed the measured ^{238}U, ^{232}TH, and ^{40}K levels are satisfactory for JUNO. Low radioactivity raw materials for other ingredients of the Pyrex glass have also been identified. Costs of high purity raw materials are significantly higher than those of materials commonly used to make Pyrex glassware. However, the cost of raw materials for glass, even the high grade materials used, are still an insignificant part of the total PMT production cost.

Although we believe we know how to do it, so far low radioactivity glass tubes have not yet been manufactured. The 20 inch glass tubes for our prototype PMTs have been made with regular materials and using regular procedures in the factory.

This is because even just to make a test run for low radioactivity glass requires the glass factory to stop their regular production for an extended period to purge their ovens, and the test would cost a significant amount of money. We will do a low radioactive test production when we are ready to make a small batch of 20 inch PMTs.

Figure 5.6: Vacuum sealed 20inch glass bulb on a CMM for mechanical accuracy measurements

5.2.2.4 Photocathode

The Photocathode is a critical component of our PMT R&D project. Typically to make bialkali photocathode, a very thin Antimony layer is first deposited on the inner surface of an evacuated glass tube, then layers of the alkali metals Potassium and Cesium are deposited on top. Under high temperature a semiconductor layer of K_2CsSb photocathode is formed. Both XIOPM and NORINCO, on the basis of their previous experiences, have tried to make bialkali photocathode for 8 inch MCP-PMTs successfully. Recently NORINCO has also made a 20 inch photocathode with good results as shown in Fig. 5.7.

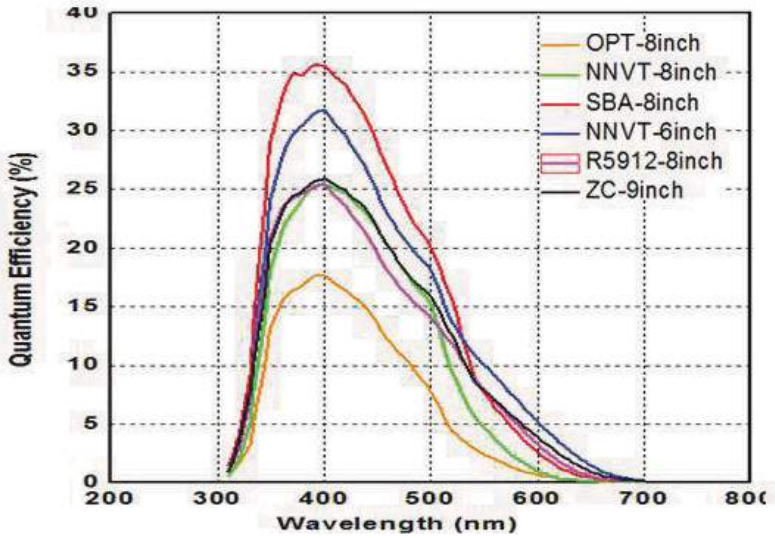

Figure 5.7: QE

5.3 Organization of the MCP-PMT R&D Project

5.3.1 Introduction

The required effort to develop a brand new product such as 20 inch MCP-PMT is very technically demanding, and the R&D process is complex and time consuming both for skilled technicians and scientists. The cost of the R&D, including the basic equipment and the investment for developing the various technologies involved, is quite high. IHEP (Beijing) would be unable to take on this task by itself. The approach we have taken is to organize a concerted effort by factories that have experience of producing PMTs and MCPs, as well as by research institutions and university groups that have strong theoretical and practical background in opto-electronic devices. This approach led to creating a collaboration able to exploit effectively the expertise of each individual member institution toward the final goal of designing and fabricating 20 inch PMTs that meet the requirements for JUNO.

Unlike other electronics devices, PMTs often cannot be tested at every production stage; instead meaningful tests can only be made after all the production steps are completed and the tube is evacuated to high vacuum level. We must do as much as possible of the testing and Q&A work before the mass PMT fabrication is started. Therefore, we divide our R&D project into the following categories, as shown in Fig. 5.8.

The development process includes many different aspects that must proceed in parallel as listed below.

1. Alkali sources: Develop and produce standardized alkali sources that ensure high QE and stable photocathode.

2. Glass: Develop 20 inch high quality and low radioactivity glass bulbs.

3. MCP: Develop and produce low noise, high gain MCPs and optimize the performance of MCP assemblies

4. Electronics: Optimize the signal propagation from the anode to readout electronics

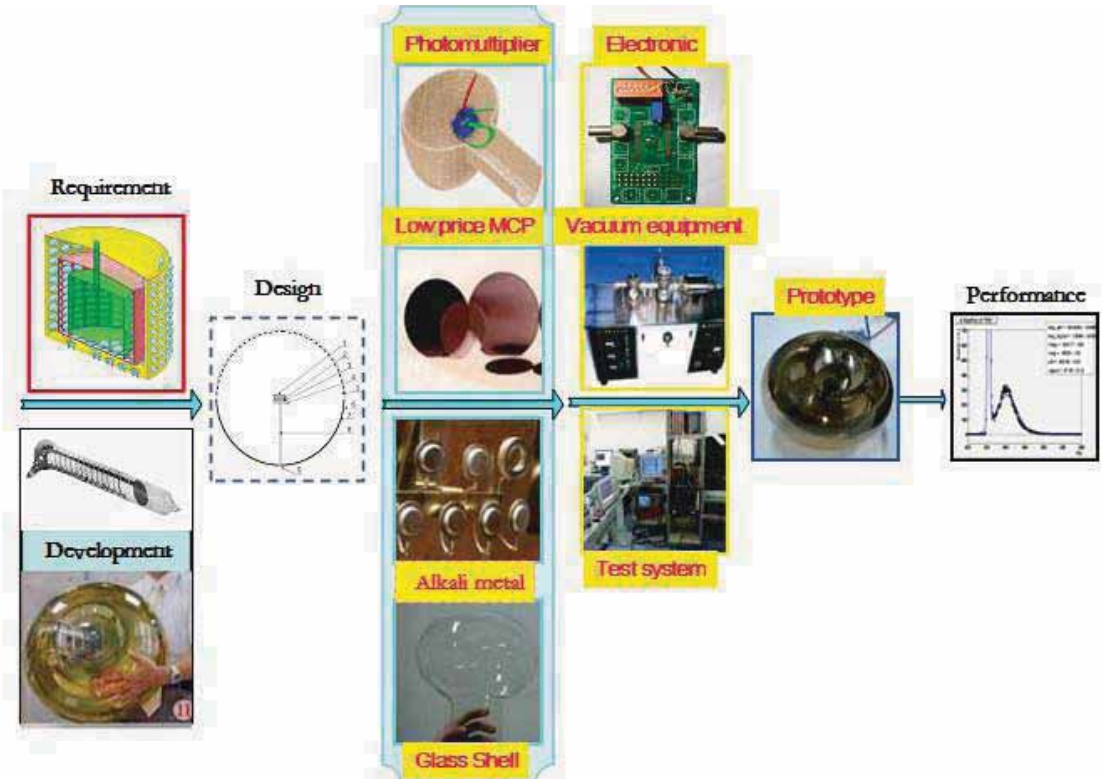

Figure 5.8: Flow chats of the large area MCP-PMT R&D process

5. R&D to fabricate large high vacuum equipment for high throughput PMT production and testing .

6. Vacuum seal: Techniques for hot Indium seal and glass seal

7. Electro-optic: Design and performance simulation

8. Performance tests: Platform for 20 inch PMT testing that can be used in the PMT factory and other places.

5.3.2 Capability of the Collaboration

5.3.2.1 IHEP (Beijing)

The Institute of High Energy Physics, Chinese Academy of Sciences, is the initiator and coordinator of the Large Area MCP-PMT Project. IHEP has extensive experience in nuclear and particle instrumentation, vacuum technology, PMT testing, and PMT applications in large particle physics experiments. The Large Area MCP-PMT Project is organized within the Time-of-Flight detector group, which is a subgroup of the State Key Laboratory of Particle Detection and Electronics at IHEP. Funded partly by the Major Research Instrumentation Initiatives of CAS, the IHEP group has built a PMT Performance Testing Lab. Many PMT parameters such as the single photoelectron (SPE) spectrum, absolute QE and photocathode sensitivity, dark current and dark pulse rate, linearity and gain curves, etc. can be measured quickly and accurately. Figure 5.9 shows graphically the functionality of the PMT testing lab.

The PMT Performance Lab is equipped with a 10000 class clean room, a dark

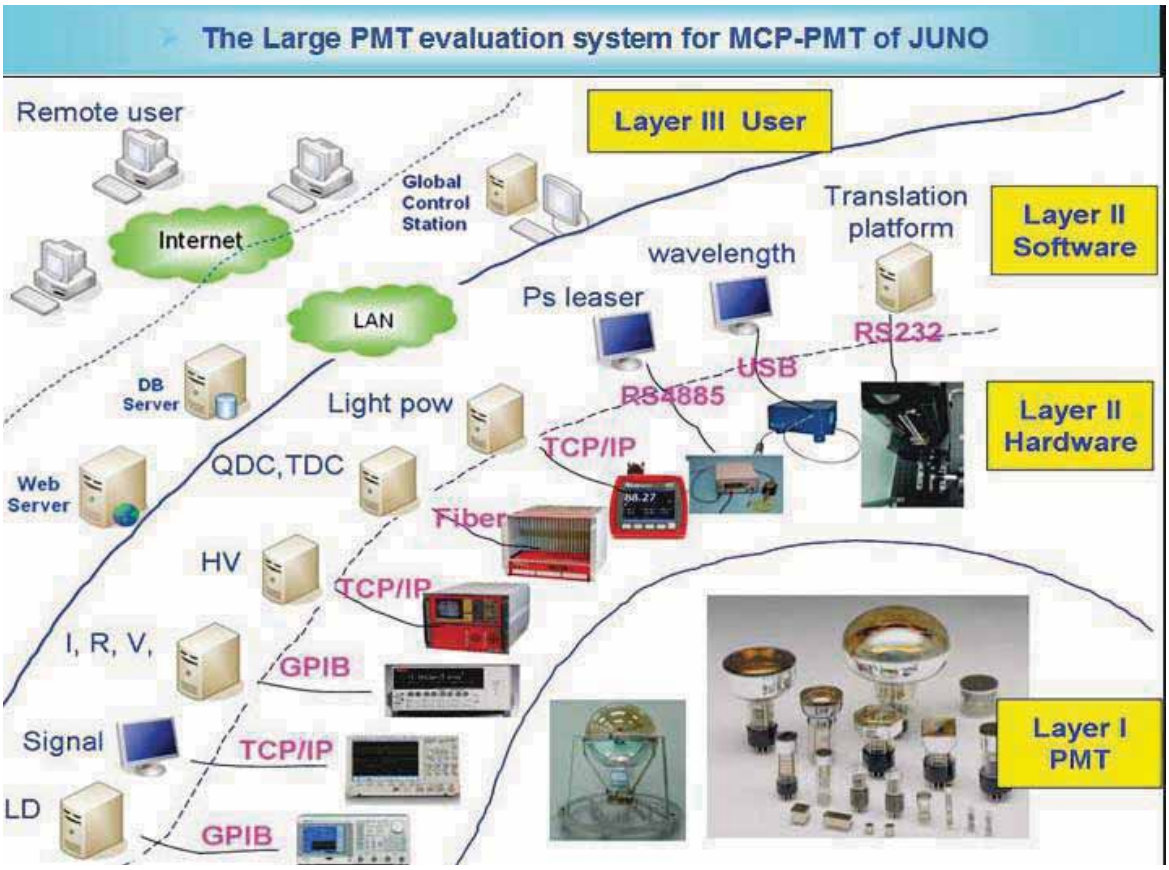

Figure 5.9: Organization of the existing PMT test lab at IHEP

room with electromagnetic shielding, an optic testing system based on LEDs, a variable frequency laser, light flux calibration systems and associated optic components. Advance testing instrumentation, including pA meters and digital oscilloscopes has been installed. With a VME based automated PMT input surface scanning system and testing system for photo gain curves, the absolute photocathode sensitivity (accurate to 1 μA/lm), QE (relative uncertainty $< 2\%$) and single photon transit time spread TTS can be measured in the frequency range 230 nm - 1000 nm (accurate to 50 ps). The dark current can be measured to pA level in the range of 1 pA - 10 nA. This test system is completely automated and the HV, laser wavelength, data recording and data analysis can be controlled by computers.

Moreover, a VME based automated single photoelectron (SPE) spectrum recording system has been built. The SPE testing usually requires the PMT gain to be set to gain $> 10^7$, but with a preamplifier the SPE spectrum can be acquired also at a reduced gain $> 10^5$. Fig. 5.10 shows measurement results by such a system.

In addition, IHEP has recently assembled a small group to perform fundamental studies on MCP optimization to prepare for the MCP-PMT production and to study optic thin films. An ultra low radioactivity analysis system based on a Canberra High-purity Germanium (HPGe) Detector with low background shielding and BGO veto counter has been built at IHEP. This system is used to study the radioactivity of PMT glass and raw material samples.

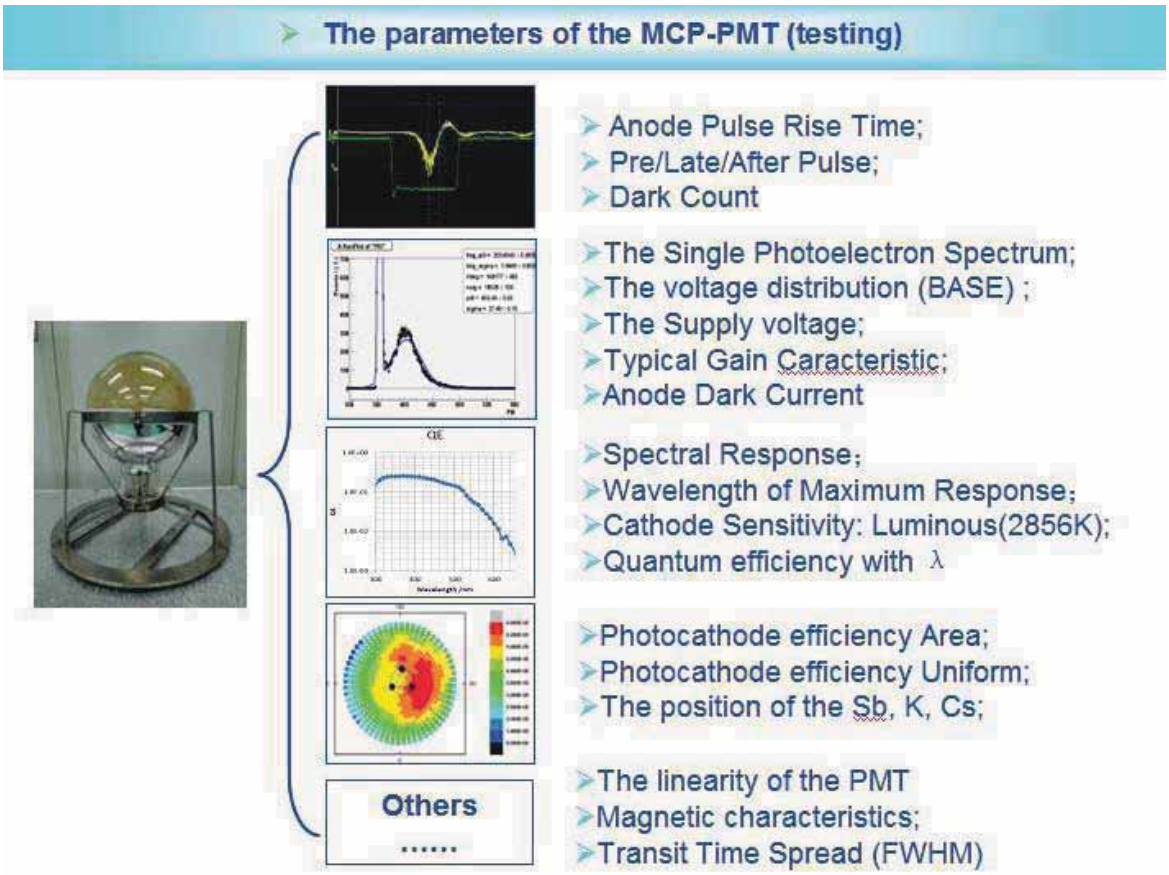

Figure 5.10: PMT measurement results at IHEP

5.3.2.2 XIOPM

The XiAn Institute of Optics and Precision Mechanics (XIOPM) of CAS has extensive experience in research and fabrication of various opto-electronic devices and related technologies. With significant government funding, the State Key Laboratory of Transient Optics, Photonics and Optoelectronics Laboratory and the Photoelectric Measurement and Control Technology Research Department at XIOPM have recently upgraded laboratories with new clean rooms and new equipment, including three research platforms.

1. Platform for opto-electronic devices: Design software for opto-electronic devices, high precision assembly table, plasma surface cleaning, vacuum seal and welding machines, vacuum leak detection systems, photocathode activation station, photocathode testing station, and others. This platform provides basic tools for high sensitivity, high quality opto-electronic devices R&D and fabrication.

2. Platform for high speed electronic fabrication and testing: Software for designing radiofrequency circuits, circuit fabrication facility.

3. Platform for opto-electronics testing: static and dynamic opto-electronics testing system, image intensify and fast DAQ system.

The 8 inch MCP-PMT design and prototype fabrication were started at XIOPM in 2011, followed by the design and fabrication of the equipment needed for the 20 inch MCP-PMTs after some success in their 8 inch MCP-PMT program. In this process,

they have performed extensive opto-electronics simulation, theoretical analysis for high QE photocathode, photocathode fabrication and measurements, MCP functionality studies and optimization. Part of their work is shown in Fig. 5.11. The 20 inch MCP-PMT fabrication equipment, both the non-photocathode transfer and photocathode transfer types, is now almost ready at XIOPM and they are essentially ready to produce some 20 inch MCP-PMT prototypes.

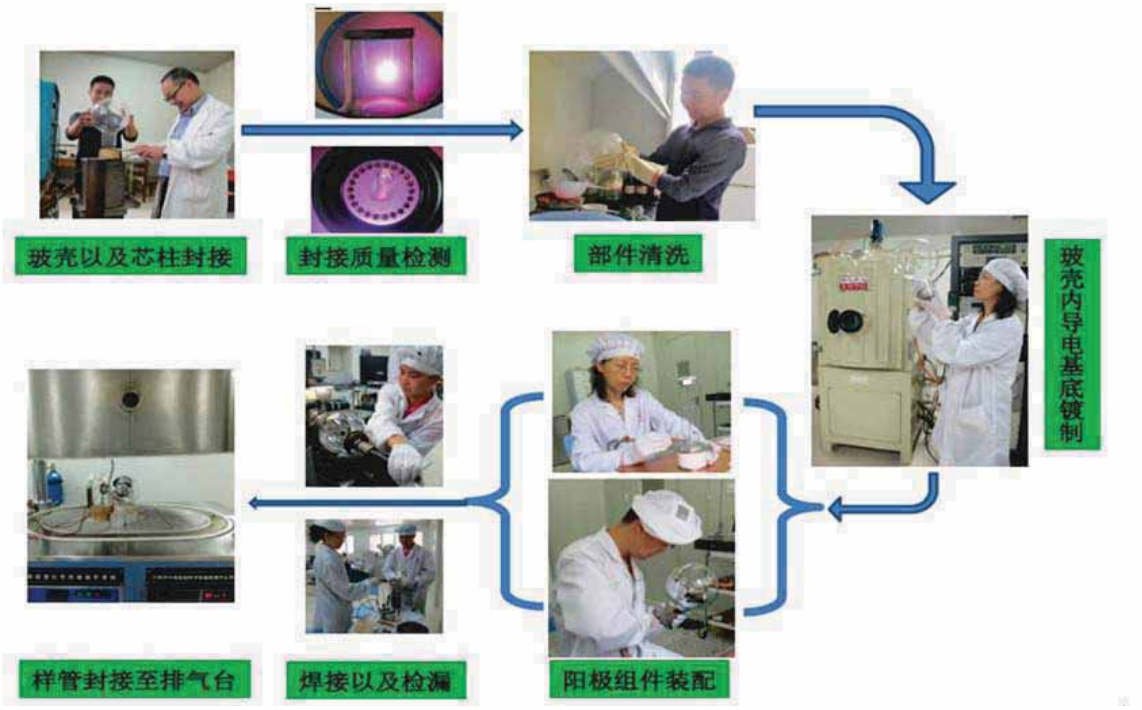

Figure 5.11: MCP-PMT fabrication process at XIOPM

5.3.2.3 NORINCO Group

China North Industries Group Corporation (NORINCO GROUP) is one of five producers of image intensifier tubes based on MCPs. NORINCO has teams of engineers to design and fabricate special equipment for fabricating and testing vacuum opto-electronic devices. In particular it has more than 30 years experiences in R&D, design, fabrication and testing for various photocathodes, MCP and MCP assemblies. Their original technology came from PHOTONIS in the Netherlands. After many years refinement, they are now able to routinely realize multialkali photocathodes in small image tubes with sensitivity exceeding 900 μA/lm, which is higher than that reached by any other manufacturer in the world. For the Large Area MCP-PMT R&D Project, their expertise in bialkali photocathode is assisted by the expertise of No. 741 PMT factory.

For the R&D of Large Area MCP-PMT project, NORINCO GROUP has organized a team of experienced engineers, made available workshops, lab spaces and equipment, and invested a large amount of capital. Three of their platforms, some new and some existing with additional equipment, can be used for various MCP-PMT R&D tasks.

1. MCP Research Platform: Glass ovens, glass fiber pulling machines, MCP slicing machines, automated etching machines, electrode deposition stations, MCP testing station.

2. Platform for low level opto-electronic devices: Software for opto-electronics design and simulation, instrument for high sensitivity photocurrent measurements, photocathode production station, including plasma cleaning, monitoring during photocathode fabrication, thin film deposition stations for high QE photocathodes, photcathode sensitivity testing station, light transmission and reflection testing station, HV power supply design and fabrication and testing, etc.

3. Platform for Large Area PMT R&D and prototyping: Glass lathe, large annealing oven, RF welding machines, large ultrasound cleaning stations, clean baking oven, point welding machines, thin film deposition stations, 20 inch PMT fabrication station using non-vacuum transfer technology, 20 inch PMT fabrication station using vacuum transfer technology (shown in Fig. 5.12), photocathode activation monitoring station, PMT dynamic testing system, PMT static testing system, opto-electronics design software, etc.

These platforms provide a solid foundation for large area MCP-PMT design, R&D, prototype testing and industrialization.

Figure 5.12: Equipment for fabricating 20 inch MCP-PMTs developed by NORINCO using the photocathode transfer technology

5.4 R&D Results and Plan

5.4.1 Status of MCP-PMT R&D

The main achievements up to June of 2014 made by the Large Area MCP-PMT Collaboration are summarized in Table 5.2.

Table 5.2: Achievements and status

Items	Status
8 inch MCP-PMT prototypes	Completed
PMT testing system	8 inch system completed at IHEP and XIOPM 20 inch system near completion at NORINCO
20 inch fabrication equipment	Near completion at XIOPM; Completion at NORINCO
20 inch glass bulb	Completed and met expectations
20 inch Prototypes	Three produced at NORINCO

5.4.1.1 8 inch MCP-PMT Prototype R&D

The Large Area MCP-PMT collaboration had its effort focused on the 8 inch MCP-PMT prototypes in the first two years in order to develop the necessary technologies for the 20 inch MPC-PMT. The opto-electronic design and simulation, photocathode fabrication techniques, design of the MCP assembly, MCP scrubbing, electrode design, etc. have gradually become mature and many difficult problems have been solved. The highest QE achieved in 8 inch MCP-PMT slightly exceeds 30%. The required gain 10^7 has been achieved and the dark current can be as low as 10 nA. The Peak/Valley (P/V) ratios of SPE spectra for prototype tubes have been in the range of 1.6 to 2.5, with one prototype tube reaching 3.8. QE and SPE spectra of the 8 inch MCP-PMT made at NORINCO and tested at IHEP are given in Fig. 5.13.

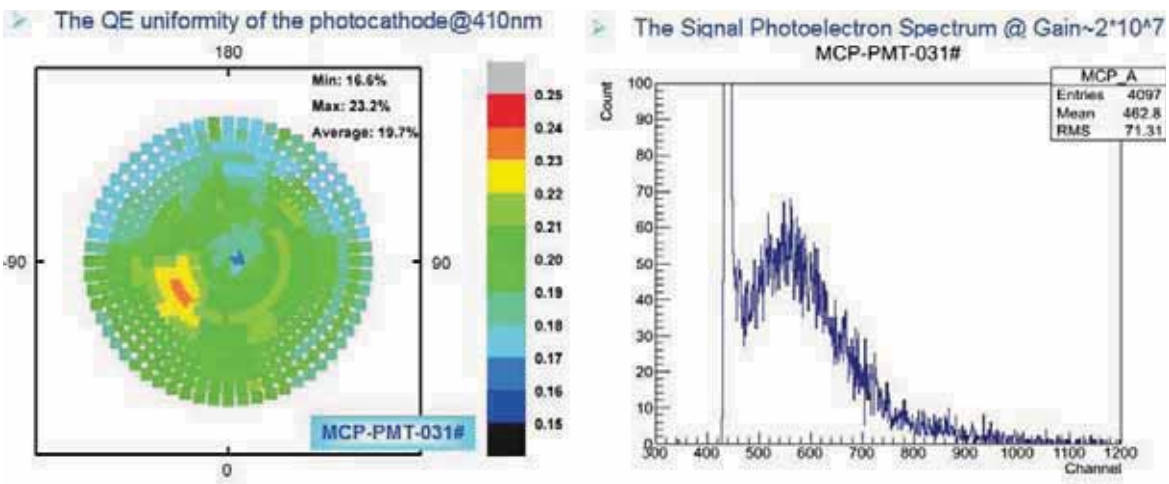

Figure 5.13: QE values and SPE spectra of the 8 inch MCP-PMT

5.4.1.2 20 inch Glass Bulb and Transition Section

As discussed previously, we use the so-called Beijing hard glass (Chinese standard CG-17), that is equivalent to the Pyrex borosilicate glass, to make the 20 inch glass bulbs. The CTE of the CG-17 glass is very low at 0.0000033/°C. It has very high mechanical strength and can withstand various strong acids, alkalis and pure water. Glass bulbs as large as 508 mm are hand-blown by skilled glass technicians. Very few people have such skills and experience in the country. The collaboration was able to identify a glass factory that was very cooperative, which successfully made more than 50 sample bulbs with very good quality. In particular, the achieved mechanical tolerance (< 0.6 mm) is outstanding.

We have tried three methods to make the glass transition section match the low CTE of the Pyrex glass with the slightly higher CTE of the glass used to make the vacuum seal with the Kovar pins and the end flanges. After being sealed and annealed, the evacuated glass bulb was placed in a test container filled with water at 1 MPa pressure (equivalent to 100 meters of water) and observed for 24 hours without any problem. Photos of a 20 inch glass bulb, its visual defect inspection and transition sections are shown in Fig. 5.14.

Figure 5.14: 20 inch glass bulb, its defect inspection and transition sections

20 inch MCP-PMT prototypes were successfully made at the Nanjing factory of the NORINCO in June, 2014 by using the photocathode vacuum transfer equipment. After increasing the pumping capacity of the fabrication station, a QE level of 26% has been reached. More detailed testing is in progress and we expect there will be further improvements when more prototypes will be made. In addition, prototypes of 20 inch MCP-PMT will be fabricated by using the non-vacuum transfer station and comparison will be made of the 20 inch prototypes made by both technologies.

5.4.1.3 Improving the Testing System

The testing system for large MCP-PMTs with spherical photocathodes are different in many aspects from the system used for conventional PMTs. IHEP, XIOPM and NORINCO are all in the process to improve their current testing system. The existing testing system at IHEP is shown in Fig. 5.16. Photocathode sensitivity, QE, dark current, SPE spectra, gain, etc. can be measured. The automated scanning station can accommodate 8 inch PMTs. Test results using this system agree well with parameters provided by Hamamatsu and Photonis for their standard PMTs.

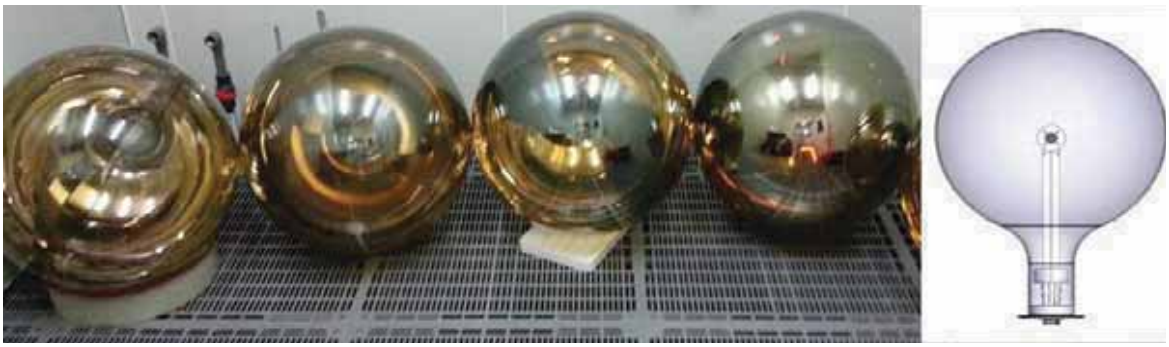

Figure 5.15: 20 inch MCP-PMT Prototype

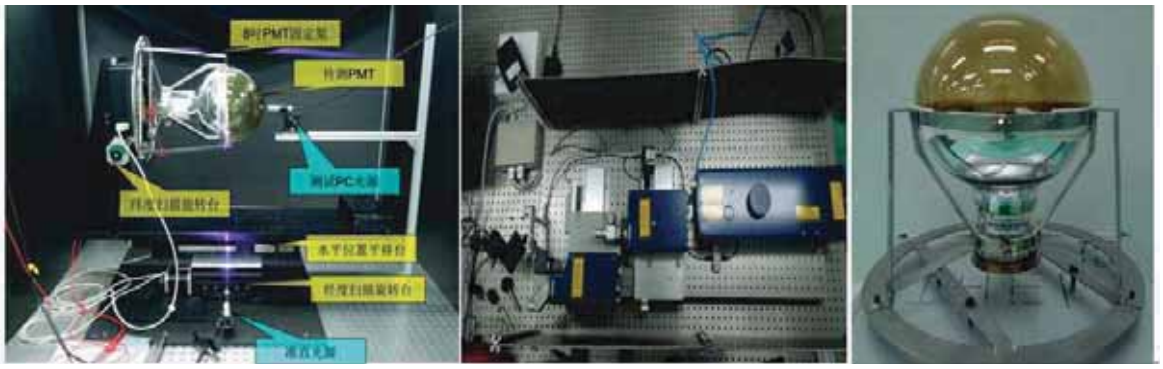

Figure 5.16: PMT test system at IHEP

5.4.2 Status of Commercial PMTs

5.4.2.1 Hamamatsu

In recent years, some PMT manufacturers have been developing so called SBA photocathode and try to use such photocathode in large size PMTs. Hamamatsu has made a new SBA 20 inch R3600-02 with Venetian Blind type dynode. Five such tubes have been recently tested. [1]. Hamamatsu is also developing a 20 inch PMT (R12860) with box and line type dynodes, expecting 93% photoelectron collection efficiency compared to about 80% for the R3600-02. The TTS will also be improved with the box and line type dynodes. The QE of the Hamamatsu 20 inch SBA is expected to be about 30% (Private communication with Hamamatsu) at the sensitivity peak. The sensitivity peak of the current SBA photocathode is located at 390 nm, which matches the requirement of the HyperK water Cherenkov detector, but slight mismatchs the scintillation light, which is mainly emitted at 390 nm to 450 nm. Based on what we know now, we can expect that the PDE of Hamamatsu R12860 may reach 25% for scintillation photons. Another problem of using theR12860 for JUNO is that the size of its effective photocathode is somewhat smaller than the 508 mm outside diameter , which would affect the global useful coverage. Hamamatsu has promised to deliver samples of the R12860 to IHEP in June 2014.

5.4.2.2 HZC Photonics

HZC Photonics in Hainan Province, China acquired PMT production line and related technologies, including the SBA technology, from PHOTONIS, France in 2011. HZC Photonics started their PMT production in late 2013 and now have a 12 inch PMT XP1807 available. Its stated photocathode sensitivity 60 µA /lm is rather low. Their preliminary product, the XP53B20 3 inch circular tube, has a very high peak photocathode sensitivity, listed as 160 µA /lm, but with rather low gain of 6.25×10^5 . HZC Photonics have promised IHEP to produce samples of 20 inch SBA PMT for JUNO soon.

5.5 Risk Analysis

5.5.1 Risk due to Low Photon Detection Efficiency

PMTs are critical components for JUNO. The current MCP-PMT R&D plan and backup options carry certain risks that need to be considered. In order to achieve the required energy resolution of less than 3% at 1 MeV, which is expected to be dominated by photon statistics, high efficiency liquid scintillator with a long attenuation length must be used to detect enough photons when neutrinos interact in the liquid scintillator. In addition, the fraction of the detector surface that is covered by PMT photocathodes must be as large as possible and the PDE of PMTs must be as high as possible. For a 508 mm diameter spherical PMT, assuming glass wall thickness of 4 mm, the maximum diameter of the photocathode would be 500 mm, or 97% of the area of the PMT is actually covered by photocathode. Space needed for anti-implosion covers and gaps among PMTs futher reduce the maximum possible photocathode coverage.

We also must make the QE of PMTs as large as possible. As stated earlier, the PDE of PMTs equals the QE of the photocathode multiplied by the photoelectron collection efficiency (PCE). The goal of the peak photocathode QE for the JUNO PMTs is 38%, which is a very demanding goal. In Fig. 5.17 (taken from Hamamatsu PMT handbook), the solid black curve is the typical cathode radiance sensitivity in unit of mA/W. The typical QE curve can be calculated from it. The computed QE as a function of wavelength is given as the dashed curve in Fig. 5.17 and the scintillation light spectrum is plotted as the red solid curve (linear scale) with double peaks at 400 nm and 425 nm.

It can be seen from Fig. 5.18 that the typical QE of regular bialkali photocathode is 20 - 25% within the wavelength range 350 nm to 450 nm. The value of the peak QE typically is no more than 30% in commercial PMTs. In recent years, Hamamatsu has developed SBA and UBA photocathodes with higher QE. The QEs as functions of wavelengths of these new photocathodes are given in Fig. 5.18. We will not discuss the UBA photocathode since the UBA is only available in small flat faced PMTs made by Hamamatsu. The peak QE of the SBA photocathode shown in Fig. 5.17 is about 35% and the peak sensitivity occurs at 390 nm. There are two important issues to be considered. It can be seen that the spectral response curve of the Hamamatsu SBA is rather narrow and there is a slight mismatch between the SBA spectrum response peak at 390 nm and the scintillation light emission peak at 425 nm. In Fig. 5.18,

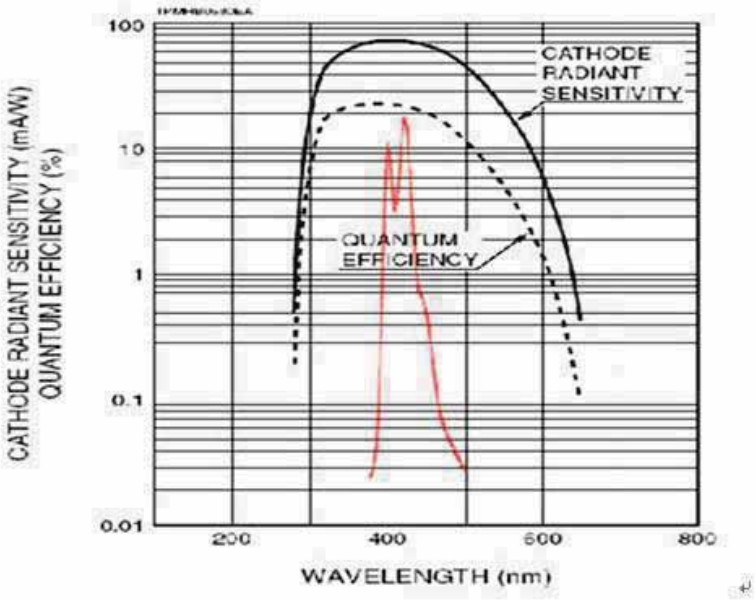

Figure 5.17: Spectral response of common bialkali photocathode and the emission spectrum of liquid scintillator (red curve)

the black curve that is shifted slightly toward longer wavelengths indicates the desired spectrum response, which matches the spectrum of emitted scintillation light better. The second issue is that according to our conversation with Hamamatsu, the typical peak sensitivity they expect for the future 20 inch SBA PMT is 30%, not the 35% given in their published documents. The average QE for scintillation light is expected to be less than 30%. With the stated 93% photoelectron collection effiiency of the new SBA R12860, we speculate that its average PDE may be less than 25% due to the spectral response mismatch discussed above.

The specified peak QE for JUNO PMTs as listed in Table 5.1 is 38% and we hope the average PCE of JUNO PMTs can be higher than 30% in the wavelength range 400 nm to 450 nm. Therefore one of the critical risks is whether or not we can achieve this. Our approaches to limit this risk are the following.

1. Transmission + Reflection Photocathode Use the spherical photocathode, combining the power of transmission and reflection photocathodes. We hope the targeted peak QE 38% and average QE > 30% within 400 - 450 nm can be achieved by optimizing the photocathode design and fabrication process.

2. Transmission photocathode + reflection film Coat a layer of thin film with high reflectivity in the bottom half of the sphere to reflect photons that have penetrated the transmission photocathode back and convert these photons into photoelectrons.

5.5.2 Risk Related to MCP Aging

The operational lifetime of JUNO is 20 years and the working lifetime of the PMTs must also be greater than 20 years. It is expected that as long as the vacuum in the

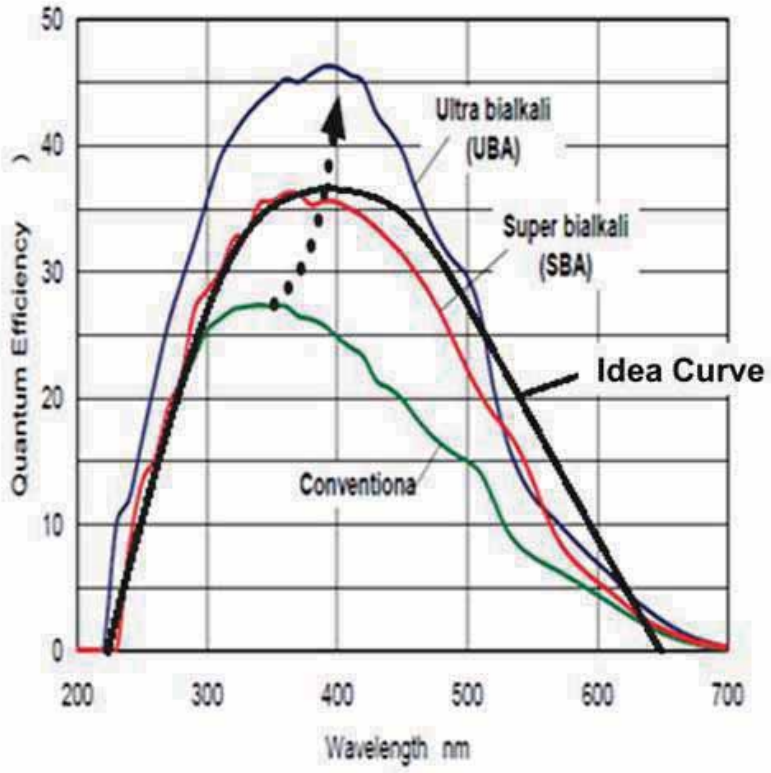

Figure 5.18: QEs vs. wavelengths for conventional bialkali, SBA and UBA photocathodes

MCP-PMTs can be maintained, their lifetime will mainly be determined by the gain reduction due to MCP aging. It is expected that in the completely dark environment of JUNO, accumulated charges will mainly be caused by the photocathode thermal noise and the dark current of MCPs. At gain 10^7 and dark counting rate 10 kHz (equivalent to dark current 16 nA), the accumulated charge due to photocathode thermal emissions will be 10 C for 20 years operation. The dark counting rate of a PMT is typically measured by counting dark pulses with a threshold of 0.25 pe. The true dark current, including the MCP dark current and dark current from other sources, can be much higher than the 16 nA used in the above estimations. Some of this additional dark current should be considered when the MCP aging effect is evaluated.

At this level of charge accumulation, MCP aging can become a problem for MCP-PMT operation. The charge accumulation level of the MCPs developed by NORINCO can reach 30 C. In addition, PMT anode assembly typically has a gain of 3 - 5 and the charge accumulation is reduced by the same factor if such an anode design is used. This implies that the accumulated charge that the MCP-PMT can be operated with can reach the level of 100 C.

In order to control the dark pulse rate and dark current due to MCPs, we are testing two different methods to fabricate the MCP-PMTs. The photocathode vacuum transfer method has separate vacuum chambers for photocathode fabrication and MCP processing and can in principle lower the risk of MCP contamination by

alkali materials, thus achieving lower dark current.

In the past few years, MCP manufacturers and research labs have developed a new type of MCP that use the ALD technique to deposit a thin secondary electron emission layer on top of a resistive layer on the wall of the microchannels of the MCPs. It has been shown that the lifetime of ALD coated MCPs can be an order of magnitude higher than the conventional MCPs. IHEP has started a R&D program to develop MCPs using ALD technology.

5.5.3 Risk due to PMT Radiation Background

5.5.3.1 Radiation Background Requirements

The PMT radiation backgrounds are dominated by the radioactive elements, most importantly ^{238}U, ^{232}Th and ^{40}K in the glass bulb. In the current 20 inch spherical MCP-PMT design, the weight of the glass bulb is 9 kg. According to the current detector physics simulation, the upper limits for ^{238}U, ^{232}Th and ^{40}K contents in the PMT glass are 12.1 ppb, 26.1 ppb and 1.5 ppb, respectively. For comparison, the contents of these elements in Hamamatsu R5912 8 inch PMT glass are 153 ppb, 335 ppb and 18.5 ppb, while they are 540.3 ppb, 568.3 ppb and 75.2 ppb in the 20 inch R3600-02 PMTs. The radioactivity levels of Hamamatsu PMTs are many times higher than that allowed by JUNO. In a sample of regular CG-17 borosilicate glass, the type of glass to be used to fabricate the 20inch bulbs for MCP-PMTs, ^{238}U, ^{232}Th and ^{40}K contents are measured to be 349.1 ± 18.7 ppb, 851.2 ± 72.8 ppb and 26 ± 3.1 ppb, which are 29, 32 and 17.5 times higher than the limits for JUNO PMTs. Clearly new glass materials with lower radioactive contents must be developed.

In order to meet the required extra low radiation background requirements, we must use ultra-pure raw materials for making the glass and also control the possible contamination occurring in the material handling and glass melting process. Chemical composition of the GG-17 glass and of raw materials are listed in Table 5.3.

Table 5.3: Chemical composition of the GG-17 glass and raw materials

Items	Status				
Compostion	SiO2	B2O3	Na2O	Al2O3	NaCl
Content (%)	80.0	13.0	4.0	2.5	0.5
Raw materials	Quartz sand	Boric acid	Na2CO3	AlOH	Salt

We have acquired a large number of raw material samples from different manufacturers in different regions of China and measured contents of the three radioactive elements in these samples carefully. We have identified suppliers who can provide the necessary raw materials with ^{238}U, ^{232}Th and ^{40}K contents that are low enough to meet JUNO PMT requirements. Obviously these high purity materials must be handled properly to prevent any contamination. We have also investigated the possibilities for contamination during the glass melting process. The most worrisome concern is that at high temperature radioactive elements can be introduced from crucibles and other debris into the molten glass in the oven. A Platinum crucible can mostly eliminate this problem, but it would be a very expensive solution. We believe corundum crucibles commonly used in Pyrex glass factories should be good enough based on the

radiation background test for AlOH. So far, for the 50 or so 20 inch glass bulbs that have been made, regular raw materials were used and we know their radiation levels are very high. We have not attempted to make low radiation background PMT bulbs yet.

5.5.4 Risk due to Nonuniformity of MCP PCE

The photon detection efficiency (PDE) of PMTs can be expressed as $PDE = QE * PCE$, where QE is the photocathode quantum efficiency and PCE is the photoelectron collection efficiency of the electron multiplier. In our case the electron multiplier is the MCP assembly. With a spherical glass bulb and the photocathode vacuum transfer approach, we believe it is possible to fabricated completely uniform photocathode since we can place the evaporation alkali sources at the center of the sphere. To make the photoelectron collection completely uniform in our current MCP-PMT design is more difficult, since photoelectrons generated by a spherical photocathode arrive at the flat MCP input surface from different angles and they may have different efficiencies of collection and amplification. We are following several possible approaches to find remedies for this potential problem.

1. Optimize the focusing design to limit the incident angular spread of photoelectrons.

2. Optimize the MCP assembly design to add a metal mesh in front of MCP and coating the MCP with MgO or Al2O3 thin film, which has a high secondary electron emission coefficient, or use other schemes to improve the MCP photoelectron collection. Fig. 5.19 shows the metal mesh and MCP coating schemes.

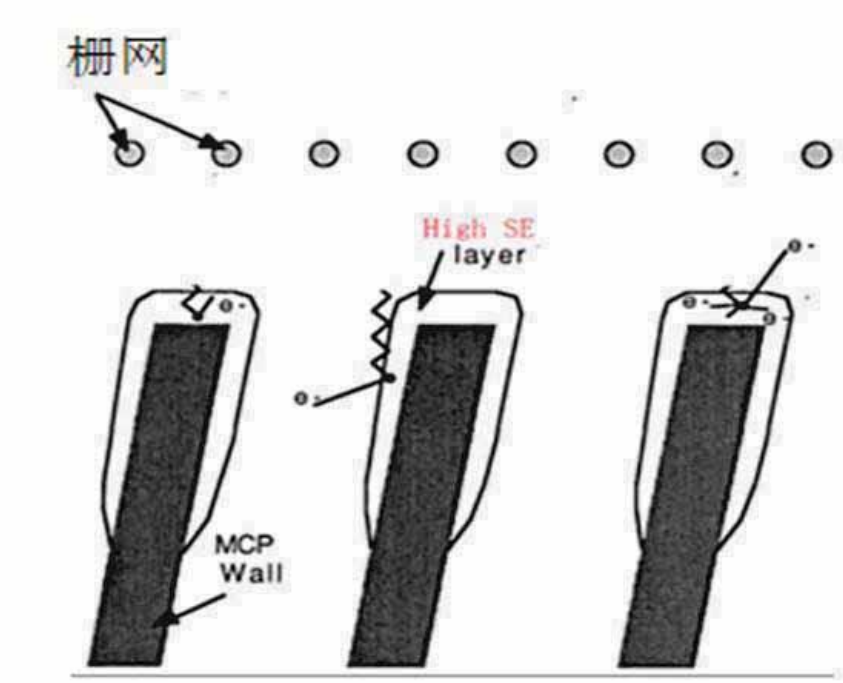

Figure 5.19: The MCP coating scheme

3. Further increase the gain saturation level of the second MCP such that the output

pulse heights are less dependent on the numbers of secondary electrons produced by the photoelectron striking the first MCP.

5.6 Schedule

The global schedule from prototyping to mass production is shown in Table 5.4.

Table 5.4: the schedule of the mass production

Year	Tasks	Parameters
2013	8inch prototype	QE $\geq$ 25%, P/V $\geq$ 1.5
2014	20 inch prototype	QE $\geq$ 30%, P/V $\geq$ 2.0, other parameters meet specs
2015	Engineering design	QE $\geq$ 30%, P/V $\geq$ 2.0, other parameters meet specs and Yield $\geq$ 80%
2016	Preproduction	1000 20inch PMTs
2017	Mass production	5000 20inch PMTs
2018	Mass production	5000 20 inch PMTs
2019	Mass production	5000 20inch PMTs

Bibliography

[1] Y.Nishimura, RCCN, University of Tokyo, Measurement of Large Aperture Photo-Detectors in a Water Tank, 4th Hyper-Kamiokande open meeting 28 Jan., 2014.

Chapter 6

The Central Detector Calibration System

6.1 Requirements on the Calibration System

The neutrino oscillation signal in the JUNO experiment will be quantified by the measurement of the positron energy in the inverse beta decay (IBD) interaction. The oscillation patterns are driven by the atmospheric mass-squared splitting Δm^2_{32} and the third neutrino mixing angle θ_{13}, and the solar mass-squared splitting Δm^2_{21} and the solar mixing angle θ_{12}. The interplay of the two contains the neutrino mass hierarchy (MH) information through the energy dependence of the effective atmospheric mass-squared splitting. Therefore, one needs to determine the positron energy spectrum with high precision in order to determine the neutrino MH and to carry out the precision measurements of the oscillation parameters. As stressed in Chapter 1 as well as in independent studies [1], the JUNO central detector energy resolution needs to be better than 3% at 1 MeV (1.9% at 2.5 MeV where the MH signal lies), and the absolute energy scale uncertainty to be much better than 1% for the MH determination. On the other hand, the requirement on the energy resolution and the energy scale uncertainty is more relaxed for the sub-percent precision measurements of the oscillation parameters.

There are two main contributors for the energy resolution of the liquid scintillator (LS) detectors. The first is the number of collected scintillation photons, which is influenced by the intrinsic light yield and attenuation length of the LS, the photocathode coverage of the detector, and the quantum and collection efficiencies of the photon detectors. The second is the non-uniformity of the detector response, governed by the detector geometry as well as the optical properties of the relevant detector components (e.g., the attenuation of the liquid scintillator and acrylic vessel). Nevertheless, the non-uniformity can in principle be reliably evaluated by deploying radioactive sources with known energies inside the detector during the calibration data taking.

Based on experiences from the Daya Bay experiment, liquid scintillator detector has two major sources of energy non-linearity. The first one is the intrinsic energy non-linearity of the liquid scintillator, which includes the quenching of the scintillation light and the amount of the Cerenkov light within the energy ranges of interest. The second one is the energy non-linearity introduced by the electronics. A precise determination of both effects to sub-percent level is the primary challenge that the JUNO calibration system has to confront. The most reliable handle on the non-linearity effects is through

the *in-situ* calibrations, since the dependence on particle types as well as the Cerenkov radiation is difficult to evaluate in a bench setup elsewhere.

To accurately address both the the non-uniformity and non-linearity in the detector energy response, the calibration system is required to deploy multiple sources (light or radioactive) to a wide range of positions inside the detector. Specifically, a summary of different types of detector response calibration envisioned is shown in Table 6.1. In addition to actively deploying sources, the reconstructed background events can also provide critical inputs to the detector response.

Based on the considerations above, we set the following requirements to the calibration system,

1. In order to carry out periodical calibrations, the most frequently used calibration system should be fully automated (similar to the ACU system in the Daya Bay experiment). It should be simple and extremely reliable. Such a subsystem should be able to deploy multiple radioactive and light sources into the detector, likely along the central axes;

2. The calibration system is required to access the off-center positions in order to control the position non-uniformity. The source deployment to such locations is likely to occur, on the other hand, less frequently compared to that of the central axis;

3. Gamma source energies should cover a significant part of the IBD energy spectrum (1-7 MeV). Positron and neutron sources are also needed to calibrate the detection efficiencies;

4. A dedicated deployment system that has nearly $\sim 4\pi$ coverage to the central detector should be considered;

5. The absolute source positions should be controlled to better than 5 cm (preliminary Monte Carlo simulation has shown that the event vertex reconstruction accuracy can be $\sim$ 10 cm);

6. An accelerator that can supply mono-energetic e^+ and e^- beams is important to measure the positron non-linearity directly;

7. Multiple types of particles such as α, e^-, γ, and e^+ should be deployed to understand the LS quenching and Cerenkov light contribution to the energy non-linearity;

8. With the photo-luminescence effect in liquid scintillator, a UV laser and optical fiber system has superior properties than those of an LED. Such more stable and versatile laser systems should be considered as light sources to calibrate the nonlinearity of the photo-sensors and the electronics.

Considering all these requirements and the mechanical constraints, we selected the following mutually complementary calibration options for further investigations.

1. A central automated calibration unit (ACU) for vertical source deployment;

2. A rope loop system for off-center source deployment;

Table 6.1: Summary of the different types of calibration goals, methods and requirements

Calibration Goal	Calibration Method	Requirements
PMT gain	Low intensity light sources at the center	Periodical, low intensity, automatic
Light yield (energy scale)	Radioactive sources at the center	Periodical and automatic
PMT timing, time walk	Light sources at the center	Periodical and variation in the light intensity
Optical property of scintillator	Radioactive sources at various positions	Periodical with optimized positions
Boundary effect of energy response	Pre-installed guide tube system with radioactive sources	Scan the detector boundary and 1-2 times during whole period compare source and cosmogenic data
Detector response non-uniformity	Radioactive sources at various positions and full volume cosmogenic data	Need based calibration frequency, targeted positions, compare source and cosmogenic data
Capture time non-uniformity	Neutron source at various positions	Need based calibration frequency, targeted positions, compare source and spallation neutrons
Energy non-linearity	Various radioactive sources	Full calibration with various sources 1-2 times during the entire period, compare source and cosmogenic data, periodical check for 2-3 types of sources at targeted positions,
Energy non-linearity of positrons	Mono-energetic positrons to the center and various position along the central axis	Need based calibration frequency
Position-dependent energy non-linearity	Various radioactive sources at fine position coverage	1-2 times during the whole period, compare source and cosmogenic data, periodic check at targeted positions with 1-2 sources

3. A pelletron system which can provide mono-energetic positron beams;

4. Remotely operated under-liquid-scintillator vehicles (ROV) for "4π" coverage;

5. Pre-installed guide tubes; and

6. A diffuse system that can introduce short-lived radioactive isotopes into the central detector.

The ACU, the rope loop system and the ROV can all scan the interior of the central detector but with different ranges and frequencies - we will describe them together. The pre-installed guide tube system is uniquely designed to understand the boundary effects of the central detector. The pelletron calibration system provides an excellent bench mark of the energy non-linearity for the IBD. A diffuse source system can validate the energy non-linearity and its position dependence. We will describe these three systems separately.

6.2 Conceptual Designs

6.2.1 Housing and Interfaces

Calibration sources are deployed into the detector through the top chimney. To avoid Rn contamination, the entire calibration system should be enclosed in a clean and Rn free volume ("calibration house"), as shown schematically in Fig. 6.1.

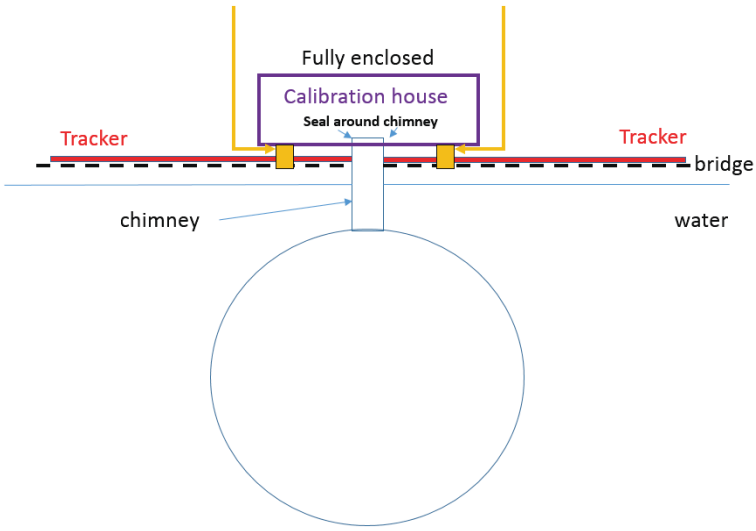

Figure 6.1: Illustration of a seal calibration house on top of the detector.

A concept of the calibration house is shown in Fig. 6.2. The ACU system is located at the top. Two rope loop systems are placed inside the house. The source changing area can be accessed via two glove boxes to allow manual operation. The ROV system is also kept inside the house and moved along the rails attached to the roof.

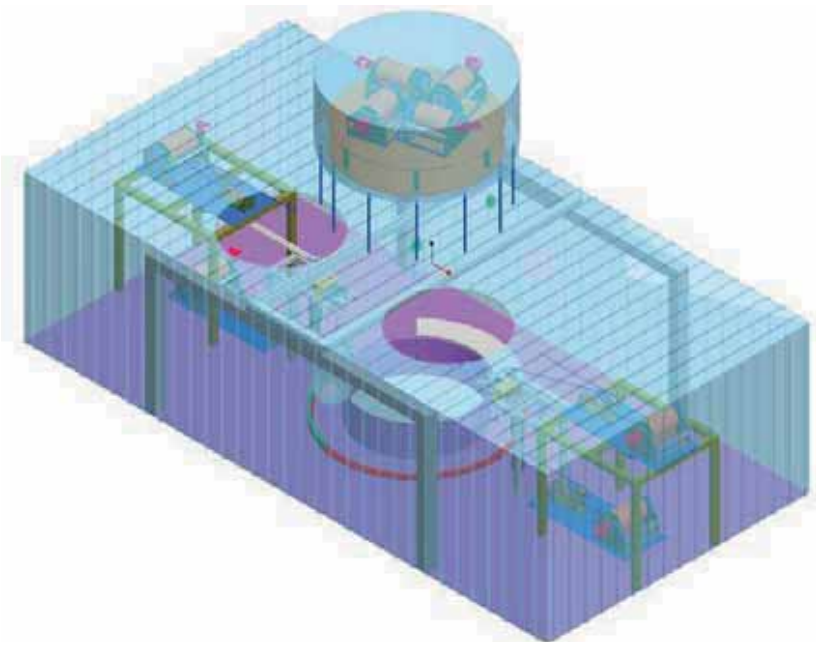

Figure 6.2: Concept of a calibration house.

Table 6.2: Radioactive sources under consideration in JUNO.

Source	Type	Radiation
^{40}K	γ	1.461 MeV
^{54}Mn	γ	0.835 MeV
^{60}Co	γ	1.173 + 1.333 MeV
^{137}Cs	γ	0.662 MeV
^{22}Na	e^+	annil + 1.275 MeV
^{68}Ge	e^+	annil 0.511 + 0.511 MeV
^{241}Am-Be	n, γ	neutron + 4.43 MeV
^{241}Am-^{13}C or ^{241}Pu-^{13}C	n, γ	neutron + 6.13 MeV
^{252}Cf	multiple n, multiple γ	prompt γ's, delayed n's

6.2.2 Sources

6.2.2.1 Routine Sources

To set the energy scales and to calibrate the positron and neutron detection efficiencies, radioactive sources for JUNO include routine gamma and positron sources together with neutron sources with correlated high energy gamma ray emissions, shown in Table 6.2.

To minimize the risk due to contamination of the radioactivities, the enclosure of these sources should be thin-walled ($\sim$ mm) stainless steel (SS) capsule, enclosed by a round-headed acrylic shell to ensure chemical compatibility with the liquid scintillator. The deployment rope, made with SS, shall be robustly attached to the SS source enclosures. Two steel weights are attached above and below the source to maintain a minimum tension in the rope. A typical source/weight assembly used in Daya Bay is shown in Fig. 6.3.

Simulations are underway to optimize the geometry in order to minimize impacts of

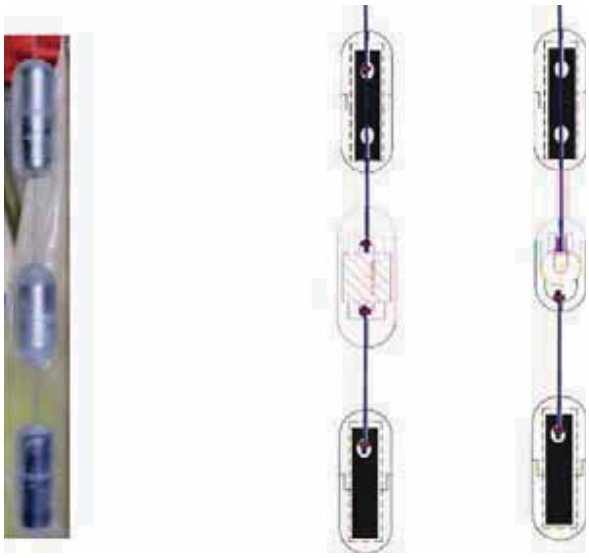

Figure 6.3: Illustration of a typical source/weight assembly used in Daya Bay, envisioned for JUNO as well.

the source assembly to the energy scale. In Fig. 6.4 a typical ^{60}Co spectrum is shown. The "dead volume" of the source assembly affects the low energy shoulder, but has a much smaller effect on the full absorption peak. The optical shadowing of the source assembly, on the other hand, will bias the location of the full absorption peak.

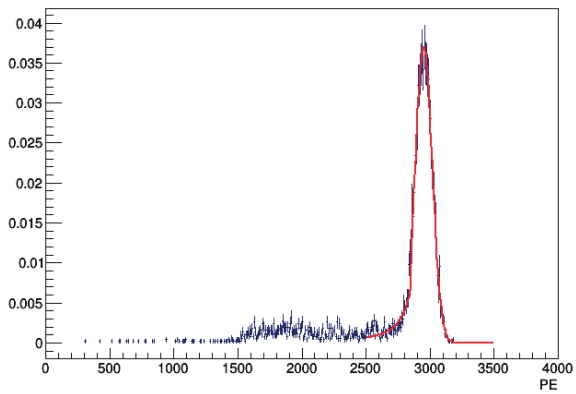

Figure 6.4: an example JUNO Monte Carlo spectrum in photoelectrons for the ^{60}Co source with source geometry.

6.2.2.2 Mini-balloon

In order to study the liquid scintillator response to charged particles (electrons, positrons, α's) thereby to control the quenching effects, we are pursuing a "mini-balloon" concept (Fig. 6.5). Radioactive isotope is loaded into the liquid scintillator inside a small, thin-walled, and transparent balloon ($\sim$ 10 cm OD). The balloon is further enclosed by an acrylic cylinder ($\sim$ 20 cm OD) filled with undoped liquid scintillator. Such a design will minimize the energy loss of the charged particles across the balloon wall to simulate real events, while maintaining a double encapsulation of the radioactive

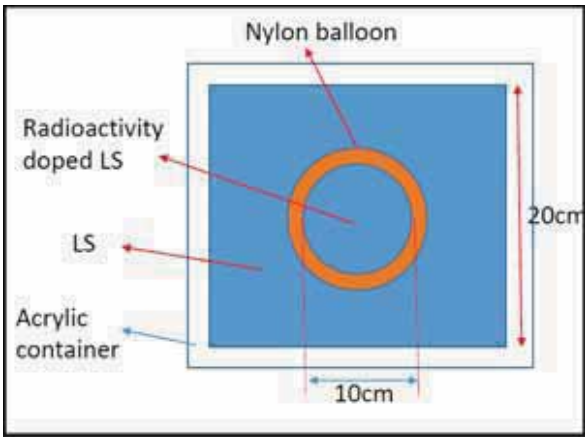

Figure 6.5: The mini-balloon source concept.

isotopes. A comparison of the ^{40}K-loaded 10 μm thick balloon and that without the balloon from the Monte Carlo is shown in Fig. 6.6, in which the bias in beta energy is estimated to be less than 0.3%. One important advantage is that the choice of the

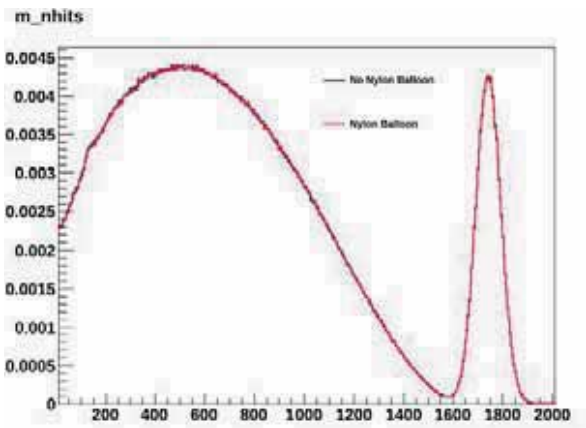

Figure 6.6: Comparison of ^{40}K spectra with a 10 μm balloon and without.

dopant in the balloon is very versatile, for example ^{222}Rn (α's), ^{40}K (γ's and β's), ^{137}Cs (γ's, β's and conversion electrons), ^{68}Ge (positrons), and even short-lived isotopes. The source deployment system can then take the source into given locations inside the detector for calibration.

6.2.2.3 Pulsed Light Source

Unlike the radioactive sources, the pulsed light source can generate photons at a given time with tunable intensity. These features are important to calibrate the gains of the photomultipliers as well as the response of the electronics system. Based on the experience in the Daya Bay calibration system, the stability of the pulses from light emitting diodes or LEDs ($\sim$5 ns timing) is not as good as pulsed laser system (which could achieve a ns level timing precision). Furthermore, a UV laser of $\sim$260 nm wavelength can excite the LAB molecules thereby producing photons with similar timing characters as those generated by real particle interactions. In addition, commercial

light sensors, e.g., Si diode can monitor the intensity of the laser pulses to very high precision. Based on these considerations, we are developing a UV laser system coupled to a flexible optical fiber with a diffuser sphere at the end to achieve a stable, uniform, tunable, and deployable light source for JUNO.

6.2.3 Source Deployment Systems for the Detector Interior

As mentioned in Sec. 6.1, three complementary subsystems are under consideration, the ACU system, the rope loop system, as well as the ROV system. They cover different ranges inside the central detector, and are envisioned to be used at different frequencies. In addition to the mechanical means to position a source, independent source locating systems will be critical to ensure the required high position accuracy.

6.2.3.1 Source Locating Systems

Although the rope loop can position itself via the lengths of different rope sections, mechanical uncertainty such as deformation of the ropes would introduce uncertainty to the absolute source position. Similar uncertainty arises in the ROV system as well. A dedicated source locating system is required to determine the source position to better than 5 cm.

Two options are being considered. The first option is an ultrasonic system with an array of ultrasonic receivers and an ultrasonic emitter attached to the source. The emitter generates pulsed sonar waves and the receivers reconstruct the origin via the timing or phase difference. The wavelength of 150 kHz sonar wave is ~ 1 cm, introducing negligible uncertainty. The dominating systematics is the positioning accuracy of the receivers as well as the speed of sound in LAB under different temperature/pressure conditions. Reflections at the interface are also systematics under study. To allow package of the sound waves, the receivers have to be installed in the inner wall of the vessel if the central detector housing is acrylic, and not so critical if the balloon option is adopted. In principle, the larger the receiver array, the higher the positioning accuracy. Studies are undergoing to optimize the array. A typical arrangement is shown in Fig. 6.7, with 9 redundant receivers mounted on the wall.

An alternative technology is to locate the source via optical cameras (CCD) and one reconstruct source position via image analysis. Such a system is used by the Borexino experiment. The infrared lighting of the CCDs poses minimal risk to the PMTs. Alternatively, a battery driven LED can be attached to the source assembly to ease the analysis.

6.2.3.2 ACU

The Automated Calibration Unit (ACU) system is a unit very similar to that used in Daya Bay, capable of deploying a few different sources along the central axis of the detector. As illustrated in Fig. 6.8, four source deployment units will be arranged on a turntable, which can select the source to be deployed. A hole on the bottom plate of the ACU will be aligned to the center of the chimney to the central detector. Three of the sources (one light source and two radioactive sources) will be attached permanently to three deployment units. The fourth unit will have a changeable source fixture, providing flexibility for the attachment of special sources. The operation of the

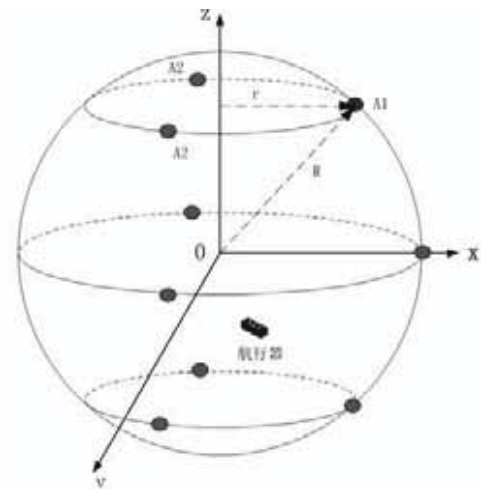

Figure 6.7: A typical placement of the ultrasonic receivers.

system will be fully automated to ensure routine (weekly) deployment of calibration sources with high reliability. Based on the experience from the Daya Bay experiment, a weekly deployment of the light source allows PMT gain calibration to subpercent precision. A weekly deployment of a gamma source, e.g., ^{60}Co, is sufficient to track the slow drift (∼1% per year) of the overall energy scale due to changes in detector properties. Lastly, a routine deployment of the neutron source can ensure the stability of the detection efficiency.

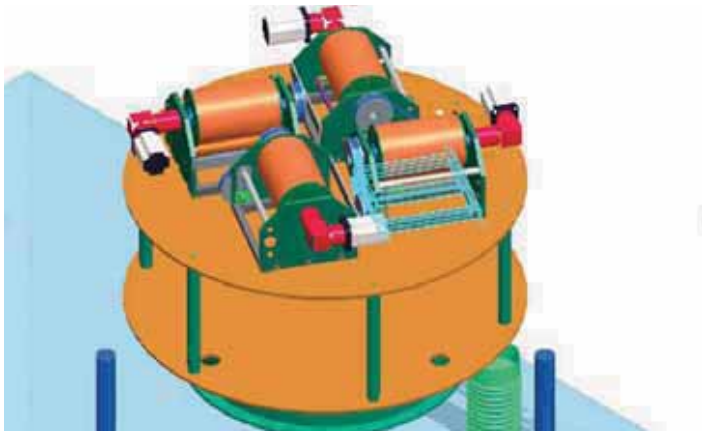

Figure 6.8: A sketch of the ACU system.

6.2.3.3 Rope Loop System

The concept of a rope loop system is similar to that used in the SNO experiment, illustrated in Fig. 6.9. The source deployment position can be controlled by adjusting the lengths of sections A and B of the rope. In this design, one of the hanging points is through the central chimney, and the other anchor is located at around 30∘ latitude, allowing a theoretically 90% 2-dimensional coverage of a half vertical plane.

A sketch to illustrate a deployment sequence is shown in Fig. 6.10. With section A going through the central chimney sources can be taken out of the detector and get

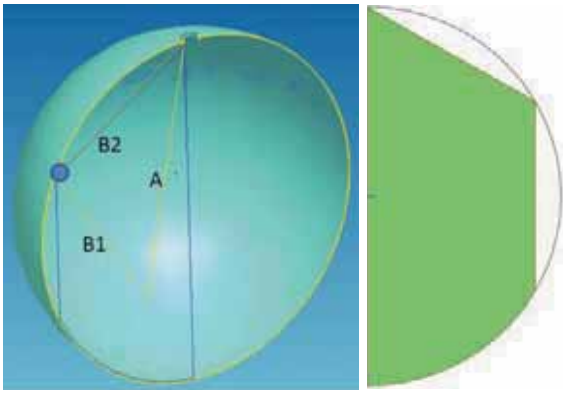

Figure 6.9: Rope loop solution and its 2-dimensional coverage

changed. We are developing a scheme which allows both an automated source change while maintaining the option of manually changing the source via glove box.

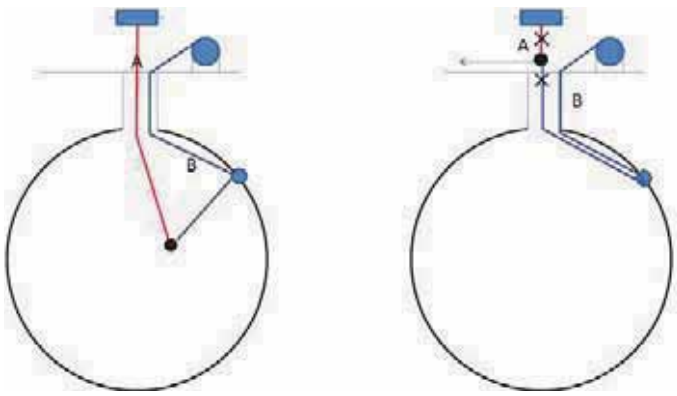

Figure 6.10: 3-point hang design and volume coverage

The overall layout of the rope loop system on top of the central detector is shown in Fig. 6.11. Two independent rope loop systems are being considered, each covering a half vertical plane to allow some control of the azimuthal symmetry of the detector response. Each system has two spool drives A and B to adjust the lengths of the A/B rope in a synchronous fashion. Rope A goes through a pulley, which is attached at an end of an extendable lever arm. During the deployment, the level arm is extended to move the pulley towards the center of the chimney to lower the source into the detector. Once a deployment is completed, the source is retrieved by extending B rope and shortening A rope. Once the source is out, the pulley arm gets retracted to the side so that the source change operation will be performed away from the chimney.

Alternative designs allowing three-dimensional coverage are also under considerations. For example, if the anchor point is allowed to move on the latitude circle, a 3-dimensional deployment can be made possible. However, with a large diameter circle attached to the inner surface of the detector, maintaining a smooth rail and reliable drive of the anchor point is a non-trivial engineering challenge. Another alternative 4-point rope design is shown in Fig. 6.12. Three hang points, separated by 120∘, are placed around the equator of the central detector. Three ropes, each going through one hanging point and the central calibration port, will connect to the source. By

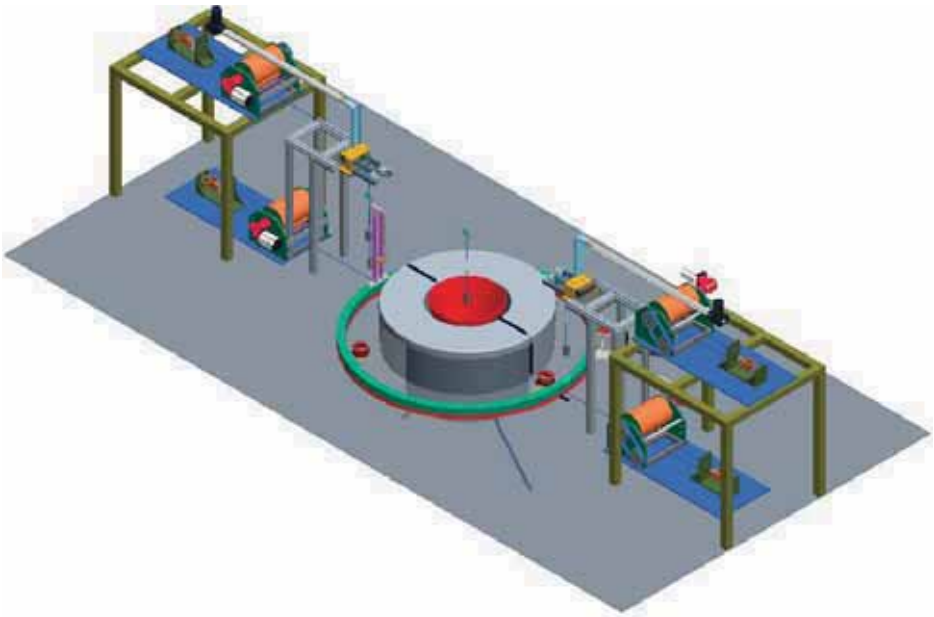

Figure 6.11: An overview sketch of the rope loop system.

adjusting the length of these three ropes, one can achieve a volume calibration in the bottom half of the sphere. With a fourth rope connecting the source directly from the central calibration port, the volume calibration on the upper sphere can be performed. In general, three dimensional rope system would introduce significantly more mechanical complexity. In such a case, a ROV system described below would become a viable alternative.

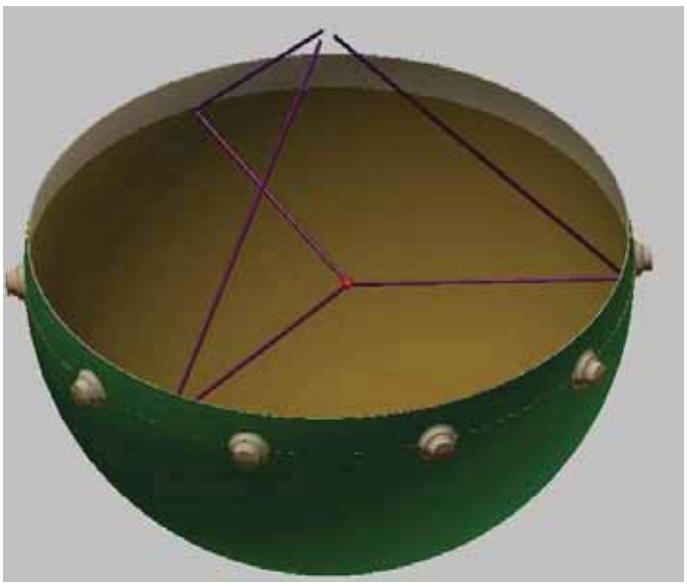

Figure 6.12: Illustration of a 4-rope design.

Details of a single spool drive in the rope loop system are shown in Fig. 6.13. The spool in the ACU will be under an identical design. The spool will be made either with acrylic or PTFE. Helical grooves with ∼mm separation will be machined on the spool, and the deployment cable of less than 1.5 mm diameter will be wound into the grooves

without overlap. The rope capacity of each spool is set to be 50 m. Several additional measures will be implemented to avoid rope slipping out of the groove, including a spring loaded Teflon press to constrain the rope, a load cell to constantly monitor the tension in the cable, as well as a co-moving spooling tracker so that the rope always gets unwound perpendicular to the spool.

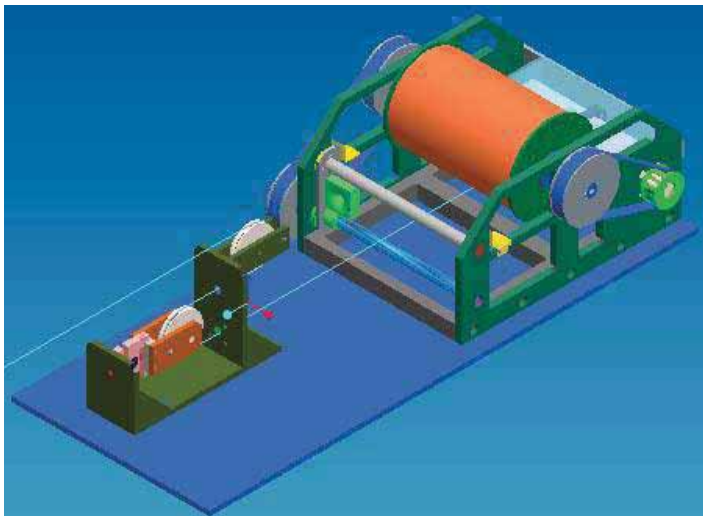

Figure 6.13: An illustration of a spool drive.

To achieve automated source changing, a key component in the rope system is a "quick connection" connector, which allows an automated system to attach and detach a source to the rope. One of the options under considerations is illustrated in Fig. 6.14. The upper piece is attached to the rope loop permanently. We envision that

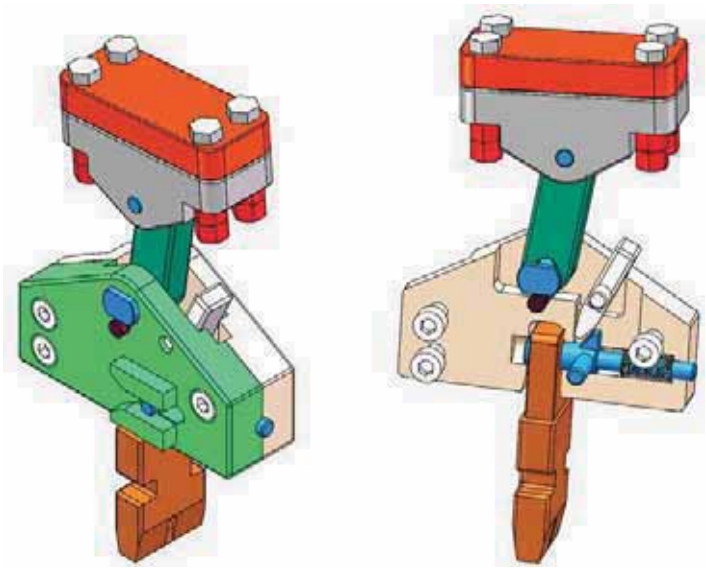

Figure 6.14: One of the quick connection option.

an ultrasonic emitter can be attached to it for accurate positioning with the SS rope being the core of a coaxial cable carrying the electrical signals. The middle piece is the female connector, which is connected permanently to the upper piece with a rotary

joint. Gravity will keep the middle piece horizontal to ease automated grabbing. The lower piece is the male connector, permanently attached to the source and the lower weight. The lock between the male and female is achieved with a spring-loaded key. During the attachment (detachment), both the male and female pieces have to be held by mechanical hands and pushed (pulled) relatively. One additional degree of freedom is needed to actuate the key in order to lock or unlock the connector. A manual key is located on the female connector to easy the manual operation through a glove box.

An alternative option of the connection is illustrated in Fig. 6.15, where the upper piece is the same and omitted in the drawing. The connection is made doubly safe with two spring loaded locks. The head of the male key has a dumb bell shape, which can be pushed in and pulled out of the upper lock with force. The lower lock requires a hand to press the side buttons in order to get unlocked.

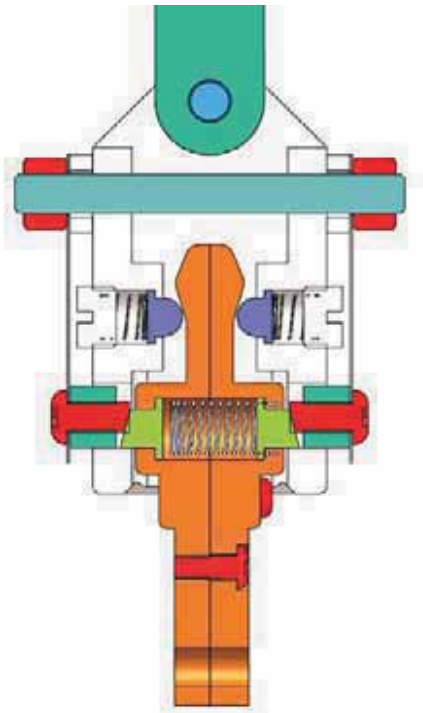

Figure 6.15: An alternative quick connection option.

All sources will be placed in a circular storage ring surrounding the chimney (Fig. 6.16), which can be driven automatically in order to select a source to get attached/detached to the rope loop. Such a design allows the two rope loops to share the same source storage. For illustration, a source assembly placed in the storage is also shown in the figure. For each rope loop, all sources share the same mechanical hand system to perform the source changes.

6.2.3.4 Remotely Operated Under-liquid-scintillator Vehicles

A ROV system can deploy the source to nearly everywhere inside the central detector. Such a system is used in the SNO experiment to deploy the ^{3}He neutron tubes. A conceptual design of the ROV is shown in Fig. 6.17. It can be made into an egg-shaped capsule with a diameter less than 300 mm and a height less than 500 mm. The

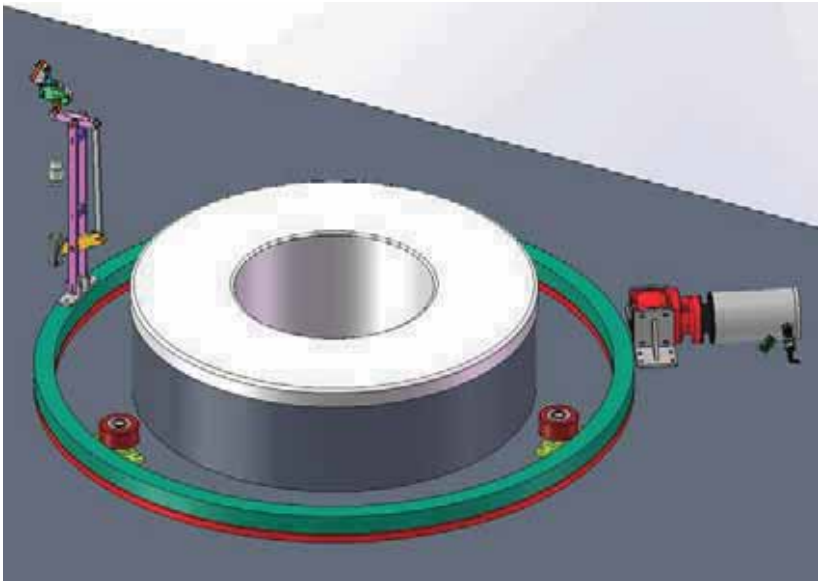

Figure 6.16: The source storage ring.

ROV is driven by pump jet propulsion without external propeller in order to maintain a simple external geometry and a compact size. The ROV motion speed is set to be about 1 m per min, and the actual position is feedback via an ultrasonic emitter. The power as well as signals are transmitted to the ROV via a umbilical cord adjusted to nearly zero buoyancy. The ROV can also carry lighting, CCD camera and a magnet to allow emergency rescue or monitoring the interior of the detector. Radioactive source assembly is attached below the ROV, with a quick connection which would allow automated source change. For material compatibility with LAB, the enclosure of the ROV will be made with Teflon, which is also highly reflective to avoid photon losses. Monte Carlo studies are underway to optimize the ROV geometry in order to minimize impact due to dead materials or optical shadowing.

Based on its current location and destination location, the ROV software will automatically select the optimal trajectory. The pump jet propulsion engine controls the speed and direction of the device. The ROV should approach the designated locations with a speed less than 1 mm/s or less, then shuts off the engine. A piston driven buoyancy adjustment mechanism is used as the depth control. In case of system failure such as power failure, the control will shut down the pump propeller and pull the piston of the depth control via a spring to increase the buoyant force to ensure the ROV float to the surface.

6.2.4 Conceptual Design of the Guide Tube System

Based on positive experiences of the Double Chooz experiment, a guide tube system is important to understand detector response from anti-neutrino interactions occurring at the boundaries of the central detector volume. Guide tubes will be positioned along the surface of the central detector vessel. The tubes could be installed at the inner and/or outer surfaces of the vessel wall. Figure 6.18 shows the conceptual design of the guide tube system with the tubes at the outer surface (left), and with tubes at the inner surface (right) of the central detector vessel. The number of tubes shown is for

Figure 6.17: ROV, its umbilical cable and the loaded radioactive source

illustrative purposes only, and the final number and distribution of the tubes will be based on detailed simulations of the guide tube system and studies of detector energy response, currently under development. The tube can be made with stainless steel to provide a good mechanical strength, or it could be manufactured from an acrylic tube to be compatible with the central detector vessel materials. Radioactive sources as small as a few mm in diameter and ∼2 cm in length could be positioned within the tube with use of a stainless steel wire driven by a stepper motor. Figure 6.19 shows one considered design of source capsule inside the stales steel guide tube, with the source connected on both sides. Similar designs are considered with the acrylic guide tube solution. Source positioning accuracy of ∼1 cm is anticipated.

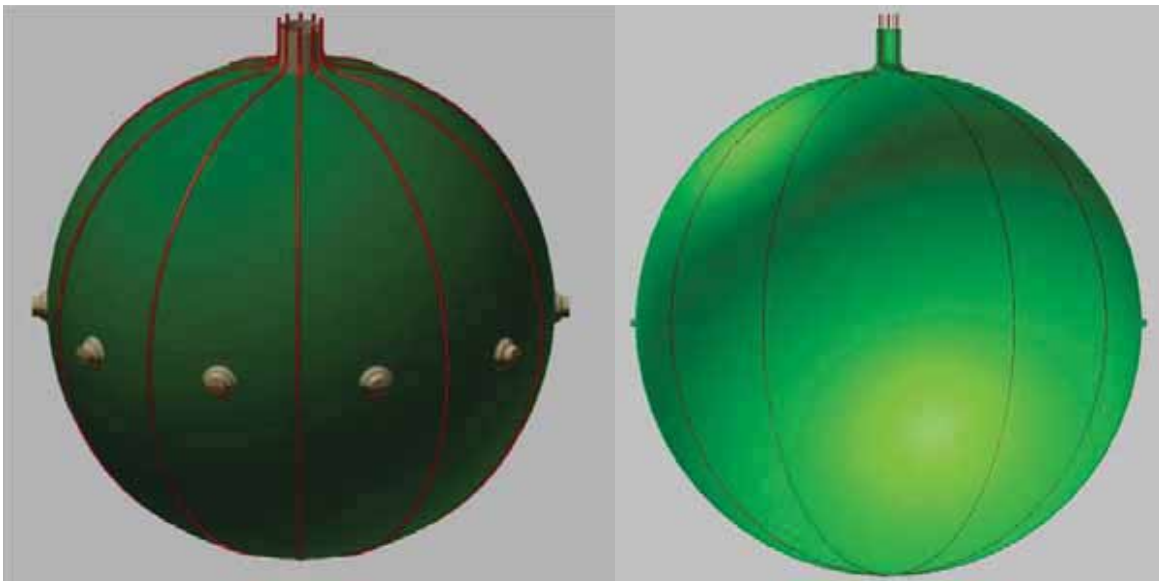

Figure 6.18: The guide tube system.

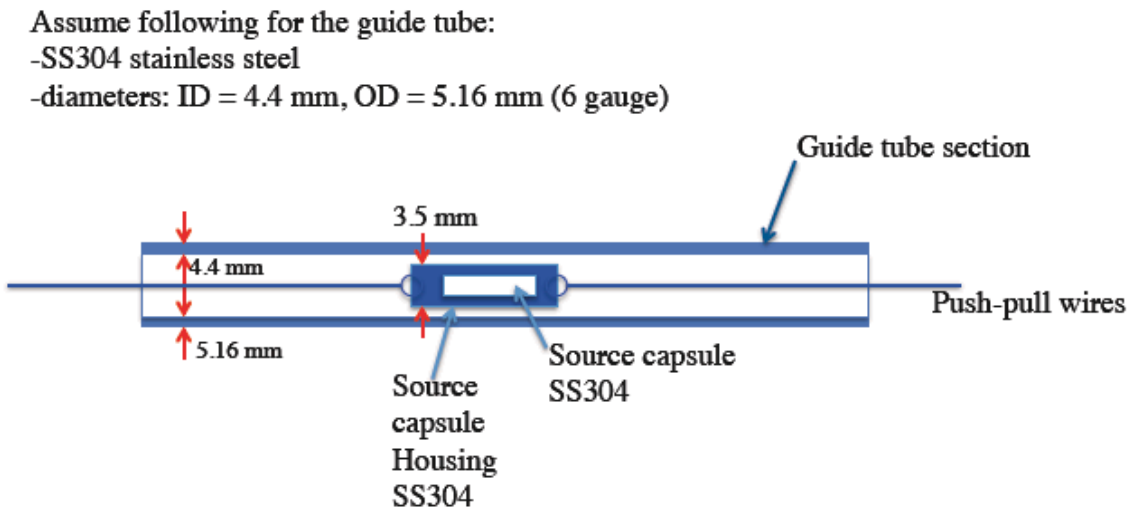

Figure 6.19: The conceptual design of the source capsule inside the guide tube.

6.2.5 A Pelletron-based Beam Calibration System

A pelletron is one type of electrostatic accelerator. The electric charge is transported mechanically to its high voltage terminals by a chain of pellets, which are connected with insulating materials (such as nylon). Figure 6.20 shows a diagram of a pelletron, taken from the website of National Electrostatics Corporation (NEC) [2]. Compared with a LINAC, the electrostatic accelerator has the advantage of being more stable. This is crucial for the intended application in JUNO, as the calibration of the Pelletron energy and the JUNO detector response calibration cannot be performed at the same time. Furthermore, below ~5 MeV in kinetic energy [3], the pelletron solution is compact and economical enough for an underground installation.

Expected positron spectra is shown in Fig. **??**. We see that most events are between 1 and 6 MeV prompt energy. Due to finite energy resolution, the mass hierarchy signal only shows up above 2 MeV prompt energy. Therefore, a pelletron system, which can provide 1-5 MeV kinetic energy corresponding to 2-6 MeV prompt energy, can satisfy the requirement of precision energy calibration for mass hierarchy determination. Figure 6.21 shows the conceptual design of the pelletron system, following the ideas from Refs. [4, 5]. The high purity Ge (HPGe) detector, which is calibrated by mono-energetic gamma sources, will be used to control the beam energy precisely. A precision of 10^{-4}, which is well below the 0.1% goal of the JUNO experiment, has been achieved with existing facilities [4, 6, 5].

The calibration of the JUNO detector with a pelletron requires the delivery of the positron beam into the detector center through an evacuated beam pipe. The positron beam will exit the beam pipe through a window designed to minimize energy losses in the beam while maintaining the vacuum of the beam pipe at the depth of the detector. The design and instrumentation of the pelletron beam pipe inside the detector is an engineering and R&D challenge.

Detector beam pipe requirements: The technical requirements for the positron beam pipe inside the detector can be summarized as follows:

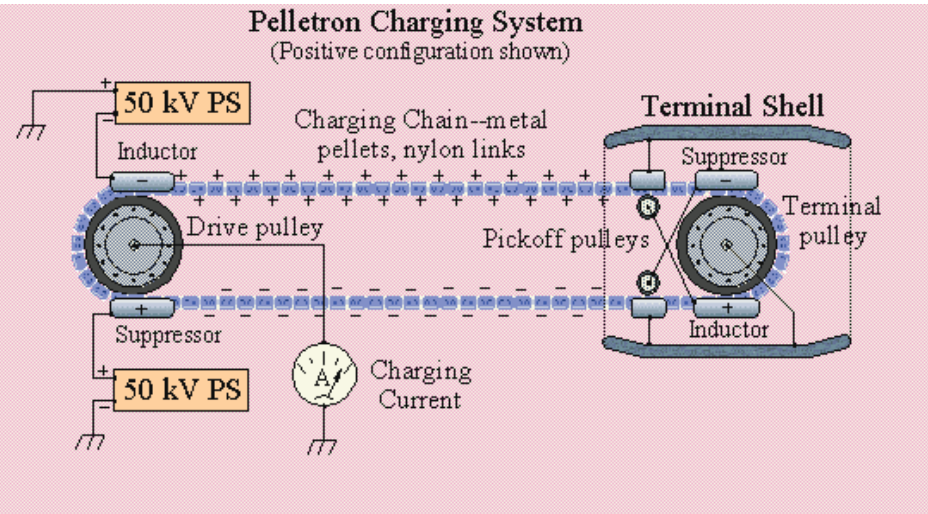

Figure 6.20: Diagram illustrating the principle of a pelletron. As the drive pulley and the terminal pulley rotate clockwise, the chain transports the positive charge to the terminal shell and builds up a high voltage that could be higher than 25 MV. By reversing the polarities of the charging voltages, the pelletron can easily switch to accelerate electrons and negative ions.

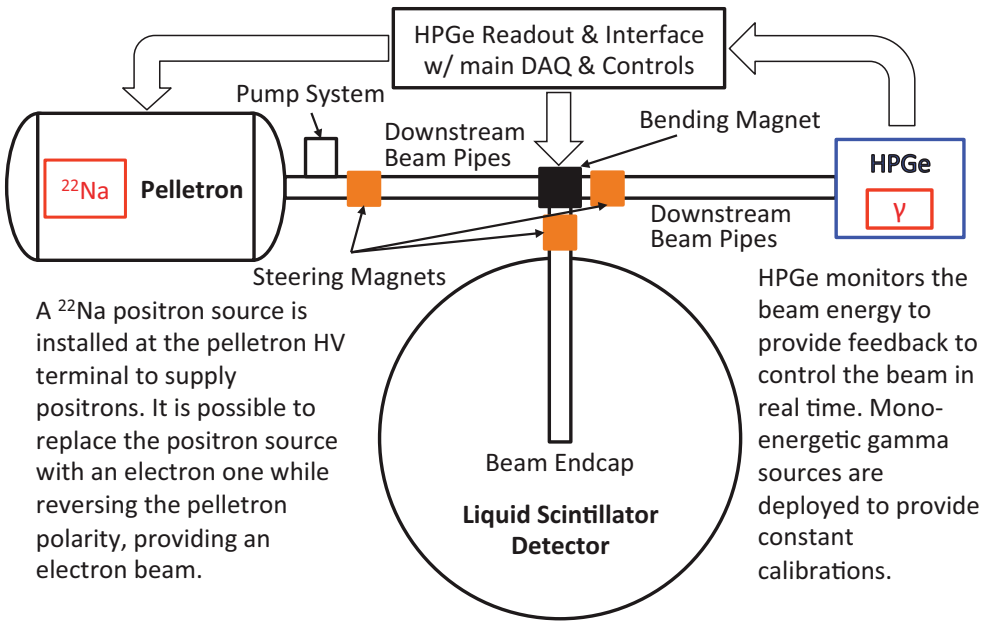

Figure 6.21: The conceptual design of the pelletron system

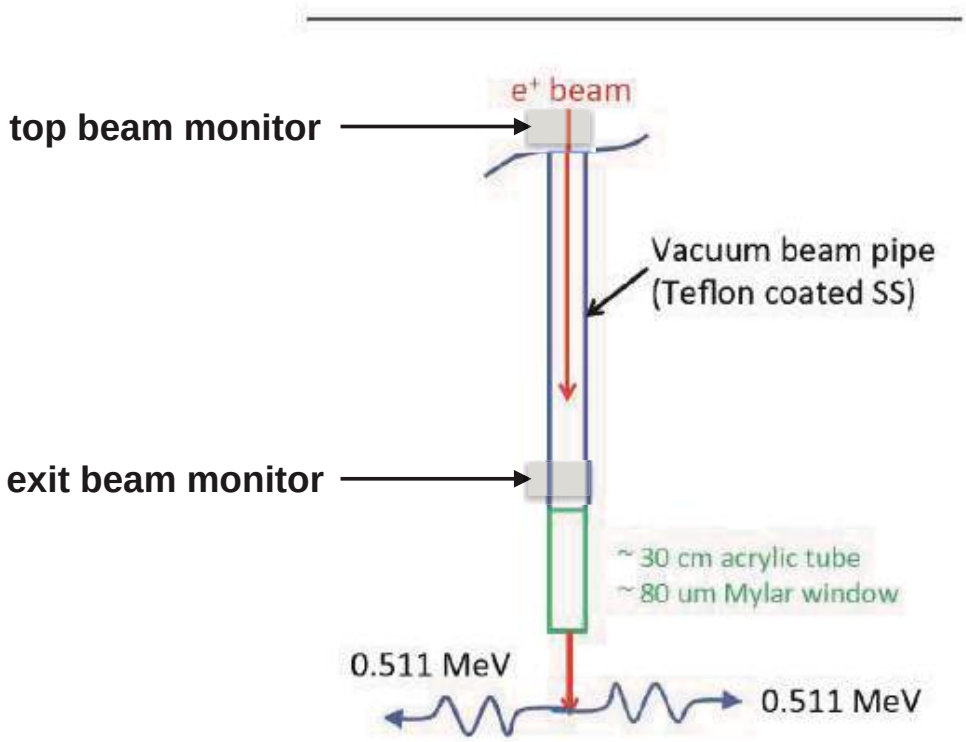

Figure 6.22: A conceptual design of the beam pipe endcap inside the LS detector. The transparent acrylic pipe and the Mylar window make sure the scintillation light can largely pass through. Two beam monitors near the top and bottom of the beam will allow diagnostics of beam position and area when the beam first enters the detector vertically downward and near the exit point of the beam out of the beam.

- Retractable, telescoping beam pipe that can be deployed into the detector during the time of calibration and retracted during normal data taking to avoid shadowing effects in the detector. During normal data taking the beam pipe is stored completely out of the detector volume.

- Beam pipe is compatible with the scintillator. To first order, the exposure of the scintillator to the beam pipe materials is limited to the duration and time period of the calibration. However, one has to account for possible long-term interaction of the scintillator with the beam pipe material after the beam pipe has been retracted from the detector. Excess scintillator may drip back into the detector or lead to unwanted contamination that may be introduced during the time of the next calibration. Compatibility issues include possible interaction with the materials of the beam pipe, damage of the deployment mechanism, leaching out of beam pipe materials into the scintillator, and degradation of the scintillator itself. The amount of beam line material to be deployed into the detector poses a challenge for the purity of the scintillator and to JUNO physics goals that require ultra low backgrounds.

- Beam pipe and its deployment mechanism have to be leak tight against the liquid scintillator to maintain the vacuum inside the beam pipe.

- Beam pipe deployment mechanism is failsafe and can always be retracted out of the detector. Since the beam pipe does interfere with the normal data taking the deployment mechanism must allow the retraction of the beam pipe even under unusual circumstances such as power failure etc. The system has to be tested to be mechanically reliable for the 10+ year lifetime of the experiment.

- It is desirable to be able to deploy the beam pipe to different depths. This would allow calibration of the detector with positrons at different points along the z-axis. The interaction region of the beam with the scintillator detector is defined by the exit point of the beam out of the mylar window. A continuous deployment along the z-axis may not be necessary, discrete steps in z are sufficient.

- Deployment of the beam pipe is automated as much as possible to allow for regular calibration and minimize the demands on the on-site personnel.

Inside the beam pipe instrumentation to monitor the beam position and profile are required to help determine the exit point of the beam and the interaction region of the calibration beam inside the detector. This monitoring instrumentation will also aid in diagnostics of the beam during tuning and setup. One of the challenges of the proposed calibration scheme is that a positron beam has to be delivered some 17 m into the detector center without active steering. We expect that from the entrance point of the beam into the detector region (at the top of the detector) to the point where it exits the beam pipe through the mylar window no active steering components can be used. As a result the beam will spread and its final position at the end of the beam pipe will depend on its direction when it enters the detector and possible divergence. As a result, we obtain the requirements for the monitoring instrumentation inside the detector beam pipe (see Fig. 6.22):

- Top beam monitor: Very precise beam position monitor at the top of the detector where the beam enters the detector to determine its direction and profile into the detector right after the last active magnetic steering and focusing. This beam position monitor can be fixed along the z-axis. It can be flipped or moved into the beam during tuning and setup and removed from the beam path during the beam delivery and calibration. The position resolution requirements for this beam monitor are set by the distance of the beam delivery into the detector and the width of the beam pipe. Depending on the position of the 90-degree bending magnet of the beam into the detector this monitoring setup can still be outside the detector but already in the vertical region of the beam pipe.

- Exit beam monitor: A second beam position monitor near the end of the beam pipe that determines the position and area of the beam spot before it exits through the mylar window. Again, this beam monitor may be designed to be movable so that it can be placed in the beam during monitoring and setup and removed (rotated or flipped) during calibration. It may be desirable to make this beam monitor movable along the z-axis to allow for a vertical scan of the beam position. Since this beam monitor will be located towards the end of the telescoping beam pipe all cabling and supplies have to be routed through the retractable beam pipe structure. This be may not required for the beam monitor at the top of the detector. With a beam position monitor near the top and the bottom of the beam pipe it will be possible to diagnose potential issues in the delivery of the position beam. More than two position monitors will likely lead to unnecessary and increased complexity.

In the following, we summarize various factors that can induce a bias in the beam energy calibration. The first one is the energy loss in beam window. At the center of the detector, the pressure is about 3 atm. A 76 μm Mylar window is more than enough to handle this pressure. The resulting energy loss is about 12 keV and can be calibrated with the HPGe detector. The variation of the energy loss due to curved window is well below the 0.1% of the prompt energy. The second factor is the shadowing effect of the calibration pipe and endcap. In order to minimize the impact of these two factors, a transparent endcap design using acrylic pipe (Fig. 6.22) is proposed. The residual shadowing effect is about 1-2%. The range of the shadowing effect is due to the kinetic energy range of positrons. A high energy positron would in general travel longer inside the liquid scintillator, thus has less shadowing effect due to smaller solid angle. This shadowing effect can be calibrated by injecting both electron and positron beams into the central detector and a bench setup. The principle is illustrated in the following:

- The energy responses of electron and positron are strongly correlated. The positron energy response is essentially the sum of the electron energy response and positron annihilation energy. The latter contains two 0.511 MeV gammas and can be calibrated using dedicated ^{68}Ge radioactive source.

- The shadowing effect for the positron annihilation energy can be calibrated with the dedicated ^{68}Ge source deployed together with the calibration tube.

- The shadowing effect can be calibrated by comparing a dedicated bench measurement with the results from the central detector calibration.

- The light pattern observed by JUNO detector provides additional handle for the shadowing effect.
- The obtained shadowing correction for positron ionization can then be applied to obtain the positron energy response together with the shadowing of the annihilation gammas.
- The resulting positron energy non-linearity model can then compared with that of the electron to further validate the energy model.

The following formula summarizes the correction strategy.

$$E_{e+}^{corr} = (E_{e+}^{rec} - E_{1.022} \cdot S_{gamma}^{shadowing}) \cdot S_{ionization}^{shadowing} + E_{1.022} + C_{window}^{eloss}. \quad (6.1)$$

Here, E_{e+}^{rec} and E_{e+}^{corr} are the energies before and after the corrections, respectively. The $E_{1.022}$ is the annihilation gamma energy for positron at rest, which can be calibrated directly with dedicated positron source. The $S_{gamma}^{shadowing}$ is the shadowing correction for annihilation gamma, which can be calibrated by combining dedicated source with the calibration tube. The C_{window}^{eloss} represents the energy loss correction in the window, it can be calibrated directly with the HPGe detector. The $S_{ionization}^{shadowing}$ represents the shadowing effect for the scintillation light for positron ionization energy. This piece will be calibrated by i) comparing the bench data vs. calibration data vs. MC, and ii) comparing the observed light pattern vs. MC. The initial simulation shows that the residual uncertainty can be controlled to about 0.1% with this strategy.

Simulation of Pelletron calibration has been carried out in the general JUNO simulation framework to demonstrate the feasibility of reaching 0.1% targeted energy scale uncertainty. First, for a 20 m long calibration tube inside the liquid scintillator, the buoyancy force needs to be taken into account. The left panel of Fig. 6.23 shows the required wall thickness of the stainless steel calibration tube to balance the buoyancy force. The right panel of Fig. 6.23 shows the weight of the 20 m calibration tube. Figure 6.24 shows the implemented geometry of calibration tube including i) ∼17.3 m long stainless steel calibration tube, ii) 30 cm long acrylic endcap, and iii) 7.6 μm thick curved Mylar window. The energy loss of the electrons and positrons inside the Mylar window was simulated and shown in Fig. 6.25. For positrons at off-center locations, the energy loss is slightly higher than those at the center of calibration tube. This is consistent with the fact that the vertical thickness of the window at off-center location is bigger than that in the center. The energy loss of electron is slightly bigger than that of positron due to additional annihilation process that positrons can go through. The difference is much smaller than the targeted 0.1% energy scale uncertainty band.

A beam of positrons are shooting through the calibration tube to study the energy response. The positron beam cross section is assumed to be a circle with radius of 1 cm. The spread in momentum is assumed to be 0.1%. The results are compared with those of injecting positrons directly inside the detector center without any calibration tube (Fig. 6.26). The increase of the difference between two cases with respect of the true prompt energy reflects the shadowing effect of the calibration tube. The bias without any correction (top panel of Fig. 6.27) indicate the magnitude of bias is about 1-2%. The bias becomes smaller at high energy, because high-energy positrons can penetrate into liquid scintillator further so that the shadowing effect is smaller. The bottom panel of Fig. 6.27 shows the residual bias after the energy loss and shadowing correction. The residual bias can be controlled to below 0.1%.

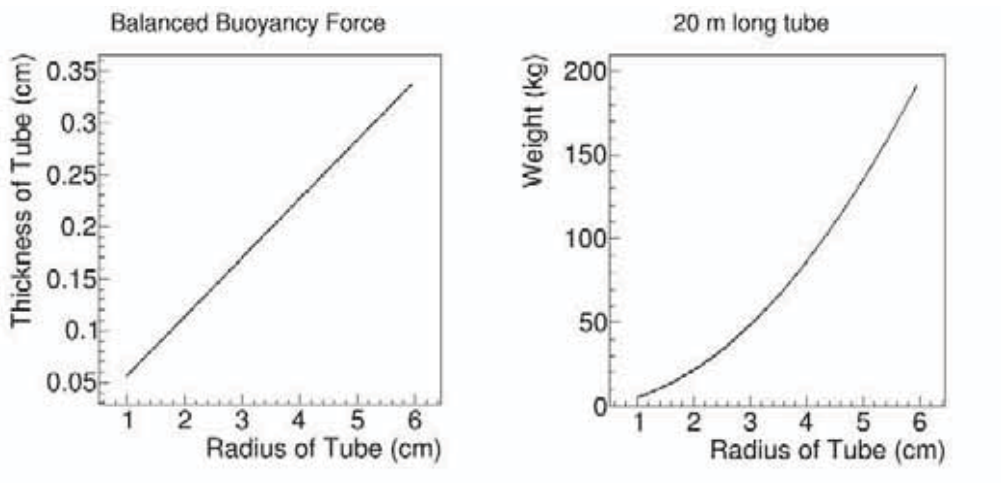

Figure 6.23: (Left panel) Calculated required wall thickness of the stainless steel calibration tube is plotted as a function of the radius of the calibration tube to balance the buoyancy force. (Right panel) The corresponding weight of the 20 m long calibration tube is plotted.

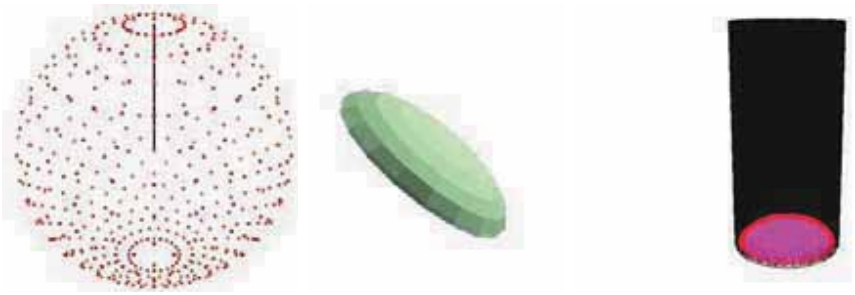

Figure 6.24: (Left) Illustration of calibration tube of Pelletron inside the JUNO central detector. (Middle) Curved Mylar window for the calibration tube. (Right) Endcap of the calibration tube with the curved Mylar window.

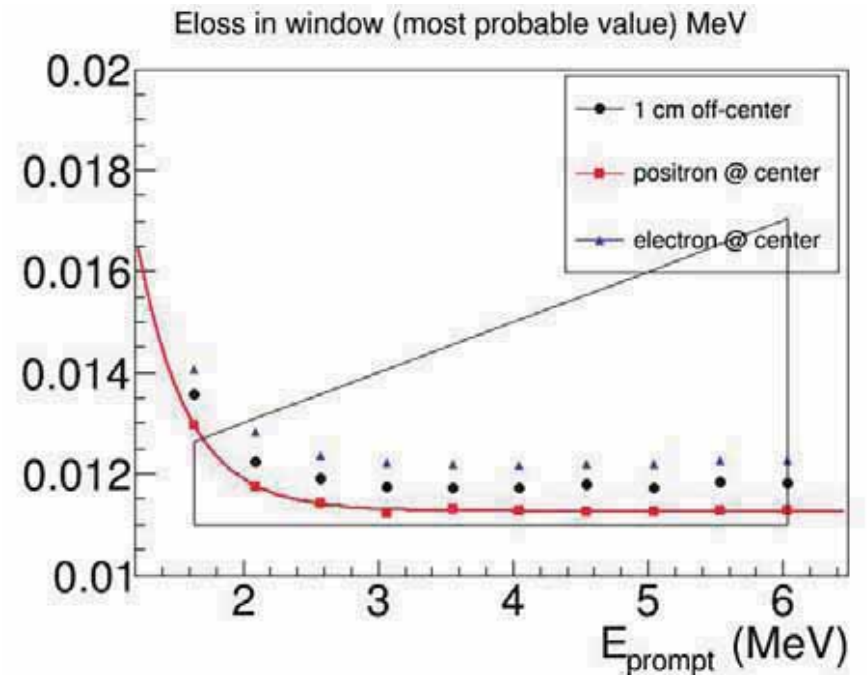

Figure 6.25: Energy loss of the electrons and positrons inside the curved Mylar window. For electron, the prompt energy was shifted to match that of positron. The traipzoid represents 0.1% band of the energy scale.

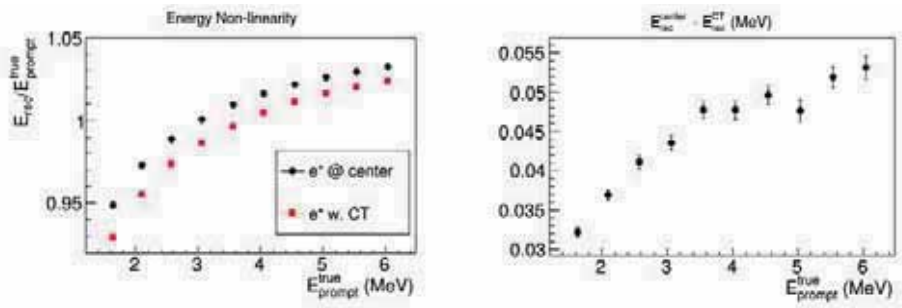

Figure 6.26: (Left) The energy response of positron injecting through the calibration tube (red) is compared to that of the positron in the detector without the calibration tube(black). (Right) The difference in energy is shown with respect of the true positron prompt energy. The increase of difference reflects the shadowing effect of the calibration tube

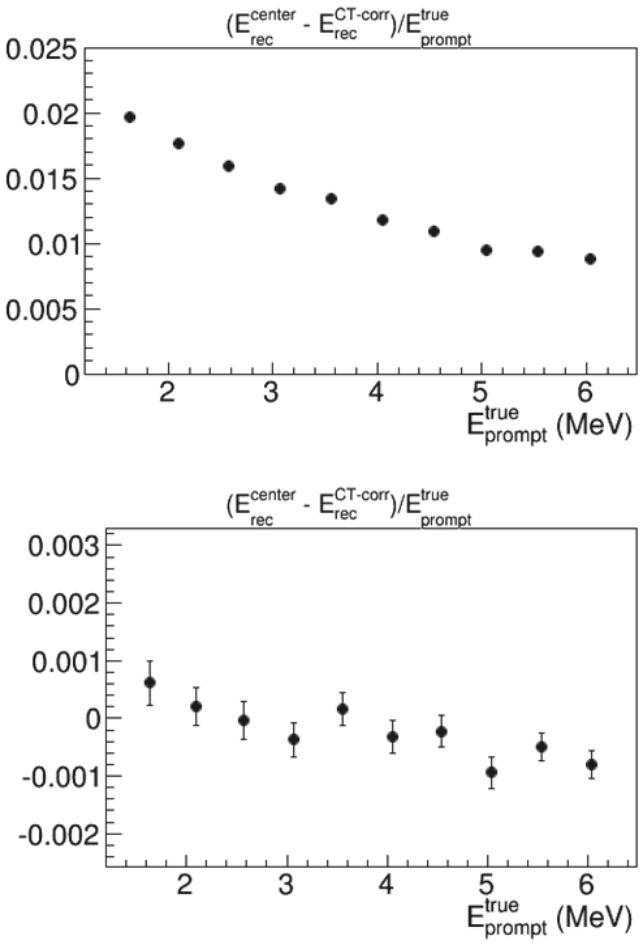

Figure 6.27: (Top) The bias of energy response (1-2%) due to the shadowing effect of the calibration tube is shown with respect of the true prompt energy. (Bottom) The residual bias of energy response ($< 0.1\%$) after the correction of energy loss and the shadowing effect is shown with respect of the true prompt energy.

6.2.6 Diffused Short-lived Isotope Calibration

Homogeneous energy calibration of a large liquid scintillator detector throughout the entire volume can only be achieved with distributed sources in the scintillator. The use of uniformly distributed sources was successfully demonstrated by the Sudbury Neutrino Observatory using ^{16}N, ^{8}Li, as well as *in-situ* spikes from ^{24}Na and ^{222}Rn. Injection and deployment of such sources in a 20 kt-detector pose challenges including the production and injection of isotopes over long distances and their distribution throughout the detector volume. We will survey suitable short-lived isotopes, their production method and develop concepts for the injection with a gas or scintillator stream into the detector. We will pay particular attention to the possible use of positron sources. We will identify possible isotopes and develop a technical concept for the injection and distribution of sources. The principles of the isotope injection will be studied with the test chamber developed for various R&D purposes or a re-purposed Daya Bay detector.

6.3 R&D Status and Plans

6.3.1 Sources

Source selection and conceptual design of the geometry need to be determined via Monte Carlo. Mini-balloon source requires prototype both mechanically as well as test loading of radioactive isotopes. A robust and simple UV laser system needs to be developed allowing ∼ns level timing and sub-percent intensity control.

6.3.2 Rope Loop System

We have learned much from the Daya Bay calibration experiences. The challenges of the rope loop approach lie in the automatic source swapping devices, interfacing with the central detector and the installation procedure. A 1:1 prototype for the mechanical system is required before the final design. We shall also find high bay area to performance deployment tests similar to that in the real detector. Additional key considerations are:

- The rope loop subsystem will be installed after the cleaning of the central detector, or even after LS filling, thus installation procedures should be simple and they must be carried out quickly to avoid contamination;
- LS detector with such a large size is unprecedented. Calibration system should be designed so it can accommodate potential structural distortions; and
- The reliability of the source changing devices and life span should be understood well with destructive tests.

6.3.3 ROV

To achieve good physics performance, we need to optimize the shape and the dimension of the ROV via extensive simulations.

The ROV shall be designed with high cleanliness and be fully compatible with liquid scintillator. Prototype studies are needed in a realistic deployment condition.

6.3.4 Source Positioning System

An ultrasonic emitter's diameter is roughly 30 mm and its working frequency 150 kHz with a pulse width of ∼1 ms. The emitter can be installed either on the source or on the ROV.

The receiver array is mounted on the detector sphere and at least three receivers can realize 3D positioning. The actual arrangement of the array need to be optimized. To increase the reliability, we plan to have ∼10 receivers so when some malfunction or break down, the system can still function. Longer array baselines means better positioning precision, which implies receivers are better placed near the equator from the perspective of positioning. However, this also means the cables serving these receivers are longer and it might cause more potential issues. The material compatibility between cables and LS needs to be checked and addressed. Compared with the oceanic environment, JUNO central detector is an isolated environment. Impact to positioning uncertainty due to reflections and refraction shall be well studied and understood.

6.3.5 Pre-installed Guide Tubes

How to mount the guide tubes next to the acrylic panels is quite challenging due to the distortion after the detector is filled. The maximal distortion of the acrylic panel is expected to be ∼5 cm thus if the guide tubes are fully attached to acrylic panels, this level of distortion is highly harmful for the smoothness of the tube even the joint does not get destroyed. We need to allow certain level of distortion thus probably the two should not be fully coupled. Instead we should allow the relative movement to some level while still keep the positioning accurate enough.

In addition to the mechanical concerns, the impact of these additional, tube materials to the detector performance needs to be understood better. It should not make much difference they are deployed either inside or outside of the acrylic sphere if refraction indices match well with LS and/or mineral oil. Acrylic, stainless steel, and Teflon tubes tubes are considered.

Right now, the system realization and impact to the detector performance are undergoing discussion. Argonne National Lab has a high bay area, suitable for performing deployment tests of the rope loop system, and tests of the guide tube systems.

6.3.6 Pelletron System

The need of space and transportation underground have been checked and no obvious obstacles were observed. Currently, we need to detail out the beam line design and the interfacing with the central detector.

6.3.7 Diffused Short-lived Isotope Calibration

Various sources are being studied. The concept of source injection is being investigated.

6.4 System Reliability and Safety Concerns

It would be difficult to make large scale repair to the calibration system during the life span of the experiment. This places very stringent challenges on the reliability and longevity of the calibration system, especially that there should absolutely be no source dropping.

For the automatic source swapping component of the rope loop system, we have considered the following multi-layer safety protection mechanism,

1. The position and the clamping force of the robotic hands are constantly monitored after each motion;
2. Robotic hands and other clamping devices are designed to be normally-close to make sure that sources are still secured during power or control signal loss;
3. To make sure of the reliability of the quick-connects, they are pull-tested each time they engage;
4. A fall-prevention shutter is installed beneath the source-swapping device. During source swapping, the shutter is closed; and
5. A piece of annealed iron will be installed inside the source. In case of dropping, a ROV with a strong magnet can be deployed to recover it.

The ROV umbilical cable can take certain load besides functioning as a power and control signal cable. Thus in case of malfunction, it can be pulled out of the central detector. In addition, the design of the ROV also has some built-in safety considerations and the ability of self test.

The effective density of the ROV should be roughly 95% of LAB. During power loss or other situations of losing motion, the ROV would float automatically. The liquid dragging force shall be chosen so that the rising speed is not too high, avoiding damaging the vessel. The internal pressure of the ROV should be either positive or negative and should be constantly monitored. Larger-than-normal fluctuations would indicate a leak might have developed and an alarm signal shall be sent out.

6.5 Schedule

A major contribution to the calibration system and additional contributions in support of central detector, liquid scintillator and PMT QA are being investigated for US JUNO deliverables.

Table 6.3: Yearly targets

Year	Goals	Deadlines	Milestones
2013	Form a working group, start conceptual designs and simulation	Form a few preliminary mechanical designs	Form 3 alternative conceptual mechanical designs before November

(See Next Pages.)

2014	Continue design and gradually converge; Technique R&D; Design light sources and build mock-ups	Finish the simulation of source selection; finish the design of a stable light source	Finish the stable light source design before June; Finish the simulation and analyses of the 3 alternative designs; Select 2 out 3 in September
2015	Build and test a prototype; finalize both the mechanical and the electronic designs	Finish the R&D of selecting radioactive sources; finalize the choice of radioactive sources	Finalize the mechanical design before June; finalize the construction and testing of the prototype, and the radioactive source designs before December
2016	Bid, order and start the construction of calibration systems	finish one complete calibration system and testing	finish bidding before June and complete one calibration system and finish its testing before December
2017	Continue the construction of the calibration system	Complete the remaining half of the project	Complete the remaining half of the project
2018	Complete the construction of the calibration system; order all radioactive sources; complete DAQ and the interface with DCS	Compelete the last half of the project	Complete all remaining constructions, DAQ and the interface between DAQ and DCS before December

(See Next Pages.)

2019-2020	Installation and commissioning	Complete the installation and commissioning of the system	complete the calibration system before the completion of the central detector installation

Bibliography

[1] X. Qian et al., Phys. Rev. D87 (2013) 3, 033005

[2] National Electrostatic Corp. `http://www.pelletron.com/`

[3] F. Hinterberger, Berlin, Germany: Springer (2008) 417 p

[4] W. Bauer, Nucl. Instrum. Meth. B **50**, 300 (1990).

[5] H. Huomo, P. AsokaKumar, S. D. Henderson, B. F. Phlips, R. Mayer, J. McDonough, H. Hacker and S. McCorkle *et al.*, BNL-41953.

[6] W. Berg, R. Fuja, A. Grelick, G. Mavrogenes, A. Nassiri, T. Russell, W. Wesolowski and M. White, "Beam measurements of the ANL-APS linac injector test stand,"

Chapter 7

Readout electronics and trigger

The JUNO readout electronics system will have to cope with the signals of 15,000 PMTs of the central detector as well as 1,500 PMTs installed in the surrounding water pool. The average number of photoelectrons being registered by an individual PMT will reach from below one for low-energy events up to several 1000 in case of showering muons or muon bundles. In both extreme cases, the number of photoelectrons has to be counted and their arrival time profiles have to be determined. A dedicated trigger system will be necessary to perform a pre-selection of correlated PMT hits caused by physical events from a sea of random dark noise hits. Based on the selected arrival time and pe pattern, software algorithms will reconstruct energy, type and position of the event vertex. Thus, the main task of the readout electronics is to receive and digitize the analog signals from the PMTs and transmit all the relevant information to storage without a significant loss of data quality. The basic concepts considered in the design of the system as well as a list of specifications are given in Sec. 7.1.

The PMTs will be submerged in the water pool surrounding the acrylic sphere that contains the LS. Based on this layout, three different approaches for the realization of the read-out electronics are discussed: A mostly "dry scheme" for which individual cables carry the analog signals out of the water pool to an external electronics hut containing front-ends and digitization units. A "wet scheme" for which digitization happens at the PMT bases and the digital signals are bundled in submerged central underwater units before being passed on to an external online computer-farm. And finally, an intermediate readout scheme where a considerable part of the electronics is submerged inside the water pool but still accessible for replacements. The three schemes are presented in Secs. 7.2−7.4.

Sec. 7.5 will provide an overview of further R&D efforts to be undertaken. A first time line for the realization of the system and the most important aspects to be dealt with is laid down in Sec. 7.6. Possible risks are summarized in Sec. 7.7.

7.1 Design considerations and specifications

The concept for the design of the electronics is driven by the following goals, which are listed here in order of their priority:

1. **Energy reconstruction:** Optimization of the energy measurement of $\bar{\nu}_e$, especially at the lowest energies. A basic limitation on the energy resolution arises

from the statistics of detected photoelectrons (pe). This limit must not be worsened significantly by the effect of electronics. At a photoelectron yield of 1100 pe per MeV, the achievable relative resolution is ∼3 % at 1 MeV.

2. **Reconstruction of the photon arrival time pattern:** A precise measurement of the arrival times of the photons is required to reconstruct the position of the events. This is particularly important for the IBD events induced by $\bar{\nu}_e$'s because (a) the energy response of the detector will be position-dependent and (b) the formation of spatial coincidences between prompt positron and delayed neutron events will support background suppression. Moreover, track reconstruction for cosmic muons and especially for muon bundles is very sensitive to timing and will be an important tool for the veto of cosmogenic backgrounds.

3. **Low dead time and dynamic acquisition rate:** During usual data taking conditions, all neutrino events from reactor, solar or geological origin should be acquired without in-efficiency, i.e. with a minimum or zero dead time. In addition, readout electronics have to be able to cope with short episodes of extremely high trigger rate that might be caused by the neutrino burst from a nearby galactic Supernova. Dependent on the distance, thousands of neutrino events are expected within a period of 10 seconds. Therefore, the system has to be able to bear a dramatical increase in its acquisition rate for short periods without significant data loss or dead time.

7.1.1 Energy reconstruction

For the low-energy events, the deposited energy can be almost directly inferred from the overall amount of photons or pe detected by the PMTs. However, there are several ways of performing this integral measurement of collected pe (see below). Additional complications arise for high energy events, where the accuracy of determining the number of pe detected for a given PMT will depend on the dynamic range of the readout electronics.

7.1.1.1 Photoelectron counting

There are two basic methods to determine the visible energy created by an interaction in the detector. One can either integrate the charge created by the PMTs or one can try to identify individual photons and count them. The reconstruction is complicated by the spread in the arrival time of the photons, which is caused both by the fluorescence time of the LS, photon time-of-flight and photon scattering which all we contribute to delays in the order of several hundred nanoseconds[1]. An additional distortion of the time pattern will be introduced in case of cosmic muons where the light is generated along the extended particle track, causing a delay by the time-of-flight of the muon (≤120 ns). The trigger system will have to take into account this spread in arrival times when defining a threshold condition.

Charge Integration is technically the simpler solution. During a certain time window

[1]Note that once the vertex position is known, the delay from the time-of-flight can be approximately corrected offline. Based on this, most of the light will be concentrated towards the start of the event.

the signal of the PMTs is integrated and the integrals are summed up into a global charge. This global charge is proportional to the visible energy of the event. For an online measurement the time window has to be in the order of 300 ns from the arrival of the first photon at a given PMT. If time-of-flight effects are taken into account, e.g. for an off-center event close to the surface of the acrylic sphere or a cosmic muon, the acquisition gate has to be extended to 500 ns. The length of the time window must be optimized between two aspects. With longer time windows more and more of the scintillation light is included, but the contribution from the electronics noise increases. Due to the electronics noise the potential of the baseline will vary around zero. Integrating such a baseline even without a signal will not give exactly zero. The contribution from the baseline noise will scatter around zero with a width of the distribution that increases with the square root of the integration time.

There are two subversions of the charge integration. One can either sum all the PMTs or just those PMTs above a certain threshold (e.g. 0.3 pe). Due to fluctuations in the amplification process of the PMTs (in the dynode structures of a conventional PMT or in the MCP) the charge produced by a single photoelectron varies. The variation is usually classified by the so-called peak-to-valley ratio of the PMT. Due to these fluctuations it can happen that the signal of a single pe is not visible above the baseline noise level. But the information is not completely lost. In the absence of electronics noise the sum of all PMTs will give a better estimate of the visible energy than just the sum of those PMTs above a certain threshold. For a real system one has to optimize the threshold. It largely depends on the noise of the system and on the average number of pe per PMT for the relevant events . For JUNO it is not yet clear what the best value is. For Daya Bay it turned out to be zero, i.e. one adds all PMTs. Note that this charge integration threshold is not necessarily the same as the trigger threshold applied for self-triggering of a channel.

Photon Counting is usually a self-triggered method. One analyzes the wave-form of each PMT individually in an attempt to identify the arrival of individual photons. Then the number of these photons is counted over at time window comparable to the above. The total number is proportional to the visible energy. The advantage of this method is that the number of photons is more directly related to the energy than the total charge. Some photoelectrons produce higher charges and some lower. This introduces an additional fluctuation into the charge measurement which is unrelated to the visible energy. With photon counting this additional fluctuation is eliminated.

With the method of photon counting a threshold for each PMT is unavoidable. Photo electrons with very low charge due to fluctuations in the amplification process will be lost. This degrades the resolution by an amount that strongly depends on the peak-to-valley ratio of the PMTs. Whether photon counting is superior or inferior to charge integration depends on the details of the detector and the electronics. For JUNO the answer is not yet known. A detailed simulation is necessary to produce it. For Borexino photon counting turned out to be the preferred method at low energies and also DoubleChooz is using a method of approximate photon counting. For Daya Bay the electronics does not allow to do photon counting.

To extract the number of photons from the waveform of a PMT algorithms of different levels of sophistication are possible. In case of a software trigger, a very simple algorithm that counts the number of transitions of the photon pulse(s) across a threshold is probably sufficient. A more sophisticated algorithm will identify the charge

of a pulse and its shape. Effectively at very low occupancies any pulse consistent with the charge of a single pe will be counted as one photon. At very high occupancies, the shape of the pulse will not contain any significant information. Therefore the number of photons will be derived from the integrated charge. The two basic methods become identical at very high occupancies. At intermediate occupancies, when the pulses of a few photons partially overlap in time, shape information like satellite peaks in the wave-form combined with the integrated charge will give the best answer

7.1.1.2 Dynamic range

The electronic system must be able to cope with a large range of signal heights (and also durations). For low-energy neutrino events, the average occupancy is below 1 pe per PMT. Therefore the electronics must have good resolution for single pe's. Cosmic muon events are forming the high-energy end of the the dynamic range. These events can reach hit occupancies of 4000 pe for individual PMTs, and this has been defined as the maximum occupancy the electronics will have to cover. However, even larger signals are expected in case the muons arrive in bundles or create hadronic showers inside the target volume.

7.1.2 Photon timing

For all event types, the arrival time of the first photons at the individual PMTs will be the primary information available for the reconstruction of the vertex position (in case of neutrino events) or the particle track (in case of muons). This will be of particular importance for the energy reconstruction of antineutrino events because the effective pe yield will be position-dependent. A precise reconstruction of the vertex position will allow for low systematic uncertainties when applying correction terms.

7.1.2.1 Reconstruction of point-like events

Reconstruction algorithms will start from the hypothesis of a simultaneous emission of all photons from a single event vertex inside the detector. Then, the assumed vertex position will be adjusted to fit the observed photon arrival time pattern when considering the time-of-flight of the photons. The assumption of simultaneous emission is usually well fulfilled for the first photons detected for an event. More sophisticated algorithms will take into account the time delays introduced by the finite fluorescence times, photon scattering in the LS and the transit time spread of the PMTs by using appropriate probability density functions. Moreover, also the density of photon hits distributed over the surface of the detector sphere bears information on the vertex position.

What is more, the precision of the photon timing will be decisive for the practicability of pulse shape discrimination. Heavy particles like α's or neutrons (proton recoils) create more light than electrons in the slow components of the fluorescence profile (cf. Fig. 7.1). Based on the information of the vertex position, individual hit times can be corrected for the time-of-flight of the photons. The resulting sum pulse of all detected pe corresponds to the original scintillation profile of the event (plus impact of light scattering). Profiles can be characterized for their long-lived decay component,

allowing to quite clearly distinguish electrons from α-particles and proton recoils and with lower efficiency even positrons from electrons.

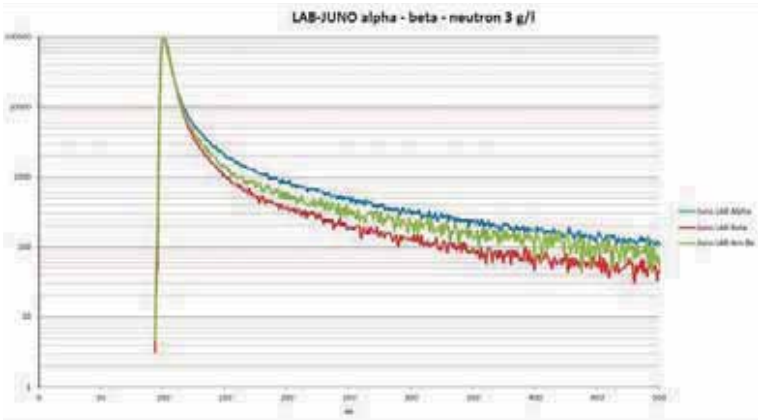

Figure 7.1: Example pulse shapes of α, β, and neutron-like events measured for the JUNO liquid scintillator (LAB + 3 g/l PPO).

The quality of the separation will largely depend on the gate length over which the photoelectrons are acquired. The time window should cover a significant portion of the slow fluorescence component which is of the order of several 100 ns. In this respect, a decentralized trigger schemes featuring a variable gate start time and gate width for each channel seems preferable. In this case, acquisition will stop only when the acquired pulse becomes indistinguishable from dark noise (see below).

7.1.2.2 Reconstruction of cosmic muons

Reconstruction of cosmic muon tracks is more complex. For single, minimum-ionizing muon tracks, the emitted light front will closely resemble a Cherenkov cone in the forward-running direction[2], plus a superposition of spherical backward-running light fronts. Such events are reconstructed in a similar fashion as point-like events, relying on a fit of the muon time-of-flight plus the photon time-of-flight for a given track hypothesis to the arrival time pattern of first photons observed at the surface of PMT photocathodes. Also charge information from the many hundred photons per channel may be included as the collected number of photoelectron at a given PMT will depend on the distance from the muon track.

However, showering muons as well as muon bundles create much more complex event topologies that lead in effect to a superposition of several light fronts arriving at the photocathodes with short time-delays. First attempts at the reconstruction of such events suggest that the full time profile of photon arrival times have to be recorded for each individual PMT in order to be able to discern secondary maxima or at least substructures that are created by the delayed arrival of subsequent light fronts. While a variety of algorithms are currently investigated, none has reached a state from which hard requirements on the necessary photon timing information can be formulated.

[2]This shape is due to the relative speeds of muon (speed of light in vacuum) and photons (speed of light in the medium) which results in the same geometrical condition as in case of the Cherenkov effect.

Note that especially for these events, the ability for a separate detection of the true Cherenkov cone might provide valuable information for disentangling the contributions of individual particles. However, it seems unlikely that conventional or MCP-PMTs will reach the necessary time resolution.

7.1.2.3 Limitations in timing

While accurate timing information is for sure of great value, there are intrinsic limitations to the accuracy that can be reached in JUNO that are inherent to the LS detection technique. The first one arises from the finite time width of photon emission from the scintillator that is described by the fluorescence time profile. The fast component that is most relevant for timing questions features a decay time in the order of 4 ns. This leads to a smearing of the timing information especially in the regime of low-photon statistics, i.e. at low energies. The second and more severe constraint arises from the transient time spread (tts) of the PMTs. The tts characterizes the variation of the time between the arrival of the photon and the creation of of the electrical pulse. As the final PMT is not yet available, the precise tts profile is not known. But the (1σ) uncertainty introduced is expected to be in the range of 3−4 ns.

Taking both inaccuracies into account, MC simulations of scintillation signals have been performed to obtain realistic PMT signals that were then "digitized" with different sampling rates. These studies indicate that a time resolution of 1 ns resp. a sampling rate of 1 GS/s will be sufficient to record the signals without loss of information.

7.1.3 Triggering schemes

A further important consideration is the triggering scheme: It may either be global, i.e. based on the information of all channels, or de-centralized, i.e. based on self-triggering channels that send all their digitized signals (including all dark noise photoelectron) to a computing farm. In the latter case, a (online) software trigger is used to identify physical events. Both options are discussed more closely in the following.

In case of a **Global Trigger**, the information of all PMTs is combined in order to form a global triggering decision that starts the readout of all PMT signals. The information from a limited local group of PMTs will not be sufficient to form the trigger decision. Information from all of the PMTs is required. Monte Carlo studies have shown that a simple trigger logic based on the total number of active PMTs (PMTs with at least one hit) within a 300 ns window is sufficient to suppress the background from random coincidences of dark noise and to guarantee 100 % efficiency for the detection of $\bar{\nu}_e$ events. Threshold would be set to 500 hits ($\sim$ 0.5 MeV) which is well above the average number of 225 dark noise hits within the same time span[3].

Such a trigger can easily be realized in the more conventional scheme of the external readout electronics (sec. 7.2) that relies on the collection of the analog signals in a physically confined space. In this case, the delay introduced by the decision for triggering reaching the digitization units is fairly small. However, a global trigger is much harder to apply for a de-centralized digitization as it is propagated by the underwater electronics scheme (sec. 7.4). Hit information from the spread-out PMTs

[3]This number is based on a trigger coincidence window of 300 ns and 15,000 PMTs featuring a dark noise rate of 50 kHz each.

would have to be transmitted either by individual cables/fibers or by combining the information from a group of PMTs underwater into one cable/fiber per group. The trigger decision would then be sent back along the same network to the PMTs to start the readout. During the latency of the trigger (several ms) the wave forms of the PMTs would have to be buffered either on the PMTs or in the underwater units.

An important aspect regarding energy reconstruction that potentially favors a global trigger is the fact that this is the only configuration that will allow the recording of waveforms for channels in which the PMT signals are below an individual triggering threshold, i.e. the detection of low-charge photoelectron. On the other hand, the existence of a global trigger threshold at $\sim$0.5 MeV poses a special challenge for data acquisition during a Supernova. Besides a large number of $\bar{\nu}_e$ events a substantial amount of the resulting neutrino interactions in JUNO will be from elastic scattering of protons. Due to reaction kinematics and quenching, the visible light will be fairly low and necessitate a temporal lowering of the threshold below 500 pe. While this does not pose a problem from point of view of radioactive background (there might be an interference with dark noise, though), the only information available to make the system aware of the on-going neutrino burst is the sudden increase in event rate. It will take a certain number of triggers to realize that neutrinos from a nearby supernova are arriving. Then the threshold will have to be lowered in retrospective. This is not impossible with an appropriate amount of buffers, but it does impose a significant complication of the trigger scheme.

Decentralized triggering. In principle this "untriggered" scheme is much simpler. The signal from each PMT is continuously monitored. If it exceeds the acquisition threshold for a single photoelectron (SPE), i.e. probably around 0.3 of the single photoelectron charge, the signal is digitized and transmitted to the online farm. On the online farm the signals from the individual PMTs are combined into events and a decision is formed whether to store the event or to drop it. It is mainly a question of data reduction and storage capacity to decide which fraction of events or even individual PMT waveforms to store.

The advantage is that much more information is available for the decision on storage of the event. Time-of-flight information can be taken into account to associate true photon hits inside a 300 ns window to the emission by a single vertex. This potent mean for the suppression of background from random dark noise coincidences will allow to lower the threshold below 0.5 MeV during normal data taking.

For the underwater readout electronics, this scheme bears the considerable advantage of reducing the required cabling. There is no need for a network to send trigger information to the central trigger and to return the trigger decision. The disadvantage is a higher load on the data links to the farm and on the required computing power. In this scheme not only the waveforms of signal but also background events have to be transferred to the farm in order to form a trigger decision. The difference in the data transmission rates between the two trigger schemes is somewhat reduced by the length of the time windows required for the readout. For the global trigger scheme it must cover the full events ($\geq$ 300 ns) for all PMTs while in the untriggered scheme the gate width can be adjusted to the number of photoelectrons detected, e.g. 32 ns per single photoelectron pulse. If for a given event multiple photoelectrons are detected by a single PMT, several internal triggers will occur and several such windows will be transferred.

Also the timing between the PMTs is simpler in the untriggered scheme. There is no need to synchronize the clocks between the PMTs. t_0-corrections can be applied in the farm. A White Rabbit system as proposed for the global triggering scheme is not necessary. Only the synchronization of the FADC frequencies has to be ensured, which will be achieved by locking the internal oscillators by a centrally distributed clock.

Last, but not least one should mention that a software algorithm for data reduction on a farm is much more flexible to react to unforeseen complications or opportunities than a hardware-based trigger.

7.1.4 List of specifications

Based on the above discussion, the following list of specifications has been compiled:

- **Waveform sampling** should be available over the whole energy range with a sampling rate of 1 GS/s.

- **Photoelectron resolution:** In the signal range from 1−100 pe, the charge resolution should increase linearly from 0.1−1 pe.
  In the background range of 100−4000 pe, the charge resolution should be 1 %.
  Signal range and background range should overlap.

- **Dynamic range** should reach from 1 to 4000 pe per channel.

- **Arrival time resolution**, e.g. by fitting of the signal leading edge, should be $\sigma_t \approx 100ps$.

- **Noise level** should be below 0.1 pe for single photoelectron detection.

- **Maximum acquisition rate** should be on the order of $10^3 - 10^4$ triggers per second.

- Acquisition should be low in or without any dead time.

Beyond these performance requirement, it has to be ensured that the system can be reliably and continuously operated for at least 10 years with no or minimal access to the parts of the readout system submerged inside the water pool. It is also important to facilitate the installation by minimize the cabling between the PMT matrix and the outside electronics.

7.2 External readout scheme

The philosophy of the external read-out scheme foresees to place as large a part of the electronics as possible in a dedicated electronics area or hut outside the detector. In particular, the analog-to-digital converters are to be located outside the water pool.

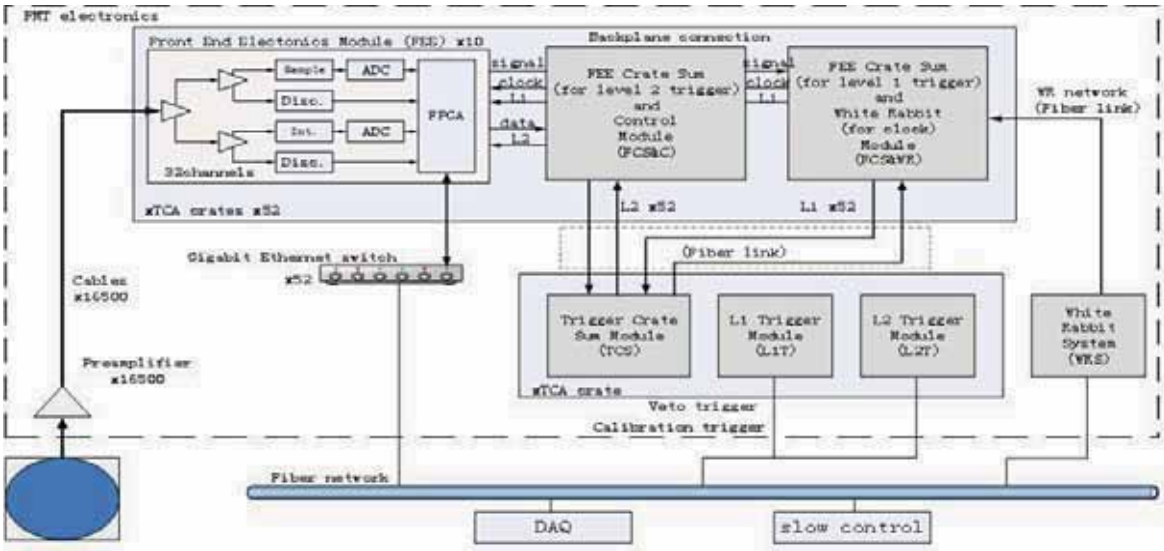

Figure 7.2: Schematic drawing of the external readout scheme.

7.2.1 System layout

The general layout is shown in Fig. 7.2: The electronics attached directly to the PMTs is kept to a minimum. At the base of the PMT, the signal is decoupled from high voltage and increased by a pre-amplifier. From there, the analog signal travels along a 100 m long cable to the input at the external front-end electronics (FEE). These will be arrayed in crates of the ATCA chassis specification. Each crate will hold ten FEE modules and two trigger modules. Each FEE module will provide for 32 channels backend amplification, signal distribution and processing, analog-to-digital conversion and data processing, as well as signal processing for the trigger system.

The FEE modules will send the digitized data to the trigger modules via the backplane of the ATCA crate. These will create the trigger information that will be sent to the central trigger crate by fiber links. In case of a positive trigger decision, the trigger signal will be sent back to each signal processing crate and then fanned out to each FEE module. Each FEE module buffers the data and sends the necessary data asynchronously to the DAQ. Trigger and slow control system will follow the White Rabbit protocol to transfer the clock and other service signals to each crate. The clock signal will be distributed together with the DAQ and slow control through an optical fiber network.

This has several advantages: The simple structure of the external scheme allows for an easy implementation. A global trigger can be easily formed. Maybe most importantly, broken components of the FEE and trigger logic are easy to access for repairs or replacement, and an upgrade of the system is easy to realize during the 10 years or more of detector operation time. The main disadvantage is the transmission of the analog signals from each individual PMT over the 100 m long cables. While signal attenuation can be compensated by placing the preamplifier at the PMT, some shaping of the leading edge of the analog pulses will be unavoidable. In addition, the sheer amount of underwater cables complicates the installation and is a severe cost driver.

7.2.2 Signal amplification and digitization

In the external electronics scheme, pre-amplification will be performed directly at the PMTs and a second amplification stage is located directly after the input of the FEE modules. The bandwidth of the amplification circuit has to be chosen appropriately to minimize information loss by shaping. From there, as displayed in Fig. 7.3, the signal will be divided into two paths: One is fed to a discriminator in order to provide a trigger flag, the other is sent to an FADC for charge measurement. Due to the large dynamic range of the PMT signals (1 pe to ≥4,000 pe), the use of a single FADC for the digitization seems hard to achieve while meeting the resolution requirements for low pulses. Therefore, the amplification will be divided into two or three paths with different amplification gains [1]. In each path, signal amplitude will be adjusted to match the input range of the FADCs. For most of the fast, high-resolution FADCs [2] the maximum range of the input voltage is only 0.5−1 V. Furthermore, minimization of the input electronics noise is quite important to keep up the specified voltage resolution. This can be achieved both by design and by filtering.

The FADCs will be operated in differential mode to increase the performance. The foreseen sampling rate is 1 GS/s, the required voltage resolution 14 bit. There are two possibilities: Either to purchase commercial chips or to design a customized ASIC. In the first case, the ADS5409 from TI and AD9680 from Analog Device would fulfill the requirements. If relying on a self-designed ASIC, the most practicable approach is a multi-channel time-interleaved architecture which will feature a low power consumption compared to a realization based on a single channel. For each channel, a 12 bit, 500 MS/s pipeline quantizer (or a 12 bit, 250 MS/s SAR quantizer) will be used for meeting a good balance between power, speed and accuracy. Offsets and gain mismatches between channels can be calibrated offline. A differential clock input will be used to control all internal conversion cycles.

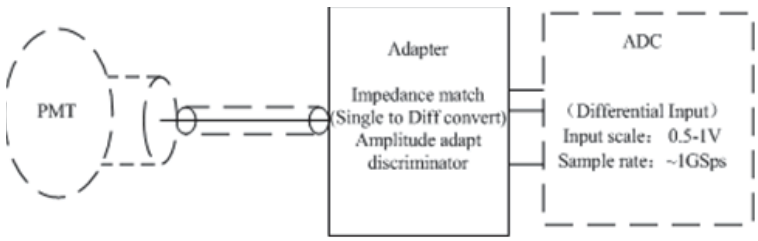

Figure 7.3: Scheme for signal amplification and digitization.

7.2.3 Data processing and transmission

In a first step the FEE system will process the data and provide some simple information to the trigger system. Only when a trigger decision is formed and a corresponding signal is sent back to the crates, the full data (including waveforms) of all channels will be read out, bundled to a combined output in units of modules and crates and then transferred to the DAQ.

There are 10 FEE modules plus 2 trigger modules in each crate. Data is transmitted between the modules via the backplane BUS system of the crates. Communication is

done by a dual-star structure. Each FEE module can receive the trigger signal from either of the two trigger modules via a pair of high-speed serial connections. The digitized data is transferred via ethernet connection to a switchboard and from there to the DAQ. A block diagram of the system is shown in Fig. 7.4.

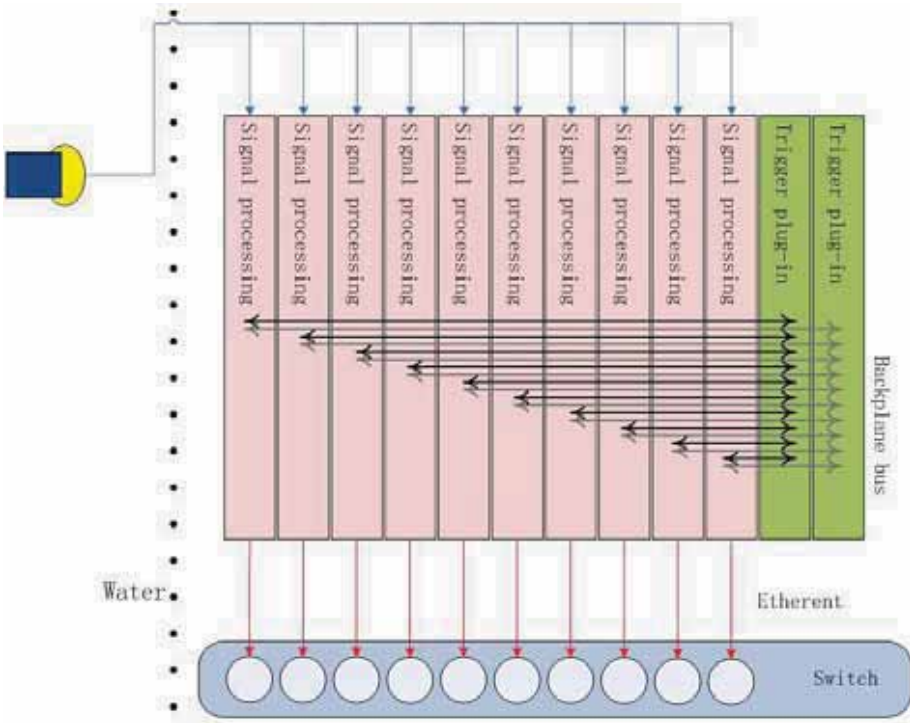

Figure 7.4: Block Diagram of the data processing and transmission of the external electronics scheme

7.2.4 Trigger system

The design goals for the trigger system are the following:

- The trigger efficiency for IBD events induced by reactor $\bar{\nu}_e$ should be high, i.e. reach 99 % detection efficiency for an energy deposit of ~0.7 MeV, so well below the minimum energy deposit of a prompt positron.
- The system should be able to suppress detector-related backgrounds as PMT dark noise coincidences and surface radioactivity to reduce the overall event rate.
- The latency introduced for the processing of 15,000 PMTs should not exceed a few μs.

7.2.4.1 Trigger rates and threshold

The expected trigger rates generated by neutrino signals and backgrounds were studied by simulations. The assumed preliminary detector design comprised the target of 20 kt

of liquid scintillator (LS), surrounded by a layer of mineral oil and the PMTs installed on a stainless steel frame. Signal sources considered were IBD signals, residual radioactive background events in the LS, cosmic-ray muons, and the dark noise of PMTs. We assumed that the buffer was thick enough to shield the gamma-ray background from the PMTs and support structures.

The details on signal and background assumed are summarized in Tab. 7.1: Radioactive background levels in the LS were estimated conservatively based on the conditions in the Daya Bay detectors [1]. However, radiopurity requirements for JUNO are much stricter. If i.e. levels from KamLAND [19] are used, the rates will be lower by several orders of magnitude. Muon background was estimated with 1,500 mwe of rock overburden, taking into account a coarse image of the three-dimensional surface topology. Muon-induced spallation isotopes (i.e. ^{9}Li etc.) were not considered.

Signal or background	Calculation standard	Event rate before trigger
IBD	90 /day	90 /day
Background in LS	^{238}U: $4.5{\cdot}10^{-5}$ ppb	226 Hz
	^{232}Th: $2.7{\cdot}10^{-3}$ ppb	3.17 Hz
Muons	1,500 mwe	16 Hz
PMT dark noise	150 kHz/PMT	3.3 MHz

Table 7.1: Input for trigger rate simulations

For the parameters characterizing the detector, we assumed an LS light yield of 6,000 photons per MeV, an attenuation length of 30 m, a PMT coverage of 80 %, and a quantum efficiency of 35 % [4].

In the simplest approach, the trigger decision will be based on the hit multiplicity inside a coincidence window of 300 ns (see above), i.e. on the number of simultaneously occurring PMT hits. Fig. 7.5 shows the event rate as a function of this number of coinciding PMT hits. Based on these spectra, it seems that a simple hit multiplicity trigger will return both sufficiently low trigger rates and high trigger efficiency for IBD events if the trigger threshold is placed at ∼500 coincident hits. This coincidence trigger scheme is technically easy to implement and will create only low latencies.

7.2.4.2 Trigger setup

Each FEE will handle 32 PMT signals. The hit flags of ten FEEs inside a crate will be bundled by one Level 1 Trigger Collection Board (L1TCB). In turn the information of ten L1TCB will be fanned to one level-2 board (L2TCB). The Trigger Board (TB) itself will receive data from five L2TCBs. This will be sufficient to read out the trigger flags of 15,000 channels. The L1TCBs and L2TCBs will also work as a fan-out for re-transmitting the trigger decision from the TB to individual FEEs.

7.2.5 Clock system

The clock system for JUNO has two major functions. It will provide:

- a standard reference frequency to all FEE modules to support the waveform sampling, TDC measurement and process logic;

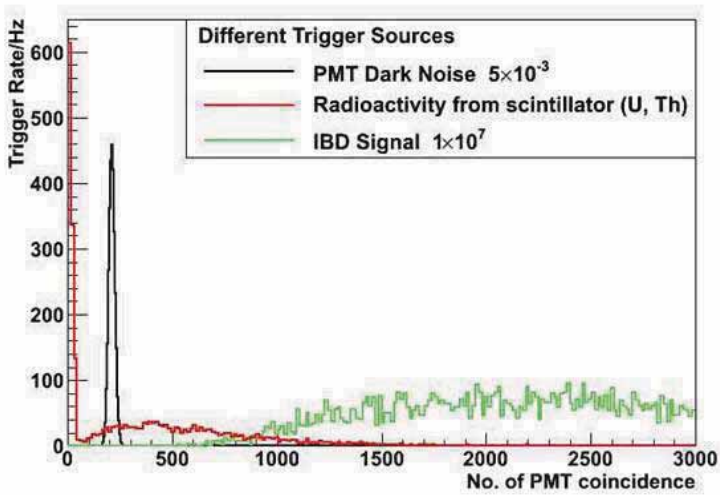

Figure 7.5: Event rates as a function of the number of PMT hits coinciding in a 300 ns trigger window.

- an absolute timestamp for each event to correlate the events of the central and veto detectors and for comparison with other experiments.

Based on the experience gained in the Daya Bay experiment and following the latest developments, a distributed clock network based on the "White Rabbit" standard will be applied for JUNO.

The "White Rabbit" (WR) system is a technology originally developed by CERN and GSI for the use at accelerators. It is based on IEEE1588 (PTP) including two further enhancements: The precise knowledge of the link delay and a possibility of clock synchronization over the physical layer with Synchronous Ethernet (SyncE). Applying WR in JUNO will offer the following advantages:

- The low-jitter recovery clock from SyncE provides a reference frequency for the electronics.

- Sub-ns clock phase alignment can be achieved among all nodes by phase measurement and phase compensation.

- The precise time protocol (PTP) synchronizes the timestamp among all nodes.

- An external Rubidium oscillator and GPS can be used for frequency and UTC reference.

The system will synchronize all electronics crates. Each crate will contain a custom-designed clock module to recover the reference frequency and the absolute timestamp. This will then be broadcasted to all FEE and trigger modules in the crate via the dedicated high-speed clock traces on the back-plane for ATCA crates and via front-panel fan-out cables for non-ATCA crates.

7.2.6 Power supply and electronics crates

Conventionally, high voltage for the PMTs would be generated by a dedicated HV supply outside the water pool. However, the preferred solution is the generation of the HV by a Cockroft-Walton type power supply either attached to the PMT base or in underwater units. In this case, these generators have to be fed with low or medium voltage cables from outside the tank. Solutions with voltages of 5 V or 24 V are conceivable, the former requiring a larger cable diameter to transfer the larger current without loss. In order to avoid the power loss by using a linear power supply, a DC/DC module should be used for high efficiency. In order to reduce the ripple, the power supply should be independent.

The FEE and trigger modules will be designed according to the specifications of the ATCA standard. Fig. 7.6 shows the ATCA crate that will house the modules. It provides a large bandwidth for digital transmission which allows to pass trigger information between FEE and trigger modules via the bus system of the crate.

Figure 7.6: The ATCA crate

7.3 Intermediate readout scheme

The primary disadvantage of the external electronics scheme (Sec. 7.2) is the length of the coaxial cables needed for the transmission of the analog PMT signals. This will lead to a shaping of the leading edge of the signals, deteriorating the time resolution. To avoid this problem, the intermediate scheme shown in Fig. 7.7 places not only the pre-amplifier but most of the FE electronics including digitization in a water-tight box inside the tank, considerably shortening the signal transmission length for the analog signals. Each of these 500 submerged processing units will supply an array of 32 PMTs.

From the box, only few cables carrying the digitized signals as well as trigger and clock information will run to the external electronics.

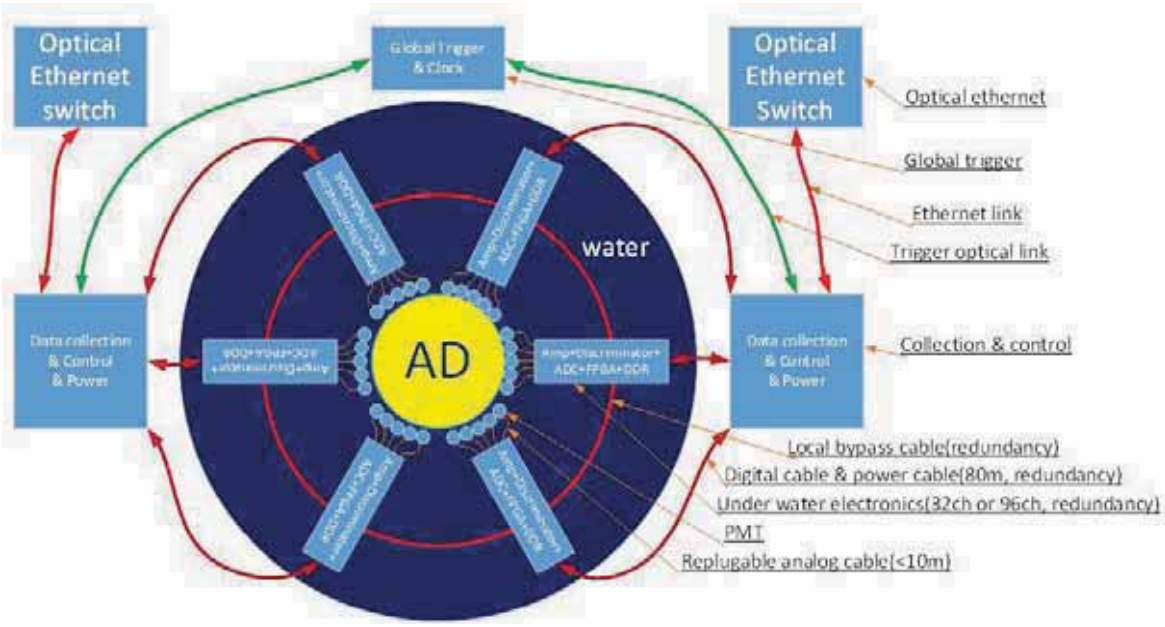

Figure 7.7: Schematic drawing of the intermediate, partially submerged readout scheme.

7.3.1 Signal processing

In this partially submerged configuration, the analog PMT signal will be transmitted only over a short cable to the amplification stage included in the underwater processing units (cf. figure7.3). Therefore, the signal shape will not change significantly. Otherwise, the design of the FEE boards inside the processing units will be mostly analogous to the external scheme. The digitized signals will be bundled for all channels connected to one box and passed by an optical fibers to external modules collecting the acquired data. From there, data will be passed on via ethernet. The block diagram is shown in figure7.8.

7.3.2 Trigger and clock systems

To simplify the design and maintenance of the trigger system, the trigger modules will be located with the other external electronics. The trigger flags from the FEE discriminators as well as the trigger signals can in principle be transmitted on the same optical fibers as the data. It is possible to transmit the same optical cable the data. However, separate cables might be used for the trigger system in order to increase the flexibility.

As for the external scheme, a White Rabbit system can be applied for synchronization of the FEEs in the watertight boxes, providing both a reference frequency for FADCs and an absolute timestamp. In case the optical fibers required by White Rabbit are not compatible to oil, a dedicated clock and data recovery (CDR) link could be

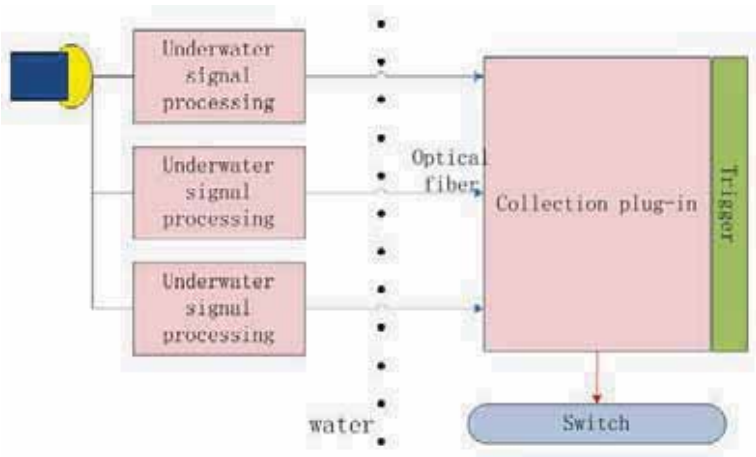

Figure 7.8: Block Diagram of the data processing and transmission of the under-water scheme

designed to provide the reference frequency. The physical calibration system could be exploited to determine the absolute timestamps of events relative to calibration pulses fed in from outside for which GPS time would be known.

7.3.3 Submerged processing units

An important aspect for the long-term stability of the system is the possibility to replace the part of the electronics submerged in the water, i.e. the processing units. The structure of a readout strand including one processing unit is shown in Figure7.9. The enclosing box will be 30 cm high, 40 cm wide and 60 cm long. There will be mounting holes and the possibility to remove the top lid. Fig. 7.10 shows a three-dimensional representation, Fig. 7.11 displays the side panels: The left panel of each watertight case is connected to coaxial-cables by 32 connectors, while the right panel is connected to a composite cable including an optical fibre for signal transmission and a power cable for HV generation inside the underwater box.

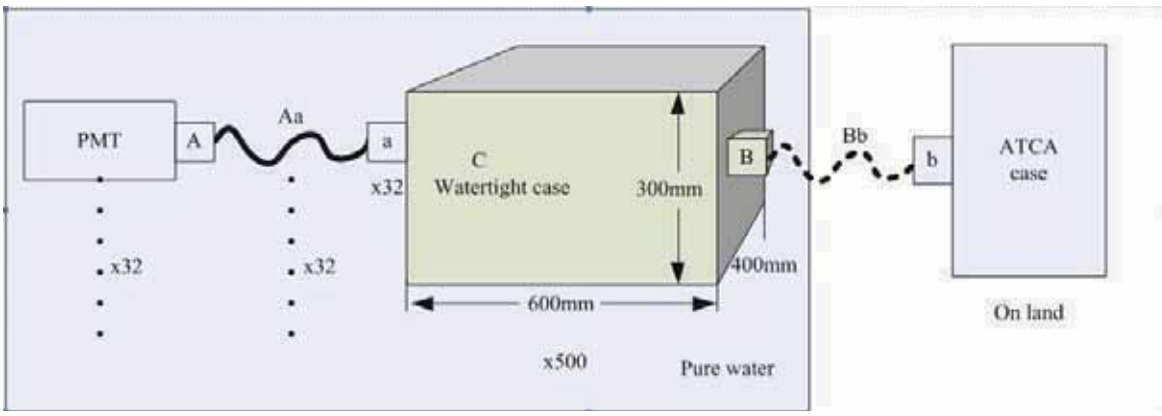

Figure 7.9: Structural representation of the readout chain in the intermediate scheme.

The further components shown in Fig. 7.9 have to fulfill a number of requirements:

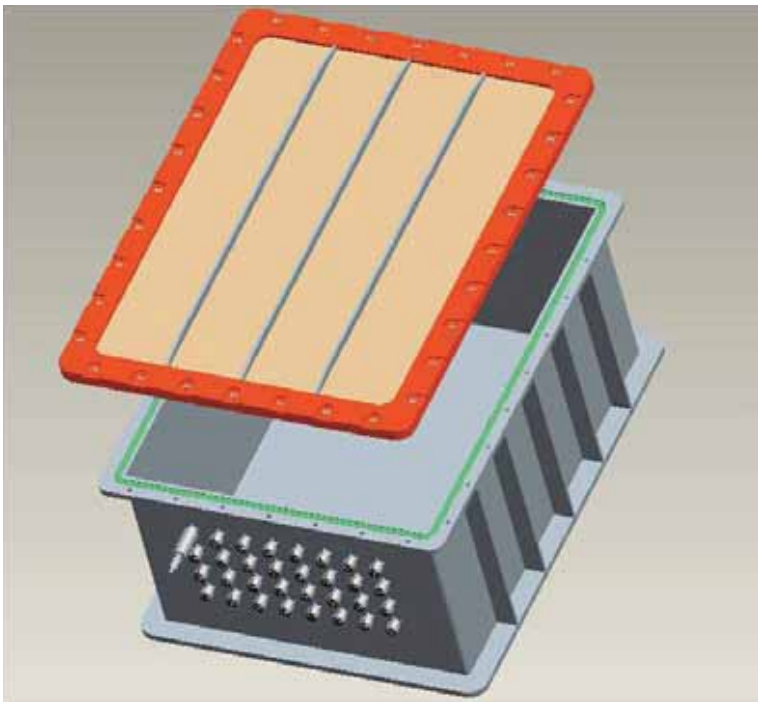

Figure 7.10: The diagram of the watertight case appearance

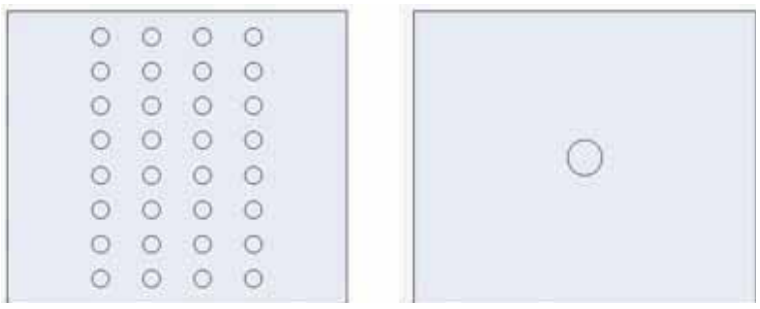

Figure 7.11: Diagrams of the side panels of the submerged processing units

- Cable Aa should be coaxial, 10−20 meters long, and with a characteristic resistance of $50\,\Omega$.
- Connector A is watertight.
- Connector a is watertight and has to be pluggable under water.
- Cable Bb is a composite cable of 100 m length containing at least 4 optical fibres and 4 power wires (24-48V, 10-20A) usable for underwater environments.
- Connector B is watertight and does not have to be pluggable under water.
- No special requirements are set for connector b.
- Parts B, Bb and b can be replaced by non-watertight cables covered by a corrugated pipe.

7.4 Underwater readout scheme

The underwater concept places almost the entire readout electronics inside the water pool, as close as possible to the PMTs themselves. Front-end electronics (FEE) and HV generation are done at the PMT base, all data transfer is done based on digitized data and bundled in central underwater units (CUU). Thus, the underwater scheme minimizes the deteriorating effects of analog signal transmission over long cables and the overall amount of cables needed. On the other hand, it seems unlikely that broken FEE channels can be replaced during operation, while CUUs probably can.

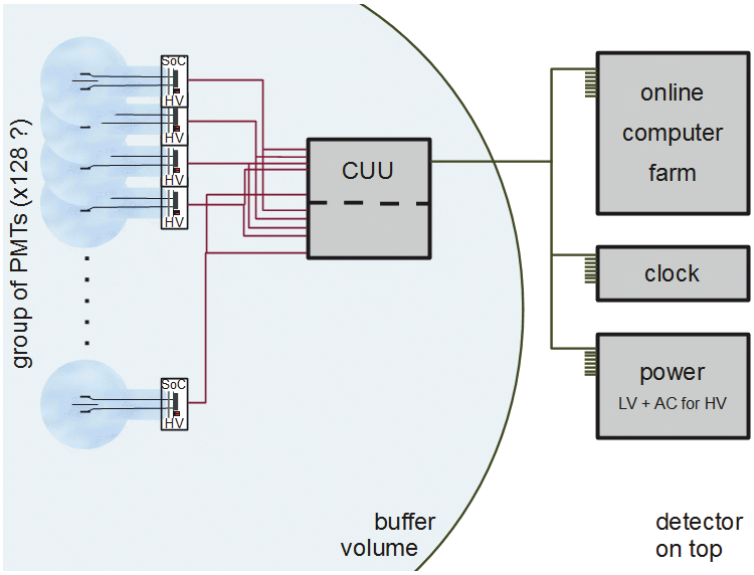

Figure 7.12: Schematic drawing of the underwater readout scheme.

7.4.1 Overview

The layout of the fully-submerged readout scheme is sketched in Fig. 7.12. At the end of each PMT there is a small water-tight housing that contains the front-end electronics (FEE) with all the essential electronics of the system. It contains the base of the PMT and a module that generates the HV from a low-voltage AC input. And it contains a PC-board with a system on a chip (SoC) that includes the digitization of the signal, the discriminator to detect photoelectrons, and other functionalities.

The FEE is connected to the online computer farm through data links. It transmits the data to the farm and receives commands from it. It also receives a clock signal from a central clock unit and the power for the PCB and the HV from corresponding power supplies.

In order to reduce the cabling the PMTs are grouped together under water. We estimate that up to 128 PMTs might be grouped together. In this case the full detector would consist of 128 groups. The grouping of the PMTs takes place in central underwater units (CUU) mounted between the backend of the PMTs. To reduce the length of the cables from the PMTs to the CUUs the groups will be formed from nearby PMTs. The cables from the PMTs to the CUUs will have a unique length somewhere

between 5 and 10 meters. They contain a by-directional data link, the clock signal, the low voltage power for the PCB (probably 3V), a 24 V AC power for the generation of the HV and a ground potential. On the PMT end the cables will be glued into the housing of the FEE. On the end of the CUU there will be a water-tight connector to allow for the mounting. From the CUU there will be a by-directional data link to the farm (probably two for redundancy) and power cables and the connection to the clock on top of the detector.

7.4.1.1 The 'intelligent' PMT

With the FEE the PMT is turned into an 'intelligent' PMT that can be connected directly to a computer. No further electronics is needed. Besides the module that generates the HV and contains also the voltage divider to derive all potentials there is a PCB in the FEE with an ASIC. It contains the SoC with the following functionalities:

- Amplification of the signal.
- Shaping of the signal, should it be necessary.
- Regulation of the baseline to zero.
- Detection of single photon signals through a leading-edge discriminator.
- Generation of a time-stamp for each readout window.
- Digitization of the input signal with an FADC.
- If necessary, a TDC to measure the precise start of each pulse (relative to the time-stamp of the readout window.
- Feature extraction, i.e. determination of the number of photons contributing to a pulse and their arrival-time.
- Self-calibration, i.e. adjustment of the charge integral of single photons to a predefined value through a regulation of the HV and the amplification of the input stage.
- Creation of test pulses and injection into the input of the chip and into the PMT.

These functionalities are provided for each of the two MCPs of one PMT individually (2 channels). The following additional functionalities are common to both channels:

- Creation of an optical test pulse through an LED on the PCB that illuminates the photo cathode.
- Creation of an internal clock signal with the appropriate frequency locked to the input of the external clock.
- Internal functionality tests.
- Data exchange with the CUU.
- Limited data buffer.

A sketch of the SoC components is displayed in Fig. 7.13. Its functionalities are described in more detail in Sec. 7.4.2.

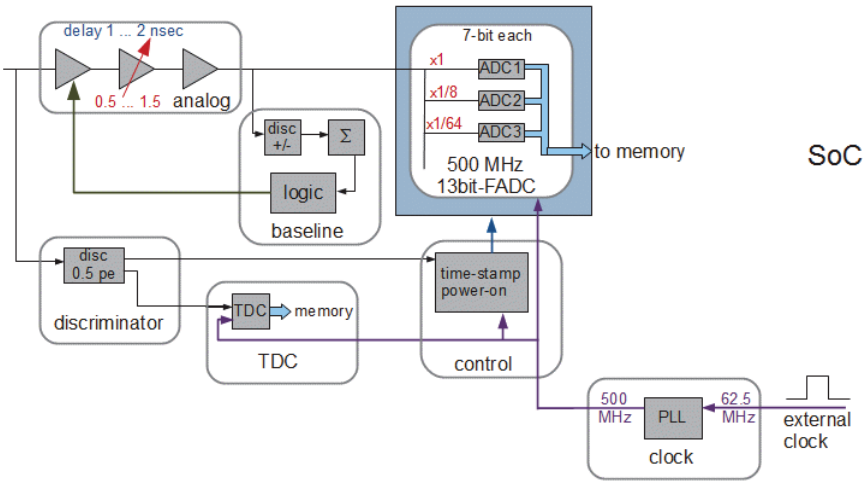

Figure 7.13: The SoC scheme

7.4.1.2 Central Underwater Units

The CUU functions as the connection between the PMTs of the assorted array to the infrastructure on top of the detector. It receives the data from the PMTs. It combines the data and sends it by a single optical link to the computer farm. It must have a sufficient data buffer to compensate fluctuations in the data rate. At the moment it is envisioned to use a commercial PC-board for the CUU. For the data-links to the PMTs the USB-2 standard might be appropriate. Commercial USB-routers could combine the data from the PMTs into a single data-stream which is then sent to the farm through an optical 10 GBit/s link. If this works out, no development is necessary for the hardware of the CUU. The CPU power of the CUU could be used for monitoring, pre-sorting of the data, data reduction, or other purposes.

The most critical parts of the CUU are the many connections attached to the CUU in an under-water environment (at least one connector per PMT plus the up-links). The distribution of the power and the clock to the PMTs will also be done inside the housing of the CUU, so that only one combined cable with connector is necessary for each PMT. For the uplink this is less critical. One could use a power cable separate from the fiber(s).

A substantial amount of monitoring will be necessary to control the detector. The CUUs are also the proper place where the data can be injected into the data stream. Sensors for temperatures, voltages, scintillator flows, can be mounted in or near the CUUs and connected to dedicated inputs of the PC. Monitoring data on the PMTs will be collected by the SoC in the FEE and transmitted through the data link to the CUU.

An interesting alternative to the routing of the data as described above is a passive routing of many data streams through one fiber. Such systems transmit each data stream with light of a different color. They are commercially available. They are potentially more reliable than a CUU based on a PC in a water-tight housing. In this case we would need a connector on the PMT to connect its fiber and a separate power cable to connect to a power distribution box under water.

7.4.1.3 The Online Computer-Farm

The online computer farm will receive the data through 128 optical links with 10 GBit/s capacity. The data will arrive asynchronous. First is has to be sorted into proper time order. Then events are created as time-slices with a minimum activity of the PMTs. These proto-events are subjected to a reconstruction algorithm and from there the decision is derived whether to keep the event or to drop it (or to keep a reduced amount of data). After another sorting in time the accepted events are permanently stored. More details need to be worked out by the DAQ group.

7.4.1.4 Expected data rates and buffer sizes

As PMT pulses are converted early into digitized data, the amount of data to be transferred via fibers and data links as well as local buffers for temporary storage are important characteristics in this scheme. An estimate of the data volume to be processed starts with the amount of digital data caused by the detection of a single photoelectron (SPE). We assume a sampling rate of 500 MHz with one out of three 7-bit FADCs. With a typical rise time of 5 ns and a fall time not much longer a time window of 32 ns per spe is quite conservative. With the MCP-PMTs we will always digitize both channels at the same time. The data volume per spe is summarized in the table7.2: A single waveform is recorded with 144 bits. For two channels and with the auxiliary information this adds up to 360 bits per photoelectron. For the potential TDC we have assumed 8 bits with 125 ps per unit to cover the full length of the readout window.

Data volume of a single waveform	
sampling frequency	500 MHz
readout window	32 ns
number of time-slices per readout	16
number of bits	7
range bits	2
number of channels	2
Intermediate sum	288 bit
Additional information	
address (PMT-ID within group, channel)	8
time stamp	40
control flags	8
TDC (2 x 8 bit)	16
Total sum	360 bit

Table 7.2: Data volume needed per single photoelectron.

Based on the spe volume, the data rate to be transmitted between a PMT and the CUU can be derived. It is completely dominated by the dark rate of the PMT consisting of single photons. We assume a conservative 50 kHz for the dark rate, which corresponds to 18.2 Mbit/s. Any data volume of physics events is negligible compared to the dark rate, even if the physics events contain much more than single photons. For comparison the maximum data rate of a USB-2 link is 280 Mbit/s.

In the event of a supernova the data rate will probably exceed the capacity of the link to the CUU. Therefore a buffer is needed that allows a temporary storage of the data on the FEE itself. A nearby ($\sim$3 kpc) supernova will create 60,000 neutrino events in the detector within $\sim$10 seconds. The event energy ranges up to $50 to 100$ MeV and will create relatively large pulses in almost all of the PMTs. Therefore, we assume that the average sampling period per neutrino event corresponds to five 32 ns readout-windows for each PMT. This produces a data volume of $60,000 \times 5 \times 360$ bit = 13.7 MByte for each FEE channel. On top of this there is the data volume from the dark noise which adds up to 22.8 MByte in 10 seconds. The total sum is 36.4 MByte. This is the minimum size of the buffer on each FEE.

Further along the readout chain, the uplink from the CUU to the computer farm has to be considered. A maximum of 128 PMTs will be combined into one group read out by a single CUU. For smaller numbers the requirements are less severe. To obtain rates and data volumes, the requirements for of a single PMT have to be multiplied by 128, corresponding to a data rate of 2.3 Gbit/s for the link. A link capacity of 10 Gbit/s which is available for standard PCs today will be sufficient. The overall buffer storage needed for a supernova event amounts to 4.7 GByte. The data can potentially be stored in the RAM of the CUU.

7.4.2 The 'intelligent' PMT

This section describes the functionalities of the single elements contributing to the underwater readout scheme.

7.4.2.1 High Voltage

The high voltage (HV) will be generated directly on the PMT from a low-voltage input. A single HV potential will be generated for each PMT from which all voltages required for the photo cathode, the field shaping electrodes, and the two MCPs are derived through a voltage divider. The final PMTs will have their cathodes on ground potential. Consequently the output of the signal will be on positive HV. Fig. 7.14 shows the corresponding circuit proposed by the Dubna group. The HV will be derived with a Cockcroft-Walton multiplier, also known as a Greinacher cascade, displayed in Fig. 7.15.

The Dubna group has already developed a working module for the 8" MCP-PMTs, which is displayed in Fig. 7.16. The input is an AC voltage of 24V. For the final module the input voltage might be higher (up to 200V). The value still needs to be decided. The cascade is embedded in a HV-module that allows regulation of the output voltage. The module already includes the voltage divider and the capacitor necessary to decouple the signal from the HV. It also has the ability to monitor and limit some of the parameters, i.e. the output current. The current prototype is controlled through a USB interface. The final version will be controlled by the SoC on the PMT.

7.4.2.2 Clock System

It is essential that all PMTs are running with the same frequency. This frequency will be provided by a central clock in the cavern above the detector. The clock signal is distributed to all PMTs. For most physics topics knowledge of the absolute time is not

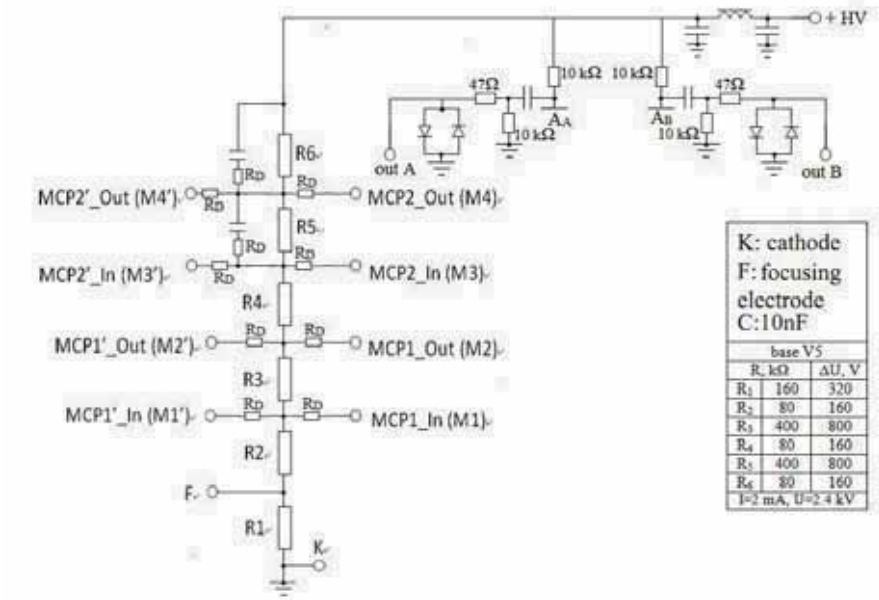

Figure 7.14: Circuit for the voltage divider at the MCP-PMT base

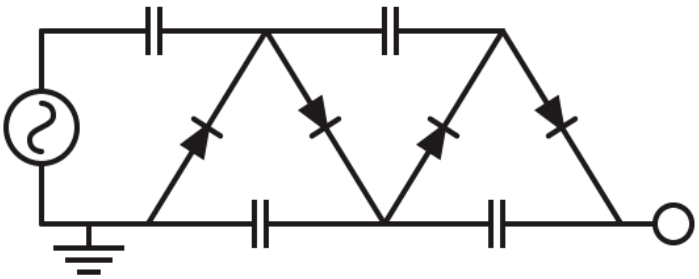

Figure 7.15: The Cockroft-Walton multiplier for HV generation.

required, with the exception of the signals from a nearby supernova. A GPS-system that allows absolute timing should be considered for this case. The GPS receiver must be mounted on the surface, probably in one of the entrance areas.

The cables or fibers that connect a PMT to the central clock generate a time delay between the clock in the PMT and the central clock. These are called time-offsets t_0. For the reconstruction of events in the detector these offsets must be calibrated on the level of 100 ps. If the system runs with a global trigger, a rough calibration is necessary already during running (maybe on the level of 1 ns). For the untriggered system online-calibration is not required. The values of the t_0's can be measured from calibration runs with a light-pulser (LED) in the center of the detector and from the data itself. The electronics must ensure stable t_0's over longer running periods to reduce the calibration runs to a reasonable frequency.

A White Rabbit system has been proposed to calibrate the offsets between the PMTs and the central clock . Such a system seems well suited for a triggered system. For the untriggered system such an effort is not necessary. Offsets (t_0's) from the

Figure 7.16: Prototype of the HV module for the 8” MCP-PMT prototype

previous calibration run will be more than sufficient. In the event of a nearby supernova all offsets (including the offset between the GPS receiver and the central clock) must be calibrated in absolute terms (maybe on the level of 1 ns). The calibration can be done before or after the supernova event. A calibration after the event would save the effort, if no supernova appears, but a plan must be available in any case.

The simplest method to distribute the clock to the PMTs is through individual cables. Distribution of the clock signal could use the same infrastructure as the CUUs, i.e. a single cable transmitting the signal from the surface to the CUU that than spreads it out to the whole group of PMTs. Alternatively one could add the clock signal to the power cables or distribute it through the data links. In principle a wireless distribution is also possible. The central clock will produce a reference frequency from which the PMTs derive their frequency through a phase lock loop (PLL). Most likely the reference frequency will be lower than the PMTs frequency. To give an example: For a 500 MHz digitization on the PMTs one could distribute a 62.5 MHz reference frequency and divide the clock cycles by a factor 8 on the PMTs.

7.4.2.3 Baseline Adjustment

The output of the PMTs will be on the potential of a positive high voltage. A capacitor will be used to decouple the signal from the HV. This capacitor will be integrated into the HV module. The potential behind the decoupling capacitor will be referenced to ground. For the determination of the charge integral of signal pulses a precise knowledge of this potential (i.e. the signal baseline) is essential. One possible approach uses the FADC to measure the baseline directly prior to the pulse. The digitization of the input is started already before the arrival of the pulse. It is important not to under-sample the baseline. It must be determined with the same precision as the pulse itself. The baseline must be sampled for the as long as the pulse itself, doubling the data output.

Here we propose to use a different approach. We want to measure the baseline

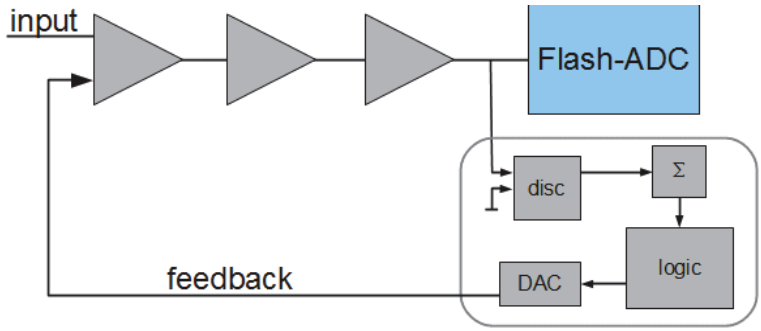

Figure 7.17: Circuit for the baseline adjustment

continuously and adjust it to ground potential through a feedback loop (Fig. 7.17). The concept is very simple. A discriminator compares the input against ground potential with the frequency of the clock. Due to noise on the input the input potential will fluctuate between positive and negative potentials. On average, time slices with positive (+'s) and negative (−'s) voltage bits will be balanced. The discriminator will produce as many +'s as −'s. If the input potential changes, the balance between +'s and −'s will be distorted. For example an excess of +'s will indicate a deviation of the input potential to positive values. A simple logic will determine the difference of the number of time slices with +'s and −'s. The result will be used to adjust the potential in one of the input amplifiers until the balance is restored.

Two special situations must be considered to avoid a bias in the baseline:

- If a true pulse arrives the feedback loop will detect it as a positive deviation of the baseline and counter-correct the deviation. To avoid this bias the feedback loop has to be stopped if an input pulse is detected.

- The return of the signal to the baseline after a pulse will take some time. If a second pulse arrives before the signal has returned to zero, its charge integral will be measured with a too large value. This effect can be corrected offline. All photon pulses will be read out. Time and charge of the previous pulse can be determined independently. An algorithm on the online-farm can either correct for the previous pulse, or store the previous pulse for later correction, or do both.

There is, however, one special case, where this will not work. If the pulseheight of the previous pulse is below detection threshold, the correction cannot be applied. But one should keep in mind, that close pre-pulses will be rare, the undetected fraction of pre-pulses even rarer, and the bias will be very small, especially for pulses below threshold.

A number of parameters of the baseline adjustment need to be optimized. The difference of +'s and −'s outputs of the discriminator needs to be averaged over a certain amount of time slices. The larger the number, the more precise the adjustment becomes, but it also gets slower. This parameter should be kept flexible to adapt to the situation in the real experiment. Another important parameter is the step-size with which the baseline is adjusted.

The overall concept of the intelligent PMT will include a random trigger. That is, at adjustable time intervals the electronics will digitize a readout window and store the

output. These readout slices should be empty and can be used to check the performance of the baseline adjustment.

7.4.2.4 Internal Trigger

A simple level discriminator will be used to trigger the readout of a single PMT. It will continuously monitor the output of the PMT. The threshold must be programmable. It will be set directly above the noise, as low as acceptable in terms of rate of noise triggers. The threshold can be adjusted individually for each PMT. We envisage a threshold at a level of 0.3 photoelectrons. In the case of the MCP-PMTs there will be separate triggers for each MCP. Most likely the electronics will be configured in such a way that a signal above threshold from one of the MCPs will trigger the readout of both channels.

The readout window will be adjusted to the length of a pulse from a single photoelectron, probably around 32 ns. In the case of high energy events such as cosmic muons or atmospheric neutrinos several or even many photons will be detected by a PMT. The output signal will extend over more than 32 ns. If the photons are separated in time, they will be read out as individual triggers. If not, the full signal will be covered by reading several consecutive 32 ns windows. The trigger logic monitors the threshold discriminators. If at a certain time during the readout (i.e. in the middle of the 32 ns window) the signal has not returned to below threshold, the logic will continue the readout for another 32 ns. The readout will be sustained until the signal finally falls below threshold. No information is lost.

7.4.2.5 Flash-ADC

A FADC will digitize the input signal. For the MCP-PMTs two separate FADCs will be needed for the two MCPs. The required dynamic range of amplitude has been estimated to 1000 pe for a whole 20” MCP-PMT, or 500 pe per MCP. The prototypes of the MCP-PMTs show an electronic noise level which is in the order of 10 % of the amplitude of a single photo-electron. Therefore a 10 % resolution on the amplitude of a single pe will be appropriate. The corresponding resolution on the spe charge integral will be better, on the level of a few percent. If the amplitude of a single pe corresponds to 10 ADC units, a dynamic range of 5,000 to 10,000 ADC units will be needed, corresponding to 13 bits. It is technically not possible to derive 13 bits from a single ADC. Multiple ADCs with staggered ranges are required. We propose to use 3 ADCs with 7 bits each, featuring the following scheme:

amplitude	range	resolution
$\times 1$	0−13 pe	0.1 pe
$\times 1/8$	0−100 pe	0.8 pe
$\times 1/64$	0−800 pe	6.4 pe

7.4.2.6 Time Measurements

For the reconstruction of vertices or tracks it is necessary to measure the time of arrival of the photons on the PMTs. A resolution of 1 ns is required. The arrival time can be extracted from the waveform recorded by the FADC. With the proposed 500-MHz FADC (2 ns time slices) it is possible to extract the starting time with 1 ns resolution.

More precise timing information is encoded in the digital pulse of the level discriminator of the internal trigger. The discriminator triggers the first photon of the pulse. This is the most valuable information for the reconstruction. A TDC could be included to measure the time of the trigger relative to the preceding clock pulse. For example to get a 500 ps resolution a 2-bit TDC would be sufficient.

7.4.2.7 Self-Calibration

The ASIC will contain a mechanism to calibrate its PMT to a predefined charge integral of a single photoelectron (SPE). The basic scheme is shown in Fig. 7.18. Whenever the input signal crosses the trigger threshold for a single photoelectron the flash-ADC will digitize the input and write the data into an internal memory. The logic in the digital part of the chip will analyze the pulses within a single photoelectron window and determine the average charge integral, $\langle q_{\mathrm{pe}} \rangle$. The $\langle q_{\mathrm{pe}} \rangle$ of each channel is compared to a default charge value, and the HV applied to the PMT adjusted until the predefined value is reached.

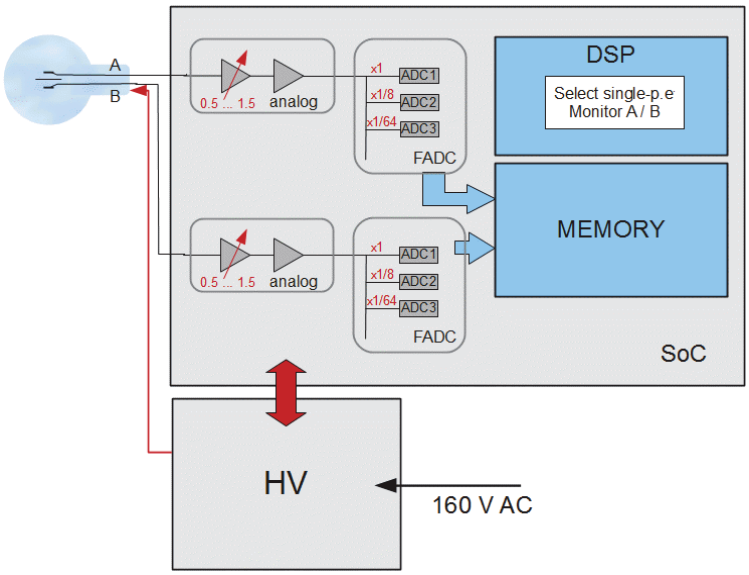

Figure 7.18: Schematic drawing of the self-calibration feedback loop

The presence of two MCPs with different gains inside one PMT adds a complication because both MCPs are powered from a common high voltage. The algorithm on the chip will compare the $\langle q_{\mathrm{pe}} \rangle$ of both MCPs to the predefined value. It will first adjust the gain of the input amplifiers until the $\langle q_{\mathrm{pe}} \rangle$ of the two MCPs agree with each other. Then it will adjust the high voltage to match the $\langle q_{\mathrm{pe}} \rangle$ to the predefined value.

7.4.2.8 Internal test devices

The circuitry will incorporate extensive possibilities for testing. This is important to guarantee the functionality of the system and to understand how to react in case of problems. The details still need to be worked out. Two test installations that will be integrated for sure are:

- A test pulser within the SoC: The pulser can be used to inject charge into the input of the chip. It could either be an analogue circuit which produces pulses similar to the real pe's or a digital pulse generator.
- A light pulser: A LED will be mounted in the electronics in a position where the light illuminates the transmission cathode from the backside (through the glass neck of the PMT).

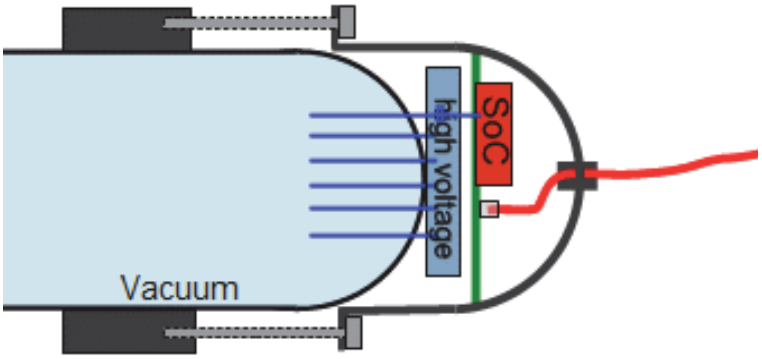

Figure 7.19: Mechanical realization of the intelligent PMT design.

7.4.2.9 Mechanics

The scheme for mounting the FEE directly to the base of the PMT is shown in Fig. 7.19: The HV module plugs directly onto the pins that connect to the electrodes in the PMT. It includes the wire(s) that carries the output signal. A capacitor is needed to decouple the signal from the high voltage. This capacitor will be included in the high voltage module. On top of the high voltage module there will be a PCB that carries the ASIC with the SoC and some external components (voltage regulator for the low voltage, etc.). The cable to the central underwater units is connected to this PCB. The whole electronics is inside a watertight metal cap that connects to the mechanical fixture of the PMT. The details on how to seal the housing still need to be worked out.

For the default scenario, where data is routed through the central underwater units (CUU) there is a single cable from each PMT to the CUU. It contains power, clock and the data line. It is firmly attached to the electronics housing on the PMT without a connector. The cable length will be between 5 and 10 meters. It has a watertight connector that connects to the CUU. For redundancy there might be two such cables per PMT connecting to two different CUUs.

In case passive data links will be used, an optical fiber will be connected to each PMT. The driver circuit and the laser will be included on the PCB. There must be a watertight optical connector on the fiber where it connects to the PMT. For each PMT there will be a separate cable for the power that connects the PMT to the power distribution box.

7.4.2.10 Power

Each PMT needs a low voltage DC-power for the SoC and a low voltage AC-power for the high voltage module. The exact values have not yet been defined. For the

time being we assume a +3V DC-voltage for the SoC and a +24V AC-voltage for the high voltage module. The voltages are generated in power supplies in the cavern on top of the detector. They are accessible and can be replaced in case of failures. From the power supplies, cables will transmit the power to distribution boxes inside the water pool. Each PMT is connected to one of the boxes with a cable and a water tight connector on the power distribution box. The cable contains the DC and the AC voltage, the ground potential and maybe the clock. In case the scheme with active data links is adopted, the power distribution will be integrated into the CUUs. In the case of passive data links there will be distribution boxes just for the power.

One power distribution box or CUU will supply power to a group of 128 PMTs. This system must be protected against failure of the whole group. If a cable to one of the PMTs breaks, a single PMT will be lost which is not catastrophic. However, a short in one PMT could take out the whole group. Therefore a serial resistor RP has to be introduced in the PMT contacting scheme shown in Fig. 7.14. These resistors must be large enough to limit the current through a PMT with a short, at the same time avoiding a too large power consumption in the resistor if the voltage on the PMT changes. For example, if 3 V is required for the SoC, a 6 V power supply could be used. We choose a value for RP that creates a 1 V voltage drop. A voltage regulator located on the PCB at the PMT base will reduce the remaining 5 V to 3 V. The protection resistor increases the power consumption by 20 %. which will still be acceptable. In case of a short the power of this channel goes up by a factor of 5. This is still negligible compared to the power of the whole group.

Another critical item is the cable from the power supply to the distribution box. It might break or shorten out. We propose to have two identical cables, but only one is connected to the power supply. Inside the distribution box there are switches on the power. Without power the switches are closed. Let's assume cable A is connected to the power supply. If we turn on the power, it will open the switch on cable B and disconnect it completely from the system. If cable A fails, it will be disconnected from the power supply. This closes the switch to cable B. Cable B can now be connected. It will open the switch on cable A and disconnect it from the system, bringing the system is back into operation.

7.5 Development plan

7.5.1 Characterization of PMT response

To get a better understanding of the dynamic range and voltage span required, the PMT response and in particular the pulse height and linearity will be studied as a function of the incident number of photo-electrons. For this, a laboratory test stand is currently realized. As the MCP-PMTs are not yet available, characteristics will be first determined for the 20" PMT (R5912) produced by Hamamatsu. For covering the whole range specified, waveforms containing 1−4000 pe have to be recorded.

To match this requirement, the tests will be performed following this procedure:

1. Record **single photoelectron pulses** at a gain level of 10^7. The right gain is assured by integrating the single photoelectron waveform (cf. Fig. 7.20), subtracting the baseline pedestal and dividing by the elementary charge. An additional

factor of 2 has to be taken into account as a double-end termination is used in the R5912 PMT base.

2. **Ramp up of LED intensity** until 4000 pe are reached, while continuously recording the waveforms for different LED output and thus multiple photoelectron levels. As before, the equivalent charge will be calculated based on waveform integration.

At low hit multiplicities, a discret cascade of broadening peaks will be observed that corresponds to defined numbers of photoelectron. At higher LED intensities, the charge spectrum will become a Gaussian distribution. The number of incident photoelectrons can be calculated based on the gain.

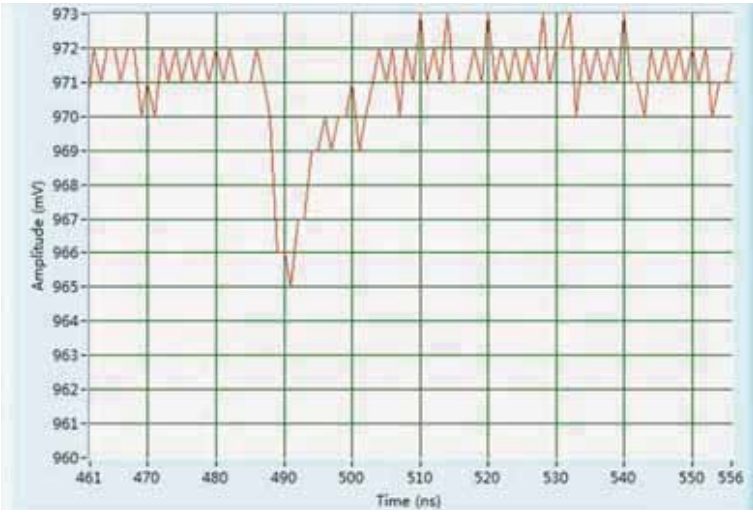

Figure 7.20: The waveform for SPE

7.5.2 Signal amplification

A careful study of the amplification requirements will be performed for the three readout schemes, including pre-amplification, gain division, and ASIC design. The relevant design specifications are the dynamic range of 1−4000 pe and an equivalent input noise RMS of less than 0.1 pe. The following aspects should be investigated:

- **Impedance matching for long cable.** Reduce the reflection between transmission lines and other devices, considering the effect of parasitics and couplings of cables and transmission lines.
- **Gain division.** The dynamic range is divided into three overlapping FADC acquisition ranges, 1−67 pe, 1−529 and 1−4000 pe. As the original amplification by the PMT dynode chain or MCP will depend on the PMT chosen in the final design, so will the amplification stages.
- **Amplifier selection.** Commercial amplifiers have to be selected for large dynamic range and low noise. Signal clipping and overload protection will be studied carefully for MCP signal.

- **Amplifier for FADC driver.** Since the PMT signal amplitude is large, the amplification factor will be small (less than 2), which makes the noise of ADC driver important to the resolution of the total system. Low noise of this amplifier is thus mandatory. Other performance parameters such as settling time have to be studied.
- **Discriminator selection**. A discrimination level of less than 1/4 pe is required.
- **ASIC design.** Amplifiers and discrimators have to be integrated in an ASIC holding 16 or 32 channels.

7.5.3 Cables and connectors

7.5.3.1 External readout scheme

The external scheme will employ 20,000 coaxial cables of 80−100 in length and compatible with the underwater environment. Due to the great length, special attention should be given to low signal delay and attenuation to ensure a high quality for the transmission of the analog signals.

A selection of coaxial cables from the have been surveyed Tianjin 609 Cable Co. Ltd.. Samples of 100 m length have been tested for attenuation. Results are listed in Table7.3. While the Type III cable clearly shows the best performance in terms of signal dampening, it is also the most expensive.

Parameter	Type I	Type II	Type III
Product Model	SYVF -50-3-1	609C5021A	609C5019A
Outer Diameter	10.5 mm	3.5 mm	4.5 mm
outer sleeve	ordinary sleeve	FEP	FEP
Attenuation @ 100 MHz	17.7 dB	15.9 dB	12.3 dB
Attenuation @ 200 MHz	24.8 dB	23.4 dB	17.7 dB
Price (RMB/m)	10	14	18

Table 7.3: Survey and attenuation results for three samples of 100 m long coaxial cables from Tianjin 609 Cable co.

The sleeves have also been tested for compatibility with the LS. The effects on the attenuation spectra of LS samples that have been left for some time in contact with the cables are shown in Fig. 7.21. The resulting changes for cables of Type II and III are less severe than for Type I.

7.5.3.2 Intermediate readout scheme

The requirements for the cabling of the intermediate readout scheme are somewhat different. As the FEE are moved into the submerged processing units, watertight boxes as well as underwater connectors are needed. In detail, this scheme needs:

- About 20,000 coaxial cables of 10−20 m length for the signal transmission from PMT to the processing units. Cables should be covered by a sleeve from fluoroplastics.

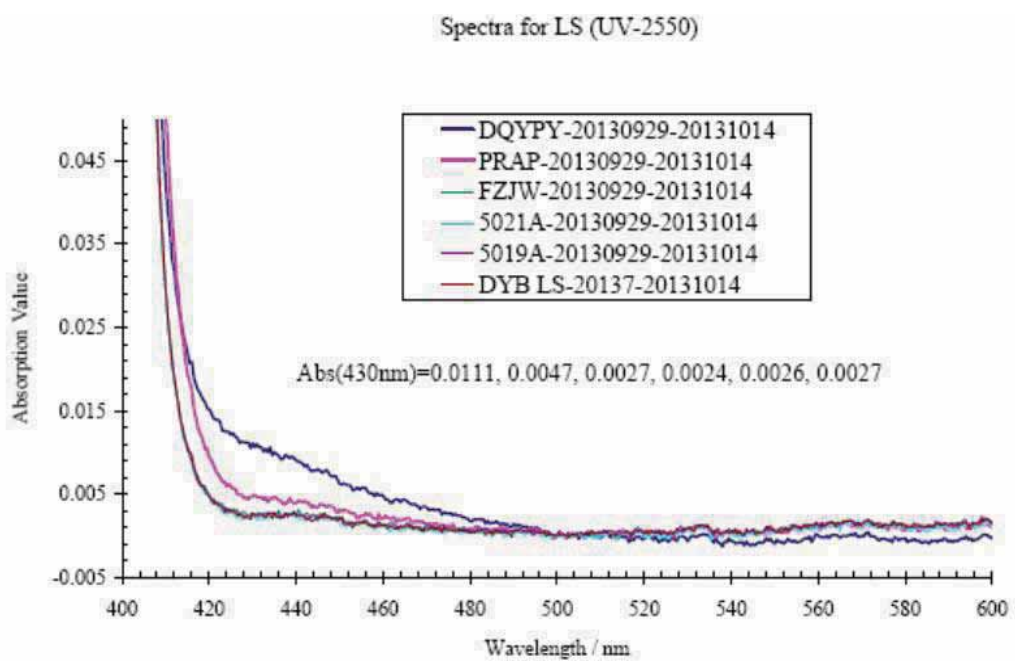

Figure 7.21: Effect of the exposure of LS to the cable sleeves on the LS attenuation spectrum.

- About 20,000 connectors that can be plugged under water. Fig. 7.22 displays suitable products by the Shanghai Rock-firm Co. Ltd.
- About 500 watertight cases for the central processing units
- About 500 composite cables for data transmission via optical fibers and low-voltage power supply

The feasibility of this scheme is currently evaluated at IHEP. Contacts have been established to a variety of providers for watertight connectors and cases, including Beijing the Great Wall Electronic Equipment Co., Ltd. China aviation optical-electrical technology CO., Ltd. Shanghai Rock-firm CO., Ltd. No.23 Research Institute of China Electronics Technology Group Corporation and others. While watertight cables can in any case be provided, the sleeve material and the fluorination treatment of the rubbers are still under investigation. This is an important aspect as fluorination will protect the rubber against the corrosive strength of pure water, allowing for a life time of 10−20 years. Further important questions are the impermeability of the watertight cases, the characteristics of the signal transmission and last but not least the additional cost introduced by this scheme.

7.5.4 ADC selection and circuit design

A further important step is the selection of the FADC chip. Several FADC chips have been included in a preliminary survey. Tab. 7.4 summarizes the main characteristics for a variety of commercial and self-developed chips. Circuit designs are currently studied to evaluate the FADC performance and its compatibility.

Figure 7.22: Under-water connectors from Shanghai Rock co.

Type	Model	Sampling rate [GS/s]	No. of channels	Resolution bits	ENOB
FADC	ADC10D100D	2/1	2	10	9.1
	ADC12D1000	2/1	2	12	9.6
	EV10AQ190A	1.25	4	10	8.6
	ADS5409	0.9	2	12	9.8
	ADS5407	0.5	2	12	10.3
	Stefan's (ASIC)	1	1	N/A	N/A
	Fule's (ASIC)	1	1	12	>10
Sampling + ADC	DRS4 + AD9252	1-5	8	11	8(?)
	Weiw's (ASIC)	1	1	N/A	N/A

Table 7.4: Overview of selected (Flash-)ADC chips

7.5.5 Design of waveform digitization ASIC

To fulfill the requirements of JUNO concerning timing and pulse height resolution, the acquisition and digitization of PMT waveforms at a sampling rate of 1 GS/s and an acquisition range of 12 bit is mandatory. However, commercial high-speed FADCs meeting these specifications are currently banned from import to mainland China. While possibilities exist to obtain suitable chips by transfer via a Sino-American collaboration, the resulting price will be undoubtedly high. In order to reduce the cost per electronics channel, design efforts for implementing a new form of ADC on an ASIC or for a self-made high-speed FADC have been started.

7.5.5.1 Design of an ASIC for high-speed waveform sampling

The bottleneck of the design of the high speed-waveform sampler is the huge data throughput. It is very difficult to store a huge data volume within a very short time as it would be encountered during a supernova. However, as long as the event rate is limited, continuous storage will not be necessary as most of the acquired date is either baseline or background signals.

The waveform-sampling chip will rely on the online selection and caching of the analog data. The chip will first sample the waveform at high speed, and save the resulting waveform information in an analog memory. When there are no physics triggers, the sampling process will keep running, thus refreshing the cached analog data and overwriting the old one; when a trigger is issued, the waveform stored in the analog cache will be digitized immediately. The post-processing logic therefore only has to deal with waveforms of the length of the analog buffer. This method allows for both high-speed sampling and caching. Moreover, the conventional approach of simultaneous analog-to-digital conversion and readout are thus separated. The analog memory first acquires the pulse, then the ADC is converting the stored waveform and sends only a short piece of waveform to the backend system for storage. Therefore, the data processing load for the backend systems is greatly reduced.

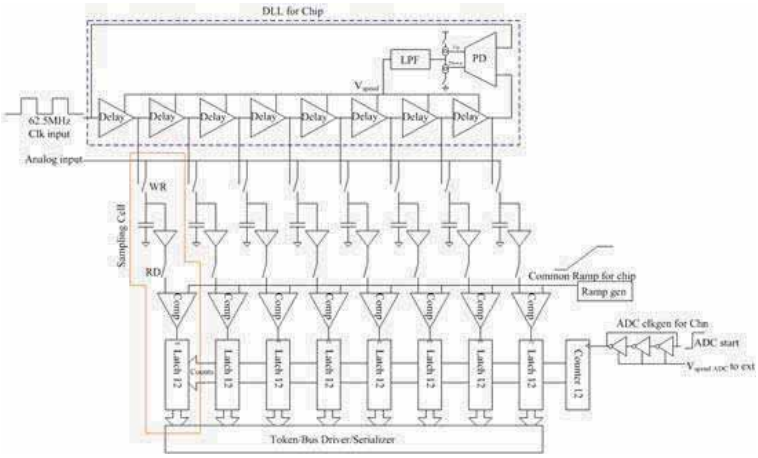

Figure 7.23: The architecture of one channel of the waveform sampling ASIC

The architecture of the waveform sampling chip is given in Fig. 7.23. The high speed sampling and analog memory is realized by a large switched-capacitor array (SCA). When no trigger comes, the SCA will keep sampling in a cycling style, and the voltage values held on the capacitors are consequently refreshed; when a trigger is issued, the held voltage will be compared with the common ramp signal of the chip by an exclusive comparator for each capacitor. Meanwhile, a counter will monitor the time duration from the start of the common ramp signal until stop signals are issued by the comparators. The stored analog information is then converted to digital output in a single step. The individual start-to-stop time counts will be stored in the corresponding latches. When the the ramp signal ends, the latched data will be transmitted by the serializer.

In order to be able to cope with the expected dark rate per channel of 50 kHZ, each ASIC channel will include 256 storage cells.

7.5.5.2 Design of a high-speed FADC

A further solution is a self-designed high-speed FADC. The idea is based on a more conventional architecture, for which a high-speed ADC will take charge of sampling the waveform and digitization in a single step. All the converted digital data will then be

transmitted to the backend system for data buffering, trigger selection processes and so on. Due to the import prohibitions, a self-designed FADC put into mass production will greatly decrease the cost of the system.

The ADC will be based on a hybrid architecture combining a pipeline A/D convertor and flash type. The signal will be sampled through an input buffer and a sample-and-hold circuit, and then be pre-converted by a four-stage pipeline conversion. A flash conversion stage will finally digitize the signal. In this way, the stress of high sampling speed and high voltage resolution are distributed to multiple stages. Also power dissipation per area will be reduced. The chip is expected to achieve asampling rate of 1 GS/s and a resolution of 12 bit, with a guaranteed effective number of 10 bits.

7.5.6 Data processing and transmission

7.5.6.1 External readout scheme: ATCA modules

The FEE modules used in this electronics scheme will be based on the ATCA standard. The structure block diagram is shown in figure7.24: The modules will be based on a daughter-mother board structure. The function of the daughter board is to receive the PMT signals and to perform the digitization. The mother board is a standard ATCA module. As the main unit of data transmission and processing, it will aggregate the data from all daughter boards, transfer the clock and trigger signals via the high-speed backplane bus, transfer the final data to the DAQ via a Gigabit ethernet connection and take care of system control and configuration. The FPGA of the module will perform the digital signal processing and information extraction.

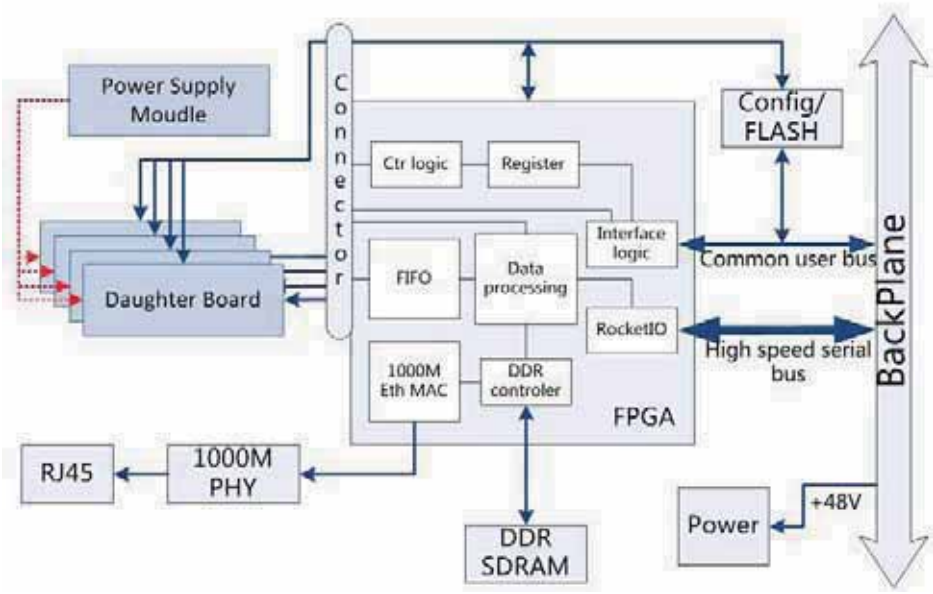

Figure 7.24: Standard ATCA module structure block diagram

7.5.6.2 Intermediate readout scheme

Submerged processing unit. In the partially submerged scheme, the signal processing unit will still be based on a daughter-mother board structure. The FEE daughter board will be mostly identical to the external case. The mother board will package the data and transfer it to the external electronics via an optical fiber. For reliable data transmission, some redudancy will be introduced for the mother board:two FPGAs will serve as backup for each other. When one of the FPGAs is not working properly, the system will switch to the other one. A corresponding diagram is shown in Fig. 7.25.

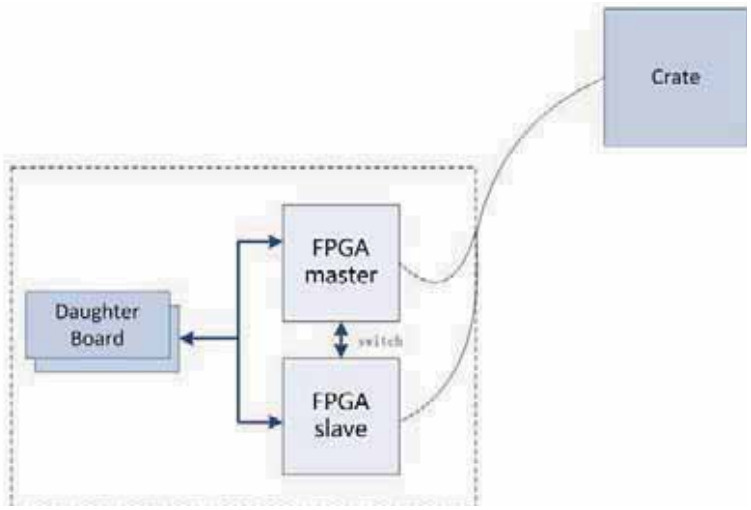

Figure 7.25: Diagram of the submerged processing unit

Signal collection unit. The data sent by the underwater processing units via optical fibers will be received by a collecting ACTA module based on a daughter-mother board structure. The motherboard is an ATCA standard module, while the daughter board completes some simple function like the collection of the optical data and the transmission to the mother board.

7.5.7 Design of trigger and clock

The White Rabbit technology has been used extensively in the LHAASO experiments. A compact FMC-form White Rabbit node (cute-wr) has been developed which can be easily integrated as a network mezzanine card on other electronics system. It will provide a uniform 125 MHz clock signal, a Pulse-Per-Second signal and an encoded UTC timestamp signal. First tests with a prototype system show a 100 ps accuracy and 21 ps precision among several cute-wr cards.

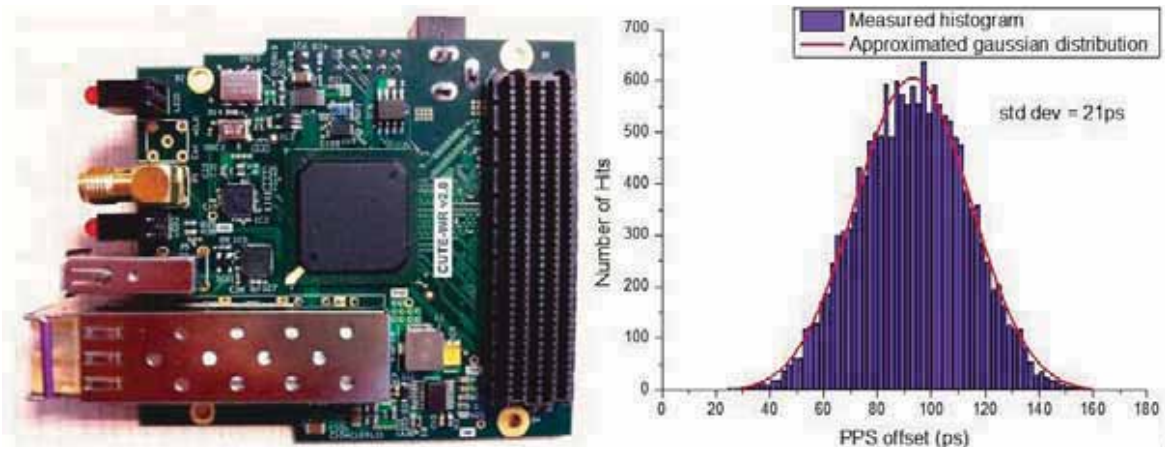

Figure 7.26: Compact FMC-form White Rabbit nodes and the measurement of PPS synchronization

7.5.8 Design for system reliability

7.5.8.1 Specifications for reliability

The reliability requirement for the electronic system is a failure rate of less than 0.1 % per year of operational time for each of the 16,500 detector channels. The design life time of the system is 20 years. At the desired failure rate, it should be able to run for at least 10 years without need of maintenance action.

In the intermediate and underwater schemes, most of the electronics will be put into sealed boxes at a maximum water depth of 40 m. The temperature of the water will be in the range of +10 to +20 Centigrade. The ambient radiation levels will be normal.

7.5.8.2 Reliability engineering

As an important aspect of product assurance management, reliability engineering will cover the entire electronics design and development for JUNO. This will include:

- **Management of components.** The used parts will extremely affect the quality and reliability of the final product. There will be a management plan for the components, and a list of preferred components to provide guidance in their selection and quality control.
- **Reliability design,** including reliability definition, system reliability analysis, reliability allocation, reliability design and prediction
- **Analysis of failure modes and effects**, including a fault tree analysis.
- Analysis of **sneaks**
- Analysis of **ASIC reliability**
- Assurance of **firmware reliability**.

For achievement of the high quality and reliability requirements for the electronics, all steps of production and installation of the JUNO electronics (except the reliability design in R&D procedure) should be controlled by the overall Product Assurance (PA) management plan. This will include

- Risk management
- Safety management
- Control of critical items
- Procurement, verification, screening, handling and storage of components
- Control of techniques and production procedure
- Verification and Environmental tests.
- Software assurance, etc.

There will be a PA organization supervised by PA manager to establish and implement the management plan.

7.6 Manufacture and assembly

7.6.1 Production

Production of ∼20,000 channels will be a demanding task that must be subject to a strict quality management and continuous supervision. The final design will be chosen after a phase of elaboration and prototyping of the three design concepts that have been introduced above and a careful evaluation of their respective merits and disadvantages. Once the design is fixed, production will start in several steps:

- **Ordering of electronic components**, including cables and crates. Each supplier and batch will be strictly controlled to ensure the reliability.
- **PCB manufactory and assembly** will be carried out by professional manufacturers. A close personal contact with the companies will be established to allow for quality supervision and sampling at the production site.
- **Aging tests** with the components that should be performed well in advance of the start of JUNO data taking. Components failing the tests can be repaired and re-introduced after the performance has been tested.

7.6.2 Aging and long-term tests

According to typical reliability curves for electronic devices, the failure rate will be relatively high in the beginning while forming a plateau of constant low failure rate after. Therefore, all critical components should be installed and running for some time before the experiment starts, allowing to pick out and repair malfunctioning components.

Aging tests will be performed by exposing electronic parts for a period of the order of one week to an environment of increased temperature. If 1000 channels can be tested simultaneously, the whole process will require about 20 weeks. In order to optimize the conditions of the aging tests, pre-studies risking the destruction of some of the components should be conducted.

Before installation, the system needs to undergo a long-term test run at a dedicated test stand at a laboratory that allows for debugging, identification of failing components and further aging control. This thorough test of at least part of the system should last at least for 3−4 months, and should be performed with real PMTs connected.

7.6.3 Installation

The readout system will be installed along with the central detector and PMTs. The foreseen time span for installation is 6−8 months. It will start from the bottom and end at the top cap. The external testing stand should be completed before installation to allow to perform the tests during the installation phase. After completing the installation, a debugging phase to test the stability of the whole system is foreseen to ensure optimal working conditions at the start of the experiment.

7.6.4 Reliability

All steps require rigorous quality and reliability management and control, from ordering the components to the finalization of the installation. This will ensure the system stability, reduce losses in the production process, and minimize the consumption.

7.7 Risk analysis

7.7.1 Three read-out schemes

Some risk obviously exists for such a 20,000-channel high-speed sampling system, in which all of the PMTs are located inside the water pool and therefore not immediately accessible to repairs. The "external readout scheme" (Sec. 7.2) will place most of the electronics outside the water pool. This will greatly simplify the replacement of broken modules but potentially reduces the measurement quality and increases the costs. In the "underwater readout scheme" (Sec. 7.4), almost all the critical components of the electronics will be placed underwater and are possible without reach for replacement (especially the FEE). This assures optimum measurement performance, but will increase the risk of failure unless special attention is given to an increased redundancy of vital system components. In case of the "intermediate readout scheme" (Sec. 7.3), a large part fraction of the electronics is located inside the water. All vital electronics are concentrated inside the central processing units that are designed to be replaceable. Compared to the other schemes, both performance and repairability are optimized but costs and design difficulty are increased. The final design will be chosen after all three designs have been properly elaborated and prototypes have been tested.

7.7.2 Design risks

Design risks comprise mainly four aspects:

- Quality of signal measurement
- Reliability
- Cost control
- Design integrity

The biggest risk is the signal measurements, which followed by the risk of reliability and design integrity. The reliability is associated with cost control. Risks in design integrity will be mostly caused by two aspects: Insufficient communication of the groups designing different parts of the system and a lack of understanding of the system itself. These risks can be mitigated by a good collaboration in between the participating groups.

7.7.3 Production risks

Production risks are mainly arising in the procurement of electronic components, PCB manufactory and assembly, aging tests and cost control. A very strict quality control system will be established.

7.7.4 Installation risks

Risk in installation will also be minimized by a strict management and quality control, including three aspects: installation quality, time and safety.

7.8 Schedule

2013 Start of design of the readout schemes.

2014 R&D for key components.

2015 Test of a prototype system of 200 channels for the "external readout scheme" at Daya Bay.

Finalization of a 32-channel demonstrator for the "intermediate readout scheme".

Review of all three schemes and choice of the final scheme.

2016 Prototype system for the final scheme, about 200 channels

2017 Mass production

2018 Mass production, testing ans start of installation

2019 Installation and testing

Bibliography

[1] Li Qiuju *et al.*, "The PMT Charge and Time Readout Scheme for Daya Bay Reactor Neutrino Experiment". The 14th Nuclear Electronics and Detection Technology conference, 2008, 84-88

[2] AD9234 datasheet `http://www.analog.com/static/imported-files/data_sheets/AD9234.pdf`

[3] ANTARES Collaboration, arXiv:1007.2549; S. Kleinfelder *et al.*, "A multi-GHz, multi-channel transient waveform digitization integrated circuit", Nuclear Science Symposium Conference Record, 2002 IEEE, vol.1, 544 - 548

[4] "Dayabay Reactor Neutrino Experiment report for feasibility study", Institute of High Energy Physics, Internal documents, IHEP-DB-SB-02-R1, 2006

[5] "Design of Prototyping PMT Electronic System for Daya Bay Reactor Neutrino Experiment", Z.Wang *et al.*, IEEE NSS/MIC Conference proceeding, NSS-2008-N30-456.

[6] "Front-End Electronics System of PMT Readout for Daya Bay Reactor Neutrino Experiment", Q.J.Li *et al.*, IEEE NSS/MIC Conference proceeding, NSS-2009-N25-240.

[7] "The Study of PMT Charge and Time Measurement of Daya Bay Reactor Neutrino Experiment", Qiu-ju Li, Master Thesis, 2008.

[8] "The Study of Readout electronics system of Daya Bay Reactor Neutrino Experiment", Wen-qi, Jiang, Ph.D. Thesis, 2011.

[9] "High-speed Digitization Technique Study and Application", Hai-sheng Xiang, Ph.D. Thesis, 2010

[10] "The Research of Key Technologies of JUNO RPC Readout Electronics", Lei Zheng, Ph.D. Thesis, 2014.

[11] BESIII EMC readout electronics report, 2003

[12] C.L. Cowan, F. Reines, F.B. Harrison, H.W. Kruseand, A.D. McGuire, Science 124,103 (1956); Phys. Rev. 92, 830 (1953).

[13] G. Danby, J.M. Gaillard, K. Goulianos, L.M. Lederman, N. Mistry, M.Schwartz and J.Steinberger, Phys. Rev. Lett. 9, 36 (1962).

[14] DONUT Collaboration, K. Kodama *et al.*, Phys. Lett. B 504, 218 (2001), hep-ex/0012035.

[15] Benjamin W. Lee *et al.*, Phys. Rev. Lett. 39, 165 (1977)

[16] B. Pontecorvo, Sov. Phys. JETP 26, 984; V.N. Gribov and B. Pontecorvo, Phys. Lett. 28B, 493 (1969)

[17] Super-Kamiokande Collaboration, Phys. Rev. Lett.81, 1158, hep-ex/9805021.

[18] SNO Collaboration, Phys. Rev. Lett. 87, 071301(2001), nucl-ex/0106015

[19] KamLAND Collaboration, Phys. Rev. Lett. 90, 021802 (2003), hep-ex/0212021.

[20] KamLAND Collaboration, Phys. Rev. Lett .94, 081801(2005), hep-ex/0406035

Chapter 8

DAQ and DCS

The data acquisition (DAQ) system and detector control system (DCS) are introduced separately as followed.

8.1 Data Acquisition System

The main task of the data acquisition (DAQ) system is to record antineutrino candidate events observed in the antineutrino detectors. In order to understand the backgrounds, other types of events are also recorded, such as cosmic muon events, low energy radioactive backgrounds etc. Therefore, the DAQ must record data from the electronics of antineutrino and muon detectors with precise timing and charge information. DAQ should build event with separated data fragment from all electronics devices. Then DAQ needs to analyze and process data to compress data and monitor data quality. At last, DAQ should save most relevant data to disk.

8.1.1 System Requirements

This section presents the DAQ main design requirements.

8.1.1.1 Event Rate

The central detector (CD) of JUNO is composed of about 16000 PMTs. According to MC simulation order of 100 antineutrino candidates per day can be acquired by the CD. Most events of the CD come from radioactive backgrounds of PMT glasses, steel and liquid scintillator material. The trigger system could reduce PMT dark noise and radioactive backgrounds event rate order of 1 kHz. DAQ system will be designed to handle a maximum trigger rate of 1 kHz.

The water shield detector is composed of about 1500 PMTs and adopt the same electronics design. But the trigger rate could be less than 100 Hz with radioactive backgrounds and muon events. The top muon detector design is under design and the bandwidth requirements should be small and ignored.

The calibration system could bring several hundreds to 1 kHz additional events. But the trigger rate could be set to a reasonable volume level. A supernova explosion will generate many neutrino events over a very short time scale. For example, about 10k events will be generated in 10 seconds from a 10kpc distance supernova explosion.

8.1.1.2 Readout Data Rate Estimation

The electronics system plans to use 12 bits FADC at 1 GHz sample rate with 2 range to acquire signal waveform in 1 μs time window. In case of 16 bits occupation of one sample, the data size of single PMT signal could be estimated about 2k bytes including bytes of time stamp and header. Table 8.1 shows DAQ readout data estimation, and the total data rate of CD is about 2.1 GBytes/s which means data rate per PMT is 140 kBytes/s in Physics mode. The high energy cosmic muon events of CD are estimated to be about 3 Hz and will fire all 16000 PMTs of the CD. Neutrino and background low energy events are estimated to be less than 1 kHz with less than 3000 and average 1000 PMTs fired. Water shield detector is estimated to be with 100 Hz event rate and 10% channels fired per event.

We can set up both high and low energy calibration with similar data rate. The data rate of calibration run modes is 4.1 GB/s and means 273 KByte/s per PMT, which is about 2 times of the data rate of normal physics run mode. According to the table, 3000 PMTs are assumed to be fired by one supernova event. The additional supernova event data rate is about 3 times larger than that of normal physics running modes. So DAQ was required 10.1 GB/s of total readout bandwidth at least and means 675 KB/s per PMT as 5 times physics mode when supernova happens with calibration together. But it will make remarkable increase for closed supernova explosion.

Supernova events will only continue about 10 seconds, LED based calibration run can be paused to improve the performance. So DAQ only needs to keep about 4.2 GB/s data processing performance for calibration run mode and buffer additional 60 GB supernova data in memory to process latter.

Due to the signal width is very small than 1 μs data window, we can assume to compress waveform to about 50 ns effective width with about 100 Bytes per signal. As estimated in the table about 95% low energy event data will be removed. Then only about 200 MB/s data in Physics run mode and 300 MB/s in calibration run mode need to be built to full events and save to disk. The maximum data storage requirements is 600 MB/s when supernova happens during calibration run.

8.1.1.3 Data Process Requirements

There are several type read out data link between DAQ electronic. Ethernet with TCP/IP protocol could be a simple option. DAQ could organize readout branch with groups of PMTs. To deal with tens GB/s readout bandwidth, DAQ could use multiple 10 Gbps link to readout. Then DAQ should assemble completed events with data fragment from different link by trigger number or time stamp.

DAQ needs to finish waveform compression if electronics cannot do that. If we want to reduce data rate further, we need software trigger to remove more background events.

DAQ also needs to merge different detectors events together and sort events by time stamp.

8.1.1.4 Other Functional Requirements

DAQ also needs provide common functions like run control, run monitoring, information sharing, distributed process manager, software configure, bookkeeping, Elog, data

quality monitoring, remote monitoring and so on.

8.1.2 Conceptual Design Schema

The JUNO experiment has many similar cases with BESIII and the Daya Bay experiments in DAQ part. We can design and develop JUNO DAQ based on BESIII, Daya Bay and ATLAS DAQ[1, 2, 3]. Figure 8.1 is the conceptual design schema of JUNO DAQ, DAQ readout electronics data through network. Except that network access switches are placed in underground experiment hall, all other DAQ computers are deployed at ground computer room. DAQ constructs a blade servers' farm to process data, and the farm is connected with underground switches through multiple 10 gigabit fibers.

Due to electronics systems are not easy to dynamically distribute different DAQ hosts, it is better to design a two level event building at DAQ. The first level (ROS, read out system) reads out front-end electronics (FEE) data and builds event fragments and then the second level finishes full event building. It is better that DAQ compresses waveform data at the first level to reduce unuseful data transferring. The simplest waveform compression algorithm is zero compression with a configurable threshold. Only sample data exceeding the threshold can be reserved.

JUNO DAQ can use same two level event building data flow scheme refer to BESIII event building as shown in Fig. 8.2 [4]:

1. front-end electronics (FEE) send data to ROS(read out system) through network.
2. ROS receive all data slice of one event and send event id to TSM(trigger synchronizing manager).

Table 8.1: JUNO DAQ Data Rate Estimation

	Channels	Data size per channel(Bytes)	Fired nPMT	Trigger rate(Hz)	Data Rate (MBytes/s)
CD (Low energy events)	16000	100(50ns)/ 2000(1us)	1000	1k	100/2000
CD (High energy events)	16000	2000(1us)	16000	3	96
Water Shelf Detector	1500	100(50ns)/ 2000(1us)	150	100	1.5/30
Sum (Physics mode)					197.5/2126
CD (Calibration events)	16000	100(50ns)/ 2000(1us)	1000-16000	1k-62.5	100/2000
CD (Supernova events)	16000	00(50ns)/ 2000(1us)	3000	1k	300/6000
Sum (Maximum)					597.5/10126

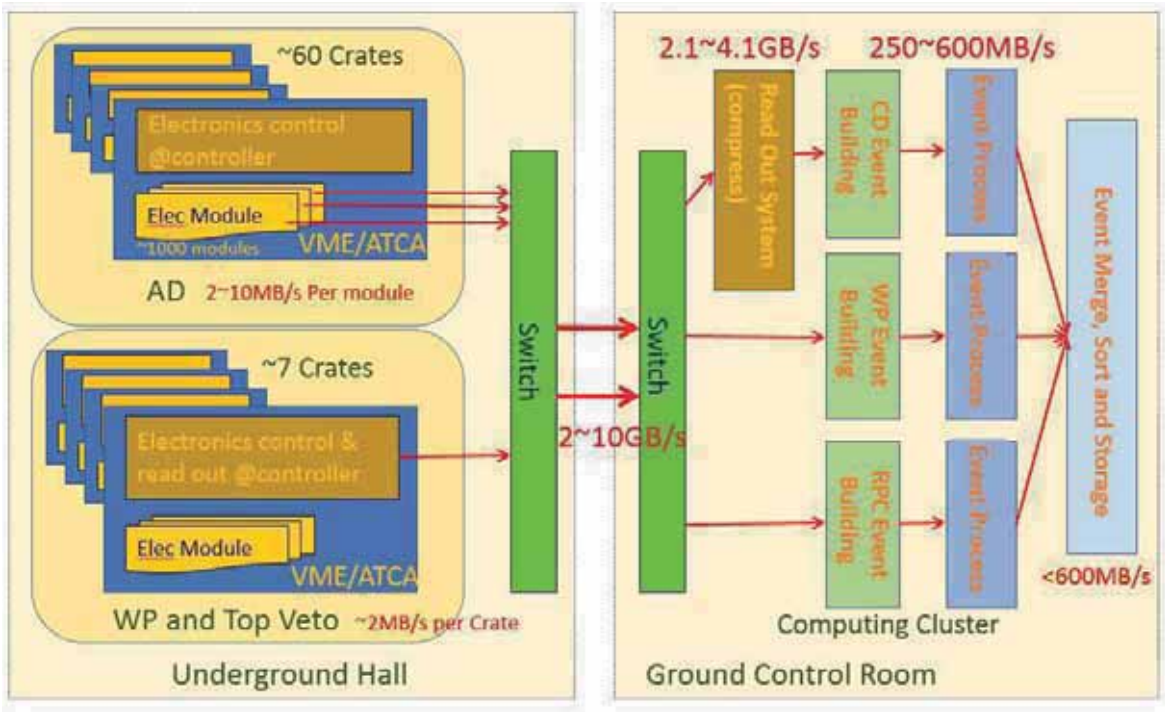

Figure 8.1: DAQ Conceptual Architecture Design Diagram

3. TSM send event id to DFM(data flow manager) when TSM get all same event id from all ROSs.

4. DFM assign event id to a free EBN(event building node).

5. EBN send data request to each ROSs.

6. ROSs send requested data to EBN.

7. EBN receive all ROSs data fragments of one event and finish full event building, then send event id back to DFM.

8. DFM send event id to ROSs to clear data buffer. . . .

Software trigger can be performed as BESIII event filter[5]. The figure 8.3 shows event filter collaboration diagram, each EF (event filter) node requests events from EB node, then send them to PT (process task) to analyze data for software trigger and data quality monitoring, at last send triggered event to DS (data storage) node for storage. Another option is performing software trigger before full event building as Atlas Level 2 trigger. It is better if DAQ need compress waveform.

All three detectors can share one DS node to save data to disks. Then event merging and sorting can be performed at DS node.

8.1.3 R&D Plan

JUNO DAQ needs the following technical research for detail design:

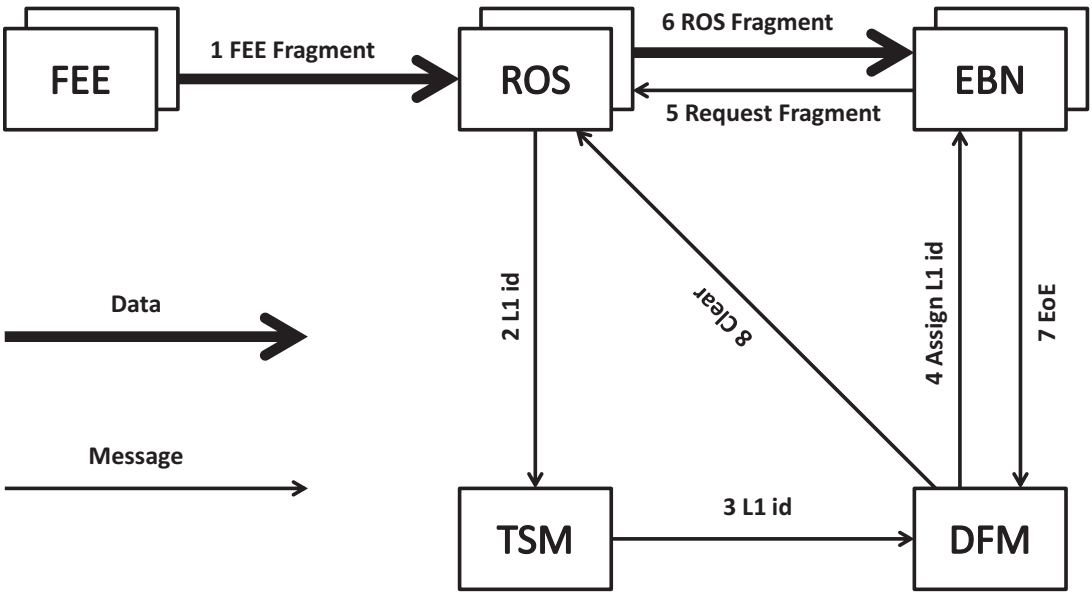

Figure 8.2: DAQ Event Building Collaboration Diagram

1. Waveform compression algorithms and read out host performance.
2. Software trigger algorithms.
3. Event building network and performance.
4. Event sorting and storage.
5. Big scale computer farm computing and software developing.
6. Integrating and test with dedicated electronics and detector system.

8.1.4 Manufacture, Developing and Installation

DAQ will not rely on custom made DAQ hardware, so there are no manufacture issues. But we need to investigate and survey different brands and types to integrate design schema. Hardware installation will be outsourced to vendors or system integration company. DAQ software will be designed and developed based on BESIII, Daya Bay and ATLAS DAQ software.

8.1.5 Risk Analysis and Safety Evaluation

The wave form data compression ratio could not reach expectation with detectors and electronics real performance.

There are two another challenges for DAQ up to now. One is that electronics might adopt none hardware trigger schema, the other is that supernova explosion could happen in a closer position.

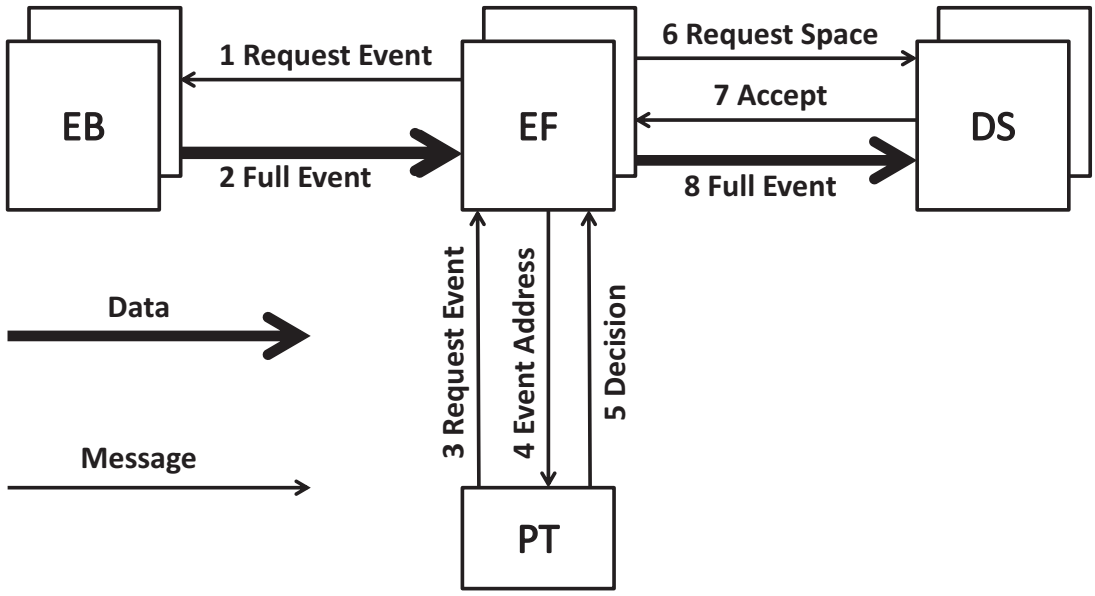

Figure 8.3: DAQ Event Filter Collaboration Diagram

8.1.6 Schedule

Major technical issues research according to electronics design finish DAQ technical design in 2013-2015.

Software developing, test and debug with electronics in 2016-2017.

Installation, deployment and integration in 2018-2020.

8.2 Detector Control System

8.2.1 Requirements

The main task of the Detector Control System is to establish long-term monitoring of the parameters affecting the performance of the experimental equipment. The parameters include pressure, temperature, humidity, liquid level of the scintillation, electronics, gas pressure and the pressure in the lobby and the entire electrical and mechanical environment working status of the devices. Some subsystems need to provide device control such as calibration system, gas system, water cycle system and power system. The real time operation states of the devices will be monitored and recorded into database. When an exception occurs the system can issue timely warnings at the same time through a secure interlock. Meanwhile, the devices can be protected by the safety interlock automatically to prevent equipment damage and personal protection.

8.2.1.1 System Requirement

The system will meet the requirement of an effective mass of 20,000 tons of central detector, which contains about 16,000 photomultiplier tubes. Due to the large scale

of the detector there are about 1000 temperature and humidity monitoring points, about 20,000 channels of high voltages, and thousands of power supplies etc. There is also pure water system, gas system as well. The collection of the system requirement is based on the design of the detector, electronics and trigger system. The design requirements include the hardware and software design, the testbed of the subsystem design and the system integration.

8.2.1.2 Function Requirement

According to the experimental requirements the general software framework will be designed. The high voltage, the temperature monitoring module, the hardware interface, and the hardware and the software protocols will be defined. Drivers and data acquisition framework of the exchange process will be developed. The function modules of the DCS system are shown below.

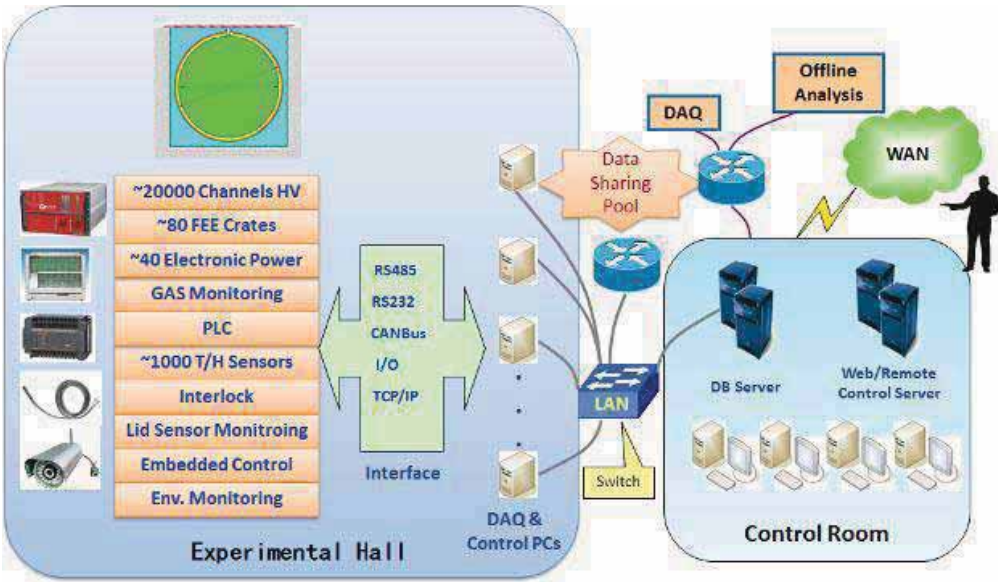

Figure 8.4: Framework Design of Detector Control System

8.2.1.3 System Schema Design

- Content

  According to the actual hardware and software requirements of the experiment the system uses a hierarchical design framework. The system will be divided into the global control layer, the control layer and the data acquisition layer. The global control layer will realize the overall experimental equipment information collection, safety interlock, remote control, data storage, network information release and permissions management. Local control layer will realize the local control of the local equipment in the experiment hall. And support the local device monitoring, data recording, data upload and alarm. The data acquisition layer is response for the various hardware interfaces. It can support for embedded systems such as ARM, FPGA and standard industry interface hardware such

as PLC, USB and serial RS232 interface and acquisition, which based on the network devices such as the TCP/IP data acquisition interface.

The system will be built on a distributed system development method. According to the experimental equipment distribution characteristics the distributed data exchange platform will be used for the development. Global control systems share the data and the interactively control commands by information sharing pool. Configuration files will use the text format specification which can realize the remote configuration, distributed sharing and management.

The system uses a module based approach of development. This method can achieve rapid integration of complex systems. From a functional view the system will be divided into data acquisition, control module, alarm module, memory module, data sharing and processing, system configuration, privilege management and user interface. Each subsystem can choose module assembly interface based on the actual system requirements. The modules can be divided by subsystem as following:

1. High voltage monitoring system, including the central detector PMT high voltage system, RPC high voltage etc.
2. Detector electronics chassis monitoring system, including the central detector electronics, RPC detector electronics, both inside and outside the pool detector electronics, monitoring content includes electronic temperature, power supply, fan, over current protection, low-voltage power supply.
3. Temperature and humidity monitoring system, including liquid temperature detector, temperature monitoring room.
4. Gas monitoring system, including the gas support system and center detector cover gas system
5. Center detector overflow tank monitoring, oil monitoring, liquid level clarity, camera monitoring and the calibration system of monitoring center.
6. Experimental hall of environmental temperature, humidity, pressure monitoring system, the radon monitoring system, video monitoring.
7. Control room monitoring system, database system and Webpage remote monitoring system.
8. Water system

- Key Technology

  The key technology of detector control system is the integration framework development of the software. The system will develop a set of integrated management module according to the detector hardware requirements. The system functions will be realized by the conceptual design and the detailed modular design. For the hardware system using commercial framework or special design system the data acquisition module will be designed for the integration. The commercial software will interface with the DCS framework by the integration. The software design is completed after repeated assembly test and performance test before put into use. The user feedback will be fully considered during the software design

and the commissioning period. The software will enter the formal running when the stage of training finished.

The traditional design of the JUNO central detector is a stainless-steel tank plus an acrylic sphere, where stainless-steel tank is used to separate the shielding liquid (mineral oil or LAB, to be decided) from the pure water in the water pool, and the acrylic sphere is to hold the 20kt LS. The design principle and key technology of the Daya Bay neutrino experiment could be a reference. The LS separated by an organic glass container is 34.5 meters in diameter. For the quality of the target substance which is one of the most important factors affecting the precision of experiment the quality change of the target material this requires for long-term supervisory. At the same time, the temperature inside the detector needs to be monitored. Environmental temperature variation not only impact on detector performance, the detector energy scale but also on photomultiplier tube noise, amplification and electronics precision. This requires many point of monitoring from the experimental hall. Therefore, the design of reliable, compatible of monitoring system is needed. Various experimental parameters such as temperature, humidity, voltage, electronics currents, radon density accurately level need to be achieved in the long-term and stable running of the experiment.

Software tools and applications which provide a software infrastructure for use in building distributed control systems will be used to operate devices. Such distributed control systems typically comprise tens or even hundreds of computers, networked together to allow communication between them and to provide control and feedback of the various parts of the device from a central control room, or even remotely over the internet. System will use Client/Server and Publish/Subscribe techniques to communicate between the various computers. Most servers (called Input/Output Controllers or IOCs) perform real-world I/O and local control tasks, and publish this information to clients using the Channel Access (CA) network protocol.

- Development Process Top development platform can be used to configure software such as LabVIEW or open source platforms such as EPICS (a widely used software platform for the large-scale control system physical device). The device driver can be developed by hardware I/O controller (IOC) server. Subsystems in the pre-design stage will build a testbed for the development of hardware drivers to test the hardware and software functions. Each detector subsystem model will be tested in testbed platform, as well as data acquisition interface. For the hardware which has no testbed device simulation models should be made with the software development team and a common definition of the interface specification, including data format, the transmission frequency, control flow, the interface distribution, database table and so on.

Bibliography

[1] BESIII Experiment TDR, in chinese

[2] Dayabay Neutrino Experiment TDR

[3] F. Li et al, DAQ Architecture Design of Daya Bay Reactor Neutrino Experiment, IEEE Trans. Nucl. Sci., vol. 58, no. 4, pp. 1723-1727, Aug. 2011

[4] F. Li, Research and Implementation of BESIII DAQ Online Distributed Data Monitoring , Ph D dissertation

[5] Y. Liu, Research and Implementation of BESIII DAQ Online Event Filtor, Ph D dissertation

Chapter 9

Offline Software And Computing

9.1 Design Goals and Requirements

9.1.1 Requirement Analysis

The offline software plays an important role in improving physics analysis quality and efficiency. From the point of view of physics analysis, the following requirements need to be applied to the offline software system.

- Compared to collider experiments, neutrino experiments have two specific characteristics: 1). There is time correlation between events. 2).There is only a very small fraction of signal events among a large number of backgrounds. The software framework should therefore provide a mechanism of flexible data I/O and event buffering to enable high efficiency data access and storage, as well as the capability to retrieve the events within a user-defined time window.

- An interface should be provided for different algorithms to interchange event data. There should be a unified geometry management. Software and physics analysis parameters should be managed by a conditional database. An interface to retrieve correct parameters according to software versions should be also provided.

- There are many kinds of events in the JUNO experiment. Apart from reactor neutrino events, they are supernova neutrinos, geo-neutrinos, solar neutrinos, atmospheric neutrinos, radioactivity etc. The offline software should provide accurate simulations to describe interactions of neutrinos and background events with the detector.

- The detector simulation software should be able to simulate detector performance and guide detector design. In addition, the calculation of detector efficiencies and systematic errors, which are needed by physics analysis, also relies on detector simulation.

- The detector performance depends on event reconstruction. In order to get better energy resolution, optical model in liquid scintillator detector should be constructed, using PMT charge and time information to get event vertex and energy. Event vertex can also be used to veto the natural radioactivity background

events from outside the liquid scintillator. To reduce the isotope background from muons, accurate muon track reconstruction is needed. For atmospheric neutrinos, the reconstruction of short tracks inside the liquid scintillator and identification of different charged particles are needed.

- Event display software is needed in order to show the detector structure, physics processes in the detector, and reconstruction performance.

The JUNO detector will produce about 2 PB raw data every year, which will be transferred back to the Computing Center at the Institute of High Energy Physics (IHEP) in Beijing through a dedicated network connection. Due to the large data volume, a big scale of offline computing platform is required by Monte Carlo production, raw data processing and physics analysis, as well as data storage and archiving. A rough estimation suggests a level of 10,000 CPU cores, 10 PB disk storage and 30 PB archive be required in the future. The computing nodes and storage servers will be connected to each other by a 40-Gbps backbone high-speed switching network. In order to improve data processing capacity, the platform will integrate the computing resources contributed by outside members via a distributed computing environment. So the experiment data can be shared among collaboration members and computation tasks can be dispatched to all of the computing sites managed by the platform. Considering the above needs, requirements on data processing, storage, data transfer and sharing, can be summarized as follows:

Data Transfer A data transfer and exchange system with high performance, security and reliability is required. To guarantee the timely transfer of raw data from the experiment site to the IHEP data center, the system should monitor and trace the online status of data transfers and it should provide a data transfer visualization interface. This should also guarantee data is dispatched and shared among different data sites within the collaboration smoothly.

Computing Environment A computing farm with 10,000 CPU cores will be established at the IHEP Computing Center to facilitate successful processing of the JUNO data. The collaboration members will provide additional computing resources. The computing environment includes not only the local computing farm, but also those remote resources contributed by outside collaboration members.

Data Storage JUNO will generate a huge amount of experiment data. Data from the experiment site will be transferred and stored at the IHEP Computing Center. The capacity of storage at IHEP will be 10 PB for storing both real and simulated data. It should support concurrent access by applications running on 10,000 CPU cores. Data migration between tape repository and disk pools should be transparent to users.

Maintenance, Monitoring and Service Support To improve the stability of the JUNO computing resources, an intelligent monitoring system will be developed. With this system, the status of both platform and network connection can be monitored through a fine-grained control. The monitor system can not only give the status assessment of the whole platform but also give predictions and prior warnings for various

platform services. A set of information management tools should be developed including conference support, document management and online-shift management etc.

9.1.2 Introduction

The offline software and computing system consists of two separate parts: offline software and computing. It not only closely connects data processing and physics analysis, but also it can be regarded as a bridge between detector operations and physics analysis. The primary tasks of this system are to process raw data collected by the detector and produce reconstructed data, to produce Monte Carlo data, to provide software tools for physics analysis, and to provide the networking and computing environment needed by data processing and analysis.

The offline software includes software framework, event generator, detector simulation, event reconstruction and event display etc. The framework is the underlying software supporting the whole system. Based on this framework, experiment related software will be developed such as software for event data model, data I/O, event generation, detector simulation, event reconstruction, physics analysis, geometry service, event display, and database service etc. To facilitate the development, the infrastructure of offline software provides various useful tools such as tools for compiling, debugging, deployment and installation etc.

The offline computing is designed to build a high efficiency and reliable computing environment for the JUNO experiment. It has the following major parts: a data transfer platform to transfer raw data from the experiment site to the Computing Center at IHEP, a large scale of computing farm for data processing and data analysis, a massive data storage subsystem and a monitoring and management platform providing fine-grained monitoring and management of the computing resources.

9.2 Offline Software Design

9.2.1 Software Platform

The offline software system is designed to meet the various requirements of data processing. As JUNO software developers are dispersed all over the world, a unified software platform is required, which provides a formal working environment. This has advantages for resource optimization and manpower integration, which can improve the software development, usage and maintenance.

Based on our experience, Linux OS and GNU compiler are the first choice for the JUNO software platform. However other popular OSes and development environments should be considered for the sake of compatibility. The CMT [1] tool, which can calculate package dependencies and generate Makefiles, is used for the software configuration and management. An automated installation tool can ease the deployment of the JUNO software, and is also helpful for daily compilation and testing. Users are able to concentrate on the implementation of software functionality, without suffering from different development environments.

Nowadays, mixed programming with multiple languages is practical, so we can choose different technologies for different parts of our software. The main features of the application are implemented via C++ to guarantee efficiency. User interfaces are

provided in Python for additional flexibility. Boost.Python, as a widely used library, is a good choice to integrate C++ and Python. If it is included properly at the beginning of the system design, most users will be able to enjoy the benefits of mixed programming without knowing the details of Boost.Python.

We will implement a software framework, SNiPER, as the core software of the JUNO platform. SNiPER stands for "Software for Non-collider Physics ExpeRiments". As shown in Fig.9.1, components of the JUNO software, such as simulation and reconstruction, are executed as plug-ins based on SNiPER. The principle of this new framework is simplicity and high efficiency. It depends on a minimal set of external libraries, fully meeting our requirements without over-engineering or loss of efficiency.

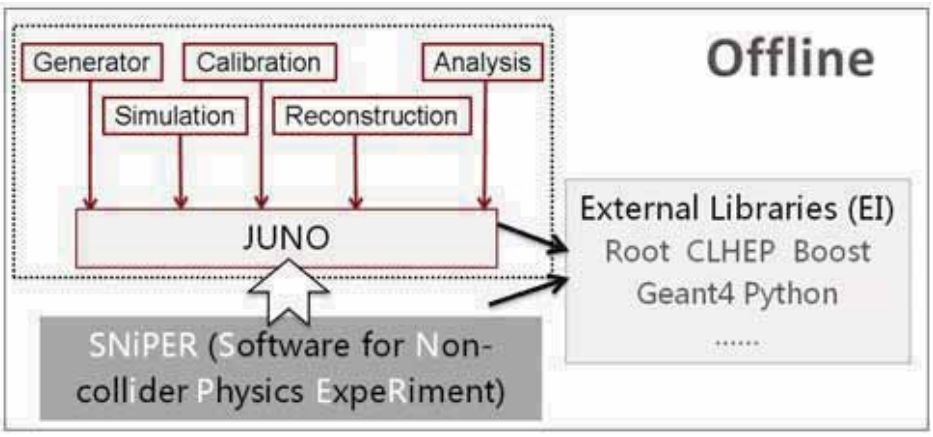

Figure 9.1: The structure of the offline software system

The SNiPER kernel is the foundation of the JUNO software system, and determines the vitality of the whole platform. We design and manage SNiPER modularly. Every functional element is implemented as a module, and can be dynamically loaded and configured. Modules are designed as high cohesion units with low couplings between each other. They communicate only through interfaces. We can replace or modify one module without affecting any of the others. Since it's flexible and expandable, users can contribute to it independently.

The model is inspired by other pioneering software frameworks such as Gaudi [2]. Expandable modules are strategically distinguished as algorithms and services. An algorithm provides a specific procedure for data processing. A sequence of algorithms composes the whole data processing chain. A service provides useful features that can be called by users when necessary. Algorithms and services are plugged and executed dynamically. They can be selected and combined flexibly for different requirements.

Data to be processed may come from different places and be in different types and formats. The results may also be stored in different ways. In the framework we reserve interfaces for multi-stream I/O support, so that the I/O service can communicate conveniently with other modules via the interface. At present, the disk access could be a serious bottleneck in massive data processing. This should be considered in I/O service developing. Many techniques, such as lazy loading, are adopted to optimize the I/O efficiency.

The framework also involves many frequently used functions, such as the logging mechanism, particle property lookup, system resource loading, database access and histogram booking, etc. These contents are wrapped in services in SNiPER, which will ease the development procedure. Users can configure a job interactively with the Python command line or in batch mode with script files. The flexibility of Python will ease the job execution procedure.

The JUNO experiment has a long lifetime and software technology is still evolving rapidly, so the framework has to be very expandable. It should be able to integrate with new tools and libraries in future. This will save the manpower needed for developing, and improve the system robustness.

It is expected that JUNO will have a huge amount of data. In order to make use of all possible computing resources, it is necessary to consider parallel computing techniques. Modern CPUs are generally multi-core. Multi-threaded programming extracts the capacity of multi-core CPUs, and speeds up a single job significantly. In PC clusters, a server/client distributed system can be implemented and deployed, too. The latest computing technology and HEP computing techniques, including GPUs, Grid and Cloud, should be explored and used as appropriate.

9.2.2 Event Model

The event model defines the key data units to be processed in the offline data processing. It not only defines the information included in one event at different data processing steps such as event generation, detector simulation, calibration, reconstruction and physics analysis, but also provides the ways for events to be correlated between different processes.

Since ROOT [3] has been extensively used as the data storage format in most particle physics experiments, it is decided that the JUNO event model is based on the ROOT TObject. So all the event classes are inherited from TObject. In this way, we can directly take advantage of the powerful functionalities provided by ROOT, such as schema evolution, input/ouput streamer, runtime type information (RTTI), inspection and so on.

In order to quickly view event information and make the decision whether or not a given event is selected, the event information is divided into two levels: Event Header and Event. The Event Header defines the sequential information (such as RunId, EventId and Timestamp etc.) and characteristic information (such as energy of events), while Event defines more detailed information about the event. In this way, the event header can be read in from data files or other storage and its characteristic information can be used for fast event selection without taking extra CPU time or memory required to read in the contents of a full event.

Event correlations are very important for neutrino physics analysis since inverse beta decay (IBD) events will be regarded as two separate event signals: prompt signal and delayed signal. Both of them actually refer to the same physics event. In the JUNO experiment, we design SmartRef to fully meet this requirement and to avoid the duplication in writing these information into ROOT files. SmartRef is based on the TRef class in ROOT but has more powerful functions. It not only provides correlations between events but also provides the information for lazy loading of the data.

For the JUNO event model, the class EvtNavigator is designed to organize all the

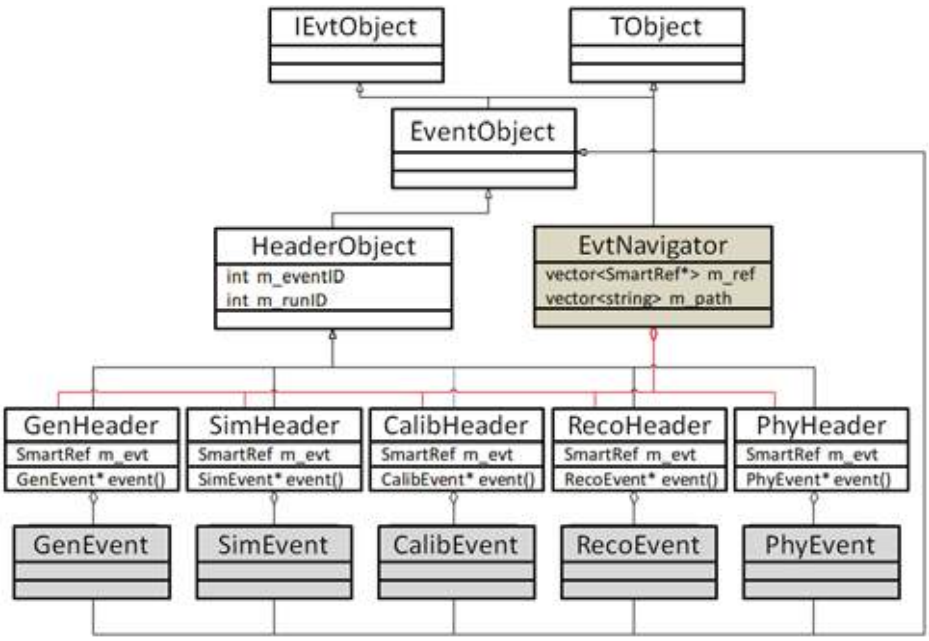

Figure 9.2: Design Schema of JUNO Event Model

event information at different processing steps and acts as an index when processing events. In Figure 9.2, we can see that EvtNavigator has several SmartRefs which refer to the headers of this event at different processes. Event model classes are usually simple. Only some quality variables and functions need to be defined. These functions can be divided into three types: Set-functions to set new values, Get-functions to return the variable's value, and streamer functions for reading/writing data from/to files. Most of the code is similar event by event, so an XOD (Xml Object Description) tool is developed and used to describe the event information with a more readable XML file. XOD can automatically produce the event header file, the event source file and the dictionnary file needed by ROOT.

9.2.3 Geometry

The geometry system describes and manages the detector data and structure in software, providing a consistent detector description for applications like simulation, reconstruction, calibration, alignment, event display and analysis. All subsystems, including the Central Detector, Top Veto Tracker, Water Cherenkov Pool and the Calibration system, will be described in the geometry system. The design of the JUNO detector also requires the geometry system to be flexible and able to handle time-dependent geometry and the co-existence of different designs.

Several detector description tools have been developed and implemented in high energy physics experiments, with some of the most popular languages being XML (eXtensible Markup Language) [4], HepRep [5], VRML(Virtual Reality Modeling Language, updated to X3D) [6] [7] and GDML (Geometry Description Markup Language) [8]. At the stage of conceptual design for the JUNO detector, the detector description geometry is based on GDML, including geometry data, detector structure, materials

and optical parameters. In consideration of the co-existence of multiple major designs and frequent minor modifications to the designs, we adopt GDML as the main tool to transfer detector description data between different applications, because GDML requires less human work and has the advantage of automatic translation of detector data between Geant4 [9] and ROOT, the two most popular HEP programs, which are widely used in simulation, reconstruction and anlysis. However, it is noteworthy that GDML also has some limitations. For example, its Geant4 and ROOT interfaces are not completely consistent, so some information like optical surface description and matrix elements may be lost in the detector data translation. The GDML interfaces do not support complicated (user defined) shapes and require more work to implement the extensible functions. These small problems need to be solved in future geometry software development.

At the current stage, the detector geometry is described in each individual Geant4 simulation code, which also serves as the unique source of detector description. When a simulation job is running, it constructs the detector structure in Geant4 and exports it in GDML format; at the end of the simulation job, the GDML detector data is read back and converted into ROOT geometry object format, which is bundled with the output event data ROOT file while being written out. When another application such as reconstruction or event display wants to read in the geometry information, it searches the bundled ROOT file for the geometry object to initialize the geometry offline, and uses the geometry service package to retrieve the detector unit information it requires. This mechanism gives every detector designer the maximum flexibility to modify his specific design, uses a single module to handle multiple detector designs at the same time and guarantees the consistency of detector description between different applications.

In the future, when the detector design is fixed, it is preferred to generate the detector description within the geometry system and provide it to all applications through interfaces, rather than the current solution of generating geometry data in Geant4.

9.2.4 Generator

Generators produce simulated particles with desired distribution of momentum, direction, time, position and particle ID.

The generators for the JUNO experiment include inverse beta decay (IBD) generator, radioactivity generator, muon generator, neutron generator, and calibration source generator. Some of the generators can be imported from the existing Daya Bay software, while the others need to be developed for JUNO specifically. The generators are grouped into three kinds according to their development platform. One is based on Geant4 ParticleGun for shooting particles with specified particle ID, momentum and position distribution. The second kind, such as ^{238}U and ^{232}Th radioactivity generators, is developed with existing Fortran libraries, . The third kind of generators, such as IBD and GenDecay, will be developed in C++ language,. The output data of generators should be in the format of HepEvt or HepMC [10] for better communication with other applications. The design of particle vertex position generation need to be flexible and allow the distribution to be geometry related, for example, a random distribution on the surface of a PMT, in liquid scintillator or in acrylic.

The muon generator particularly depends on the muon flux, energy spectrum and angular distribution at the JUNO site. A digitized description of the actual landform at the JUNO site need to be acquired first, and then used as input to MUSIC [11] to simulate muons passing through the rock, getting the flux, energy spectrum and angular distribution of the muons finally reaching the JUNO detector. The effect of muon bundles also needs to be considered for such a large detector as JUNO.

9.2.5 Detector Simulation

The detector simulation package for JUNO is based on Geant4. Detector simulation includes detector geometry description, physics processes, hit recording, and user interfaces.

9.2.5.1 Description of detector geometry

An accurate description of detector geometry is the foundation of detector simulation. In JUNO simulation, the geometry of the liquid scintillator, acrylic/nylon ball, PMTs, stainless steel tank or trusses need to be described in simulation software. About 17,000 PMTs are placed on a spherical surface. Geant4 is very sensitive to the geometry problem of volume overlaps or extrusions, which in general reduce the simulation speed or waste time in infinite loops. Some built-in or external tools can help to find such problems. At the stage of detector design, the detector geometry keeps changing. It is preferable that the geometry and event data can be exported in the same data file after simulation, so that the reconstruction job can read both information at the same time to ensure geometry consistency between simulation and reconstruction. In addition, the detector description method should allow easy modifications to the geometry with changes made to the detector design. In simulation of the liquid scintillator detector, the simulation of optical photon processes is a key issue. The optical parameters for materials such as liquid scintillator, acrylic, mineral oil and PMT should be carefully defined. The optical parameters include refractive index, absorption length, light yield factor, quantum efficiency and so on. Each optical parameter varies with the wave-length of optical photons and may be time-dependent in the future. Due to the production technique, the parameters of each individual PMT may be different. How to effectively manage these optical parameters is an important issue in the detector data description. A possible method is to combine Geant4 with GDML/XML and database technology to manage the detector geometry and optical parameters. In addition, simulation of the optical processes requires the definition of an optical surface, on which optical photons can have different behavior like refraction, reflection and absorption.

9.2.5.2 Physics processes

The physics processes in the JUNO detector simulation include standard electromagnetic, ion, hadronic and optical photon processes and optical model for the PMTs. Optical photon processes include scintillation, Cerenkov effect, absorption and Rayleigh scattering. When a charged particle passes through liquid scintillator, ionization energy loss is converted to scintillation light. The non-linearity between scintillation light and the ionization energy loss is called the quenching effect. During the propagation

of light in the liquid scintillator, the re-emission effect needs to be considered, which is not included in standard Geant4 processes and needs to be implemented in our experiment. For such a large liquid scintillator detector as JUNO, the simulation of high energy muons in liquid scintillator can be too CPU-time consuming to be affordable. Reducing light yield or using a parameterized model for fast simulation are possible solutions to speed up the muon simulation.

9.2.5.3 Hit recording

The hit information, including the number of hits in each PMT and the hit time, is output at the stage of Geant4 tracking. This information will be used as input to electronics simulation in the next step. In addition, particle history information should be saved, including the information of the initial primary particles, neutron capture time and position, energy deposition and position, direction and position of the hit on the PMT, and the relationship between track and hits.

9.2.5.4 User interface

A friendly user interface is necessary to use the simulation package, which should provide easy configuration of simulation parameters such as radius of LS volume, buffer thickness, vertex position, particle type and flags to switch on/off a specific physics process.

9.2.6 Digitizer Simulation

The digitizer simulation consists of electronics simulation, trigger simulation and readout simulation. The main goal is to simulate the real response of the three systems and apply their effects to physics results. The readout simulation transforms Monte Carlo data into the same format as experimental data and simplifies the analysis procedure. The digitizer simulation will be implemented in the JUNO offline framework, SNiPER.

Electronics simulation plays an important role in the digitizer simulation. The waveform from each PMT will be recorded using FADC and analyzed offline to get the final amplitude and timing information for each PMT. In electronics simulation, to transform the input hit information (given by Geant4) into electronic signals which are as real as possible, we need to build a model to exactly describe the single photoelectron response, which includes the effects of signal amplitude, rising time, prepulse, after-pulse, dark rate, etc. Electronics simulation should also have the ability to handle background noise, overlapping waveforms from multiple hits on the same PMT, and the effects from waveform distortion and non-linear effects. For very large signals like cosmic muons, however, it is difficult to save all FADC information so only integrated charge will be read out. Electronics simulation should be able to model such processeses. At the current stage, since the detailed JUNO electronics design has not been finally determined, the electronics simulation from the Daya Bay experiment is implemented as a temporary substitute for the JUNO electronics simulation. It will be updated to the real case when the JUNO electronics design is available.

Trigger simulation takes the output from the electronics simulation as its input to simulate the real trigger logic and clock system, and decides whether or not to send a

trigger signal if the current event passes a trigger. Currently, we have implemented a simple nHit trigger simulation.

Based on the trigger signals provided by the trigger simulation, FADC information in the readout window will be saved for each PMT and form an event. At the same time, the time stamp will be tagged. The final data format will be the same as for real data.

9.2.7 Background mixing

In real data, most events come from background, like natural radioactive events and cosmic muon induced events. In order to simulate the real situation, a background mixing algorithm needs to be developed to mix signal events with background events. It is an essential module if we want to make Monte Carlo data match well with real data. There are two options for background mixing: hit level mixing and readout level mixing. For hit level mixing, the hits from both signal and background are sorted by time first, and then handled by the electronics simulation. Hit level mixing is closer to the real case, but requires a lot of computing resources. Readout level mixing is much easier to implement and requires less computing resources, but it can not accurately model the overlapping between multiple hits. Since both options have advantages and disadvantages, more studies are necessary before an option is finally selected as the official JUNO background mixing algorithm.

9.2.8 Event Reconstruction

9.2.8.1 PMT waveform reconstruction

The total number of photoelectrons and the first hit time of each PMT can be reconstructed based on the waveform sampling from the readout electronics with two algorithms, charge integration or waveform fitting. A fast reconstruction algorithm has been developed using the charge integration with appropriate baseline subtraction. The first hit time is determined as the time above threshold with time walk correction. A waveform fitting algorithm based on a PMT response model is under development, which is expected to give better timing and can reduce the distortion of the charge measurement caused by the PMT and electronics effects such as after-pulse and overshoot. It also has the ability to separate the fast and slow components of the scintillation light. The fast reconstruction is designed for event selection, while the waveform fitting is expected to be used for small samples such as IBD candidates or calibration data.

9.2.8.2 Vertex reconstruction in the Central Detector

Since the energy of a reactor antineutrino is usually below 10 MeV, it can be approximated as a point source in the JUNO detector. Then the event vertex can be reconstructed based on the relative arrival time from the point source to different PMTs, defining a likelihood function:

$$F(x_0, y_0, z_0, T_0) = -\sum_i \log(f_t(t_i - T_0 - \frac{L(x_0, y_0, z_0, x_i, y_i, z_i}{c_{eff}})), \tag{9.1}$$

where x_0, y_0, z_0, T_0 are the event vertex position components and start time to be fitted, x_i, y_i, z_i, t_i are the position components and hit time of the i_{th} PMT, c_{eff} is the speed of light in the detector, and f_t is the probability density function of the PMT hit time with the time-of-flight being subtracted, which contains the decay time of scintillation light and the time resolution of the PMT. If the multiple photoelectrons in the same PMT can be clearly separated, f_t can be expressed analytically, otherwise it relies on MC simulation. A charge center method is used to calculate the event vertex to the first order, which can be used as the initial value of the likelihood fitting.

9.2.8.3 Visible energy reconstruction

The visible energy in the central detector of a point source is reconstructed using the maximum likelihood fitting:

$$\mathcal{L}(E_{vis}) = \prod_{no-hit} P_{no-hit}(E_{vis}, i) \times \prod_{hit} P_{hit}(E_{vis}, i, q_i), \tag{9.2}$$

where E_{vis} is the visible energy to be fitted, $P_{no-hit}(E_{vis}, i)$ and $P_{hit}(E_{vis}, i, q_i)$ are the probability that the i_{th} PMT has no hit and has the total charge of q_i, respectively. This probability is calculated based on the knowledge of the detector response model, including the light yield of the liquid scintillator, the attenuation length of the liquid scintillator and the buffer, the angular response function of the PMT, and the PMT charge resolution, as well as the reconstructed vertex as input. Another fast reconstruction algorithm has also been developed, which is based on the total number of photoelectrons collected from all PMTs with corrections using the calibration sources.

9.2.8.4 Muon tracking

The muon tracking in the central detector is based on the PMT hit time. Since the energy deposit from cosmic muons is at the level of GeV, the average number of photoelectrons at each PMT will be greater than 100, therefore the first hit time of the PMTs is dominated by the fast component of the scintillation light, which approximately follows a Gaussian distribution. A χ^2 function is defined:

$$\chi^2 = \sum_i (\frac{t_i^{exp} - t_i^{mea}}{\sigma})^2, \tag{9.3}$$

where t_i^{exp} and t_i^{mea} are the expected and measured first hit time of the i_{th} PMT, respectively, σ is the time resolution of the PMT, and t_i^{exp} is calculated based on the tracking parameters and the optical model in the detector. As shown in Fig. 9.3, since the scintillation light is isotropic, the intersection angle θ can be calculated analytically. For muons passing through the detector, the PMTs around the injection point and the outgoing point see more light and form two clusters, which can be used to estimate the initial tracking parameters. A muon tracking algorithm combined with the veto detectors is still under development.

9.2.9 Event Display

The event display is an indispensable tool in high energy physics experiments. It helps to develop simulation and reconstruction packages in the offline software, to analyze

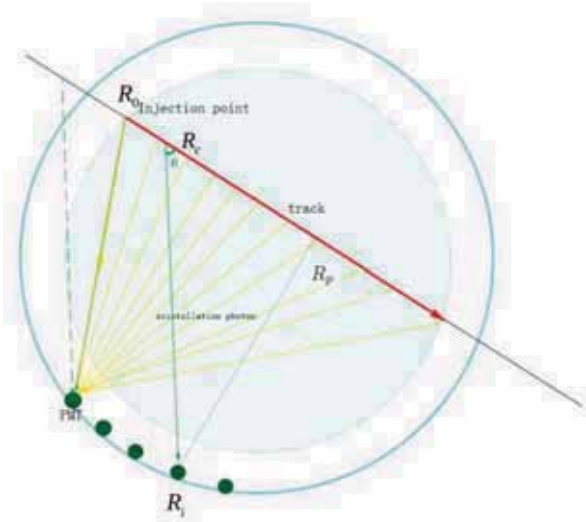

Figure 9.3: An illustration of the muon tracking. The red line is the muon track to be fitted, R_c is the light source which provides the first hit to the PMT at R_i, determined by the intersection angle θ. If R_c is calculated to be outside the detector, it will be set as the injection point R_0.

the physics in a recorded interaction and to illustrate the whole situation to general audiences in an imaginable way.

9.2.9.1 Detector description and display

The display of the detector is provided by the geometry service in the offline software. The visual attributes of every detector unit are associated and controlled by identifiers. The event display software will support two display modes – 3D display and 2D projection display. The 2D projection will be realized by the 2D histograms that are provided by ROOT. For 3D display, several popular 3D graphic engines, like OpenGL [12], OpenInventor [13] and X3D [7], have been proven as pratical choices for event display software for some other HEP experiments. More studies are necessary to determine which infrastructure 3D graphic engine will work best for JUNO and its software environment. Currently a solution based on OpenGL is under study to realize the 3D display mode.

9.2.9.2 Event data and display

The event data in the offline system has various formats, including raw data, simulation data, calibrated data, reconstruction data and data analysis results. Their data formats are uniformly defined by the JUNO offline event model. In processing the event data for display, we need to study how to display the particle trajectories, their interactions with materials and hit response in simulation data, the reconstructed event vertices, energy and display attributes, as well as the relationships between these.

9.2.9.3 Graphical User Interface

A Graphical User Interface (GUI) provides a convenient interface for users to execute complicated commands with simple actions such as pushing buttons, selections, sliding a ruler or pushing hot keys. Frequently used functions, like event control, 3D view rotation and translation, zooming and time controls can be realized through widgets. A ROOT-based GUI framework has been implemented to realize these functions, giving the advantages of seamless binding with the ROOT analysis platform, ROOT-based geometry service and event model.

9.2.9.4 Graphic-based analysis and tuning

Graphic-based analysis will further provide some useful functions such as reconstruction algorithm tuning, event trigger and event type discrimination, which can help users to quickly filter, analyze and understand the events in which they are interested.

9.2.10 Database Service

Databases play more and more important roles in offline data processing. They are used to store many kinds of information, such as, sizes and positions of complicated detector geometry, optics information, running parameters, calibration constants, schema evolution, bookkeeping and so on. At the same time databases provide access to all kinds of information through their management services, such as creation, query, modification and deletion, which will be frequently used during offline data processing.

Many types of database have been used in particle physics experiments, of which the most popular are Oracle [14], Mysql [15], PostgreSQL [16] and SQLite [17]. Many of them provide user-friendly APIs interfaces for different programming languages. Recently, NoSQL databases have become more and more popular and powerful in some other fields, so we are also investigating the possibility of using some NoSQL database.

Ragardless of which kind of underlying database will be chosen,the general schema of database services will be implemented in three levels. The lowest level is the APIs of the underlying database; the middle level is the new extension of the APIs according to the requirements of the JUNO experiment; the upper level is to provide user-friendly services for different applications such as detector simulation, event reconstruction and physics analysis.

Since Daya Bay already has one good database interface, we will implement it, optimizing and extending the current interface to provide more flexible and more powerful access to the different types of information stored by the databases. We will also set up two types of database servers, master servers,and the slave servers. The former are used to store and manage all information and can only be accessed by the slave servers, while the latter are responsible for retrieving information from the master servers and providing access for all applications.

9.3 Computing System Design

9.3.1 Computing Network and Public Network Environment

A 1 Gbps dedicated link, named IHEP-JUNO-LINK, is planned between the JUNO experiment site and IHEP. It is proposed that this link be used for data transfer between the experiment site and the IHEP data centre as well as for connecting the onsite office network and the external network. The 1 Gbps bandwidth is sufficient to fully meet the experiment's requirements for stable data transfer, based on an estimated data volume of 2 PB per year, which should take an estimated average bandwidth of 544 Mbps. The remaining bandwidth can be used for network crash recovery, experiment remote control and office network connectivity for JUNO onsite researchers.

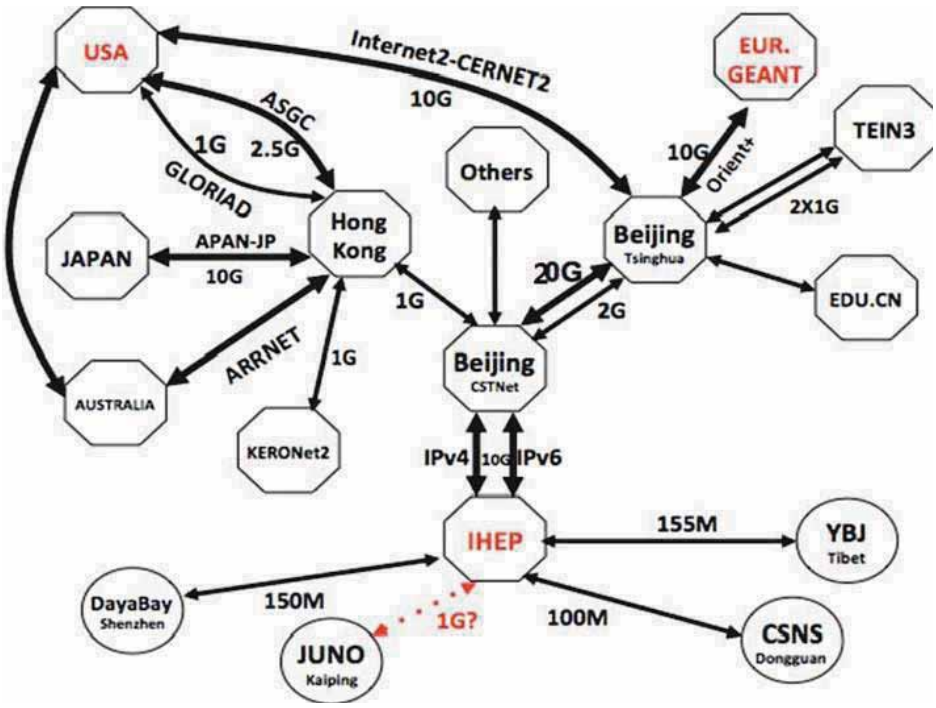

Figure 9.4: WAN Topology

The JUNO network link is planned to be provided by the Chinese Science and Technology Network (CSTNet) [18]. The data will first be transferred from the experiment site to IHEP through IHEP-JUNO-LINK, then relayed to collaborating sites through CSTNet. At present, IHEP is connected to the CSTNet core network through two 10 Gbps links, one of which supports IPv4 and the other IPv6. The bandwidth from IHEP to the USA is 2.5 Gbps and from IHEP to Europe is 5 Gbps, both of which are through CSTNet and have good network performance.

9.3.1.1 Network Information System Security

Network security is becoming more and more important in all kinds of information systems. The JUNO application system and even the computing environment also face

security risks, so we are planning to apply risk control and safety protection in the following aspects: physical layer, network layer, system layer, transport layer, virus threats layer and management layer.

The safety of the physical layer is the foundation of the whole information system security. In general, the security risks to the physical layer mainly include: system boot failure and database information loss due to power failure, whole systematic destruction caused by natural disasters, probable information loss caused by electromagnetic radiation and so on. In order to ensure the robustness of the physical layer, a powerful UPS should be deployed for the IT system and devices; proper access control policies should also be implemented for some special areas.

The risks to the network layer consist of risks to the network boundaries and risks to safety risk of the data transfer. A powerful network firewall system will be deployed in the JUNO network to aviod risks to the network boundaries. To ensure the safety of data transfers, there are two things we must consider: data integrity and confidentiality. To ensure data integrity, we can add checksums and provide multi-layer data buffering during transfers.To ensure data confidentiality, the information system should use encrypted transmission.

The system layer risk usually refers to the safety of operation systems and applications. In JUNO, a rigorous hierarchical control policy and auditing operation logs will be used to reduce and prevent security threats to the system layer.

For virus threats, while traditional viruses mainly spread through a variety of storage media, modern viruses mainly spread through the network. When a computer in the LAN is infected, the virus will quickly spread through the network to hundreds or thousands of machines in the same network. In JUNO, rigorous access control policy and real-time detection for the network traffic will be implemented for all the network nodes and IT systems to provide a safe network environment.

The risk to the management layer is usually caused by unclear responsibilities and illegal operation of the IT system, so the most feasible solution is to combine management policies and technical solutions together to achieve the integration of technology and policy.

9.3.2 Data transfer and sharing

Data transfer and sharing is the foundation of physical analysis in JUNO. In steady operations mode, raw data will be transferred over the network from the experiment site to the Computing Center for long term data storage, then distributed to the collaboration group members according to their requirements. The raw data from the JUNO experiment is open to all collaboration group members for local or remote processing and analysis.

The raw data from JUNO will be acquired by the online data acquirement system (DAQ) which will be deployed onsite, and then stored in a local disk cache with sufficient storage to keep one month's raw data. After that, the raw data will be transfered to the IHEP Computing Center in Beijing. During the transfers, the checksum of the data will also be transferred to make sure of the data integrity. If the data integrity check is failed, the raw data should be retransferred. After the data transfer is done and the data integrity check is ok, the status of the data in the DAQ local disk cache will be marked as TRANSFERRED. Moreover, a high/low water line deletion algorithm

will be used to clear the outdated data in DAQ local disk cache.

Most of the data will be transferred automatically by the data transfer system, so some possible human errors can be reduced. To ensure the stability and robustness of the data transferring system, a monitoring system will be developed and deployed which will provide the data transfer and sharing status in real-time and track the efficiency of the data transfer system. Combined with the status of the IT infrastructure (including network bandwidth), the data transfer system will optimize the transfer path and recover transfer failures automatically to improve the performance and stability of the system.

9.3.3 Computation and Storage

9.3.3.1 Local Cluster

About 10,000 CPU cores should be used for raw data simulation, reconstruction and data analysis to fit JUNO offline computing requirment. All the resources will be managed by the batch system of the IHEP Computing Center. Several job queues with different priorities will be established to share the resources in the most efficient way.

An optimized scheduling algorithm will be developed based on the features of the the JUNO computing environment and hardware performance. The scheduler should dispatch jobs to the most suitable computing resource so that high overall computing efficiency is obtained. Job types can be defined based on the computing model, characteristics and I/O bandwidth consumption for different jobs. For this, it is necessary to study and test different types of jobs running on different machines with different CPUs. It is also necessary to analyze the effect of the distributed storage system on job running time. New scheduling optimization algorithms based on the results of this study should be implemented as a plugin which can be integrated with the batch job system. This will be used for resource management and job scheduling to improve the efficiency of single jobs and the overall resource usage.

9.3.3.2 Computing Virtualization

Local clusters are managed by job management systems, with Torque [19], Condor [20] and LSF [21] being popular choices in HEP systems. These are responsible for scheduling jobs to a physical machine. With ever more powerful CPUs available, virtual machine clusters - cloud computing - can be used to relieve the pressure on computing resources at peak times. Cloud computing also reduces the burden of system management in applying upgrades to operating system and offline software, as well as satisfying requests for different software versions. Running jobs on virtual machines (VMs) can also avoid the trouble caused by hardware heterogeneity and give more flexibility in software configuration, without requiring changes in the job itself. Virtual clusters can therefore improve the availability and reliability of the computing resources as well as providing elastic resource expansion and flexible resource allocation. Rather than allocating a job to a node, as for physical cluster resource allocation, jobs are allocated to a CPU core. One CPU core supports one VM running a JUNO job. The lifetime of the VM depends on the job running time. This makes it possible to pre-empt jobs based on priority, and to migrate jobs. The VM can be migrated online

and the job running on the VM can be hung up before the migration and released after the migratioon. These features of VMs will make the computing platform more robust.

9.3.3.3 Distributed Storage Management and Data Sharing

JUNO data processing is a typical massive data computation task. Distributed storage management is necessary for its large scale of data. The following figure shows the architecture of the storage.

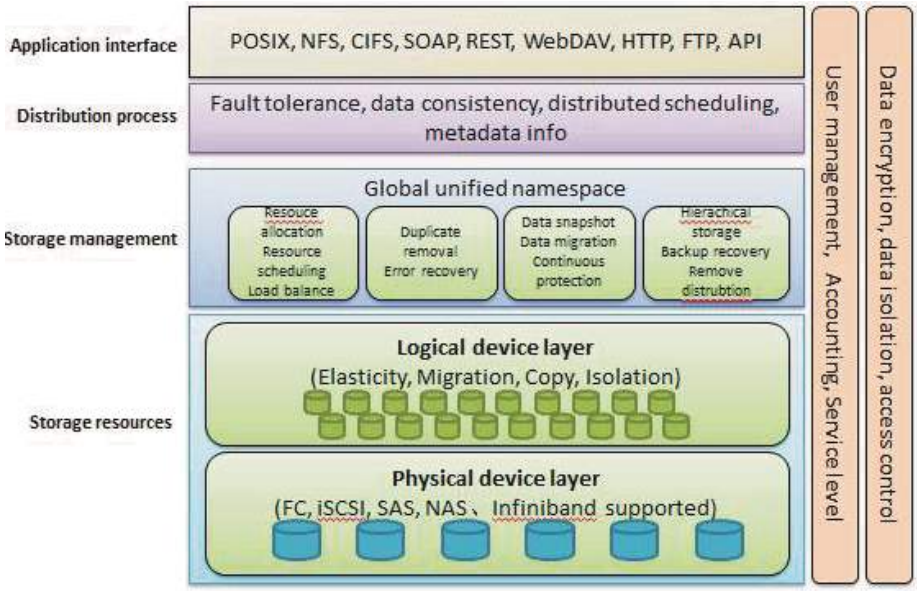

Figure 9.5: The storage architecture

The logical device layer, which is over the physical layer, provides stable and reliable storage for the upper layers. The logical storage devices are independent of the physical devices and isolated from them. They can be elastically extended or narrowed, copied and be migrated among physical devices. The features of logical devices, including high availability, high performance and high security, make it easy to satisfy the storage demands of JUNO. The logical device layer gives the storage system strong scalability with PB level capacity.

The storage management layer provides the functions of resource allocation, scheduling and load balancing. It provides a global unified name space, called the virtual storage layer. This can shield the heterogeneity of physical devices and integrate a unified virtual storage resource for users. The distribution process layer is over the storage management, providing fault tolerance, consistency, distributed task scheduling support (such as map-reduce [22]) and metadata management.

The application interface layer provides rich interfaces compatible with Posix semantics, and is transparent to users.

This virtual distributed storage system should fully satisfy JUNO's requirement of 10 PB storage, providing a high-reliability, high-performance storage service which can be extended elastically as needed. .

9.3.3.4 Distributed computation

Since JUNO has a large computation scale, it needs cooperative work among the group members. Distributed computation integrates heterogeneous resources from different sites, which could be shared by all the sites located in different region. A unified user interface would be provided to receive user jobs and job is dispatched to the suitable sites by the system. Job “pushing” and “pulling” are the two main scheduling methods.

9.3.4 Maintenance and service support

9.3.4.1 Network support platform

Network support platform provides professional and comprehensive solutions for JUNO network and public services. On the one hand, it integrates related resources on the network side, and then transfers them to the expert of the user service, which can realize quick response to network complaints, and effectively raise user service front-end settlement ratio, reduce complaint processing links, reduce complaint processing duration, and enhance user satisfaction.On the other hand,as for the information related to network complaint received from user sides, the network side will obtain it automatically and pay active attention to it, and realize the comprehensive correlation between user complaint and network execution situation, and the quality degradation warning of terminal-to-terminal network, so as to guide network optimization, enhance network quality, and further realize active care for users and enhance service quality.

9.3.4.2 Fine-grained monitoring and maintenance

Since JUNO data process is a large scale task including many devices, a fine-grained monitoring system is necessary to guarantee smooth running of the platform. It is required that the monitoring system be real-time, easy to use and can recover from some unexpected errors itself. For those errors which can not be recovered, a warning should be sent in time.

9.3.4.3 Information Service Platform

The information Service Platform is an information system which provides services for the research and management activities of the JUNO experiment. The Information Service Platform will provide system services for many aspects of the experimental research and management, such as the JUNO Experiment website, wiki, conference management, document management, collaboration management, video conference, workshop live broadcasting/recording, remote shifts, personal data sharing, science advocacy and so on.

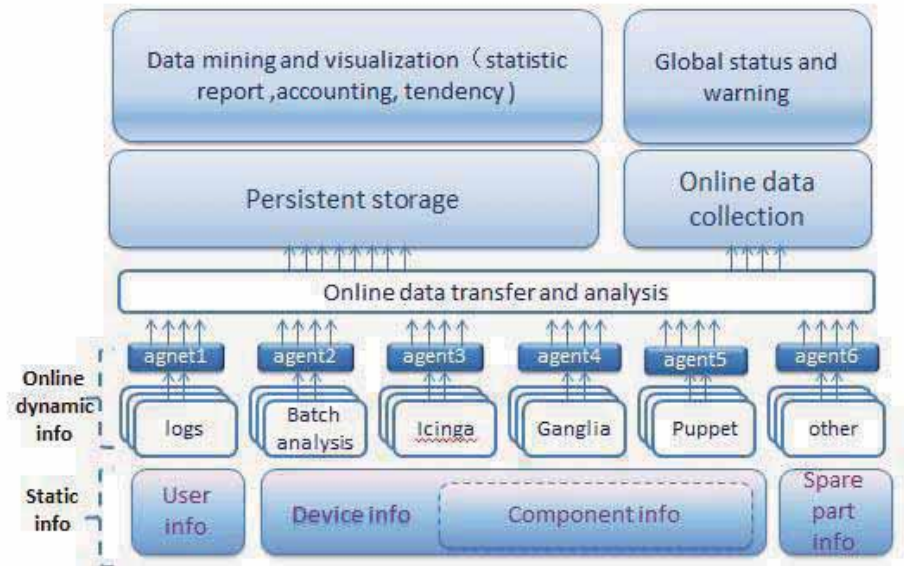

Figure 9.6: Fine-grained monitoring architecture

9.4 Software Development and Quality Control

The JUNO offline software system is composed of several sub-systems such as the framework, event generator, detector simulation, calibration, reconstruction, physics analysis and so on.

Each sub-system contains one or more packages,which are divided according to their functionalities. In principle, they are relatively independent in order to allow easy dynamic loading at the run time. The relationship between the necesary denpendencies are implemented using the Configration Management Tool (CMT) which is also used to compile each package.

Developers from different institutes and universities are collaborating together to write code in parallel. Subversion (SVN) [23] is deployed as the code repository and version control system to track the development of the offline software and tag it for releases. One central SVN server has been set up. All users and developers can easily check out the required release version and commit modifications according to their privileges.

Trac [24] is an enhanced wiki and issue tracking system for software development projects. Trac and SVN can be used successfully working together to provide cross searching and references.

Some specific tools, testing algorithms/packages will be created with the development of the offline software in order to test and monitor its functionality and make sure that the whole software is going in the correct direction. Every time a new version is released, a complete test will be performed and a report given showingthe results of some characteristic quatities, including CPU consumption and memory usage. Several kinds of documention, such as Wiki [25] pages and DocDB [26] will be provided.The Wiki pages will generally record the objectives and progress of each subsystem, while the DocDB will store technical documentation and status reports.

Bibliography

[1] http://www.cmtsite.net/

[2] Gaudi project homepage:http://proj-gaudi.web.cern.ch/proj-gaudi/

[3] Root an object-oriented data analysis framework. http://root.cern.ch/

[4] Extensible Markup Language (XML), http://www.w3.org/XML/

[5] http://www.slac.stanford.edu/ perl/heprep/

[6] http://www.w3.org/MarkUp/VRML/

[7] http://www.web3d.org/

[8] http://gdml.web.cern.ch/GDML/

[9] S. Agostinelli et al. (Geant4 Collaboration), Nucl. Instr. And Meth. A506(2003) 250

[10] http://lcgapp.cern.ch/project/simu/HepMC

[11] V.A. Kudryavtsev, Computer Physics Communications 180 (2009) 339-346

[12] https://www.opengl.org/

[13] http://oss.sgi.com/projects/inventor/

[14] https://www.oracle.com/database/index.html

[15] http://dev.mysql.com/downloads/

[16] http://www.postgresql.org/

[17] http://www.sqlite.org/

[18] http://www.cstnet.net.cn/

[19] http://www.adaptivecomputing.com/

[20] High Through Out computing http://research.cs.wisc.edu/htcondor/

[21] Platform Load Sharing Facility http://en.wikipedia.org/wiki/Platform_LSF

[22] Dean J, Ghemawat S. MapReduce: simplified data processing on large clusters[J]. Communications of the ACM, 2008, 51(1): 107-113.

[23] https://subversion.apache.org/

[24] http://trac.edgewall.org

[25] https://www.mediawiki.org/

[26] http://docdb-v.sourceforge.net/

Chapter 10

Civil Design and Facility

10.1 Experimental Site Location and Layout

The location of the JUNO experiment and its supporting facilities should meet the following criteria:

1. The site should have an equal distance from both the Yangjiang and the Taishan Nuclear Power Station with a largest possible overburden;
2. The site plan and support facilities should be comprehensive for safety, access to the site, and ease in managing the logistics of equipment and personnel above and below the ground for construction and operational considerations of the experiment;
3. The site engineering design and construction plan should be comprehensive in its consideration for energy conservation and emissions reduction, along with minimizing the impact on the local ecological environment;
4. The site should have readily available access to adequate utility water and electric power;
5. The surrounding transportation infrastructure of road should be reasonable for transportation of experimental equipment to the site. The road on site should be comprehensive in its consideration for easy equipment transportation;
6. The site plan for the above ground campus should be comprehensive in its design consideration for seamless and harmonious integration with the local topography, landforms and foliage for civil construction, experimental installation and onsite workforce;
7. All the design should meet applicable national building and construction codes and specifications for civil construction should be followed.

10.1.1 Experiment Site Location

The site location is driven by the physics requirements to be optimally equidistant from both nuclear power complexes, along a central axis determined by the latitudes

and longitudes of the (6) reactors at Yanjiang Station and (4) reactors in Taishan Station. The site, with surface and underground facilities, and experimental detector should be located in an area approximately 2,000 m in length and 200 m in width along this central axis at a distance approximately 53 km from the Yangjiang and Taishan Nuclear Power stations for the baseline physics requirements. In addition, the experimental hall should be at a depth greater than 700 m. The lithology and rock formation should be carefully considered for optimum stability, along with mountain topography to maximize rock overburden.

Prospective site locations along the central axis are shown in Fig. 10.1 and Fig. 10.2, at points (1-3) with elevations of 230 m, 210 m and 205 m respectively. In view of the changes of boundary condition of the Mesozoic granite stocks intruding into the Paleozoic rock mass, point (4) at 268.8-m elevation away from this boundary of granite was selected. This preliminarily location for the experimental hall is far enough away from the granite boundary to offer adequate safety margin.

10.1.2 Experiment Hall Layout

With site location determined, access options to the underground experimental hall must be considered. Life safety and emergency egress requires that at least two independent access paths from the underground experimental hall to the surface be available. With this requirement in mind, the site plan layout for underground access is either: "vertical shaft and inclined shaft" or "vertical shaft and normal tunnel". Both options would have the same vertical shaft with cage-lift, but the normal tunnel with an 8% grade slope would be 6 km in length as compared to an inclined shaft at a grade slope of 42.6% and 1.34 km in length. The normal tunnel construction cycle is too long and costly with transportation safety issues using motorized vehicles for access. The inclined shaft option was selected for its short construction cycle, lower cost, and the use of rail cars for equipment transport underground provides a safer and controlled environment.

Fig. 10.3 is a general layout of the site and facilities with the "vertical shaft + inclined shaft" scheme. Here the vertical shaft is 581 m in depth; the inclined shaft is 1,340 m in length with a slope of 42.6%; and the overburden at the experimental hall is 728.8 m. The access entry to the inclined shaft will be close to the experimental hall, located in the granite mountain area. All of these factors are favorable for civil construction and stability of the rock. A site survey was conducted to determine the optimal location of both access shafts. The vertical shaft is located at the abandoned quarry. Impact of this site during the construction and the operation to the surrounding area, traffic conditions and local residents, have to be studied well. as well as the construction cycle. To facilitate the construction and reduce the impact to the local residents, the construction yard and rock disposal area should be arranged near the entry shaft construction site. With full consideration of these site conditions and other factors, such as difficulties in land acquisition, etc., the entrance portal of the inclined shaft was determined to be at Shenghe Village, Jinji Town, Kaiping City.

The entrance portal of the inclined shaft (Fig.11.3) includes permanent buildings, a construction yard area, and a waste disposal area. All stone debris will be disposed in the waste disposal area, along with that from the vertical shaft. The waste transportation route to the waste disposal area does not pass through neighboring villages

or poultry farms, to limit the impact to the local life and economy.

10.1.2.1 Underground Cavities

The layout of the underground facilities (Fig.10.4) includes a cavity for the main experimental hall, ancillary rooms with connecting tunnels.

The experimental hall contains a spherical detector tank 38.5 m in diameter located in a cylindrical water pool with inner diameter of 42.5m, as shown in Fig10.5. Shape of the experimental hall ceiling, either a dome or a vault scheme, was studied. Criteria such as workflow, construction cost and schedule, rock stability, experimental equipment installation and operation were considered. Vault scheme was selected with two crane bridges on a common rail to span installation hall to water pool. A 2.75 m wide walkway on both side of pool is chosen, and the span of upper vault structure becomes 48 m. A 10 m wide area at the entry of experiment hall will be used for equipment un-loading, resulting in a hall 55.25 m long. The total height of the hall from vault apex to the bottom of the water pool will be 69.5m.

The underground assembly hall, pump room, and electrical equipment room are arranged at the same elevation as the inclined shaft entry into the experimental hall. The assembly hall is right next to the experimental hall. This hall is 40 m in length, 12 m span, and 12.5 m height and connected with the inclined shaft through a tunnel with cross-section of 5.7 m in width and 6.5 m in height. The rail car can transport the equipment directly to the experimental hall or to the door of assembly hall. Two bridge cranes on the same rail, each equipped with two 12.5 ton hooks, are arranged in the experimental hall, for handling of experimental equipment. An additional 10 ton crane is located in the assembly hall, for handling of the cargo and equipment from the inclined shaft rail car.

Liquid scintillator storage room, processing room, and filling room are located at the same elevation and opposite to the assembly hall towards the vertical shaft at a distance far enough away from the experimental hall for fire safety consideration. Electronics room, water purification room, gas room, and refuge room are also arranged around the experimental hall. A single access/drainage tunnel with 4.5 m in width that encompasses the experimental hall interconnects these ancillary rooms.

The inclined shaft being 1,340 m in length, 5.7 m in width, and 5.6 m height, bottoms out at elevation -460 m. From there it proceeds at the same level to the experimental hall by way of an 85 m long interconnecting tunnel with a turning radius of 35 m. The slope of the inclined shaft at 42.6% (23.08°) is consistent with requirements for debris transportation during the excavation and rail car vehicle specification, while minimizing the length of the inclined shaft. The transport equipment in the inclined shaft is a single-drum cable winch, which operates at a speed of 4 m/s. A walkway is located on one side of the inclined shaft for the maintenance personnel to carry out patrol check and for underground evacuation in case of an emergency. Utilities such as cable bridges, fire water pipeline, air conditioning water pipeline, and liquid scintillator pipeline, etc. are secured on the side walls of the inclined shaft, while air conditioning conduit and air supply conduit, etc., are located under the upper crown of the shaft.

The access entry to the vertical shaft is at 130 m elevation. The shaft is 581 m in depth, with the bottom access entry connected to the experimental hall through an

interconnection tunnel of 300 m in length at 3% slope. The cross-section of this tunnel is 4.5 m x 5.2 m. A lift-cage elevator is used in the vertical shaft with a maximum lifting speed of 6 m/s, and a load capacity of 8-10 people. In addition, a vertical ladder stairway is installed for personnel evacuation in case of emergencies and for equipment maintenance access. Vent duct and cable utilities also pass through this vertical shaft.

10.1.2.2 Layout of Surface Constructions

The ground campus comprises inclined shaft entry area and vertical shaft entry area. The two areas are connected by a 2.5Km road.

Exhaust room, electrical power room, and an access room are arranged near the vertical shaft entry.

The inclined shaft entry area is a comprehensive area for assembly, office, dorms, and other service. A rock disposal area is also arranged in this area. The landscape at the rock disposal area will be recovered after the construction is completed. The living area is near the entrance of the campus, and is provided with two houses and one dorm building with 54 rooms. There is a canteen on site to provide food service. The experimental office building consist of a control room, a computer room, meeting rooms, and offices. The assembly area is arranged at the inclined shaft entry, and comprises one assembly building (3000 m^2) and temporary storage buildings. The assembly building is air-conditioned and provided with a crane to facilitate equipment transportation. In addition, power station, utility buildings for pure water, LN2, et al are all in the area. The liquid scintillation area is arranged away from the living area in the valley area at the access entry. It includes liquid scintillation storage tanks, purification and nitrogen facilities.

Figure 10.1: Physics required site region, shadow is granite area

Figure 10.2: Experimental Hall Location (position 4) in the granite area with dash line

Figure 10.3: Layout of the Site

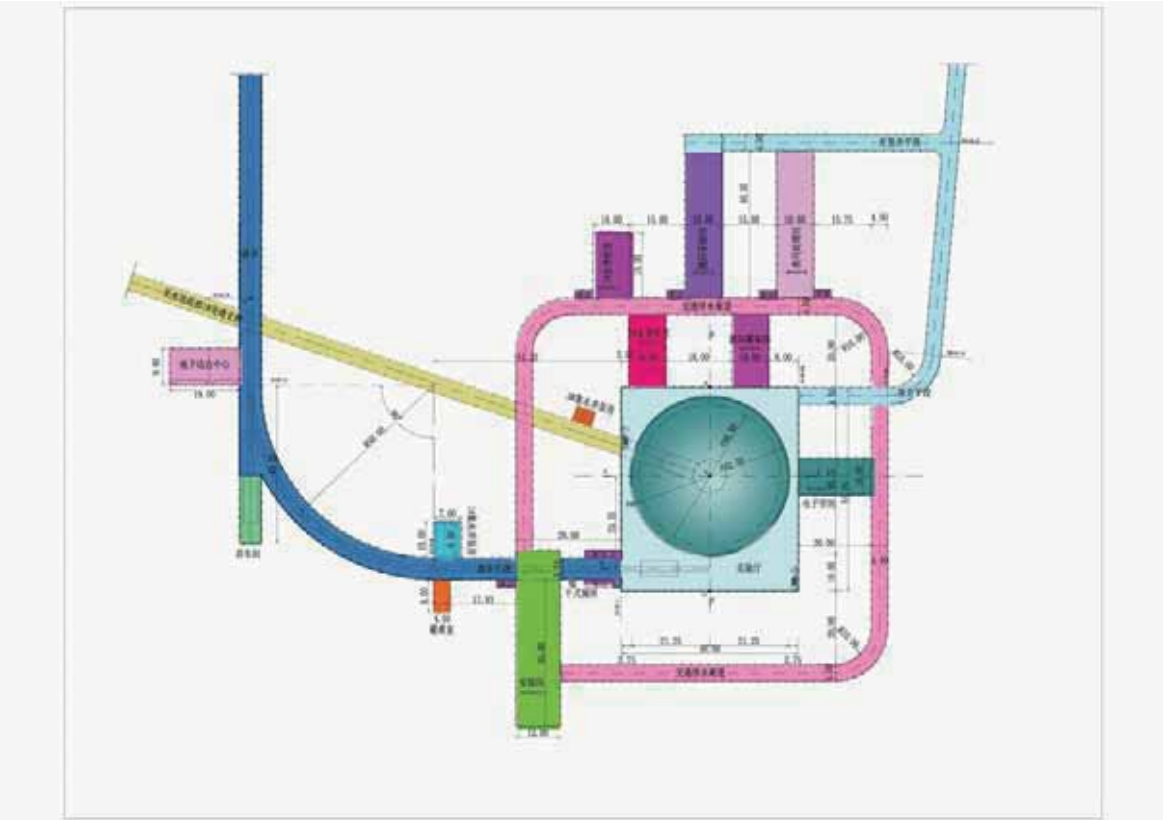

Figure 10.4: Layout of the Underground Facility

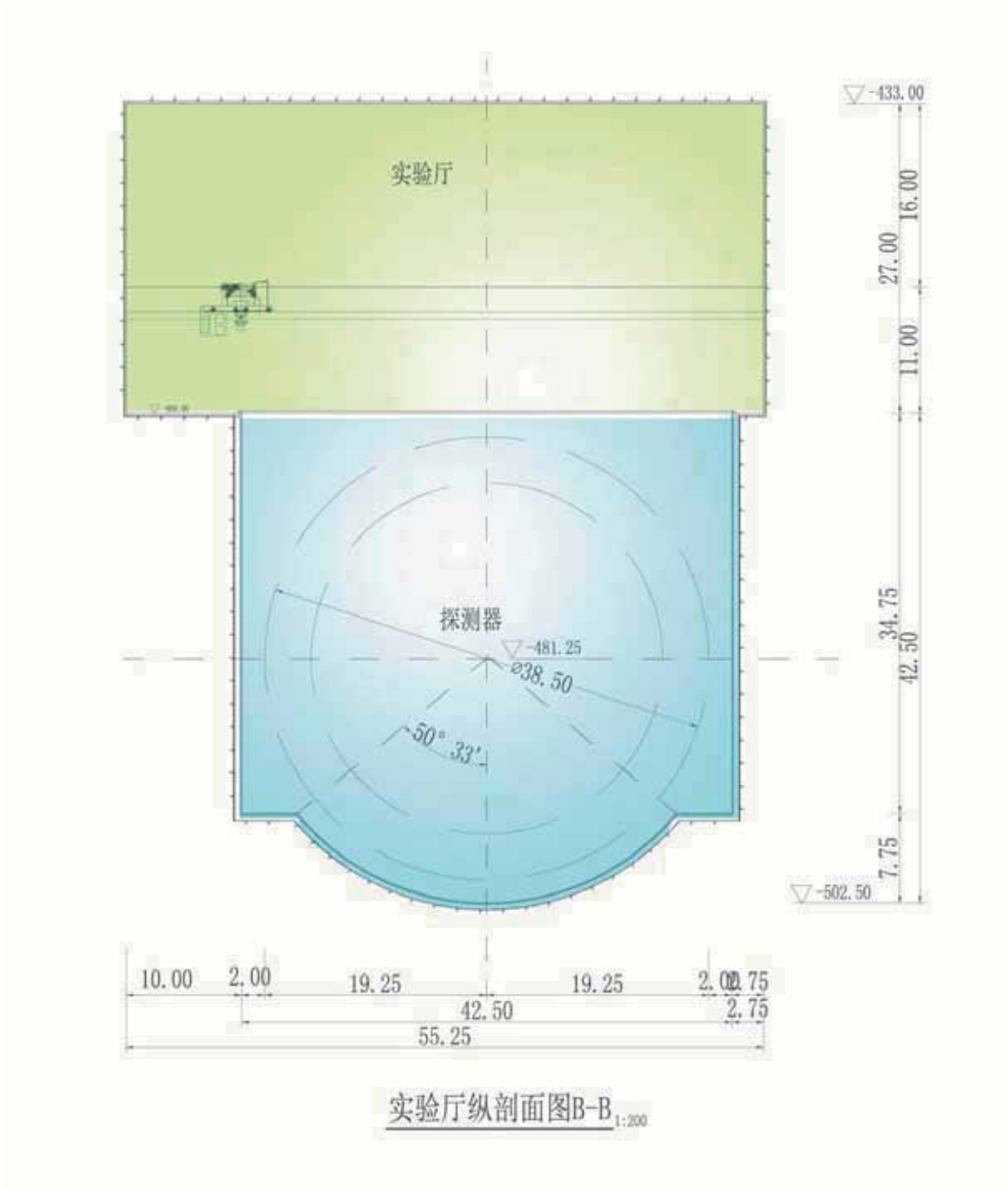

Figure 10.5: Sideview of the Experimental Hall

10.2 Geological Survey

10.2.1 Geographical Conditions of the Region

The site is 5 km away to Jinji Town, which is 40 km away to Kaiping City (figure (10.6)). There are provincial road S367, S275 and villege roads connecting the towns and villages. A new road will be built to connect the site to the outside.

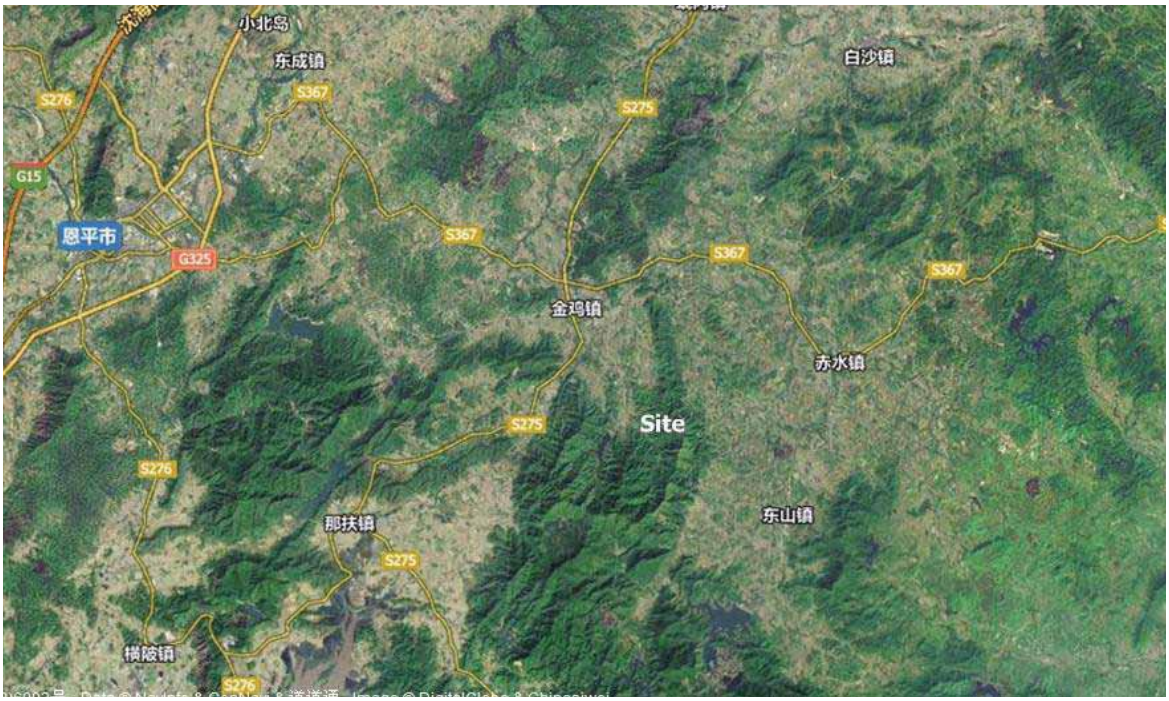

Figure 10.6: Map of the Project Region

The underground facility is underneath the Dashi Mountain area in Jinji Town, which has an elevation of 326 meters. The main mountain ridge extending approximately in south-north direction. The elevation of the hill area is about 30m∼300m while the topographic slope is usually 10° to 20°. The main gulch exists and extends approximately in east-west direction. The depth of gulch cuts is 50 meters to 100 meters, and there is perennial water in the gulch. The largest river in the area, Dongkeng River, originates from Dongkeng Forest Farm and flows across the project area and Shenghe Village. Rivers in the region usually flow approximately in south-north direction. All of rivers are branches of Chishui River. Niuao Water Reservoir (a small reservoir) and several ponds are distributed at the southeast side of the mountain.

The project area is of Southeast Asian tropical maritime monsoon climate, with frequently strong typhoons in the transition period from summer to autumn, which bring abundant rainfall. Kaiping City is surrounded by the plenty of rivers with wide water area. It is not severely cold in winter and very hot in summe. The climate is mild and abundant in rain. The annual mean air temperature is 21.7°C while the annual mean humidity is as high as 82%. Annual rainfall varies from 1,700mm to 2,400mm. The rainy season mainly concentrates from April to September while the dry climate distributes from October to Feburary. The perennial dominant wind direction is east.

Affected by the subtropical monsoon, the period from June to October in every year is a strong wind season with a force of 6-9 from east.

Active fracture zones in the region is mainly Enping-Xinfeng zone, which is at approx. 60Km distance to the project area. A magnitude-6 earthquake once happened near Mingcheng long fracture zone. Magnitude-4 or lower earthquakes happened near Kaiping, and a magnitude-4 earthquake happened in Hecheng area. The rmoluminescence survey value of the fracture near Gaoming is 245,200 years, and the the rmoluminescence survey value of the Hecheng-Jinji fracture is 153,300 to 350,000 years. The fractures belong to Mid-Pleistocene active faults.

According to the earthquake catalogue of China Seismic Network (CSN), although there were more than 64 earthquakes happened within 150 Km range of project area with magnitude-3.0 or higher since 1970, wherein, only 3 moderate earthquakes higher than magnitude 4.75 happened. No earthquake higher than 4.0 happened near the project area (within 25Km range). The earthquake distribution map in the project region shows that the earthquakes are mainly distributed in Yangjiang region in southwest. The highest earthquake is a magnitude-4.9 in Nanhai region on Mar. 26, 1995, which is 100 km away from the project area. Therefore, the impact of earthquakes on the project area is low.

According to the "Seismic ground motion parameter zonation map of China", the seismic ground peak acceleration is 0.05g in 50 years. The characteristic time of the seismicresponse spectrum is 0.35 s, and the corresponding basic seismic intensity is degree VI.

10.2.2 Geological Survey

A detailed geological survey for the inclined shaft, vertical shaft, and experimental hall areas of the experimental station was carried out in 2013 to ascertain the geological conditions of the main constructions in the project region and provide a geological basis for engineering design and construction and raise proposals for handling main geological problems.

The survey result is summarized in the Figure 10.7. There are Yanshanian granite stocks at the location of the experimental hall. The granite mass intruded into the Palaeozoic sand rocks. The contact zone between them is a hornfelsic zone. Details are described in the following.

10.2.2.1 Engineering Geological Conditions of the Inclined Shaft

The access entry of the inclined shaft is in a mild gulch with width of 400 m in northeast to Shenghei Village. Vegetation near the access entry is dense. The gulch in front of the access entry is open and favorable for organization of construction and arrangement of surface buildings (see Fig. 10.8). The formation penetrated by the inclined shaft mainly consists of Ordovician Xinchang (O_{1x}), Cambrian Bacun ($\in bc^c$), hornfels and granitic intrusions.

There is a water reservoir (Shantan Water Reservoir) at the upstream of the main gulch at the access entry of the inclined shaft (see Fig. 10.8). The water reservoir has only $5 \times 10^4 m^3$ storage capacity, which has no feeding river at its upstream. The water is mainly supplied by rainfall and ground water discharge. The catchment area of the

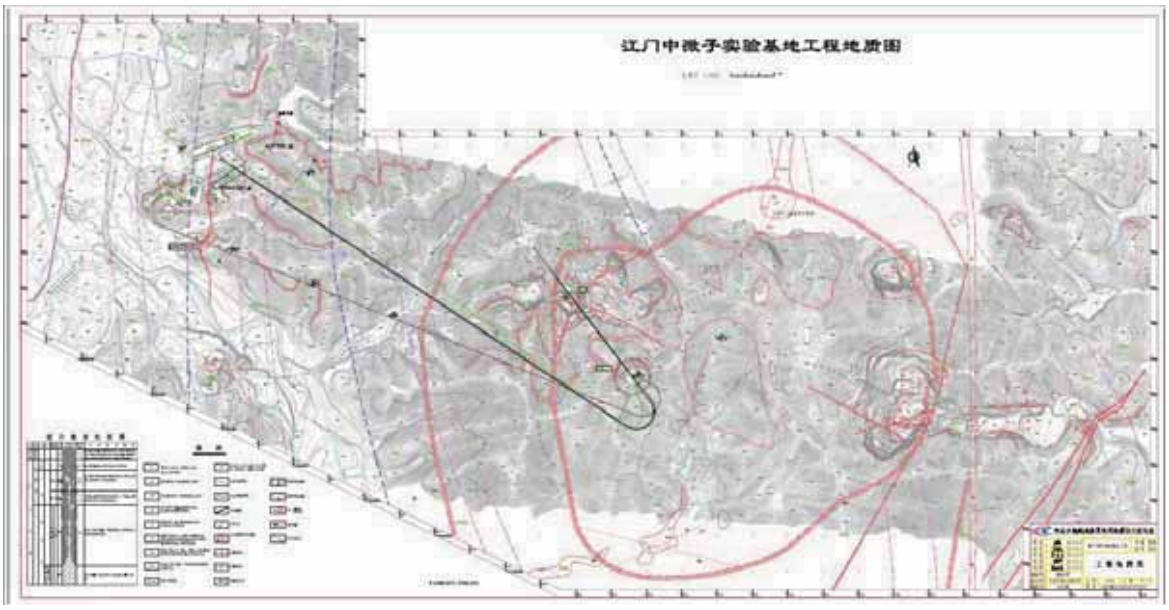

Figure 10.7: Engineering Geological survey in the Experiment Region

water reservoir is approximately $0.3Km^2$. Therefore, the water inflow into the water reservoir is not heavy even in the rainy season, and will not cause severe flood discharge. There are two floodways behind the dam of the water reservoir. The minimum distance from the floodways to the access entry of the inclined shaft is approx. 130 meter. The elevation of the floodways is lower than that of the access entry by approx. 5 meter. The area at the downstream of the flood discharge area is a lower and wider plain terrain. In summary, the flood discharge from Shantang Water Reservoir in the rainy season will have no impact to the access entry of the inclined shaft.

From the geological survey, the covering layer at the access entry is silty clay gravel soil in $1m \sim 3m$ thickness. The bedrocks are mainly Xinchang Fm(O_{1x}) gray and dark gray siltstone mixed with feldspar-quartz sandstones and clay shale stones in $N6°E$, $SE\angle 58°$ occurrence. The bedrocks are completely weathered, locally intensely weathered, and fractured in fractured-loose structure. The condition is not perfect for shaft construction. Slope protection and water drainage should be considered.

The classification of the tunnel enclosing rocks is predicted and evaluated as follows (see Fig. 10.9):

1. 1413m∼1350m section: The enclosing rocks near the tunnel entrance are mainly silt rocks with locally distributed quartz sandstones and clay shale stones. They are fully or intensely weathered while some are moderately weathered. Joints and fractures are developed and filled with silt. The rocks are mainly in silt filled cataclastic structure while some are in mosaic cataclastic structure. The crown and side walls have water seepage or water dripping. The quality rating of the enclosing rocks is grade V. The cavity stability is very poor without self-stabilization time or with very short self-stabilization time.

2. 1350m∼1283m section: the tunnel enclosing rocks in the region are mainly silt rocks and quartz sandstones with developped moderately or slightly weathered

Figure 10.8: Topography near the Access Entry of Inclined Shaft. The underground facility is at left. The entry of inclined shaft is at right.

Joints and fractures. The rocks are mainly in mosaic cataclastic structure while some are in layer structure. The crown and side walls have water seepage or water dripping. The quality rating of the enclosing rocks is grade IV. The crown enclosing rocks are unstable, and the self-stabilization time is short. Various large-size deformations and damages may occur.

3. 1283m∼808m section: The tunnel enclosing rocks are mainly quartz sandstones, with silt rocks distributed locally, and are slightly weathered. Joints and fractures are developed. The rocks are mainly in mosaic cataclastic structure while some are in layer structure. The crown and side walls have water seepage or water dripping. The quality rating of the enclosing rocks is grade III. The crown enclosing rocks have poor local stability.

4. 808m∼418m section: The rocks are hornstones and slightly weathered. Joints are developed or undeveloped. The rocks are mainly in layer structure. The crown and side walls have water seepage or water dripping. the quality rating of the enclosing rocks is mainly grade III, and grade II locally. The cavity enclosing rocks have high overall stability.

5. 418m∼0m section: the rocks are granite rocks and slightly weathered. The joints are undeveloped. The rocks are mainly in block structure. The crown and side walls have water seepage or water dripping. The quality rating of the enclosing rocks is grade II. The cavity enclosing rocks have high stability and will not have plastic deformation.

Attention should be paid to water abundance in the sandstones as indicated on the cross section of geophysical prospecting along the route (A) near the ditch of Dongkeng River in the original inclined shaft route (see figure 10.9).

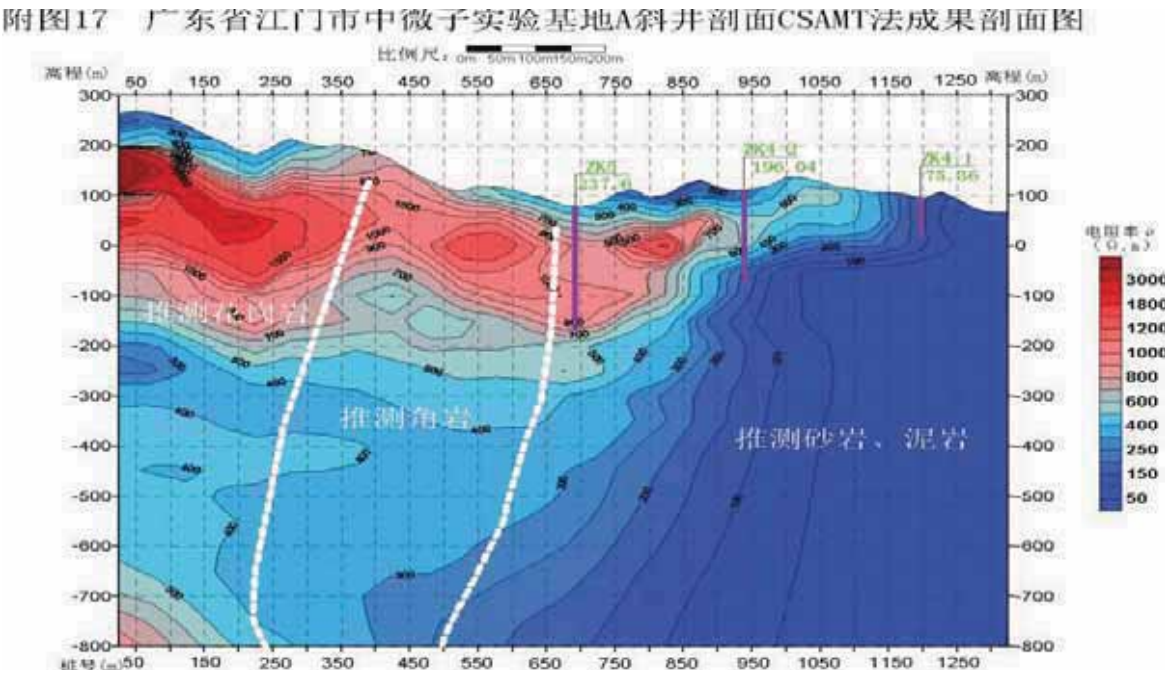

Figure 10.9: Geophysical Investigation of Inclined Shaft

10.2.2.2 Engineering Geological Conditions of the Vertical Shaft

The vertical shaft is located in the Dongkeng Quarry. It is 589 m in depth and 6 meter in diameter.

The vertical shaft is located in a quarry and at the end of the gulch (see Fig. 10.10). The upstream catchment area of the gulch is approx. $0.1km^2$. In the rainy season, heavy torrential flood will be produced in the gulch. Water drainage and special care must be considered during construction and operaton.

The vertical shaft is in granite mountain. An exploring borehole ZK1 was drilled at the location of vertical shaft for the geological survey. The borehole was deeper than bottom of water pool in the experimental hall. Variout borehole tests were carried out, including terrestrial stress test, high pressure water test, specific resistance test, natural gamma test, borehole televiewer test, acoustic wave test, and ground temperature test, etc.

The vertical shaft is near the granite intrusion boundary. In the area of vertical shaft, the joints, fractures, and faults are developed. 5 exposed faults in different sizes are distributed nearby. Eleven or more faults or compresso-crushed zones in different sizes were unveiled in the borehole.

The classification of the vertical shaft enclosing rocks (Fig. 10.11) is predicted and evaluated as follows:

The rock quality of vertical shaft entry section with depth of 10 meters is grade IV. The granite rocks are moderately weathered. Joints and fractures are well developped. The section is in mosaic cataclastic structure or block structure.

The shaft depth to the -118 meter, the rocks are mainly slightly weathered or moderately weathered rocks in some regions. As unveiled in the borehole surveying work, there are several small developed faults and compressive structural planes (grade

IV structural planes). The rocks are mainly in sub-block structure or in block structure locally at some places. The quality rating of the enclosing rocks is grade III.

The rocks of shaft bottom section are slightly weathered or fresh. The complete section is in perfect block structure. The quality rating of the enclosing rocks is grade II. The shaft wall enclosing rocks have high overall stability and will not have plastic deformation.

The water inflow in the vertical shaft is predicted with Dupuit formula. According to the water pressure test result, the permeability factor of the rock mass of the vertical shaft is approximately 0.009 m/d. The shaft is approx. 589 meters in depth and 3 meters in radius. The calculated water inflow in the vertical shaft is estimated $1473m^3/d$.

There is only one concern that a fault of F2 may cross the horizontal tunnel between bottom of vertical shaft and experimental hall. The rock in the F2 region is grade IV. According to the survey, the F2 fault is a compressional-shear shifted reversed fault, in $N20°\sim55°E$ and $SE\angle59°\sim90°$ occurrence. The occurrence variation is severe. The fault is mainly developed in granite mass, in 0.5 meters$\sim$3.0 meters width, and extending approximately 400 meters. On the ground surface, the fault zone mainly consists of flake rocks, mylonite, cataclastic rocks, and lens with inclined scratches. The cementation is poor to moderate. As unveiled in the ZK1 borehole, the deep fault zone is mainly filled with quartz. The cementation is good to very good and is usually in healed form. The buried depth of the F2 fault is approx. 660 meters. It is speculated that the cementation in the deep part of the fault is good to very good. The F2 fault area has no surface water and is close to the dividing ridge in which the rock mass is thin and has weak water permeability. In summary, it is speculated that the F2 fault zone has weak water permeability while the water inflow is low. The fault will not have severe water inflow at the level the tunnel is excavated to the F2 fault.

10.2.2.3 Engineering Geological Conditions of the Experimental Hall

The experimental hall is located under a small hill at the southeast side of the vertical shaft. The surface elevation is 268 m, and the buried depth is approx. 763 m. The profile of hill is a mountain ridge. The experimental hall is in the granite mass, which consists of gray medium-fine grained adamellite. In the plan view, the experimental hall is relatively close to the central zone of the intruding small stocks.

A geophysical prospecting diagram of the experimental hall and the vertical shaft area obtained with high-frequency magnetotelluric method is shown in Fig. 10.12. Both the vertical shaft area and the experimental hall area consist granite mass. It is speculated that there are faults in the horizonal connecting tunnel between the vertical shaft and the experimental hall.

The major engineering geological issues include:

Terrestrial Stress and Rock Burst Analysis According to the laboratory test, the volumetric weight of slightly weathered (or fresh) granite is approximately $26.6\times10^3kN/m^3$, the saturated uniaxial compressive strength is 80 MPa$\sim$120 MPa as usual. Since the maximum buried depth of the experimental hall is 763 meter, according to the terrestrial stress test, it is estimated that the terrestrial stress at the experimental hall is not higher than 20MPa and the rock strength/stress ratio is 4.85. The deep core obtained in the borehole ZK1 has high integrality in whole. The core

near the borehole bottom (651m buried depth) is still in long column shape. Since the experimental hall is relatively close to the center of the intruding rock stocks, it is speculated that the rock mass there has high integrality. Through comprehensive analysis, it is speculated that the stress in the experimental hall is moderated, and will not result in severe rock burst.

External Water Pressure Analysis According to the water pressure test and the high-pressure water test, the permeable rate of the granite rock is usually lower than 1 Lu and considered as weak permeability. The difference between the ground water level and the bottom of experimental hall is 577.79 meter. According to the "Code for Engineering Geological Investigation of Water Resources and Hydropower", the external water pressure reduction factor of weak permeable rocks is 0.1∼0.2. Thus, the effective external water pressure of the experimental hall is only 58 meters∼116 meters, corresponding pressure is 0.58MPa∼1.16MPa. The high-pressure water test shows that most of the joints and fracture structure of the granite did not change under the water pressure and are mainly of turbulence type while some of them are of filling type. Dilatation or erosion phenomenon is not found. In summary, the external water pressure at the experimental hall is relatively low, and its impact on the cavity stability of the experimental hall is trivial.

Cavity Water Inflow Analysis The water inflow in the experimental hall is predicted with underground water dynamics methods. The maximum water inflow in the early stage and stable water inflow the long-term, are predicted with several methods.

According to the water pressure test, the deep granite is slightly permeable. The maximum water inflow in early stage calculated with HirishiOshima empirical equation is approximately $395m^3/d$. It is $527m^3/d$ with the empirical formula method. The long-term stable water inflow was estimated to be $244m^3/d$ and $120m^3/d$ respectively with Ochiai Toshiro formula and empirical formula method.

In summary, the maximum water inflow in early stage and the long-term water inflow in the experimental hall are low.

Underground Temperature According to the underground temperature measurement in the borehole, ZK1, the underground temperature at 450 meter depth (-314 meter elevation) or deeper is $31\sim32°C$ (see Figure 10.13). Therefore, temperature is not a big issue for the experiment.

pH value The pH value of underground water in borehole ZK1 at the location of the vertical shaft is analyzed to be 7.25∼7.75 while the pH value of ground water is near 7. It indicates that the deep ground water is medium corrosive.

Rock Radioactivity Table 10.1 shows the result of rock radioactivity measurement at different depths in borehole ZK1. All sample results meet the requirements for main building materials (as per "Code for Radionuclides Limits in Building Materials" (GB6566-2010)) except for the external exposure index Ir of three samples, which are slightly greater than 1.0. The rock material meets the criteria for Class B products according to the "Code for Radiation Protection Classification and Control of Natural Stone Material Products".

10.2.2.4 Stability Assessment of the Enclosing Rock

The experimental hall is 48 meters wide, and can be divided into two parts: the upper cavity is enclosed by the crown and high side walls (vertical section) that connect the crown part, and is mainly used to accommodate lifting appliances and other facilities (e.g., cable channel, etc.), and, the lower cavity is a cylindrical pool, 42.5 meters in diameter and 42.5 meter in depth. Utility halls are arranged around the experimental hall. The experimental hall is large and complex in structure. The rock types and long term stabilibty of underground facility should be assessed thouroughly.

The length of the experimental hall is 55.25 meters. The axial is directed in $N37°W$. The cavity enclosing rocks are granite, slightly weathered, in block structure. The developed joints are mainly steeply inclined while locally developed joints are slowly inclined and moderately inclined. The joint planes are straight, coarse, and are usually enclosed without filled material. Some joints are slightly open or fully open and filled with rock debris or kaolin film. There exists local water seepage or water dripping at some places. The quality rating of the enclosing rock is considered as grade II.

Overall, the cavity enclosing rocks are stable. However, local unstable blocks may be produced under the inter-cutting action of the three groups of steeply inclined joints because of the large span of the experimental hall.

According to the terrestrial stress test, the direction of maximum horizontal stress is $N10°W \sim N54°W$. Since the upper cavity is approximately in a square shape, the terrestrial stress has little influence on the selection of the axial direction. The terrestrial stress difference among different directions are small and has little impact on the stability of the side walls. Since the cavity span is large, the terrestrial stress is in static state while the redistributed stress of the cavities is complex. Stability verification must be carried out and appropriate engineering measures must be taken.

The geological conditions (e.g., lithology of enclosing rocks, joint development, and underground water, et al) in the pool are the same as those of the upper cavity. However, because the main joints are steeply inclined, water pool may form an unfavorable combination with the side walls. However, the pool enclosing rocks are overall stable.

The geological conditions of the ancillary cavities are the same as those of the experimental hall. The cavity enclosing rocks have high overall stability. Although the utility cavities are small, at intersections among the experimental hall and ancillary cavities, care must be taken for the blasting control in order to keep the integrality and stability of structcture.

Figure 10.10: Topography at the Entry of the Vertical Shaft

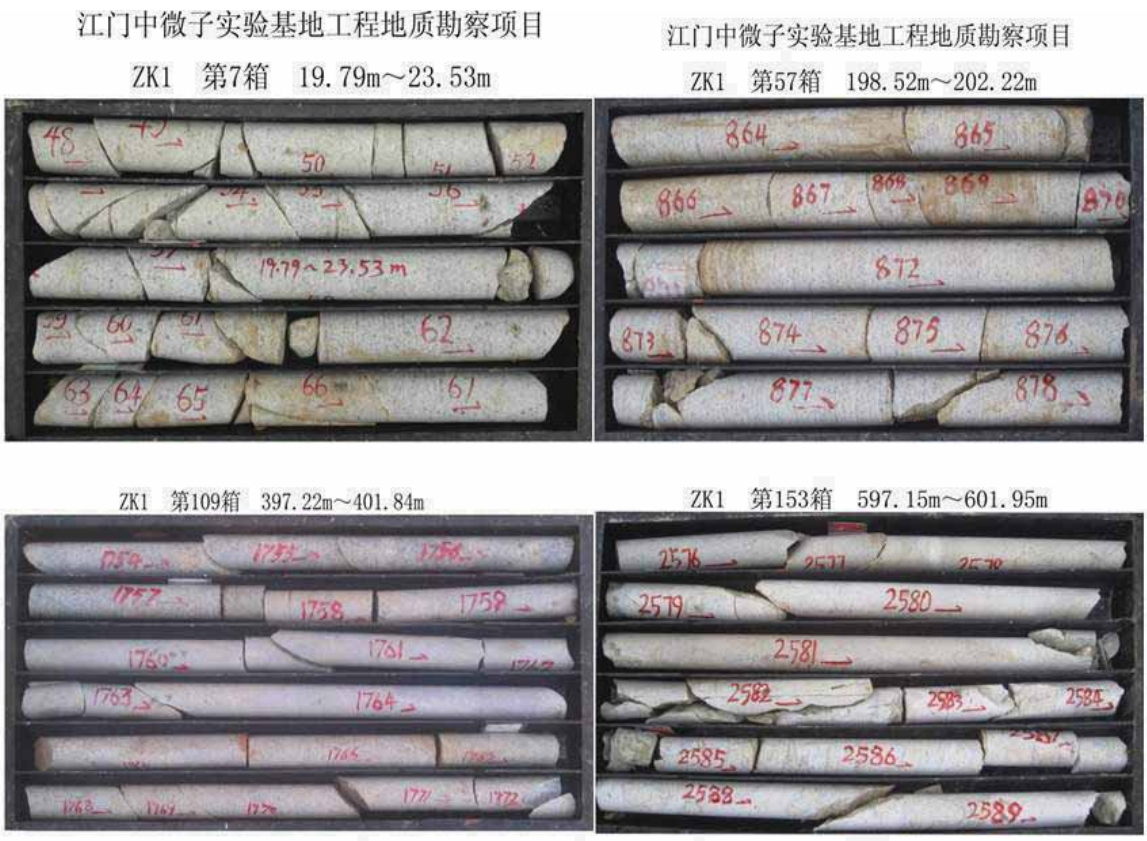

Figure 10.11: Some Cores Samples from the exploring drill well in the Vertical Shaft

Table 10.1: Result of Rock radioactivity Test in Borehole ZK1

Site No.	Sampling Depth	Radioactivity					
		Specific Activity CRa of ^{226}Ra (Bq/kg)	Specific Activity CTh of ^{232}Th (Bq/kg)	Specific Activity CK of ^{40}K (Bq/kg)	Radium Equivalent Concentration C[e]Ra	Internal Irradiation Index IRa	External Irration Index Ir
FSYY-1	299.18～300.28	166.6	122.1	1066.4	425.2782	0.8	1.2
FSYY-2	403.11～404.11	155.9	110.0	1106.3	401.7544	0.8	1.1
FSYY-3	557.28～558.38	88.6	83.6	1239.7	310.5536	0.4	0.9
FSYY-4	616.47～617.12	173.1	129.5	536.6	395.1458	0.9	1.1
FSYY-5	633.02～633.77	116.4	111.2	342.2	296.6336	0.6	0.8
FSYY-6	650.23～650.93	130.1	113.0	1062.4	376.1412	0.7	1.0

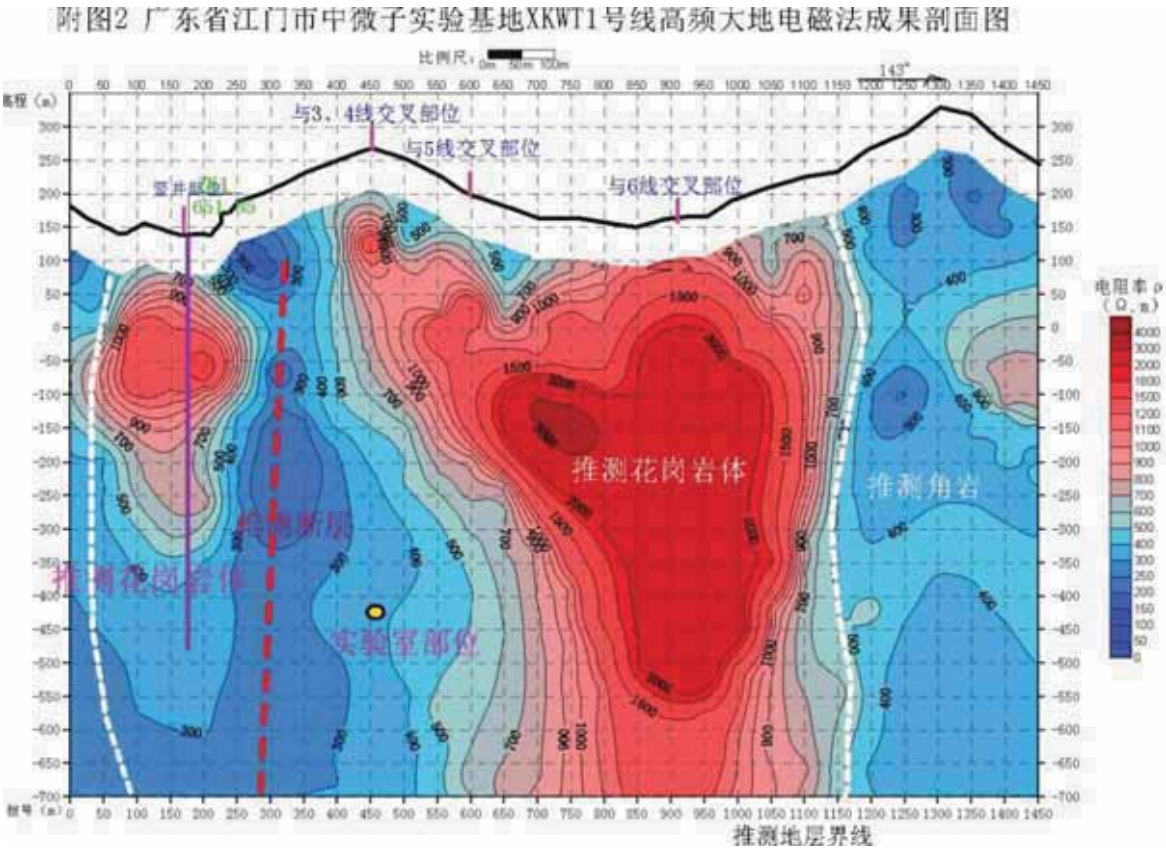

Figure 10.12: Geologic Diagram Obtained with the High-Frequency Magnetotelluric Method near the Explerimental Hall

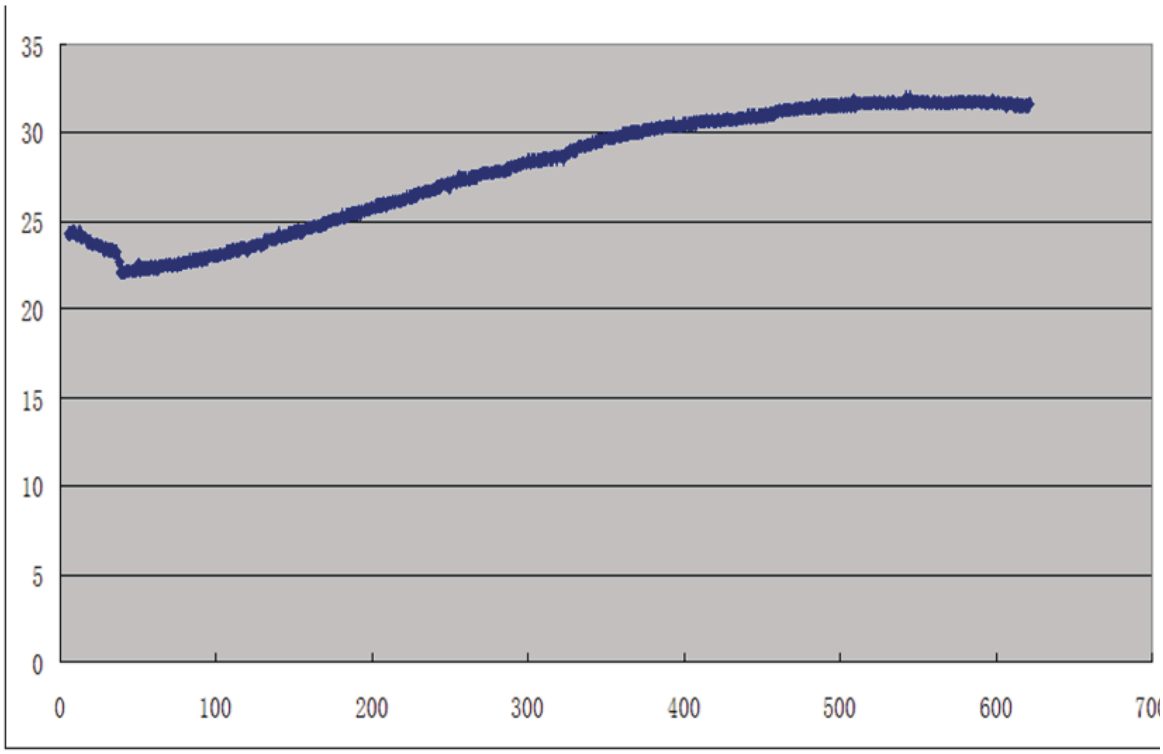

图 10-15 ZK1 钻孔地温测试结果曲线

Figure 10.13: Measured Underground Temperature

10.3 Utility Systems

10.3.1 Power distribution and grounding system

To meet the requirements of having redundant, reliable electrical power to the site, two 10 kV commercial power transmission lines will be introduced to the power distribution centers at the entrance to the inclined shaft and the vertical shaft from 110 kV transformer substations in Jinji Town and in Chishui Town, respectively. They are on different public grids. An underground 10 kV power equipment room is provided to distribute power through the experimental hall and ancillary rooms. In addition to these commercial power sources, the surface power distribution center will be equipped with a self-starting diesel generator, which will supply power for emergency lighting, ventilation or waste water sump-pumps during disruptions of the main power supply.

The total expected demand for power distribution is approx. 5,000 kVA from the combined power supply sources, each of which can provide 4,000 kVA of power. Steady-state power loads include ventilation, air-conditioning, and lighting systems along with operational experimental equipment. However, peak power capability is required during the LS distillation process and its transfer to the detector. An isolated transformer will be installed in the underground power equipment room to distribute clean electrical power on a separate grid to experimental equipment to minimize system noise.

The electrical grounding systems include both a clean ground grid for experimental equipment and a safety ground grid for utility systems. The clean ground grid for experimental equipment on clean electrical power will be connected to the secondary winding of the source isolation transformer. The two grounding grids will have no electrical connection between them. The surface safety ground grid is distributed and transferred to underground with power transmission cables, and is connected to the underground safety ground grid. The clean ground for experimental equipment is distributed locally in the underground experimental hall. It is understood that the underground geological formation mainly consists of granite, having a high electrical resistivity, not conductive for electrical grounding. Based on our experience, the electrical grounding systems should include appropriate measures, such as high-efficiency electrolytic ion grounding electrodes to mitigate electrical safety concerns. This grid should also connect to the water pool steel-bar structure, to improve the connectivity with the ground and to increase the overall capacity, hence further stabilize the ground.

10.3.2 Ventilation and air-conditioning system

The temperature in the underground experimental hall shall be maintained at a nominal $22°C$ and the relative humidity shall be lower than 70%, with adequate ventilation to sustain at least 50 people working 24/7 underground. Air quality in the experimental hall can be normal room air that meets cleanliness requirements for personnel safety. The cleanliness in ancillary halls related to liquid scintillator storage or processing should meet class-100,000-level which is comparable to the requirements for the Experimental Hall-5 at Daya Bay. Special measures (e.g., high efficiency filters) can be taken during liquid scintillator operations to improve the cleanliness to class-10,000-level.

The air exchange rate in the experimental hall is designed for 6 volumes/day, to reduce radon in the air and maintain a comfortable environment for underground workers.

Water chillier units and fresh air handling systems for supplying dehumidified cool air underground are located at the entrances to both the inclined and vertical shafts. This conditioned air supply flows through insulated ducts in each shaft for dispersion in the experimental hall. Air is then drawn from the experimental hall via exhaust ducts to a main duct in the inclined shaft, and then exhausted to the atmosphere using exhaust fans.

10.3.3 Water supply and drainage system

The underground utility water supply comes from the fire-fighting water system. Normal water usage is obtained from the fire-fighting water system main pipeline, so both water systems are from a common source.

Ultra-pure water for experimental use either in the detector water pool or in scintillator processing will have its own supply by stainless steel pipes from the surface to underground facilities.

Sources of wastewater underground come from natural rock seepage, utility water or fire-fighting water. It is collected in a series of grate-covered tunnel floor trenches and diverted to a number of sump-pits for pump-out to the surface. Since most of wastewater during normal operations comes from rock seepage, five sump-pit drainage systems have been strategically located through the underground facilities, based on the distribution of water seepage. Sump-pit-1, the main sump-pit, is located at the bottom of the inclined shaft, and is distributed through the curved interconnecting tunnel to the experimental areas. Sump-pit-2 is located at elevation of -200 m in a side portal area of the inclined shaft. Sump-pit-3 is located at the bottom area of the water pool, and is used during pool cleaning. Sump-pit-4 is located at bottom of vertical shaft. Sump-pit-5 is located at an elevation of -100 m in a side portal area of the inclined shaft where the rock formation is poor and water seepage is severe.

The water from whole underground facilities is pumped up to surface via sump-pit-1 and then sump-pit-2. This design may choose less power pump for sump-pit-1, which have less impact on the experiment during its operation.

Water pool draining will install additional dedicated pump system to sump-pit-1 temporarily.

10.3.4 Fire control system

The fire control system consists of automatic fire alarms and interlocks, fire-fighting water distribution to hydrant-hose units, numerous portable fire extinguishers, emergency smoke exhaust ventilation, emergency lighting, personnel evacuation planning, and refuge-rooms. The automatic fire alarm system covers smoke detection and alarming for all underground cavities, tunnels and shafts, along with surface facilities. All alarm signals will be sent to the surface fire control center to be monitored by dedicated fire-watch personnel around the clock. Relevant zones are interlocked to respond to alarm signals by taking the following actions: cut off main power supply sources and start up emergency power generator, close fire partition doors and relevant air exhaust

valves to isolate the ignition source, and start emergency exhaust fans. Fire hydrant-hose units and portable fire extinguishers are the preferred method for fighting fires in the underground complex over that of sprinklers systems. The emergency smoke exhaust ventilation systems can be energized based on the location of the incident and the personnel evacuation planned route. For example, smoke can be exhausted through the vertical shaft while personnel escape via the inclined shaft; alternatively, smoke can be exhausted through the inclined shaft while personnel escape via the vertical shaft. In the case of a fire/smoke emergency the main power feeds will be shut off automatically by interlocks, and the emergency power generator will start, to supply power for smoke exhaust ventilation and lighting to ensure safe personnel evacuation.

10.3.5 Communication system

A variety of personnel communication systems will be employed throughout the surface and underground facilities of the experimental complex. All fire emergency communication systems are directly connected to the surface fire control center monitored by dedicated fire-watch personnel around the clock. An intercom communication system that has broadcast, point-to-point calling, and central command functionality will be used for working communications throughout the experimental complex. Local telephone systems are furnished at several key locations at the surface construction site for off-site communication.

High-bandwidth and private optical fiber channels will be acquired from local network providers for the experimental complex, to meet the demand for transmission of experimental data and general office communication.

10.4 Risk Analysis and Measures

The risk assessment for the project depends on the results of the detailed geological survey (section 10.2). Special risk assessment of the civil construction project include: risk assessment of geological hazards, seismic studies, water and soil conservation, and ecological impact on the surrounding environment. Geological survey and recommendations will be fully complied. Only major risks during the construction and operation phase, especially unpredictable risks and mitigation measures, are discussed here.

The underground cavities in this project are deep with large open spans, and the inclined shaft passes through complex geological area. Therefore, unpredictable collapse of the cavities, shafts or tunnels, along with water seepage are the major risks in the construction phase, and they will have direct impact to the project schedule and construction cost. The geological survey also indicates that faults may exist in the interconnecting tunnels at the experimental hall elevation from the inclined shaft or the vertical shaft, to the experimental hall. This represents the greatest uncertainty to the construction and worker safety. Possible mitigation measures include: perform geological forecast in advance to make appropriate engineering plans, and prepare structural design solutions based on geological conditions as the project is implemented. Another major risk in the construction phase is rock burst. Although the rock burst intensity in the experimental hall predicted by the geological survey is not high, plans should be there to prepare for the worst.

During the operational phase of the project, underground collapse and flooding are unpredictable risks that must be considered. It is recommended that a real-time rock monitoring system, such as a 3-D visual early warning system, should be established. This would monitor the stress and deformation of the cavity enclosing rock in real-time, to provide automatic early warning so appropriate and timely measures can be taken. Additionally, rock-safety consultants can be employed to analyze the data taken from monitoring system to provide hazard analysis and timely safety warnings. Dual-egress design also provides safety assurance for underground evacuation of personnel. Underground water conditions will be monitored and alarmed for accumulation and daily discharge to the surface. In conjunction with patrol checks of underground cavities and tunnels, any water abnormalities can be acted upon.

10.5 Schedule

The total civil construction period for the entire site complex is 36 months. It is predicted that the work will commence January/2015, and the civil construction phase of the project should be finished and handed over to the experimental users by December/2017.

Chapter 11

Assembly, Installation and Engineering Issues

11.1 Introduction

After the completion of civil construction, through systems integration, assembly, installation and commissioning, all subsystems will be formed as a whole JUNO detector.

In this process, we need to establish various engineering regulations and standards, and to coordinate subsystems' assembly, installation, testing and commissioning, especially their onsite work.

11.1.1 Main Tasks

Main tasks of the integration work include:

- To prepare plans and progress reports of each phase;
- To establish a project technology review system;
- To standardize the executive technology management system;
- To have strictly executive on-site work management system;
- To develop and specify security management system on-site;
- To prepare common tools and equipment for each system, and to guarantees project progress;
- To coordinate the installation progress of each system according to the on-site situation.

11.1.2 Contents

The work contents mainly include:

- To summarize the design, and review progress of each subsystem;
- To organize preparation work for installation in the experiment region;

- To inspect and certify Surface Buildings, underground Tunnels, and Experiment Hall with relevant utilities;
- To coordinate technology interfaces between key parts;
- To coordinate the procedure of assembly and installation both on surface and underground;

11.2 Design Standards, Guidelines and Reviews

11.2.1 Introduction

There will be a document to outline the mechanical design standards or guidelines that will be applied to the design work. It also describes the review process of engineering design that will be implemented to ensure that experimental equipment meets all requirements for performance and safety. The following is a brief summary of the guidance that all mechanical engineers/designers should follow in the process. For reasons ranging from local safety requirements to common sense practices, the following information should be understood and implemented in the design process.

11.2.2 Institutional Standards

When specific institutional design standards or guidelines exist, they should be followed. The guidelines outlined are not meant to replace but instead to supplement institutional guidelines. The majority of equipment and components built for the JUNO Experiment will be engineered and designed at home institutions, procured or fabricated at commercial vendors, then eventually delivered, assembled, installed, tested and operated at the JUNO Experimental facilities, Jiangmen, China. The funding agencies in other countries as well as Jiangmen, China will have some guidelines in this area, as would your home institutions. Where more than one set of guidelines exist, use whichever are the more stringent or conservative approaches.

11.2.3 Design Loads

The scope of engineering analysis should take handling, transportation, assembly and operational loads into account as well as thermal expansion considerations caused by potential temperature fluctuations.

For basic stability and a sensible practice in the design of experimental components an appropriate amount of horizontal load (0.10 g) should be applied.

In addition, seismic requirements for experimental equipment is based on a National Standard of People's Republic of China Code of Seismic Design of Buildings GB 50011-2010. At the location of the JUNO Experiment the seismic fortification intensity is grade 7 with a basic seismic acceleration of 0.10 g horizontal applied in evaluating structural design loads. A seismic hazard analysis should be performed and documented based on this local code. The minimum total design lateral seismic base shear force should be determined and applied to the component. The direction of application of seismic forces would be applied at the CG of the component that will produce the most critical load effect, or separately and independently in each of the

two orthogonal directions. A qualitative seismic performance goal defines component functionality as: the component will remain anchored, but no assurance it will remain functional or easily repairable. Therefore, a seismic design factor of safety F.S. > 1 based on the Ultimate Strength of component materials would satisfy this goal.

Where an anticipated load path as designed above, allows the material to be subjected to stresses beyond the yield point of the material, redundancy in the support mechanism must be addressed in order to prevent a collapse mechanism of the structure from being formed.

The potential for buckling should also be evaluated. It should be noted that a rigorous analytical seismic analysis may be performed in lieu of the empirical design criteria. This work should be properly documented for review by the Chief Engineer and appropriate Safety Committee personnel

11.2.4 Materials Data

All materials selected for component design must have their engineering data sources referenced along with those material properties used in any structural or engineering analysis; this includes fastener certification. There are many sources of data on materials and their properties that aid in the selection of an appropriate component material. There are many national and international societies and associations that compile and publish materials test data and standards. Problems frequently encountered in the purchasing, researching and selection of materials are the cross-referencing of designations and specification and matching equivalent materials from differing countries.

It is recommended that the American association or society standards be used in the materials selection and specification process, or equivalency to these standards must be referenced. Excellent engineering materials data have been provided by the American Society of Metals or Machine Design Handbook Vol. 1-5 and Mechanical Industry Publishing Co. in PRC, Vol 1-6, 2002, which are worth investigating.

11.2.5 Analysis Methods

The applicable factors of safety depend on the type of load(s) and how well they can be estimated, how boundary conditions have been approximated, as well as how accurate your method of analysis allows you to be.

Bounding Analyses: Bounding analysis or rough scoping analyses have proven to be valuable tools. Even when computer modeling is in your plans, a bounding analysis is a nice check to help avoid gross mistakes. Sometimes bounding analyses are sufficient. An example of this would be for the case of an assembly fixture where stiffness is the critical requirement. In this case where deflection is the over-riding concern and the component is over-designed in terms of stress by a factor of 10 or more, then a crude estimation of stress will suffice.

Closed-Form Analytical Solutions: Many times when boundary conditions and applied loads are simple to approximate, a closed-form or handbook solution can be found or developed. For the majority of tooling and fixture and some non-critical experimental components, these types of analyses are sufficient. Often, one of these

formulas can be used to give you a conservative solution very quickly, or a pair of formulas can be found which represent upper and lower bounds of the true deflections and stresses. Formulas for Stress and Strain by Roark and Young is a good reference handbook for these solutions.

Finite Element Analysis: When the boundary conditions and loads get complex, or the correctness of the solution is critical, computer modeling is often required. If this is the case, there are several rules to follow, especially if you are not intimately familiar with the particular code or application.

1. Always bound the problem with an analytical solution or some other approximate means.
2. If the component is critical, check the accuracy of the code and application by modeling a similar problem for which you have an analytical or handbook solution.
3. Find a qualified person to review your results.
4. Document your assumptions and results.

11.2.6 Failure Criteria

The failure criterion depends upon the application. Many factors such as the rate or frequency of load application, the material toughness (degree of ductility), the human or monetary risk of component failure as well as many other complications must be considered.

Brittle materials (under static loads, less than 5% yield prior to failure), includes ceramics, glass, some plastics and composites at room temperature, some cast metals, and many materials at cryogenic temperatures. The failure criterion chosen depends on many factors so use your engineering judgment. In general, the Coulomb-Mohr or Modified Mohr Theory should be employed.

Ductile materials (under static loads, greater than 5% yield prior to failure), includes most metals and plastics, especially at or above room temperature. The failure criterion chosen again ultimately rests with the cognizant engineer because of all the adverse factors that may be present. In general, the Distortion- Energy Theory, or von Mises-Hencky Theory (von Mises stresses), is most effective in predicting the onset of yield in materials. Slightly easier to use and a more conservative approach is the Maximum-Shear-Stress Theory.

11.2.7 Factor of Safety

Some institutions may have published guidelines which specifically discuss factors of safety for various applications. For the case where specific guidelines do not exist, the following may be used.

Simplistically, if F is the applied load (or S the applied stress), and Ff is the load at which failure occurs (or Ss the stress at which failure occurs), we can then define the factor of safety (F.S.) as:

$$F.S. = F_f/F \quad \text{or} \quad S_s/S$$

The word failure, as it applies to engineering elements or systems, can be defined in a number of ways and depends on many factors. Discussion of failure criteria is presented in the previous section, but for the most common cases it will be the load at which yielding begins.

11.2.8 Specific Safety Guidelines for JUNO

Lifting and handling fixtures, shipping equipment, test stands, and fabrication tooling where weight, size and material thickness do not affect the physical capabilities of the detector, the appropriate F.S. should be at least 3. When life safety is a potential concern, then a F.S. of 5 may be more appropriate. Note that since the vast majority of this type of equipment is designed using ductile materials, these F.S.'s apply to the material yield point. Experimental hardware that does not present a life safety or significant cost/schedule risk if failure occurs, especially where there is the potential for an increase in physics capabilities, the F.S. may be as low as 1.5. Many factors must be taken into account if a safety factor in this low level is to be employed: a complete analysis of worst case loads must be performed; highly realistic or else conservative boundary conditions must be applied; the method of analysis must yield accurate results; reliable materials data must be used or representative samples must be tested. If F.S.'s this low are utilized, the analysis and assumptions must be highly scrutinized. Guidelines for F.S. for various types of equipment are:

Type of Equipment	Minimum F.S.	Notes
Lifting and handling	3 - 5	Where there is a risk to life safety or to costly hardware, choose F.S closer to 5.
Test stands, shipping and assembly fixtures.	3	
Experimental hardware	1.5 - 3	1.5 is allowable for physics capability and analysis where method is highly refined

11.2.9 Documentation

It is not only good engineering practice to document the analysis, but it is an ESH&Q requirement for experimental projects. For this reason all major components of JUNO Experiment will have their engineering analyses documented as Project Controlled Documents. Utilize your institutional documentation formats or use the following guidelines. Calculations and analyses must

- Be hard copy documented.
- Follow an easily understood logic and methodology.
- Be legible and reproducible by photocopy methods.

- Contain the following labeling elements.
  - Title or subject
  - Originators signature and date
  - Reviewers signature and date
  - Subsystem WBS number.
  - Introduction, background and purpose.
  - Applicable requirements, standards and guidelines.
  - Assumptions (boundary conditions, loads, materials properties, etc.).
  - Analysis method (bounding, closed form or FEA).
  - Results (including factors of safety, load path and location of critical areas).
  - Conclusions (level of conservatism, limitations, cautions or concerns).
  - References (tech notes, textbooks, handbooks, software code, etc.).
  - Computer program and version (for computer calculations)
  - Filename (for computer calculations).

11.2.10 Design Reviews

All experimental components and equipment whether engineered or procured as turn-key systems will require an engineering design review before procurement, fabrication, assembly or installation can proceed. The L2 subsystem manager will request the design the review from the project management office, which will appoint a chair for the review and develop a committee charge. The selected chair should be knowledgeable in the engineering and technology, and where practical, should not be directly involved in the engineering design effort. With advice from the L2, the technical board and project office chair appoints members to the review committee that have experience and knowledge in the engineering and technology of the design requiring review. At least one reviewer must represent ESH&Q concerns. The committee should represent such disciplines as:

- Science requirements
- Design
- Manufacturing
- Purchasing
- Operational user
- Maintenance
- Stress analysis
- Assembly/installation/test
- Electrical safety

- ESH&Q

For the JUNO project there will be a minimum of two engineering design reviews: Preliminary and Final. The preliminary usually takes place towards the end of the conceptual design phase when the subsystem has exhausted alternative designs and has made a selection based on value engineering. The L2 along with the chair ensures that the preliminary design review package contains sufficient information for the review along with:

- Agenda
- Requirements documents
- Review committee members and charge
- Conceptual layouts
- Science performance expectations
- Design specifications
- Supportive R&D or test results
- Summaries of calculations
- Handouts of slides

A final design review will take place before engineering drawings or specifications are released for procurement or fabrication. The L2 along with the chair ensures that the final design review package contains sufficient information for the final review along with:

- Changes or revisions to preliminary design
- Completed action items
- Final assembly and detailed drawings
- Final design specifications
- Design calculations and analyses

The committee chair will ensure that meeting results are taken and recorded along with further action items. The committee and chair shall prepare a design review report for submittal to the project office in a timely manner which should include:

- Title of the review
- Description of system or equipment
- Copy of agenda
- Committee members and charge
- Presentation materials

- Major comments or concerns of the reviewers
- Action items
- Recommendations

The project office will file the design review report and distribute copies to all reviewers and affected groups.

11.3 On-site management

According to the experience from the Daya Bay Experiment, an effective technology review system has been well practiced. In JUNO, we will take it as a good reference and carry out for standardized review from the start of all system design, scheme argument, technology checks, we should also establish management system, to cover engineering drawing control, engineering change control procedure, and mechanical design standards, guidelines and reviews, etc.

To control on-site work process, proper process should be introduced as well as a management structure. Safety training and safety management structure should be also introduced.

11.4 Equipment and Tools Preparation on Sit

All of key equipment, devices and tools should be in place and get acceptance for installation on site, including

- Cranes:
  - 2 sets of bridge crane with 12T/5T load capacity, and lifting range should cover any point for components delivery and installation in EH;
  - Several lifting equipment are needed in Surface Assembly areas, Assembly Chamber underground, Storage area for Liquid Scintillation, and other Chambers accordingly;
- Removable lifting equipment: Forklifts, manual hydraulic carriages, carts, etc.
- Mobile vehicle for smaller items: Pickup van, battery car, and so on;
- Several work aloft platform: Scissor lifts, Boom lifts, Scaffoldings and Floating platforms, etc.
- Common Tooling: complete kits of tool, fixtures, jigs, models, work-bench, cabinets, and tables, etc.
- Machine shop, Power equipment rooms, Control rooms are ready to be put into use.
- Safety measures and relevant equipment in place.

11.5 Main Process of Installation

Since there still are several optional design versions which could be decided later, and different design could have different requirements for installation, therefore, the specific installation procedures will be established and developed later, here a very roughly procedure installation is given.

- Mounting, debugging, testing of basic utilities, such as, cranes, vertical elevator, scaffoldings, test devices, etc.
- Survey, alignment, and adjustment for tolerances of form and position, include, embedded inserts, anchor plates, positioning holes, etc.
- Mounting Bottom Structure of Veto Cherenkov detector on to floor of Water Pool.
- Mounting anchor-plate for support poles of CD on the floor of Water Pool
- Pre-mounting of Top Structure of Veto system along wall of Water Pool
- Mount Substrate and Rails for Bridge over the water Pool edges
- Mount Tyvek with support structure for Water Cherenkov Detector, and with PMT positioning in the Water Pool
- Installation for CD with its PMT system and cabling in Water Pool details will be established until design final selection.
- Mount Calibration System
- Mount Geomagnetic Shielding system around Central Detector in the Pool
- Final installation for Tyvek and PMT of Veto system in the Pool
- Mount a temporary protective cover on top of Pool, to prevent from anything falling into Pool
- Mount Bridge on the rails, and drive it closed
- Mount Top Track Detector on Bridge and establish Electronic Room there
- Have Cabling completion, and test to get normal signals
- Check Grounding Electrode
- Dry Run
- Final Cleaning for Water Pool, then, drain out
- Filling Water, LS, LAB (or Oil) evenly into Water Pool and CD
- Mount Final Pool Cover, closed, and get fixation